UNIVERSITÄT PADERBORN
Die Universität der Informationsgesellschaft

Nuclear Magnetic Resonance Studies of Energy Storage Materials

Dissertation

zur Erlangung des Grades
Doktor der Naturwissenschaften
(Dr. rer. nat.)
an der Fakultät für Naturwissenschaften
der Universität Paderborn

vorgelegt von

Waldemar Keil
geboren am 30.09.1993 in Jarowoje (Russland)

Paderborn, 07.07.2022

Promotionskommission

Die vorliegende Dissertation wurde von März 2019 bis Juni 2022 im Institut für Physikalische Chemie am Department Chemie der Universität Paderborn angefertigt.

Prof. Dr. Claudia Schmidt (Universität Paderborn)	Erstgutachter
Prof. Dr. Michael Tiemann (Universität Paderborn)	Zweitgutachter

Erklärung

Hiermit versichere ich, dass die vorliegende Arbeit selbstständig angefertigt wurde. Ich habe dazu keine weiteren als die angegeben Hilfsmittel benutzt und die aus anderen Quellen entnommenen Stellen als solche gekennzeichnet. Die Arbeit ist nicht in gleicher oder ähnlicher Form zuvor zur Prüfung eingereicht worden.

Paderborn, 07.07.2022

Waldemar Keil

Danksagung

An dieser Stelle möchte ich mich zunächst bei Prof. Dr. Claudia Schmidt bedanken, bei der ich seit 2015 in der Arbeitsgruppe arbeiten und etliches lernen durfte. Danke für die Vielzahl an Projekten, an denen ich teilnehmen durfte, für die zahllosen erhellenden Gespräche, die Möglichkeit diese Arbeit anfertigen zu können und die Unterstützung über all die Jahre hinweg. Meinem guten Freund und ehemaligen Gruppenmitglied Dr. Amin Ordikhani-Seyedlar möchte ich für seinen Ehrgeiz danken, mir die Techniken und das Verständnis für die NMR mit großem Enthusiasmus beizubringen.

Weiterhin möchte ich mich bei Prof. Dr. Michael Tiemann für die fruchtbare Zusammenarbeit, die vielen gemeinsamen Projekte, die freundliche Arbeitsatmosphäre und für das Verfassen des Zweitgutachtens bedanken. Besonders Dr. Christian Weinberger, Dr. Ali Javed, Josefin Klippstein, Marvin Kloß und Linda Kothe möchte ich an dieser Stelle für die Zusammenarbeit, die fachlichen Gespräche und für die entspannten gemeinsamen Kaffeepausen danken.

Darüber hinaus möchte ich mich bei Jun.-Prof. Dr. Hans-Georg Steinrück bedanken, für die überaus motivierende Zusammenarbeit, aber auch für die Motivation den ein oder anderen längeren Lauf zu unternehmen. Besonders dank ich den Mitarbeitern Xiaodan Xu und Andreas Kuhlmann für die angenehme Arbeitsatmosphäre, für das gemeinsame Tüfteln an der Box und auch für die nichtfachlichen Gespräche.

Der Arbeitsgruppe von Prof. Dr. Thomas D. Kühne möchte ich an dieser Stelle ebenfalls danken. Insbesondere bei Dr. Hossam Elgabarty, mit dem ich nicht nur die angenehme Zusammenarbeit schätzte, sondern auch die vielen erfrischenden Laufeinheiten. Darüber hinaus möchte ich mich bei Dr. Svetlana Pylaeva für die spannende Zusammenarbeit und Wissensaustausch bedanken.

Besonders herzlich möchte ich mich bei den technischen Mitarbeiterinnen, Rita Egert-Tiesbohnenkamp, Nadine Buitkamp, Susanne Keuker-Baumann, Karin Stolte, Andrea Harbarth und Christiane Gloger bedanken, die mich in all den Jahren begleitet haben. Besonders das Zwischenmenschliche werde ich vermissen. An dieser Stelle möchte ich auch Katrin Bandzius danken, die vieles im Hintergrund organisiert. Ihr seid die guten Seelen des Departments.

Мы только смотрим, но не видим.

-Andrei Tarkovsky

Dann, wenn mein Puls zu rasen scheint
wenn Stille und Chaos gleichzeitig in mir herrschen
dann denke ich daran:

Die Vögel fliegen heute genauso schnell
wie vor hunderten von Jahren,
die Bäume brauchen genau dieselbe Zeit
um Wurzeln zu schlagen,
der Wind nimmt seine uralten Wege ein.

Und wenn mein Puls verstummt,
so wird das Wasser im gleichen Rhythmus
kommen und gehen,
die Blätter mit derselben Geschwindigkeit zu Boden fallen,
die Sonne wird dieselben Bögen zeichnen,
so wie es schon immer war.

-Marie Kortenbruck

Abstract

Different physicochemical properties of i) polymer electrolytes and their components and of ii) carbonaceous materials, were examined in this work.

i) Hydrogen bonding is found in the ionic liquid [EMIM][OTf], which is used to prepare deuterated [EMIM]$^+$. Ion dynamics (^{7}Li, ^{1}H) is studied for PVdF-HFP-based polymer electrolytes and found to corelate well with previously measured electrochemical data. Anomalous ion diffusion probed by diffusion NMR measurements is found for the studied polymer electrolytes. Further, electrochemical probes were used to follow the polymer electrolyte degradation upon cycling the latter in a symmetric lithium cell. Additional, Magic-angle-spinning (MAS) NMR measurements performed on the studied polymer electrolytes are found to increase the ionic conductivity tremendously.

ii) The process of pyrolysis of sucrose- and trehalose derived hydrochars is followed *ex situ* by means of ^{13}C NMR spectroscopy. Increasing the pyrolysis temperature causes a stepwise growth of graphite-like sheets, with a large anisotropy of the magnetic susceptibility. Further, the chemical structure of poly(C_3O_2) is analyzed and confirmed to be composed of polypyrone units. Finally, time-resolved ^{1}H measurements on H_2O impregnated C_1N_1 samples and purely carbon-based samples were used to differ between in-pore and ex-pore water, finding that water uptake is essentially absent for the C_1N_1 material.

Kurzzusammenfassung

In dieser Arbeit wurden verschiedene physikochemische Eigenschaften von i) Polymerelektrolyten und ihren Bestandteilen sowie von ii) kohlenstoffhaltigen Materialien untersucht.

i) Zunächst wird die Wasserstoffbrückenbindung in der ionischen Flüssigkeit [EMIM][OTf] untersucht, die zur Herstellung von deuteriertem [EMIM]$^+$ verwendet wird. Die Ionendynamik (^{7}Li, ^{1}H) wird für PVdF-HFP-basierte Polymerelektrolyte untersucht, wobei die Ergebnisse gut mit zuvor gemessenen elektrochemischen Daten übereinstimmen. Für die untersuchten Polymerelektrolyte wurde eine anomale Ionendiffusion festgestellt, die durch Diffusions-NMR-Messungen ermittelt wurde. Darüber hinaus wurden elektrochemische Messungen durchgeführt, um den Abbau des Polymerelektrolyten beim Zyklus in einer symmetrischen Lithiumzelle zu verfolgen. Zusätzliche Magic-angle-spinning NMR-Messungen an den Polymerelektrolyten haben ergeben, dass die Messung die Ionenleitfähigkeit enorm erhöht.

ii) Der Prozess der Pyrolyse von Saccharose- und Trehalose-Hydrokohle wird *ex situ* mittels ^{13}C NMR Spektroskopie verfolgt. Die Erhöhung der Pyrolysetemperatur führt zu einem schrittweisen Wachstum von graphitähnlichen Schichten mit einer großen Anisotropie der magnetischen Suszeptibilität. Außerdem wird die chemische Struktur von Poly(C_3O_2) analysiert und bestätigt, dass es aus Polypyron-Einheiten besteht. Schließlich wurden zeitaufgelöste ^{1}H-Messungen an mit H_2O imprägnierten C_1N_1 Proben und an rein kohlenstoffbasierten Proben durchgeführt, um zwischen Wasser in Poren und außerhalb der Poren zu unterscheiden, wobei festgestellt wurde, dass das C_1N_1 Material im Wesentlichen kein Wasser aufnimmt.

Kooperationen und Hilfsmittel

Die vorliegende Arbeit wurde in gekennzeichneten Teilen in Kooperation mit Prof. Dr. Amita Chandra (University of Delhi), Dr. Muslim Dvoyashkin (Universität Leipzig), Dr. Martin Wortmann (Universität Bielefeld), Dr. Nieves Lopez Salas und Dr. Mateusz Odziomek (beide Max-Planck-Institut für Kolloid- und Grenzflächenforschung in Potsdam) angefertigt. Die Art der Beiträge der Kooperationspartner sind an den entsprechenden Stellen vermerkt.

Folgende Hilfsmittel wurden für die Erstellung der vorliegenden Arbeit verwendet: Die Arbeit wurde mit Hilfe der Software Microsoft Word © 2020 Microsoft Corporation verfasst. Die Auswertung der Lösungsmittel NMR-Spektren wurde mit der Software TopSpin (Version 3.4) © 2021 Bruker ausgewertet. Festkörper NMR Spektren wurden mit der Software Origin 2019b © 2020 OriginLab Corporation ausgewertet. Berechnungen der Quadrupolspektren wurden mit Hilfe der QUEST software durchgeführt. Chemischen Strukturen wurden mit der Software ChemDraw Professional (Version 19.0.1.28) © 1998–2019 PerkinElmer Informatics Inc. gezeichnet. Weitere Molekülstrukturen wurden mithilfe von Avogadro (Version 1.2.0) © 2018 Avogadro Chemistry angefertigt. Andere Abbildungen und Skizzen wurden mit Inkscape (Version 1.1) © 2021 Inkscape-Entwicklerteam erstellt.

List of peer-reviewed publications

[1] Weinberger, C., Heckel, T., Schnippering, P., Schmitz, M., Guo, A., Keil, W., Marsmann, H. C., Schmidt, C., Tiemann, M. & Wilhelm, R. (2019). Straightforward immobilization of phosphonic acids and phosphoric acid esters on mesoporous silica and their application in an asymmetric aldol reaction. *Nanomaterials*, *9*(2), 249.

[2] Wortmann, M., Frese, N., Mamun, A., Trabelsi, M., Keil, W., Büker, B., Javed, A., Tiemann, M., Moritzer, E., Ehrmann, A., Hütten, A., Schmidt, C., Gölzhäuser, A., Hüsgen, B., & Sabantina, L. (2020). Chemical and morphological transition of poly (Acrylonitrile)/poly (vinylidene fluoride) blend nanofibers during oxidative stabilization and incipient carbonization. *Nanomaterials*, *10*(6), 1210.

[3] Wortmann, M., Frese, N., Keil, W., Brikmann, J., Biedinger, J., Brockhagen, B., Reiss, G., Schmidt, C., Gölzhäuser, A., Moritzer, E. & Hüsgen, B. (2020). The deterioration mechanism of silicone molds in polyurethane vacuum casting. *ACS Applied Polymer Materials*, *2*(11), 4719-4732.

[4] Wortmann, M., Viertel, K., Welle, A., Keil, W., Frese, N., Hachmann, W., Krieger, P., Brikmann, J., Schmidt, C., Moritzer, E. & Hüsgen, B. (2021). Anomalous bulk diffusion of methylene diphenyl diisocyanate in silicone elastomer. *International Journal of Heat and Mass Transfer*, *177*, 121536.

[5] Wortmann, M., Keil, W., Brockhagen, B., Biedinger, J., Westphal, M., Weinberger, C., Diestelhorst, E., Hachmann, W., Zhao, Y., Tiemann, M., Reiss, G., Hüsgen, G., Schmidt, C., Sattler, K. & Frese, N. (2022). Pyrolysis of sucrose-derived hydrochar. *Journal of Analytical and Applied Pyrolysis*, *161*, 105404.

[6] Keil, W., Zhao, K., Oswald, A., Bremser, W., Schmidt, C., & Hintze-Bruening, H. (2022). Thermostable water reservoirs in the interlayer space of a sodium hectorite clay through the intercalation of γ-aminopropyl (dimethyl) ethoxysilane in toluene. *Physical Chemistry Chemical Physics*, *24*(1), 477-487.

[7] Weinberger, C., Zysk, F., Hartmann, M., Kaliannan, N. K., Keil, W. Kühne, T. D., & Tiemann, M. (2022). The Structure of Water in Silica Mesopores - Influence of the Pore Wall Polarity. *Advanced Materials Interfaces,* (9), 2200245.

[8] Odziomek, M., Giusto, P., Kossmann, J., Tarakina, N. V., Heske, J., Rivadeneira, S. M., Keil, W., Schmidt, C., Mazzanti, S., Savateev, A., Kühne, T. D., Antonietti, M. & López-Salas, N. (2022). "Red carbon": A rediscovered polymeric, crystalline semiconductor. *Submitted to Advanced Materials*.

[9] Keil, W., Nolkemper, K., Heske, J., Kossmann, J., Elgabarty, H., Schmidt, C., Kühne, T. D., Odziomek, M. & López-Salas, N. (2022). Water interactions with polar C1N1 surfaces. *To be submitted*.

[10] Wortmann, M., Keil, W., Diestelhorst, E., Haverkamp, R., Westphal, M., Brockhagen, B., Biedinger, J., Weinberger, C., Bondzio, L., Tiemann, M., Hütten, A., Hellweg, T., Schmidt, C., Reiss, G., Sattler, K. & Frese, N. (2022). Synthesis of Hard Carbon Microspheres with Binary Size Distribution and Hierarchical Porosity via Hydrothermal Carbonization of Trehalose. *To be submitted*.

[11] Keil, W.*, Khurana, S.*, Chandra, A. & Schmidt, C. (2022). NMR studies of PVdF-HFP based hybrid ionogels with confined electrolyte and in-situ formed silica. *To be submitted*.

List of poster and conference contributions

[1] <u>Schmidt, C</u>., Keil, W., Khurana, S., Vyas, M. K. & A. Chandra, *Ionic Liquid Based Organic-Inorganic Hybrid Electrolytes Studied by Nuclear Magnetic Resonance,* Invited Talk at 7th International Conference on Electroactive Polymers (ICEP-2019), February 3–8, 2019, Udaipur, Rajasthan, India.

[2] <u>Keil, W</u>., Schmidt, C., Khurana, S., Vyas, M. K. & A. Chandra, *NMR Investigations on Ionic-Liquid-based Gel Polymer Electrolytes,* Oral presentation at the 118th General Assembly of the German Bunsen Society for Physical Chemistry (Bunsentagung 2019), May 30 – June 1, Jena, Germany.

[3] <u>Keil, W</u>., Siebrecht, M., Vyas, M. K., Chandra, A. & Schmidt, C. *Ion Dynamics in Polymer Composites for Electromagnetic Shielding,* Poster presentation at GDCH-JCF (GDCH Jung Chemiker Forum), February 27, 2020, Paderborn, Germany. *Awarded Poster*.

[4] <u>Schmidt, C</u>., Keil, W., Khurana, S., Vyas, M. K., Beerbaum, M., Issayeva, D., Dvoyashkin, M. & Chandra, A. *Structure and Dynamics of Ionic-Liquid-Containing Polymer Gel Electrolytes as Seen by NMR,* Poster presentation at ISMAR EUROMAR Joint Conference and GDCh FGMR Discussion Meeting, August 25 – 30, 2019, Berlin, Germany.

[5] <u>Keil, W</u>. Siebrecht, M., Vyas, M. K., Chandra, A., Graf, R. & Schmidt, C. *Ion Mobilities in Polymer Composites for Electromagnetic Shielding,* Poster presentation at Ampere NMR School, June 21 – 23, 2021, Zakopane, Poland (virtual event).

[6] <u>Keil, W</u>. Siebrecht, M., Vyas, M. K., Chandra, A., Graf, R. & Schmidt, C. *Ion Mobilities in Polymer Composites for Electromagnetic Shielding,* Poster presentation at ISMAR, APNMR Conference August 22 – 27, 2021, Osaka, Japan (virtual event).

List of abbreviations

BET – Brunauer-Emmett-Teller

BMS – Bulk Magnetic Susceptibility

CP – Cross Polarization

CSA – Chemical Shift Anisotropy

CT – Central Transition

DC – Direct Current

DFT – Density Functional Theory

DMC – Dimethyl Carbonate

DOSY – Diffusion Ordered Spectroscopy

DP – Direct Polarized

DSC – Differential Scanning Calorimetry

EC Ethylene Carbonate

EDX – Energy Dispersive X-ray Spectroscopy

EFG – Electric Field Gradient

EIS – Electrochemical Impedance Spectroscopy

ES – Electrolyte Solution

[EMIM] – 1-ethyl-3-methylimidazolium

FWHM – Full Width Half Maximum

GPE – Gel Polymer Electrolyte

HC – Hydro char

HCS – Hard Carbon Spheres

HIM – Helium Ion Microscopy

IR – Infrared Spectroscopy

LiF – Lithium fluoride

LiOTf – Lithium trifluoromethanesulfonate

LiTFSI – Lithium bis (trifluoromethanesulfonyl)imide

MAS – Magic Angle Spinning

MSD – Mean Squared Displacement

NMR – Nuclear Magnetic Resonance

NICS – Nucleus Independent Chemical Shift

LIB – Lithium Ion Battery

LP30 – 1 M $LiPF_6$ in EC: DMC (1:1)

[OTf] – Trifluoromethanesulfonate

PBE – Perdew-Burke-Ernzerhof

PEO – Poly(ethylene oxide)

PFG – Pulsed Field Gradient

PPM – Parts Per Million

PVDF-HFP – Poly(vinylidenefluoriud-co-hexafluoropropylene)

PAS – Principal Axis System

SEI – Solid Electrolyte Interphase
SEM – Scanning Electron Microscopy
ST – Satellite Transition
TEM – Transmission Electron Microscopy
TEOS – Tetraethyl orthosilicate
TGA – Thermal Gravimetric Analysis
TMS – Tetramethyl silane
VTF – Vogel-Tamman-Fulcher
XPS – X-ray Photoelectron Spectroscopy
XRD – X-ray Diffraction

Table of contents

Chapter 1

Introduction

1.1 Materials for Energy Transition

Since the EU and 190 other states have signed the Paris Climate Accords in 2015, they have committed themselves to reduce their CO_2 emissions drastically, in order to contain the effects of climate change.[1] As a result, fossil fuels and other climate harmful energy sources should be permanently replaced by renewable energies such as solar, hydro and wind power. However, the implementation of these energy sources comes along with a series of new problems such as storing and releasing energy on demand. In addition, there is an increasing demand of electrical energy for notebooks, smartphones and electric vehicles, all of which use portable batteries.

Therefore, research on materials for new energy storage devices can make a contribution in order to reach the mentioned climate goals and meeting the demands for efficient and recyclable portable batteries.[2] Rechargeable lithium ion batteries (LIBs) have been commercially introduced by Sony in the early 1990s and were optimized since then.[3] Until today, the basic principle of LIBs to store energy by reversible chemical redox reactions between both electrodes and the electrolyte remains the same.[4] During charging, lithium is oxidized at the site of the cathode and is released as a lithium cation. A separation of electronic and ionic current is induced at this stage. At the same time the electric current and ionic current flows from the cathode to the anode. During discharging the current is reversed.

In addition to ion batteries, which can nowadays even serve for power grid solutions, supercapacitors are a second class of energy storage devices.[5,6] Unlike batteries, supercapacitors store potential energy electrostatically in electrostatic double-layers, commonly known as the Helmholtz double-layer. Often, conductive carbonaceous matrices with large specific surface areas serve as electrodes in which an electrolyte solution is immersed. Charge is stored at the

interphase between the electrode surface and the electrolyte, whenever a potential difference is applied to a two-electrode setup. Therefore, no chemical (redox) reaction occurs in case of supercapacitors.[7, 8]

Compared to supercapacitors, lithium ion batteries exhibit much higher energy densities but lower power densities. This means that substantially more time is required to fully charge a lithium ion battery compared to a supercapacitor. On the other hand, supercapacitors can be charged within seconds and have a substantially higher cycle lifetime.[7, 8]

Powering mobile phones or electric vehicles requires high energy densities. Rechargeable lithium ion batteries suit these applications particularly well. In the past, electrolyte leakage or flammability was observed for numerous metal ion batteries, from which serious safety issues emerged. Recently, these safety issues are contained by implementing non-flammable electrolytes and electrodes.[9] Therefore, numerous approaches were focused on polymer- or solid electrolytes, which exhibit potential advantages over liquid electrolytes, such as safety, higher ion densities and flexibility, which allows adaption to the shape of the specific device.[10, 11] Additionally, electrode materials which enable cells with high specific energy densities are object of current research.

Modifying electrodes and electrolytes is useful, in order to enhance the performance of LIBs. Additionally, knowledge of already existing cells and how they work on a molecular/atomic level is gained in recent years. In this context, detailed studies about the formation of the solid electrolyte interface (SEI) (thin layer at the anode, which is formed by decomposition of the electrolyte) and its impact on the performance of cells have been carried out.[11] Concerning electrolytes, the well-established model system polyethylene oxide/ lithium bis (trifluoromethanesulfonyl)imide (PEO/LiTFSI) has been studied extensively.[10] In these studies a fundamental understanding of transport properties in PEO-based polymer electrolytes was developed, such as ion hopping along the oxygen coordination sites of PEO and further important physicochemical properties.

More recently, polymer electrolytes based on the statistical co-polymer poly(vinylidene fluoride-co-hexafluoropropylene) (PVdF-HFP) have been employed and display promising applications in lithium ion batteries.[12] A benefit of PVdF-HFP-based polymer electrolytes over PEO-based electrolytes is a higher ion conductivity, which favors a better cell performance.[9]

Complementary characterization techniques, such as electrochemical techniques and nuclear magnetic resonance (NMR) spectroscopy are combined for *ex situ* and *in situ* studies to probe transport properties and degradation from different perspectives. NMR as an established characterization technique has proven to be suitable to study energy storage materials.[13] Just recently, NMR probe heads to study *operando* the electrochemistry during charging/discharging are commercially available.[14]

1.2 Outline

The aim of this thesis is to gain a fundamental understanding of the underlying physicochemical properties of polymer electrolytes (and their constituents) and of carbonaceous electrodes. These two systems are the main subject of this work. The electrolytes studied are PVdF-HFP-based polymer electrolytes containing a lithium salt and an ionic liquid as a plasticizer. In addition, hybrid polymer electrolytes containing silica particles are examined.

Concerning electrode materials, three different carbonaceous materials were studied. The main focus, besides structural aspects, is directed towards the interaction of H_2O with these complex matrices in order to derive information about different pore systems. NMR measurements are particularly well suitable, due to its high sensitivity for different (local) H_2O environments, which can be studied non-invasive.

A brief introduction of the fundamental principles of lithium ion batteries and important electrochemical experiments are presented in Chapter 2. The basic concepts and interactions of the main technique used in this work, namely NMR spectroscopy, are discussed in Chapter 3. A brief overview about the materials studied in this work, namely salts, ionic liquids, polymer electrolytes and carbonaceous materials is given in Chapter 4.

PVdF-HFP-based polymer electrolytes are scrutinized in Chapter 5. Section 5.1 is devoted to ionic liquids. In particular hydrogen bonding interactions in two different ionic liquids are examined. H/D exchange experiments were performed, which turn out to be suitable to track back the interionic hydrogen bonding and reveal the hydrogen bond acceptor properties of the triflate anion. The relations between NMR measurements and electrochemical measurements for a polymer composite material containing silica particles are explored in Section 5.2. This section shows that ^7Li spinning-sideband intensities correlate linearly to lithium transference numbers. Multi-nuclear ion diffusion NMR experiments for the polymer composites are

discussed in Section 5.3. Fundamental differences in ion diffusion between bulk electrolyte solution and ion diffusion in polymer electrolytes are found. Section 5.4 demonstrates that electrochemical measurements in combination with *ex situ* NMR studies on polymer-electrolytes are useful to evaluate the electrolyte degradation. Section 5.5 scrutinizes an experiment specific effect that occurs during magic-angle-spinning (MAS). Physicochemical properties of a PVdF-HFP-based polymer electrolyte change drastically after exposing the material for several hours to MAS. In particular, ion conductivities increase after the material is spun under MAS.

Carbonaceous electrode materials are investigated in Chapter 6. The structural features of sucrose- and trehalose derived carbon-spheres are scrutinized in Section 6.1. The (almost) exclusively carbon-based products are structurally compared. In Section 6.2 polymeric C_3O_2 (so-called "red carbon") which contains nearly 40 atom% oxygen and its post-carbonization product are analyzed. The last section 6.3 examines the interaction of H_2O with carbonaceous materials studied in Chapter 6 and in particular with C_1N_1 (containing 50 atom% nitrogen). Differences in H_2O uptake between exclusively carbon-based materials and heteroatom containing materials are revealed by time-resolved ^1H MAS NMR.

The main results of this work are summarized in Chapter 7. Possible additional experiments are evaluated and discussed.

1.3 References

(1) Agreement Paris (2015, December). In *Report of* the *Conference of the Parties to the United Nations Framework Convention on Climate Change (21st Session, 2015: Paris). Retrieved December* (Vol. 4, p. 2017).

(2) Boyden, A., Soo, V. K., & Doolan, M. (2016). The environmental impacts of recycling portable lithium-ion batteries. *Procedia Cirp*, *48*, 188-193.

(3) Kim, J. S., Lee, D. C., Lee, J. J., & Kim, C. W. (2020). Optimization for maximum specific energy density of a lithium-ion battery using progressive quadratic response surface method and design of experiments. *Scientific Reports*, *10*(1), 1-11.

(4) Manthiram, A. (2017). An outlook on lithium ion battery technology. *ACS central science*, *3*(10), 1063-1069.

(5) Simon, P., & Gogotsi, Y. (2010). Materials for electrochemical capacitors. *Nanoscience and technology: a collection of reviews from Nature journals*, 320-329.

(6) Pandolfo, A. G., & Hollenkamp, A. F. (2006). Carbon properties and their role in supercapacitors. *Journal of power sources*, *157*(1), 11-27.

(7) Zou, C., Zhang, L., Hu, X., Wang, Z., Wik, T., & Pecht, M. (2018). A review of fractional-order techniques applied to lithium-ion batteries, lead-acid batteries, and supercapacitors. *Journal of Power Sources*, *390*, 286-296.

(8) González, A., Goikolea, E., Barrena, J. A., & Mysyk, R. (2016). Review on supercapacitors: Technologies and materials. *Renewable and Sustainable Energy Reviews*, *58*, 1189-1206.

(9) Stephan, A. M., & Nahm, K. S. (2006). Review on composite polymer electrolytes for lithium batteries. *Polymer*, *47*(16), 5952-5964.

(10) Popovic, J., Brandell, D., Ohno, S., Hatzell, K. B., Zheng, J., & Hu, Y. Y. (2021). Polymer-based hybrid battery electrolytes: theoretical insights, recent advances and challenges. *Journal of Materials Chemistry A*, *9*(10), 6050-6069.

(11) Paul, P. P.; McShane, E. J.; Colclasure, A. M.; Balsara, N.; Brown, D. E.; Cao, C.; Chen, B.-R.; Chinnam, P.R., Cui, Y., Dufek, E. J., Finegan, D. P., Gillard, S.; Huang, W.; Konz, Z. M.; Kostecki, R.; Liu, F.; Lubner, S.; Prasher, R.; Preefer, M. B.; Qian, J.; Rodrigues, M.-T. F.; Schnabel, M.; Son, S.-B.; Srivisan, V.; Steinrück, H.-G.; Tanim, T. R.; Toney, M. F. Tong, W.; Usseglio-Viretta, F.; Wan, J.; Yusuf, M.; McCloskey, B. D. and Weker, J. N., A Review of Existing and Emerging Methods for Lithium Detection and Characterization in Li-ion and Li-metal Batteries, *Adv. Energy Mater.*, **11**, 2100372 (2021).

(12) Long, L., Wang, S., Xiao, M., & Meng, Y. (2016). Polymer electrolytes for lithium polymer batteries. *Journal of Materials Chemistry A*, *4*(26), 10038-10069.

(13) Volkov, V. I., & Marinin, A. A. (2013). NMR methods for studying ion and molecular transport in polymer electrolytes. *Russian Chemical Reviews*, *82*(3), 248.

(14) Blanc, F., Leskes, M., & Grey, C. P. (2013). In situ solid-state NMR spectroscopy of electrochemical cells: batteries, supercapacitors, and fuel cells. *Accounts of chemical research*, *46*(9), 1952-1963.

Chapter 2

Electrochemical Characterization of Lithium Ion Batteries

Materials studied in this work (electrolytes and electrodes) are prepared for a possible application in lithium ion batteries and supercapacitors. Therefore, it is inevitable to introduce the basic principles of lithium ion batteries, related electrochemical measurements and relevant properties characterizing the studied material.

2.1 Principles of Lithium Ion Batteries
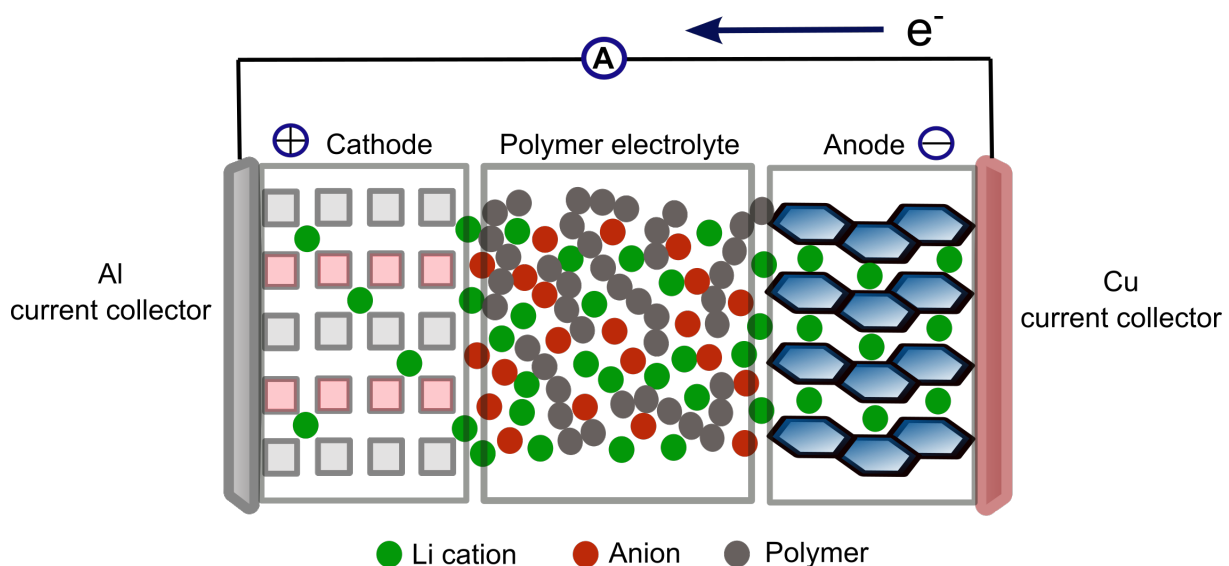
Figure 2.1: Scheme of a lithium ion battery containing a polymer electrolyte, during discharging. The cathode is lithium iron phosphate $LiFePO_4$ and the anode is graphite. During discharging, lithium cations deintercalated from the anode and migrate to the cathode. The polymer electrolyte serves as an electrolyte (ions) and separator (polymer) at the same time.

A lithium ion battery (LIB), as shown in Figure 2.1 is present, when an electrolyte solution and a separator are placed between two electrically conducting electrodes. In Figure 2.1 both of these properties are combined in the polymer electrolyte, which acts as a separator and electrolyte. The electrochemical principles of a LIB are rooted in the galvanic cell.

When an external potential difference is applied, the positively charged lithium cations start to migrate from the anode (oxidation) to the cathode. At the site of the cathode the lithium cations are intercalated between the graphite sheets and reduced. When the applied potential is removed, the lithium ions remain intercalated. Connecting an external consumer to the lithium ion battery creates a flow of electrons from the anode to the cathode. This is accompanied with the migration of lithium cations towards the cathode where they are resembled into their original structure, for example in LiFePO$_4$.[1]

When it comes to describe the battery, its half-cell reactions are considered. The reduction potentials of a cell composed e.g. of LiFePO$_4$ and graphite can be written as:[2,3]

$$C_6 + Li^+ + 1e^- \rightarrow Li_1C_6 \quad E^0 = 0.1\ V\ vs.\ Li^+/Li \qquad [2.1]$$

$$FePO_4 + Li^+ + e^- \rightarrow LiFePO_4 \quad E^0 = 3.3\ V\ vs.\ Li^+/Li \qquad [2.2]$$

$$Cell\ reaction:\ FePO_4 + Li_1C_6 \rightarrow LiFePO_4 + C_6 \quad E_{Cell}^0 = +3.2\ V \qquad [2.3]$$
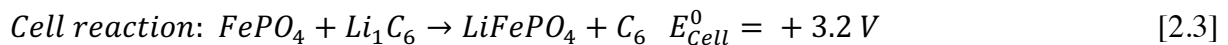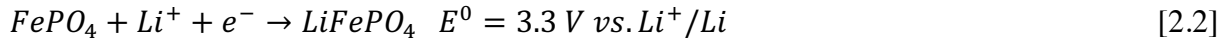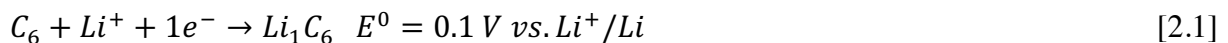
the standard reduction potential of an electrode is E^0 and the standard cell potential is E_{Cell}^0.

For the total cell reaction, the Gibbs free energy decides whether a cell reaction is thermodynamically favorable or not. Positive cell potentials reflect that the cell reaction is thermodynamically favorable. However, also the reverse reaction with negative potentials can be realized by applying an external potential. The Gibbs free energy G of the cell reaction with the cathode having the chemical formula Li$_x$B$_y$ (e.g. Li$_1$FePO$_4$) is defined by:[4]

$$\Delta G_{Cell}^0 = -nFV_{OC} \qquad [2.4]$$

$$FV_{OC}(x) = \left[\mu_C^{Li}(x) - \mu_A^{Li}\right] \equiv -\partial G(x)/\partial(x) \qquad [2.5]$$

with Faraday's constant F (C·mol^{-1}), n the number of transferred electrons, V_{OC} is the open circuit voltage of the cell, μ_A, μ_C the chemical potential of anode and cathode and x is the number of occupied lithium ion lattice sites in the structure ranging from 0–1.

For the above-mentioned cell reaction, lithium cation intercalation is often a solid-solution reaction. There are also further types, such as other two-phase reactions and complex intermediate reactions, while in the following only the solid-solution reactions are considered.

In the simplest case for a solid-solution reaction at constant temperature and pressure, the system exhibits a fixed degree of freedom of 1. This case is shown in Figure 2.2 a) and corresponds to a smooth decay of the voltage, shown in Figure 2.2 b).

Another important parameter is the theoretical gravimetric capacity Q (C·g^{-1}), which is often expressed in mA·h·g^{-1}. 1 mA·h·g^{-1} is equivalent to 3.6 C·g^{-1}. The gravimetric capacity Q is defined as:

$$Q = \frac{F \cdot n}{M} \qquad\qquad [2.6]$$

with the molar mass M (g·mol^{-1}). The cathode reaction from equation 2.2 can be considered as an example. The molar mass of LiFePO$_4$ is 157.7 g ·mol^{-1} with one electron transferred in the reaction. As a result, the theoretical gravimetric capacity is $Q = 170$ mA·h·g^{-1}.

Closely related to the theoretical capacity are the energy E supplied by the battery during discharging:

$$E = q \cdot V = \int_{0}^{t} I \cdot V \, dt \qquad\qquad [2.7]$$
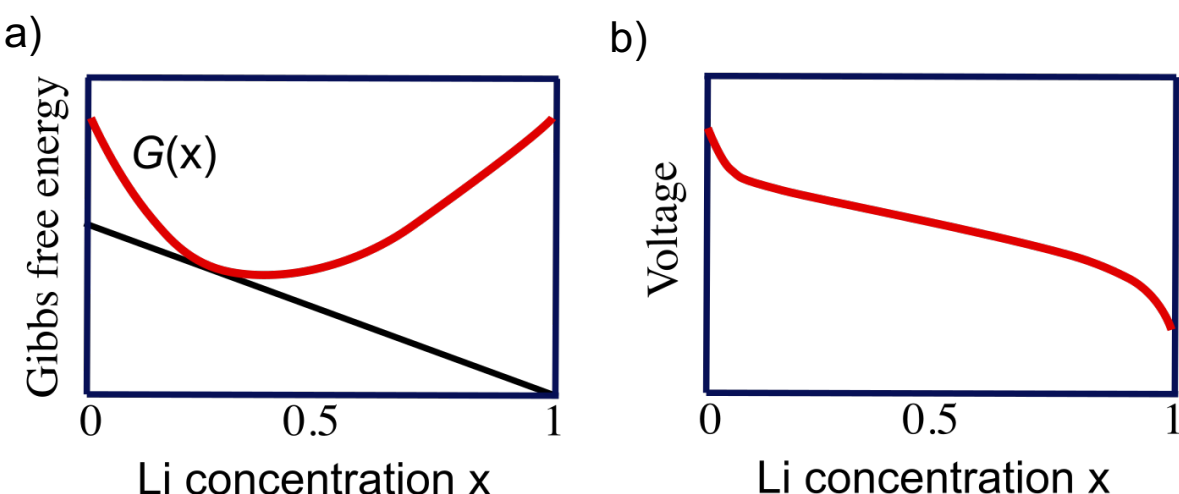
Figure 2.2: Gibbs free energy curve for a solid-solution reaction in a) and the corresponding voltage profile in b).[4]

and the power P at the time during discharging:

$$P = \frac{\partial E}{\partial t} = \frac{\partial q}{\partial t} \cdot V = I \cdot V \qquad [2.8]$$

with the charge q, the discharge energy E, current I and the voltage V.

The capacity measured of a real operating cell may deviate severely from the theoretically calculated value according to equation 2.6.[5] The notably lower measured capacity can be rationalized by taking into account that the theoretical capacity value assumes a complete removal of lithium cations while charging and a complete intercalation into the host structure upon discharging. However, complete removal of lithium cations, for instance from $LiFePO_4$ would lead to a disintegration of the structure. Therefore, partial removal of lithium cations is often found.

At the site of the anode, a theoretical capacity of 371.9 mA·h·g^{-1} for graphite (one lithium cation per C_6) is often nearly found for a real operating battery. Nevertheless, the use of graphite in a real operating cell is limited because of the low intercalation potential of lithium cations (equation 2.1) and due to the risk of lithium dendrite formation on the surface of graphite. Specifically, dendrite formation creates short circuits and as a result a fast cell death. Nowadays, alternative materials are used, such as $Li_4Ti_5O_{12}$ which reduces the formation of lithium dendrites but at the same time have higher anode potentials (> 0.1 V), which may be a limiting factor for numerous applications.

In addition, the coulombic efficiency and cycle lifetime are relevant parameters to characterize a cell. The coulombic efficiency describes the reversibility of the intercalation and removal of lithium cations, which must be as high as possible in order to guarantee high cycle lifetimes. Both parameters are typically presented by their C-rate. The conversion C/x is commonly used, where x is the number of hours required to fully discharge the cell to the theoretically calculated capacity. Discharging a cell (capacity 1 Ah) with 1 C yields a discharge current of 1 A for one hour. Specifying the C-rate is important, since discharging a cell with a rate of C/10 yields different measured capacity values compared to a C/1 discharging.

Relevant for industrial applications is the availability and cost of a material, as well as the toxicity of the material which becomes important in case of accidents. Also, the cycle life is important, which is the number of possible charge/discharge cycles, until the battery loses

typically 20 % of its initial capacity. Due to the mentioned reasons $LiCo_2O_2$ is currently replaced as a cathode material by $LiFePO_4$ which is less toxic and better available. Another current approach is looking for a complete replacement of lithium and tries to establish more environmentally friendly elements, such as Mg or other abundant rock-based elements.

2.2 Electrochemical Techniques

Chronoamperometry

In chronoamperometry, a constant potential is applied to the studied system and the time dependent evolution of the current is observed. This is illustrated in Figure 2.3. In terms of lithium ion batteries, Bruce and Vincent have introduced the nowadays most common experimental method for obtaining the transference number of the lithium cation.[6] For simplification a symmetric Li-cell with a single electron transfer is assumed.

To this system, a fixed voltage V_{app} is applied, while the evolution of the current nearly follows an exponential decay towards zero, which is given by:[7]

$$i = \frac{V_{app}}{R} \cdot \exp\left(\frac{-t}{RC}\right)$$

[2.9]

with the cell capacitance C, the cell resistance R and the time t
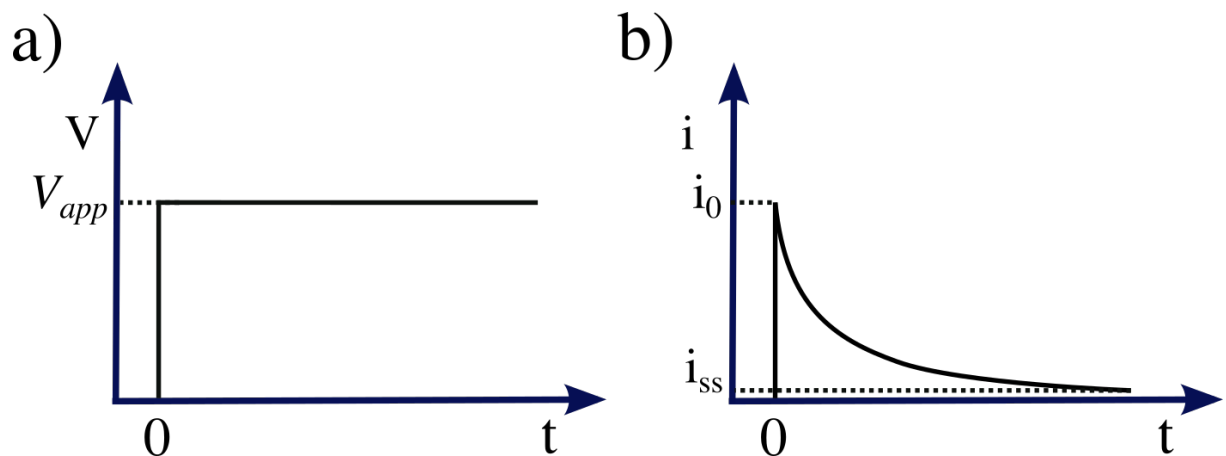
Figure 2.3: a) Constant voltage experiment and b) current response of the cell. The initial current is i_0 and steady state current is i_{ss}.[7]

t

a) $\ominus$　　　$\oplus$　b) $\ominus$　　　$\oplus$　c) $\ominus$　　　$\oplus$

$t=0$, $i=i_0$　　$t>0$, $i\approx i_0$　　$t=\infty$, $i=i_{ss}$

Li　　　Li　Li　　　Li　Li　　　Li
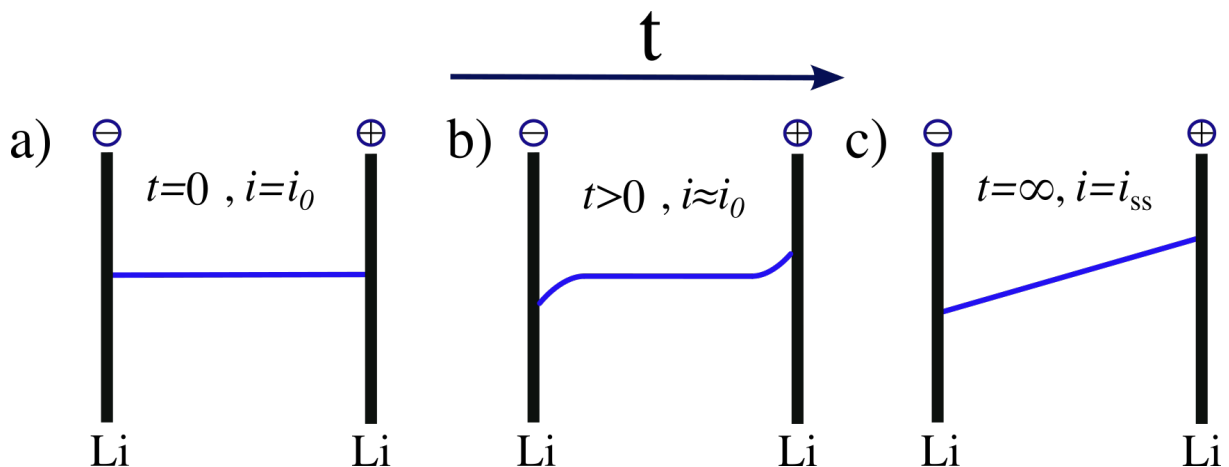
Figure 2.4: Schematic drawing of a symmetrical Li cell with the concentration of $LiCF_3SO_3$ as the lithium salt (fully dissociated) drawn at the y-axis. In a) the initial state is shown, where a uniform $LiCF_3SO_3$ concentration is present throughout the cell. b) shows the concentration profile for $t > 0$ and c) the case for the steady state.[8] The evolution of the current for this experiment is expressed by equation 2.9.

The reason for the exponential decay, seen in Figure 2.3 b) is briefly sketched in Figure 2.4. A symmetric lithium cell is shown, where a 1:1 salt (such as $LiCF_3SO_3$) is present and fully dissociated. For $t=0$ a constant salt concentration is present throughout the cell. This is known as the initial state of the cell. Upon applying a small potential difference across the cell, ions start to migrate (lithium cations migrate to the anode and the anions migrate to the cathode) while at the same time a concentration gradient is formed across the cell. At a certain time, the concentration gradient does not change notably in time and a steady state current is reached. At the steady state current, it is assumed that only lithium can be reduced and oxidized and therefore contributes to a small measurable current at long waiting times. This behavior is illustrated in Figure 2.4 c).

Chronopotentiometry

In chronopotentiometry on the other hand, a current is applied to the system and the time-dependent evolution of a potential is observed.[7] The constant current method is often called the "galvanostatic method". The latter is frequently used in cycling of an electrochemical cell, for example a lithium ion battery. Typically, three different chronopotentiometric techniques can be distinguished, which are depicted in Figure 2.5.
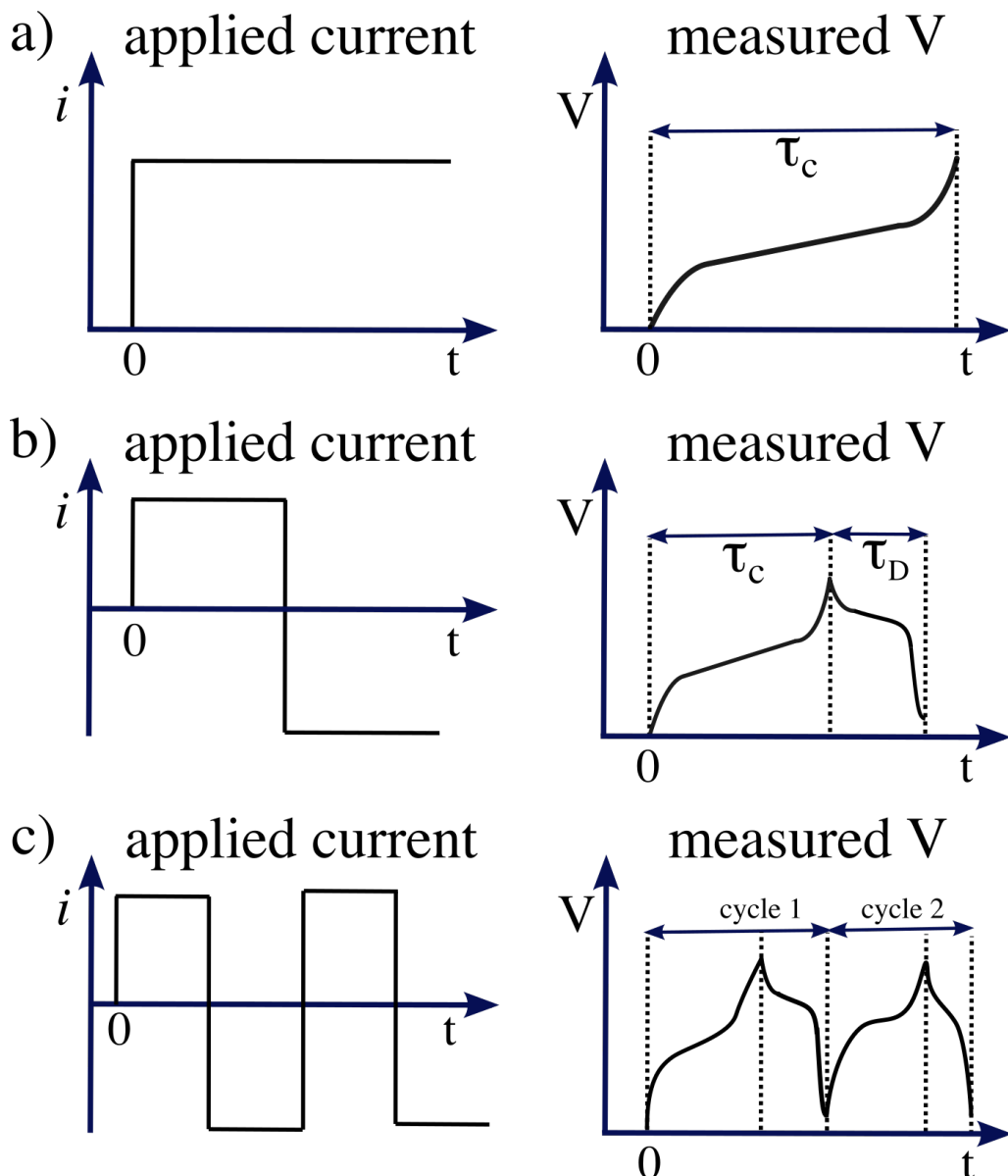
Figure 2.5: Chronoamperometric cycling techniques in a)–c). Note that the shape of the voltage curve shown in 2.5 a) resembles the shape of the voltage curve shown in Figure 2.2 b). In a) a positive constant current is applied to the electrochemical cell. The observed potential can correspond to the charging of a lithium ion battery with a characteristic time period τ_C (charging time). This section corresponds to the mentioned technique i). b) Shows a current reversal technique, where at first a positive current is applied (τ_C) and then a negative current with the same amplitude (discharge time τ_D). c) Displays two full charge/discharge cycles.[7,9]

i) Constant current mode in a single charging or discharging procedure of an electrochemical cell. ii) Galvanostatic cycling, where a full charge/ discharge cycle of an electrochemical cell is recorded and iii) a cyclic galvanostatic approach, where numerous charge/ discharge cycles are performed, e.g. in order to evaluate the cycle lifetime of an electrochemical cell. For cycling experiments, it is useful to define the sign of the current. Typically, positive currents correspond

to the charging of an electrochemical cell, while negative currents correspond to the discharging of the cell. As shown in Figure 2.5 c), the time period of the second cycle is shorter compared to the first cycle, due to an irreversible capacity loss after the first cycle. In case of complete reversibility, the time periods of all cycles will remain the same. However, in real operating systems, this is not observed.

Electrochemical Impedance Spectroscopy (EIS)
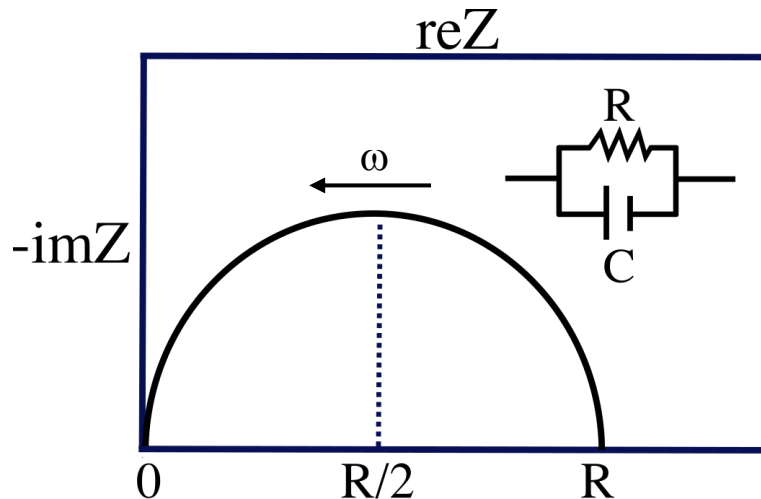
Figure 2.6: Nyquist plot of an electrochemical cell, modeled by a resistor R and a capacitor C combined in a parallel circuit.[10, 11, 12]

Electrochemical impedance spectroscopy EIS, sometimes called PEIS (potentiostatic electrochemical impedance spectroscopy) is nowadays a commonly used method for electrochemically active cells, such as batteries and fuel cells. The main advantage is that numerous processes which can occur in an electrochemical cell, such as electron transfer, adsorption of ions at the surface of the electrodes, mass transfer and charge transfer can be represented by an electric component in an electric circuit. These processes are modeled as resistors, capacitors and constant phase elements which can be combined either in series or parallel or a combination of both.

The fundamental approach in impedance spectroscopy is, independent of potentiostatic or galvanostatic input ac signal, that the responds of the system has a sinusoidal shape.[12] The impedance Z is defined as a complex number which similar to the resistance in the dc case is the ratio of V/i, with the difference that a phase shift exists between both quantities. Therefore, Z can be written as:[7, 13]

$$Z^* = \frac{V}{i} = Z^* e^{j\phi} = Z(\cos\phi + j\sin\phi) = Z' + jZ'' \tag{2.10}$$

Z^* denotes a complex quantity. With the phase angle ϕ, the complex number j ($j^2 = -1$) and the real part of the impedance Z' and the imaginary part of the impedance Z''.

A typical example of a representation of impedance data is given in Figure 2.6. The resistance (real part of the impedance at the x-axis) is plotted against the negative reactance (imaginary part of the impedance) at the y-axis. Another representation which is also commonly used is to plot either the real or imaginary part of the impedance against the applied frequencies. The diagram depicted in Figure 2.6 is oversimplified and impedance spectra recorded for real metal ion batteries (such as LIBs) are more complex. This is due to the manifold of processes which may be present in a metal ion battery, such as charge-transfer resistance which occurs at the electrode/electrolyte interface (solid electrolyte interphase (SEI)), electrolyte resistance, mass transfer resistance and double layer capacitance.[10, 13]

A more realistic example of an EIS spectrum is presented in Figure 2.7. At very high frequencies (HF), the spectrum typically shows a reactance that is (R< R_{HF}) and therefore exhibits an inductive behavior (little tail at positive im Z values). This is often associated with the response from the experimental setup (e.g. cables). At lower frequencies, two semi-circles which are often of different size can be found in the spectrum. In many cases, the semi-circle which falls at high frequencies is assigned to the electrolyte resistance R_E (plus the first element with R< R_{HF}) while the low frequency end of the second semi-circle is the sum of the previously mentioned resistances and the charge transfer resistance at the electrode/electrolyte interface (R_{CT}). At very low frequencies, the Warburg diffusion (W) can be seen, which adds as an additional element (non-ideal capacitor) to the equivalent-circuit model. The components of the equivalent circuit model given in Figure 2.7 can be obtained by impedance spectroscopy. Here, the frequency is swept, while changes in the measured impedance are obtained. The frequency dependent relation between the individual components of an electrochemical cell (similar to Figure 2.6) can be written as:[13]

$$Z(\omega) = \frac{R_E + R_{CT}}{(1 + \omega^2 \cdot R_{CT}^2 \cdot C_{CT}^2)} - \frac{j\omega \cdot R_{CT}^2 \cdot C_{CT}^2}{(1 + \omega^2 \cdot R_{CT}^2 \cdot C_{CT}^2)} \tag{2.11}$$

with the electrolyte resistance R_E, the charge transfer resistance R_{CT}, as well as the charge transfer capacity C_{CT}.
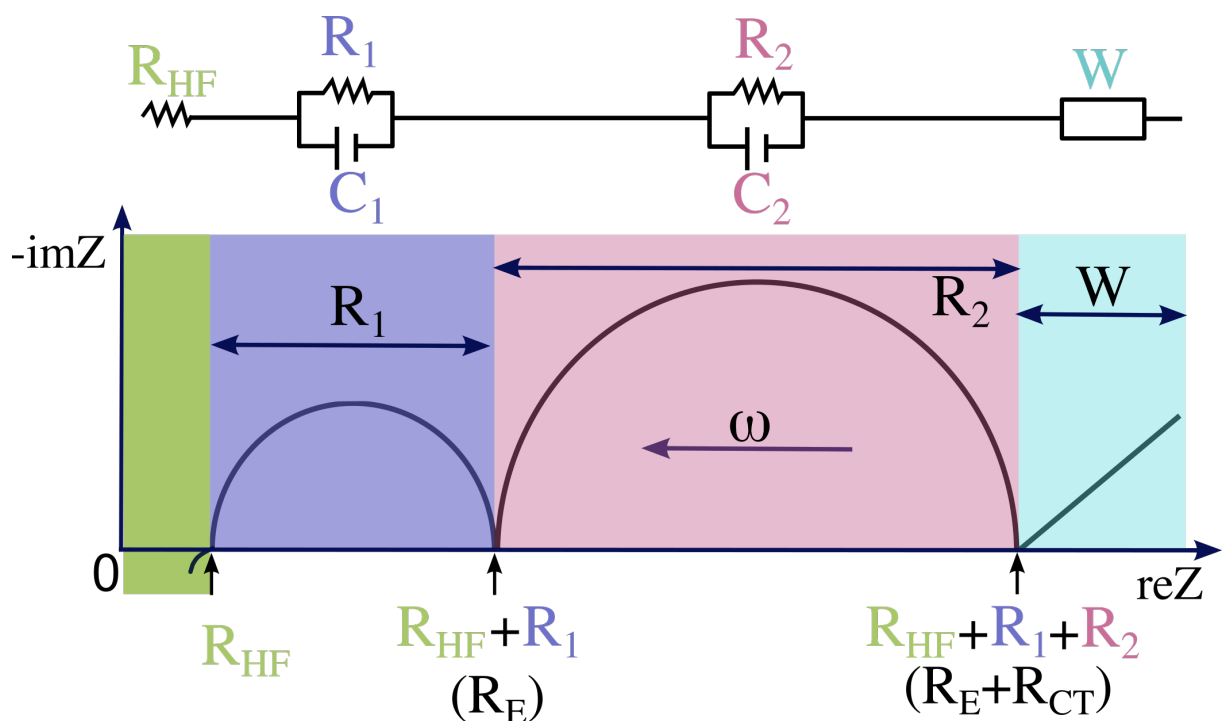
Figure 2.7: Simplified Nyquist plot of a metal ion battery.[13] The equivalent circuit model is given above the complex plane, while R_E and R_{CT} correspond to the electrolyte and charge transfer resistance, respectively.

For a neglectable R_{HF} component, the resistance of the electrolyte can be obtained from the high frequency arc, while the sum of R_E and R_{CT} can be found at the end of the low frequency arc.

Ion Transference Numbers

A crucial aspect, for the application of polymer electrolytes for lithium ion batteries are ion transport properties. In many cases research on (polymer) electrolytes is dedicated to explore ion conductivities. However, finding electrolytes with high room temperature ion conductivities is only part of the ion transport.[14]

Whether or not a lithium ion battery can be charged with high currents is also dependent on the fraction of current transported by the lithium cation. This property of the electrolyte is known as the ion transference number $t_{+/-}$ and is partly neglected in electrolyte research, while it becomes even more important in systems containing different ion species.

The concept of transference numbers goes back to Johann Wilhelm Hittorf.[15] Consider a lithium ion battery (Figure 2.1), where a 1:1 electrolyte e.g. $LiCF_3SO_3$ is fully dissociated into Li^+ and $CF_3SO_3^-$ by a solvent, as an example.

Applying a constant voltage to the lithium ion battery leads to ion migration. During charging, lithium cations migrate to the anode and the anions (here $CF_3SO_3^-$) migrate to the cathode. Obviously, a fraction of the ion current is transported by lithium cations and another part is transported by $CF_3SO_3^-$. The ion transference number is defined by:

$$t_l = \frac{i_l}{i_{total}} \qquad [2.12]$$

with the total current i_{total} and the current carried by ion species l given by i_l.

Often, the observed lithium transference number t_{Li^+} is smaller compared to the transference number of the anion t_- due to the fact that lithium cations are hard cations with a large solvation sphere.[16] On the other hand, the weakly coordinating $CF_3SO_3^-$ anion does not exhibit a large solvation sphere and is therefore more mobile.

The electrolyte (a fully dissociated 1:1) obeys the Nernst-Einstein equation, which relates the ion conductivities to the ion self-diffusion coefficients:[17]

$$\sigma_i = \frac{|z|^2 F^2 c_i}{RT} \cdot D_i \qquad [2.13]$$

with z as the number of transferred electrons and the self-diffusion coefficients of the cation and anion D_+ and D_-, respectively.

The ion transference numbers are strongly related to the diffusivities and to the ion mobilities:[17]

$$t_+ = \frac{\mu_+}{\mu_+ + \mu_-} = \frac{\sigma_+}{\sigma_+ + \sigma_-} = \frac{D_+}{D_+ + D_-} \qquad [2.14]$$

with cation and anion mobilities μ_+ and μ_- and the cation and anion diffusion coefficients D_+ and D_-.

In polymer electrolytes, the Bruce-Vincent method is the most common method to derive ion transference numbers.[16] As pointed out by Balsara and co-workers for a symmetric lithium ion battery, the initial state can be rationalized as a case where the initial current follows Ohm's law and can be written as:

$$i_0 = \frac{\sigma}{k} \cdot \Delta V \qquad [2.15]$$

and the steady-state current as:

$$i_{SS} = \frac{t_+ \sigma}{k} \cdot \Delta V \qquad [2.16]$$

with the cell constant k (distance between electrodes divided by the electrode surface), the initial current i_0 and the steady-state current i_{SS} (see Figure 2.3).

In this oversimplified view, the lithium transference number would then be the ratio of the steady state current and initial current. However, for a real operating cell the electrode/electrolyte interphase mentioned in Section 2.2. must be considered. This is in particular important, since the interfacial resistance is not constant over the experiment. The initial resistance R_{i0} (measured via impedance spectroscopy) is smaller compared to the interfacial resistance at steady-state current R_{iSS}.[16] The explanation for this is rooted in the formation of the solid-electrolyte-interphase (SEI), which increases the electrode/electrolyte resistance.[18] As a result, R_{i0} and R_{iSS} must be considered, when the transference number is calculated. Combining both equations results in the common Bruce-Vincent expression:[16]

$$t_+ = \frac{i_{SS}(\Delta V - i_0 R_{i0})}{i_0(\Delta V - i R_{iSS})} \qquad [2.17]$$

Apparent Transference Numbers

The relationship of transference numbers and the self-diffusion coefficients (equation 2.14) can be used to estimate the so-called "apparent" transference numbers or NMR transference numbers. The term "apparent" is used, since the diffusion NMR experiment averages over all nuclei of a given species, i.e. also ion pairs. Transference numbers measured by electrophoretic NMR on the other hand yield accurate ion transference numbers. [19]

The apparent transference number, based on NMR diffusion coefficients can be written as:[22]

$$t_+ = \frac{N_+ D_+}{N_+ D_+ + N_- D_-} \qquad [2.18]$$

An advantage of additionally measuring the apparent transference numbers is that it allows a comparison between the measured ac conductivity σ_{ac} to which only "mobile" and dissociated ions contribute and NMR diffusion coefficients (which averages over all ions from one ion

species, e.g. dissociated ^{7}Li ions, ion pairs) in order to estimate the fraction of ions, which contribute to the current, expressed with the activity parameter a:[20–22]

$$a = \frac{\sigma_{ac}}{\frac{e^2}{k_b T}(N_i D_i + \cdots)} \qquad [2.19]$$

with the number of ions i per volume fraction, labelled as N_i and the self-diffusion coefficient (measured by NMR), the elemental charge e and k_b is the Boltzmann constant. The activity parameter a may take values up to $a = 1$ which means that all ions are fully dissociated and active.

2.3 References

(1) Striebel, K., Shim, J., Srinivasan, V., & Newman, J. (2005). Comparison of LiFePO4 from different sources. *Journal of the Electrochemical Society*, *152*(4), A664.

(2) Kasavajjula, U. S., Wang, C., & Arce, P. E. (2008). Discharge model for LiFePO4 accounting for the solid solution range. *Journal of The Electrochemical Society*, *155*(11), A866.

(3) Sun, C. S., Zhou, Z., Xu, Z. G., Wang, D. G., Wei, J. P., Bian, X. K., & Yan, J. (2009). Improved high-rate charge/discharge performances of LiFePO4/C via V-doping. *Journal of Power Sources*, *193*(2), 841-845.

(4) Gao, J., Shi, S. Q., & Li, H. (2015). Brief overview of electrochemical potential in lithium ion batteries. *Chinese Physics B*, *25*(1), 018210.

(5) Wang, H., Liu, L., Wang, R., Zhang, D., Zhu, L., Qiu, S., ... & Zhang, Z. (2015). Design and synthesis of high performance LiFePO 4/C nanomaterials for lithium ion batteries assisted by a facile H+/Li+ ion exchange reaction. *Journal of Materials Chemistry A*, *3*(15), 8062-8069.

(6) Bruce, P. G., & Vincent, C. A. (1987). Steady state current flow in solid binary electrolyte cells. *Journal of electroanalytical chemistry and interfacial electrochemistry*, *225*(1-2), 1-17.

(7) Bard, A. J., & Faulkner, L. R. (2001). Fundamentals and applications. *Electrochemical methods*, *2*(482), 156-161.

(8) Bruce, P. G., Evans, J., & Vincent, C. A. (1988). Conductivity and transference number measurements on polymer electrolytes. *Solid State Ionics*, *28*, 918-922.

(9) Compton, R. G., & Banks, C. E. (2018). *Understanding voltammetry*. World Scientific.

(10) Yuan, X. Z., Song, C., Wang, H., & Zhang, J. (2010). Electrochemical impedance spectroscopy in PEM fuel cells: fundamentals and applications.

(11) Andre, D., Meiler, M., Steiner, K., Wimmer, C., Soczka-Guth, T., & Sauer, D. U. (2011). Characterization of high-power lithium-ion batteries by electrochemical impedance spectroscopy. I. Experimental investigation. *Journal of Power Sources*, *196*(12), 5334-5341.

(12) Andre, D., Meiler, M., Steiner, K., Walz, H., Soczka-Guth, T., & Sauer, D. U. (2011). Characterization of high-power lithium-ion batteries by electrochemical impedance spectroscopy. II: Modelling. *Journal of Power Sources*, *196*(12), 5349-5356.

(13) Middlemiss, L. A., Rennie, A. J., Sayers, R., & West, A. R. (2020). Characterisation of batteries by electrochemical impedance spectroscopy. *Energy Reports*, *6*, 232-241.

(14) Galluzzo, M. D., Maslyn, J. A., Shah, D. B., & Balsara, N. P. (2019). Ohm's law for ion conduction in lithium and beyond-lithium battery electrolytes. *The Journal of chemical physics*, *151*(2), 020901.

(15) Hittorf, W. (1902). Bemerkungen über die Bestimmungen der Überführungszahlen der Ionen während der Elektrolyse ihrer Lösungen. Das Verhalten der Diaphragmen bei derselben. *Zeitschrift für Physikalische Chemie*, *39*(1), 613-629.

(16) Evans, J., Vincent, C. A., & Bruce, P. G. (1987). Electrochemical measurement of transference numbers in polymer electrolytes. *Polymer*, *28*(13), 2324-2328.

(17) France-Lanord, A., & Grossman, J. C. (2019). Correlations from ion pairing and the Nernst-Einstein equation. *Physical review letters*, *122*(13), 136001.

(18) An, S. J., Li, J., Daniel, C., Mohanty, D., Nagpure, S., & Wood III, D. L. (2016). The state of understanding of the lithium-ion-battery graphite solid electrolyte interphase (SEI) and its relationship to formation cycling. *Carbon*, *105*, 52-76.

(19) Holz, M. (1994). Electrophoretic NMR. *Chemical Society Reviews*, *23*(3), 165-174.

(20) Zhao, J., Wang, L., He, X., Wan, C., & Jiang, C. (2008). Determination of lithium-ion transference numbers in LiPF6–PC solutions based on electrochemical polarization and NMR measurements. *Journal of The Electrochemical Society*, *155*(4), A292.

(21) Fromling, T., Kunze, M., Schonhoff, M., Sundermeyer, J., & Roling, B. (2008). Enhanced lithium transference numbers in ionic liquid electrolytes. *The Journal of Physical Chemistry B*, *112*(41), 12985-12990.

(22) Hayamizu, K., Aihara, Y., Nakagawa, H., Nukuda, T., & Price, W. S. (2004). Ionic conduction and ion diffusion in binary room-temperature ionic liquids composed of [emim][BF4] and LiBF4. *The Journal of Physical Chemistry B*, *108*(50), 19527-19532.

Chapter 3

Nuclear Magnetic Resonance Spectroscopy

The main analytical method applied in this work is nuclear magnetic resonance (NMR). Section 3.1 presents the relevant NMR interactions, before introducing the theory of diffusion NMR and water insertion in aromatic host matrices in Section 3.2.

3.1 NMR Interactions

Zeeman Interaction

As the most dominant NMR interaction, the Zeeman interaction is present whenever a nuclear spin (spin quantum number I) interacts with a magnetic field $\mathbf{B_0}$.[1,2,3] In the absence of a magnetic field, the energy levels of a nuclear spin are degenerate. However, when a magnetic field is present, the energy levels are non-degenerate and transitions between the individual energy levels can take place. Depending on the spin quantum number m_I, the number of different energy levels is determined by $2I + 1$.

Taking the most abundant nucleus ^{1}H with the spin quantum number $I = ½$, two different magnetic quantum numbers arise, namely $m_I = + ½$ and $m_I = - ½$. Their difference in energy is proportional to the so-called Larmor frequency $\boldsymbol{\omega_0}$, which is defined as:

$$\boldsymbol{\omega_0} = -\gamma \mathbf{B_0} \qquad [3.1]$$

with γ the gyromagnetic ratio. Bold symbols in equations denote vectors or tensors.

The gyromagnetic ratio can take either positive or negative values, but has a constant value for a given nucleus. In a classical vector model, the sign defines the sense of precession. The

Zeeman interaction exhibits by far the largest order of magnitude of all NMR interaction with values in the range of 10^8 Hz at typical field strengths of modern NMR magnets (100–900 MHz).

Chemical Shielding

In solution state NMR, the obtained spectra often consist of narrow and well-resolved lines with a linewidth in the order of a few Hz. For these types of spectra, most of the NMR interactions discussed in the following are averaged due to rapid random tumbling of the molecules in dilute solutions. Despite that, NMR interactions are anisotropic which can be seen especially well in solid-state NMR. Solid-state NMR spectra are typically broad, since low mobile molecules or segments are unable to average the anisotropic NMR interactions to zero. As mentioned in the previous section, nuclear spins interact with the external magnetic field $\mathbf{B_0}$. However, spins do not interact solely with the $\mathbf{B_0}$ field but also with the field generated by electrons in the vicinity of the nucleus.

The external field induces currents in the electron orbitals, while an additional induced magnetic field $\mathbf{B_{ind}}$ emerges.[4] This effect is present for all molecules and alters the effective field that a nucleus experiences. A prominent example is the benzene molecule (for which a π-current is present) shown in Figure 3.1. According to Ramsey, the shielding tensor can be considered as the sum of a diamagnetic $\mathbf{\sigma^d}$ and paramagnetic contribution $\mathbf{\sigma^p}$.[5, 6, 7] The diamagnetic term depends only on the ground-state wave function of the orbital angular momentum of the electrons.[5]
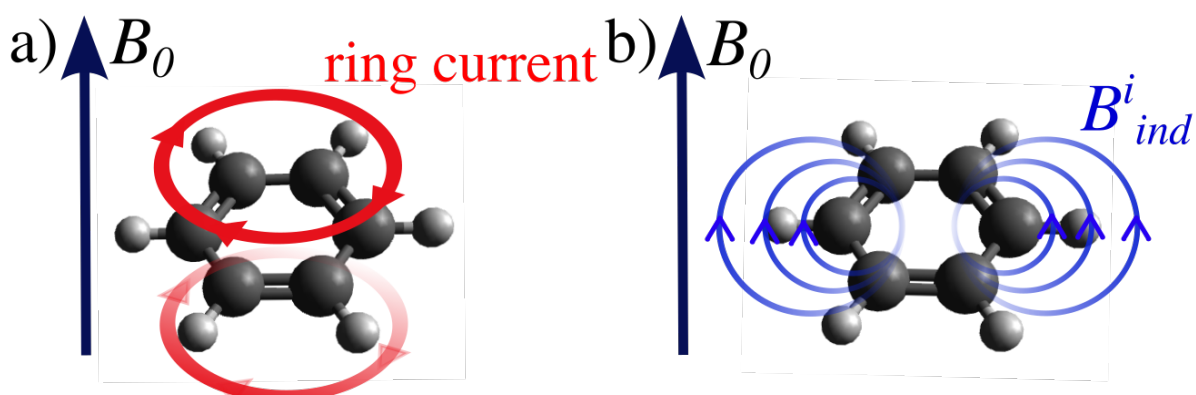
Figure 3.1: (a) Induced electric current for benzene generated by π electrons in an external magnetic field (C: dark grey spheres, H: light grey spheres). (b) induced magnetic field. The resulting field depends on the location relative to the benzene ring and on the precise molecular orientation of the ring with respect to the external field.

The latter is responsible for an induced magnetic field that opposes the external field and therefore contributes exclusively to an additional shielding. The paramagnetic contribution on the other hand originates from a mixing of the ground-state wave function with the excited states. Shielding and deshielding paramagnetic contributions are observed, which are relevant for ^{19}F in particular.[8] In the following discussion, only the diamagnetic contribution is considered. As shown in Figure 3.1, the electric current of electrons induces an additional magnetic field $\mathbf{B_{ind}}$ which can be written as:

$$\mathbf{B_{ind}} = -\boldsymbol{\sigma}\mathbf{B_0} \qquad\qquad [3.2]$$

with $\boldsymbol{\sigma}$ as the chemical shielding tensor for a given nucleus.

Even though the induced field is small compared to the external field, it still causes a measurable change in NMR frequency. A famous example, presented by Edward M. Purcell in his Nobel lecture in 1952 is the ^{1}H NMR spectrum of ethanol.[9] The effective field and therefore the resulting Larmor frequencies of the CH_3 hydrogens, CH_2 hydrogens and OH hydrogens can be resolved as individual signals, due to differences in chemical shielding for the three different chemical sites.

A commonly observed NMR spectrum, for example of the ethanol molecule, is presented by plotting the measured intensity against the chemical shift $\boldsymbol{\delta}$. This expression is particularly useful, since the field dependence from equation (3.2) is no longer present. The chemical shift $\boldsymbol{\delta}$ is defined by:

$$\boldsymbol{\delta} = \frac{\omega - \omega_{ref}}{\omega_{ref}} \times 10^6 \qquad\qquad [3.3]$$

with ω as the measured frequency of a nucleus and ω_{ref} as the frequency of a reference molecule.

The reference molecule is dependent on the observed nucleus. At this point, two types of references can be distinguished, namely primary references (whose signal is set to 0 ppm) and secondary references. The latter show signals that do not occur at 0 ppm but have fixed shifts to a primary reference. For ^{1}H, ^{13}C and ^{29}Si the primary reference tetramethylsilane is the compound of choice, while for ^{29}Si, especially in the solid-state, the secondary reference octakis(trimethylsiloxy)silsesquioxane (Q_8M_8) is used.[10] The relation shown in (equation 3.3) is in particular relevant for solution state NMR, where narrow lines can be observed shifted with respect to the signal of the reference compound.

Moreover, the chemical shielding is anisotropic and exhibits a direction dependence towards the $\mathbf{B_0}$ field. In general, the chemical shielding interaction can be expressed by a second-rank tensor which is represented as the following:

$$\boldsymbol{\sigma} = \begin{pmatrix} \sigma_{xx} & \sigma_{xy} & \sigma_{xz} \\ \sigma_{yx} & \sigma_{yy} & \sigma_{yz} \\ \sigma_{zx} & \sigma_{zy} & \sigma_{zz} \end{pmatrix} \qquad\qquad [3.4]$$

$\boldsymbol{\sigma}$ denotes only the symmetric part of the tensor. In general, the shielding tensor also has an antisymmetric part. However, this antisymmetric part is not directly observable and contributes only to relaxation processes.[11]

Expression (3.4) is multiplied with the external $\mathbf{B_0}$ field (exhibiting only a z-component along the laboratory frame):

$$\mathbf{B_{ind}} = -\begin{pmatrix} \sigma_{xx} & \sigma_{xy} & \sigma_{xz} \\ \sigma_{yx} & \sigma_{yy} & \sigma_{yz} \\ \sigma_{zx} & \sigma_{zy} & \sigma_{zz} \end{pmatrix} \cdot \begin{pmatrix} 0 \\ 0 \\ B_0 \end{pmatrix} = \begin{pmatrix} -\sigma_{xz} \cdot B_0 \\ -\sigma_{yz} \cdot B_0 \\ -\sigma_{zz} \cdot B_0 \end{pmatrix} \qquad [3.5]$$

In equation 3.5 the magnetic field and $\boldsymbol{\sigma}$ are both represented in the laboratory frame. The specific values of $\boldsymbol{\sigma}$ in the lab frame depends on the molecular orientation. An example of a calculated chemical shielding tensor and its relation to the molecular frame is shown in Figure 3.2.
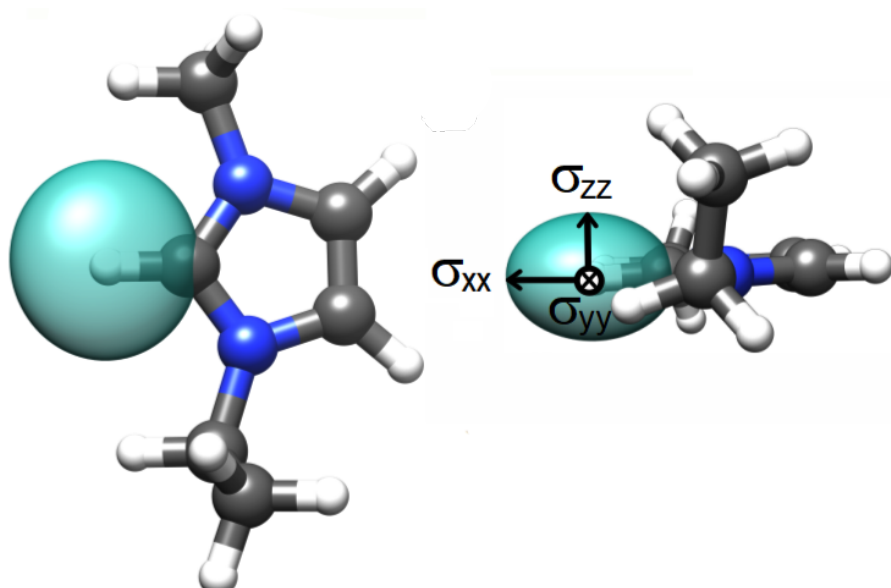
Figure 3.2: [EMIM]+ cation and the shielding tensor for the C2–H nucleus (H: white spheres, C: dark grey spheres, N: blue spheres).[12] The side view reveals that the shielding tensor of the C2–H nucleus is non-spherical.

The 1-ethyl-3-methylimidazolium ([EMIM]⁺) cation is presented in top view and side view in Figure 3.2. It is crucial to point out the relation between the molecular frame and the principal axis system. The shielding tensor presented in equation (3.4) is given in the laboratory frame (large letters X, Y, Z).[13, 14] The shielding tensor $\boldsymbol{\sigma}$ (laboratory frame) is transformed to $\boldsymbol{\sigma^l}$ (principal axis system) (Figure 3.3) from which the principal axis values can be obtained:[15]

$$\boldsymbol{\sigma^l} = \mathbf{T}^{-1} \cdot \begin{pmatrix} \sigma_{xx} & \sigma_{xy} & \sigma_{xz} \\ \sigma_{yx} & \sigma_{yy} & \sigma_{yz} \\ \sigma_{zx} & \sigma_{zy} & \sigma_{zz} \end{pmatrix} \cdot \mathbf{T} = \begin{pmatrix} \sigma_{XX} & 0 & 0 \\ 0 & \sigma_{YY} & 0 \\ 0 & 0 & \sigma_{ZZ} \end{pmatrix} \qquad [3.6]$$

with the rotation matrix $\mathbf{T}$ and the transformed shielding tensor $\boldsymbol{\sigma^l}$.

In dilute solutions with fast molecular motion the isotropic chemical shielding is observed due to averaging of the chemical shielding interaction. The isotropic chemical shielding σ_{iso} is given by:[15]

$$\sigma_{iso} = (\sigma_{ZZ} + \sigma_{YY} + \sigma_{XX})/3 \qquad [3.7]$$

However, in samples with more restricted molecular motion, such as solids or gels, the anisotropy of chemical shielding plays an important role. Two different scenarios are commonly discussed: The case of single crystals and of powder samples.

In the simplest case of a single crystal, the individual lattice sites are occupied by molecules in such a way that a uniform orientation with respect to the external magnetic field is obtained. As a result, a single resonance is observed, while the frequency depends on the orientation of the principal axis system (PAS) with respect to the applied magnetic field. The corresponding spectrum is illustrated in Figure 3.4. In the case of $\mathbf{B_0}$ being aligned with one of the principal axes of the shielding tensor, the frequency appears at the frequency characteristic for the principal axis value.
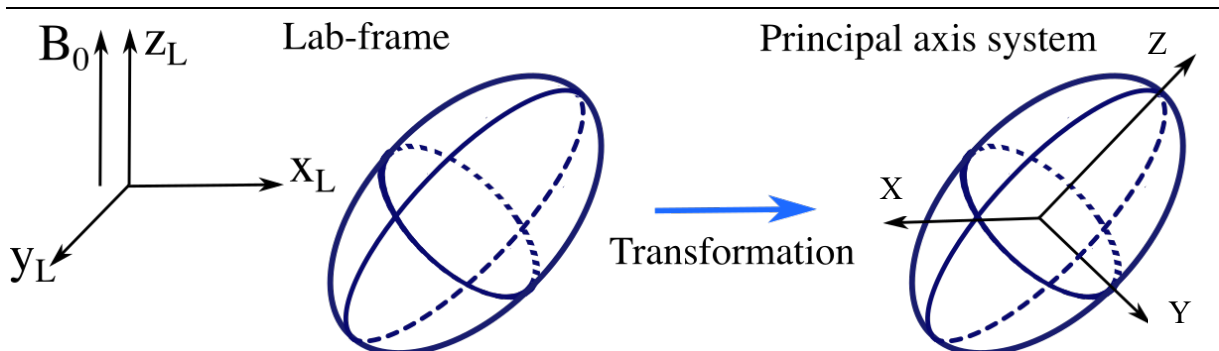
Figure 3.3: Illustration of a transformation from the laboratory frame to principal axis system (PAS).

For powdered crystalline samples, all crystal orientations with respect to the external field are present and therefore a superposition of numerous resonances is observed yielding the so-called powder pattern. The shape of the powder pattern is dependent on the values of the chemical shift tensor and whether or not the shielding tensor is axially symmetric.[15] For axially symmetric shielding tensors, $\sigma_{YY} = \sigma_{XX}$ (σ_{ZZ} is different from σ_{YY}, σ_{XX}) the powder pattern seen in Figure 3.4 is obtained. In the absence of axial symmetry, all three principal axis values take different values, which results in a powder pattern with two sharp edges. As depicted in Figure 3.4 b), the powder pattern exhibits sharp edges, which correspond to the principal axis values of an axially symmetric tensor. In more detail, the powder pattern can be described by the asymmetry parameter η_{CS} and the chemical shift anisotropy δ_{aniso} which are defined as:[1, 7]

$$\eta_{CS} = \delta_{YY} - \delta_{ZZ}/\delta_{aniso} \qquad [3.8]$$

$$\delta_{aniso} = \delta_{ZZ} - \delta_{iso} \qquad [3.9]$$

$$|\delta_{YY} - \delta_{iso}| \leq |\delta_{XX} - \delta_{iso}| \leq |\delta_{ZZ} - \delta_{iso}| \qquad [3.10]$$

with the isotropic chemical shift δ_{iso} (given by equation 3.7).

Often, static spectra of solid or rigid materials observed by NMR exhibit overlapping resonances of partially-or non-averaged signals. As a result, the observed spectra are complicated and cannot be deconvoluted easily, since the precise shielding tensor is unknown in some cases.

In order to overcome signal broadening due to anisotropic chemical shielding, magic-angle-spinning (MAS) is commonly used to increase the spectral resolution.[16] In this experiment, the sample is placed in a rotor and spun around an axis forming an angle of $\sim 54.7356°$ with respect to the direction of the external magnetic field. The idea behind sample rotation is that molecular motion can be imitated by external rotation. As a result, a narrow line can be observed in case of the spinning frequency ω_{rot} being significantly larger than the span of δ_{aniso} (Hz).

However, this is frequently not achieved due to experimental limitations in generating large spinning frequencies. Often, a series of spinning sidebands is observed which appear at $\omega_{iso} + n \cdot \omega_{rot}$, where ω_{rot} is the rotation frequency and n an integer number. The effect of MAS on the static spectrum is schematically shown in Figure 3.4 c), considering that the spinning speed is not high enough to eliminate the spinning-sidebands completely.

a) single crystal

b) crystal powder sample (static)

δ_{XX}/δ_{YY}

δ_{ZZ}

c) crystal powder sample (MAS)

δ_{iso}

chemical shift / ppm

B_0

B_0

B_0

ω_{rot}

54.74°
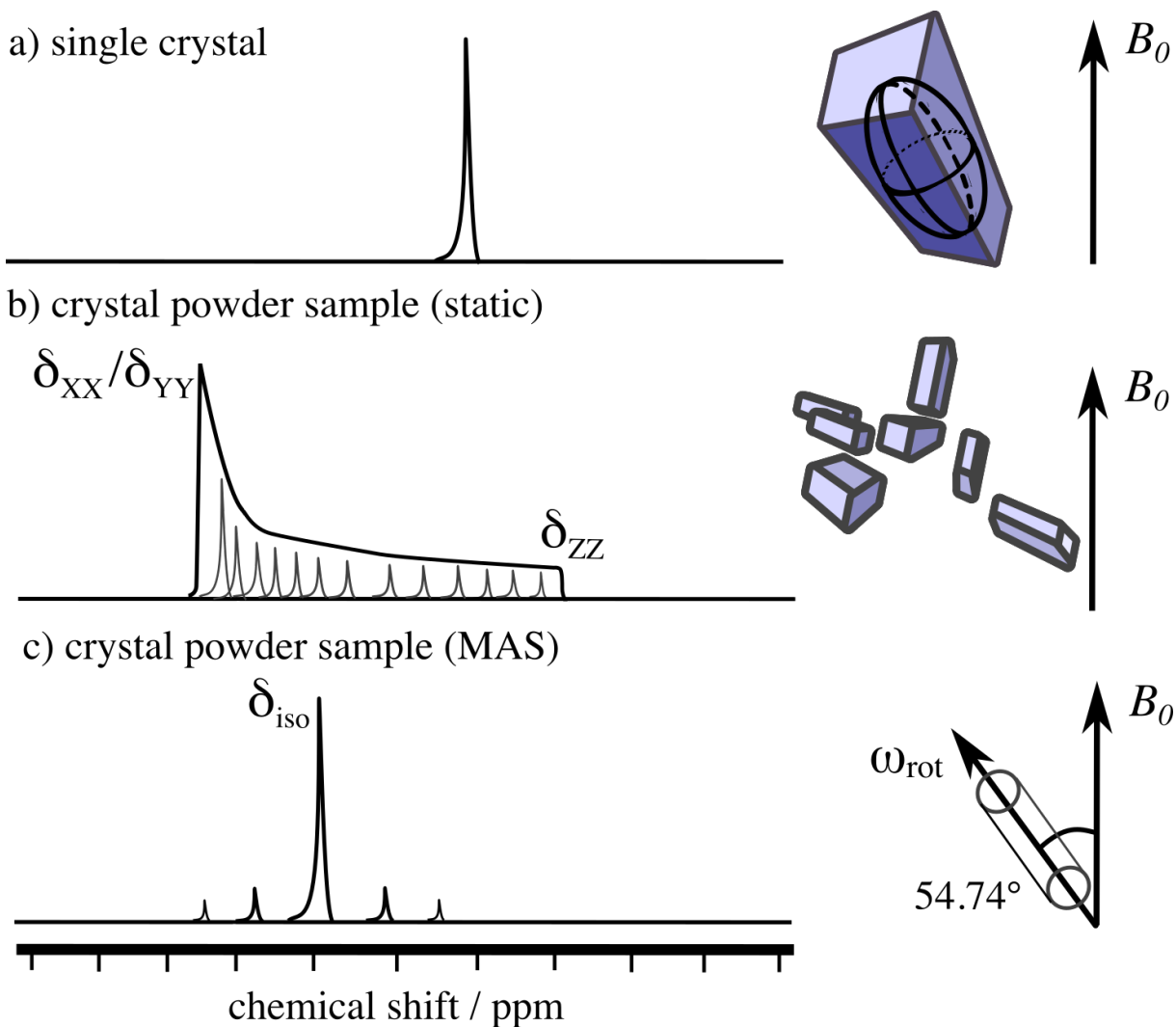
Figure 3.4: (a) Oversimplified single crystal case with a single CSA tensor, in which case a single line is observed. The precise position depends on the orientation of the chemical shielding tensor with respect to the **B₀** field. (b) Powder pattern of an axially symmetric chemical shielding tensor. The more common case of a crystal powder is schematically shown, for which a superposition of all orientations is observed. (c) The effect of MAS on the static line with a rotation frequency smaller than δ_{aniso}, causes a few spinning-sidebands at integer values of the spinning frequency.

Quadrupolar Interaction

Another crucial NMR interaction is the electric quadrupolar interaction, since most of the NMR active nuclei are quadrupole nuclei (73 %).[17] In a simplified picture, nuclei with a spin quantum number $I > \frac{1}{2}$ exhibit a non-spherical charge distribution.[1, 3] Nuclei with $I = \frac{1}{2}$ exhibit a spherical charge distribution and have no electrical quadrupole moment.
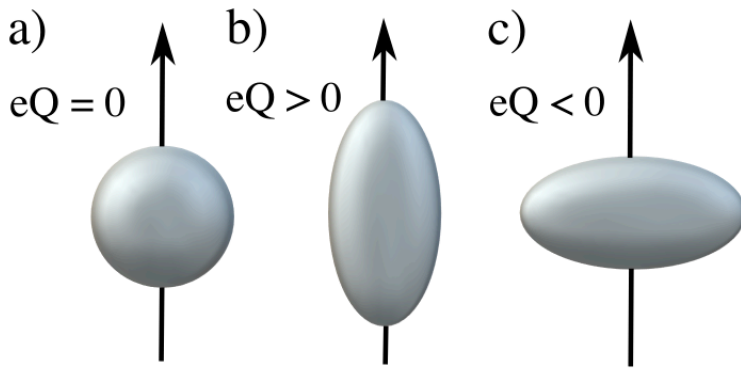
Figure 3.5: (a) Scheme of a $I = \frac{1}{2}$ nucleus which does not exhibit a quadrupole moment. (b) shows a prolate nucleus which exhibits eQ > 0. (c) displays an oblate-shaped nucleus with eQ < 0. Both nuclei (b) and (c) exhibit $I > \frac{1}{2}$.

The quadrupolar nucleus has the structure of a multipole, in which regions of higher charge density and lower charge density are present, shown in Figure 3.5. The quadrupole moment Q interacts with the non-zero electric field gradient (EFG), which yields the quadrupole interaction. This is responsible for a broadening of the observed spectra. Quadrupolar nuclei are less often studied than nuclei without a quadrupole moment, due to their complicated spectra.[17, 18]

The electric field gradient (EFG) at the site of the nucleus can be described by a traceless tensor $\boldsymbol{V}$:[17, 18, 19]

$$\boldsymbol{V} = \begin{pmatrix} V_{xx} & V_{xy} & V_{xz} \\ V_{yx} & V_{yy} & V_{yz} \\ V_{zx} & V_{zy} & V_{zz} \end{pmatrix} \tag{3.11}$$

$$\boldsymbol{V}^{\mathrm{I}} = \mathbf{T}^{-1} \cdot \boldsymbol{V} \cdot \boldsymbol{T} = \begin{pmatrix} V_{XX} & 0 & 0 \\ 0 & V_{YY} & 0 \\ 0 & 0 & V_{ZZ} \end{pmatrix} \tag{3.12}$$

with the principal values of the EFG tensor V_{XX}, V_{YY} and V_{ZZ} with the same order as for the chemical shielding $|V_{YY}| \leq |V_{XX}| \leq |V_{ZZ}|$.[14] Unlike for chemical shielding or J coupling, fast molecular motion in solution averages the EFG tensor to zero, due to the traceless character of this tensor. The quadrupolar interaction is orientation dependent. The important parameter, which determines the strength of the quadrupolar interaction is the quadrupolar coupling constant C_Q (Hz) given by:

$$C_Q = eQ \cdot V_{ZZ}/h \tag{3.13}$$

with Planck's constant h and the quadrupole moments eQ.

A quadrupolar asymmetry parameter η_Q is defined by:

$$\eta_Q = \frac{(V_{XX} - V_{YY})}{V_{ZZ}}$$

[3.14]

η_Q expresses the deviation of the EFG from axial symmetry. In case of axial symmetry, $\eta_Q = 0$.

Typically for highly symmetrical molecules, i.e. six-fold coordinated atoms, the charges are distributed symmetrically around the nucleus and their contribution to the EFG tend to cancel each other out. This gives rise to a very small EFG at the site of the nucleus.[20] As a result, narrow signals can be observed. For less symmetric environments of a nucleus broader spectra are observed.

Figure 3.6 shows the energy levels for a spin 3/2 nucleus (e.g. ^{7}Li, ^{11}B and ^{23}Na) under the influence of the first order quadrupolar interaction $\boldsymbol{H_Q^{(1)}}$ as well as the second order quadrupolar interaction $\boldsymbol{H_Q^{(2)}}$.[18] The single crystal case for a spin $I = 3/2$ nucleus would consist of one central transition and two equally spaced satellite transitions. The first order quadrupolar interaction shifts the energy levels, relative to the Zeeman energy levels. Further details are discussed in the caption of Figure 3.7. It is worth noting that $\boldsymbol{H_Q^{(1)}}$ is a second-rank tensor and therefore can be averaged by MAS,[18] while $\boldsymbol{H_Q^{(2)}}$ is expressed by fourth-, second- and zeroth-order Legendre polynomials and is not averaged to zero by MAS.[17]
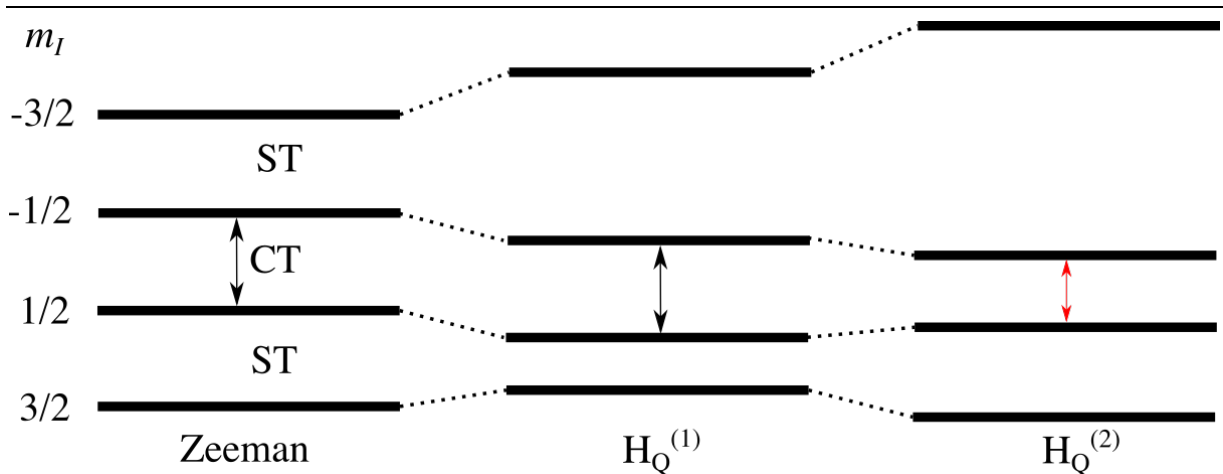
Figure 3.6: Energy level diagram for a spin $I = 3/2$ nucleus under the influence of $\boldsymbol{H_Q^{(1)}}$ and $\boldsymbol{H_Q^{(2)}}$. Central and satellite transitions (CT, ST) are shown. Note, that the central transition remains unaffected under the influence of $\boldsymbol{H_Q^{(1)}}$, while $\boldsymbol{H_Q^{(2)}}$ induces a shift of the central transition commonly known as quadrupolar induced shift.

Therefore, MAS spectra of quadrupolar nuclei often show strange shapes, which can nowadays be modeled computationally, as shown in Figure 3.7.

For disordered solid or soft materials exhibiting overlapping signals a deconvolution of MAS lines is difficult to perform. The influence of C_Q and of η_Q on the central line of MAS spectra for a spin $I = 3/2$ nucleus is presented in Figure 3.7. A clear signal shift can be seen, for increasing C_Q values.[17]
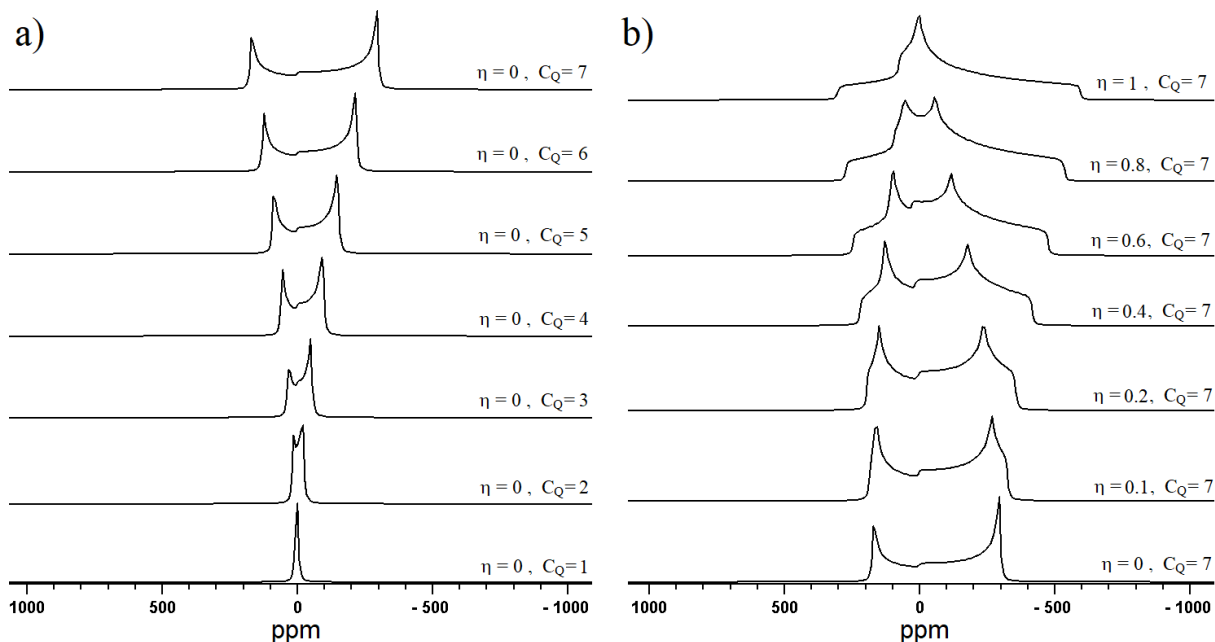
Figure 3.7: Calculated spectra for a spin 3/2 nucleus with a resonance frequency of 116.64 MHz (corresponds to ^{7}Li in an external field of 7.049 T). Here, only the central transition is shown. Satellite transitions can be found shifted far away. Spectra were simulated with the QUEST software, using a spectral width of 400 kHz, a Lorentzian broadening of 1 kHz and a Gaussian broadening of 100 Hz in order to smoothen the spectra.[21] (a) Small C_Q values ($C_Q = 1$ MHz) in an axially symmetric system ($\eta = \eta_Q = 0$) result in narrow lines. However, upon increasing C_Q, the signal clearly broadens. (b) Visualization of the effects of steadily increasing η, while $C_Q = 7$ MHz being constant. Stronger deviations from an axial symmetry causes an additional line broadening and an additional change in lineshape as seen for the complete series.

Inter-Nuclear Couplings (*J* Coupling and Dipolar Coupling)

The two interactions considered in the previous sections are caused by electrons and the charge distribution of the (local) environment which are interacting with the nucleus. Nuclei are also able to interact with each other, either through space (dipolar coupling) or through electrons in chemical bonds (*J* coupling).[1,2,3] In solution NMR, *J* couplings are of interest and contain useful information about the number of neighboring interacting nuclei. One information obtained from *J* coupling is known as the spin multiplicity, from which the number of coupling sites can be reconstructed. The *J* coupling is often only a few Hz large and therefore rarely seen in solid-state NMR in which other interactions cause a severe signal broadening. The more important interaction in solid-state NMR is the dipolar interaction which can reach several kHz. For reasons of simplification, the exclusive interaction of two nuclear spins will be considered in the following. The dipole coupling constant is defined by:[22,23]

$$D_{IS} = \frac{\hbar^2 \gamma_I \gamma_S}{4\pi r_{IS}^3} \left[1 - 3cos^2 \, \theta\right]$$

[3.15]

with the gyromagnetic ratios of nuclei *I* and *S* being γ_I, γ_S, the reduced Planck constant $\hbar$, the distance r_{IS} between *I* and *S* and the angle θ between the inter-spin vector and the external magnetic field. θ and r_{IS} are shown in Figure 3.8

From equation 3.15 it is evident that the dipolar interaction is particularly strong for nuclei with large gyromagnetic ratios, for instance a homonuclear ^{1}H–^{1}H coupling.
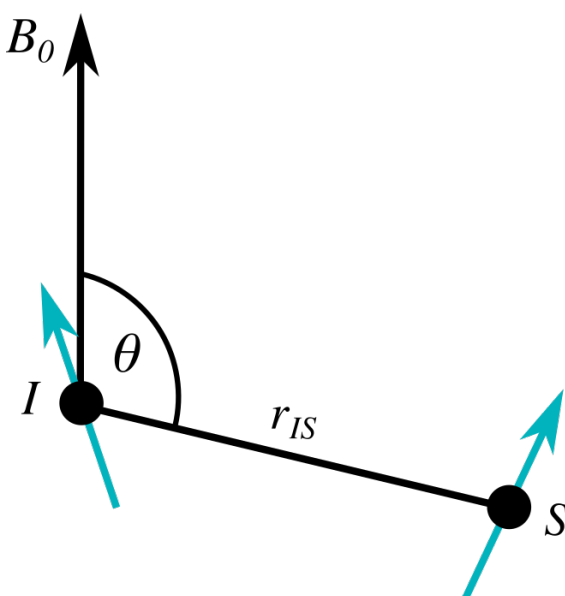
Figure 3.8: Illustration of the dipolar interaction between two nuclei *I* and *S* in an external field.

The angle θ between the external magnetic field and the inter spin-vector has a strong influence on the term $[1 - 3cos^2\,\theta]$, which is therefore sensitive to motion and is averaged to zero for dilute solutions. However, in the solid state this term is unequal zero and as a result the measured spectra of e.g. ^{1}H are broadened, leaving individual chemical sites unresolved. In the extreme case in which a large number of spins are coupled, a dipolar network is present, further broadening the spectrum. Due to the $[1 - 3cos^2\,\theta]$-dependence, the dipolar interaction can be averaged by MAS. The spinning frequency must be larger than the magnitude of the dipolar interaction in order to average out the latter completely. MAS experiments tend to be technically limited by upper boundaries of spinning speeds which are insufficient to fully average out the dipolar interaction. Nevertheless, lines observed under MAS are often narrowed notably compared to static spectra. In analogy to Figure 3.4, spinning sidebands are also present for MAS experiments on dipolar broadened spectra.

3.2 NMR for Energy Storage Materials

Susceptibility and Sample Shape

Susceptibility effects arise from the macroscopic shape of a sample in an external magnetic field. In solution-state NMR, the so-called bulk magnetic susceptibility χ (BMS) effects (e.g. from air bubbles) are well known to cause line distortions and even deviations in chemical shift.[24, 25] In general, BMS can be conceptualized as a tensor, similar to the other interactions discussed in section 3.1.

Two different BMS contributions may be considered, namely the diamagnetic BMS contribution (negative χ), which originates from orbiting paired electrons in the sample, and the paramagnetic BMS contribution (positive χ) which results from unpaired electrons. Similar to chemical shielding, additional shielding is observed for positive χ, whereas a deshielding field is induced by negative χ.

Typically, the paramagnetic contribution exceeds the diamagnetic contribution over several orders of magnitude and therefore becomes the dominant contribution. One source of the paramagnetic contribution may be molecular (triplet) oxygen, which has two unpaired electrons. For NMR experiments, a uniform magnetic field is required (parallel field lines, field is equally strong at any given place in the sample). A molecular susceptibility tensor is needed that enables a uniform internal field. Only few geometries are considered here, namely an

ellipsoid (as seen in Figure 3.3), a cylinder of infinite length and a thin disc.[25] These geometries display an additional orientation dependence with respect to the external field. In contrast, a perfect sphere does not exhibit an orientation dependence. The influence of the shape on the demagnetizing field $\mathbf{B_1}$ is given by:

$$\mathbf{B_1} = -\alpha\,\boldsymbol{\kappa}\,\mathbf{B_0} \qquad\qquad [3.16]$$

with the susceptibility tensor $\boldsymbol{\kappa}$ and the Osborne factor α (demagnetizing factor).[25] The susceptibility is now expressed as a tensor $\boldsymbol{\kappa}$ due to the orientation dependence of the magnetic response.

The Osborne factor differs for the four mentioned geometries. For a cylinder of infinite length which is placed parallel to the $\mathbf{B_0}$ field, $\alpha = 0$, while for the same cylinder placed perpendicular to the $\mathbf{B_0}$ field $\alpha = \frac{1}{2}$. For a sphere $\alpha = 1/3$ is obtained, while a thin disk placed with its normal perpendicular to the $\mathbf{B_0}$ field results in $\alpha = 1$. All geometries besides the sphere exhibit an orientation dependence of the demagnetizing field $\mathbf{B_1}$ and therefore of the chemical shift, which is the so-called bulk magnetic susceptibility shift (BMS). For a sample with arbitrary geometry and orientation to the $\mathbf{B_0}$ field, a bulk magnetic susceptibility shift as well as a line broadening can be observed. The reason for this is rooted in local variations of the demagnetizing field in the sample. The common way to consider the local field deviations is to take the so-called Lorentz sphere (small sphere within the sample) which is uniform and for which BMS is absent and subtract it from the rest of the sample. The effective compensating field in the Lorentz sphere $\mathbf{B_2}$ is then:

$$\mathbf{B_2} = \left(\frac{1}{3}\right)\boldsymbol{\kappa}\,\mathbf{B_0} \qquad\qquad [3.16]$$

The resulting magnetic susceptibility averaged field can be written as the sum of the three contributing fields:

$$\mathbf{B_C} = \mathbf{B_0} + \mathbf{B_1} + \mathbf{B_2} = \mathbf{B_0}\left\{1 + \left[\left(\frac{1}{3}\right) - \alpha\right]\boldsymbol{\kappa}\right\} \qquad\qquad [3.17]$$

Nevertheless, the susceptibility effects in solution NMR are typically small and in the order of < 0.1 Hz. However, high-resolution spectra often exhibit linewidths in the order of 0.1 Hz which is why magnetic susceptibility may be an upper linewidth limit.

In solid-state NMR, dominant interactions are the quadrupolar interaction, dipolar interaction and CSA, which broaden the spectral lines more severely than magnetic susceptibility effects.

Still, there are known examples for which magnetic susceptibility effects need to be taken into account, namely for a polymer electrolyte containing solid particles, for liquid crystal films and for graphite.[26, 27, 28, 29] The latter have in common that anisotropic orientations of the material are present, giving rise to orientation dependent line broadenings and magnetic susceptibility shifts.

Ring Current Effects and Nucleus Independent Chemical Shift (NICS)

In this work, three types of carbon-based materials are studied, namely hard carbon spheres, C_1N_1 and polymeric C_3O_2. Therefore, it is important to take into account the effect of aromatic ring currents on the observed spectra. All of the examined carbon-based materials consist of conjugated sp^2-hybridized carbon atoms. In an external magnetic field, aromatic ring currents are induced, as is schematically shown in Figure 3.1 and 3.9.
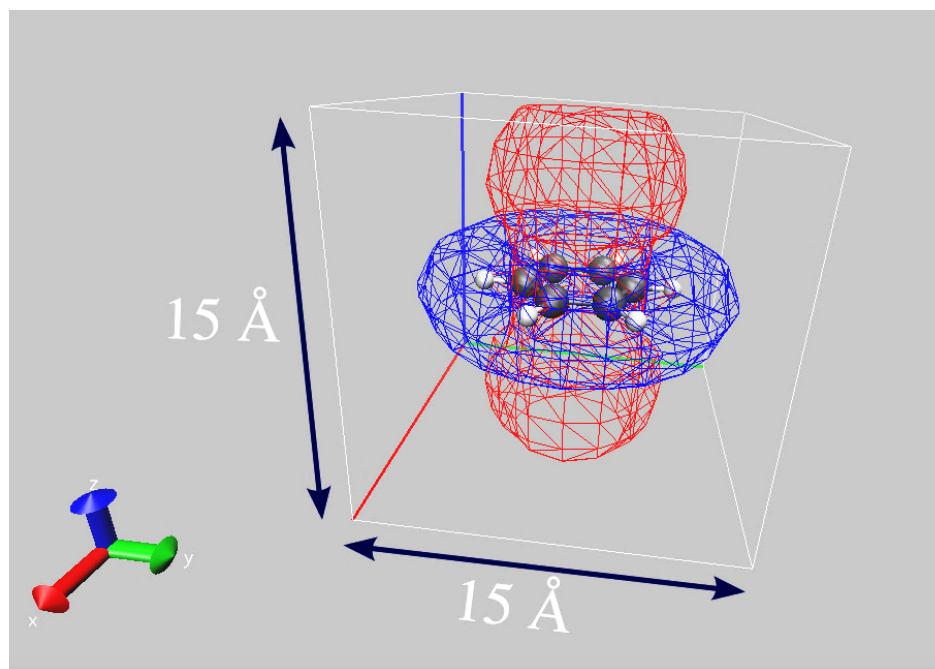
Figure 3.9: Illustration of the calculated shielding surfaces for benzene (H: white spheres, C: grey spheres). The blue isosurface shows the 0.1 ppm deshielding region, while the red isosurface shows the −0.1 ppm shielding region. Chemical shielding data were computed using density functional theory (DFT) with the Perdew-Burke-Ernzerhof (PBE) functional. The def2-SVP basis set was used, and the RI approximation was also used with the auxiliary basis set def2/J.[30] A 15 x 15 x 15 Å grid of "ghost atoms" was placed around the benzene structure.[31] The so-called ghost atoms do not have electrons or nucleons and were used as local probes for the experienced magnetic field at their position.

The down-field shift for the hydrogen atoms in benzene occurs due to a deshielding region which is generated in the plane of the benzene molecule (close to the blue surface in Figure 3.9), while a shielding region is present inside the ring and above/below the benzene molecule (red surface in Figure 3.9).

Initially, the concept of nucleus independent chemical shift was used to measure the aromaticity of chemical compounds.[25] The calculation of NICS takes an aromatic structure (for example benzene) and sets up a three-dimensional grid around the molecular structure (ghost atoms). These ghost atoms are placed for example at the junctions of the three-dimensional grid. Then the shielding tensor at the position of the ghost atom can be calculated, which is exclusively influenced by the shielding field caused by the studied molecule.

Work by Schleyer and co-workers and Oth pointed towards two main location-dependent contributions in NICS.[32, 33] Firstly, the diamagnetic ring current effect, which generates a shielding field is considered and secondly the paramagnetic ring currents which cause a deshielding field as visualized in Figure 3.9. Both effects are present for the benzene molecule, so that a second molecule/ion (frozen in motion), which is located either above the ring or close to the plane outside of the ring experiences a different induced field and therefore a different chemical shift. The relation between nucleus independent chemical shift and isotropic chemical shift is given by:[32, 33]

$$\text{NICS} = -(\delta_{\text{iso}} - \delta_{\text{ref}}) \tag{3.18}$$

with NICS having the unit of ppm.

It is important to note that the NICS effect depends on the chemistry of the surface and on the distance to the surface. According to Forse, the diamagnetic shift decays as:[34]

$$\Delta\delta = \frac{(\chi_\parallel - \chi_\perp)}{6\pi r^3} \tag{3.19}$$

with the molar magnetic susceptibility $\chi_\parallel$ (parallel to the $\mathbf{B_0}$ field) and $\chi_\perp$ (perpendicular to the $\mathbf{B_0}$ field) at the surface.

Due to the characteristics of the NICS which often yields spectral lines shifted upfield, it is commonly used to probe that molecules or ions are inserted into an aromatic host matrix. An example is the insertion of ions into a carbon-based electrode, which yields a notable upfield

shift of the signal of the studied nucleus.[34] An outstanding example of NMR being sensitive to both (shielding and deshielding) local magnetic fields is the NMR spectrum of [18] annulene.[33] Protons, which point to the inside of the [18] annulene ring are highly shielded and yield signals at −3 ppm, whereas protons pointing outwards of the plane are deshielded and give rise to signals at 9.3 ppm. Similar observations are made for activated carbons, for which the uptake of an electrolyte solution (containing cation, anion and solvent molecule) yields analogous upfield shifts independent of the studied nucleus.[35, 36] These findings highlight two aspects, i) that the aromatic ring currents are indeed the main source of the observed shift and ii) that only adsorbed "in-pore" ions/molecules exhibit the so-called diamagnetic shift.[32]

DFT calculations comparing the induced fields of entirely carbon-based matrices and hetero-cycles do not show a consistent trend, indicating that both (stronger or weaker) induced field may be present for hetero-cycles.[31]

In this context Borchard and co-workers specify the diamagnetic shift $\Delta\delta$.[37] More generally, they relate the observed $\Delta\delta$ to the radius of a spherical pore, which is defined by:

$$\Delta\delta = \int_{0}^{R-\varepsilon} w(r)\Delta\delta(r)\mathrm{d}r \qquad [3.20]$$

with R as the radius of the spherical pore, ε as the minimum distance between the guest molecule and the aromatic pore wall, the weight function *w(r)* as the probability to find a guest molecule within the distance interval $[r, r + \mathrm{d}r]$ and $\Delta\delta(r)$ the diamagnetic shift as a function of the position.

Considering the case of a homogeneous distribution of guest molecules in the pores of the matrix, equation 3.20 can be rewritten as:

$$\Delta\delta = \Delta\delta_{MAX}\frac{4\,\pi}{V}\int_{0}^{R-\varepsilon} r^2\,f(r)\mathrm{d}r \qquad [3.21]$$

$$V = \frac{4\pi}{3}\,(R-\varepsilon)^3 \qquad [3.22]$$

the function $f(r)$ which describes the distance dependence of the induced shift and the maximum of the diamagnetic shift is $\Delta\delta_{MAX}$.

One issue with equation 3.21 is that the exact function $f(r)$ is not known. Nevertheless, it is clear that the first layer of molecules directly located at the pore walls experience the maximum diamagnetic shift $\Delta\delta_{MAX} = \Delta\delta(R - \varepsilon)$. It is important to note that $\Delta\delta_{MAX}$ is a constant for a specific pore system. Even a recent computational study, carried out for numerous heterocyclic analogues of benzene showed that larger and smaller NICS values are found for these heterocycles.[38] When the distance from the pore wall increases, the observed diamagnetic shift steadily decreases.

Exchange in Porous Carbonaceous Materials

Water is used as a measuring probe, in order to obtain information about the pores of carbonaceous materials studied in Chapter 6. One important point to consider is the molecular dynamics and its impact on the observed diamagnetic shift, as shown in Figure 3.10.
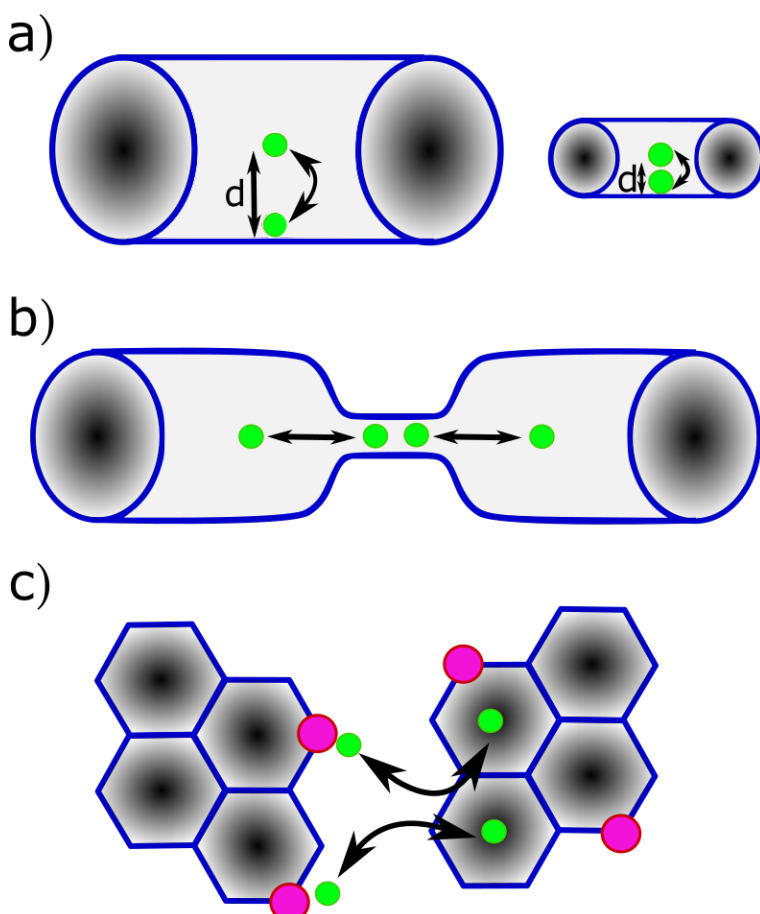
**Figure 3.10:** Scheme of different exchange sites found in porous carbonaceous materials. a) Exchange in large and small pores between water molecules (green spheres) located at the surface and at the center of a pore, separated by d. b) Exchange in pores with irregular pore diameter. c) Exchange of water molecules between heteroatom sites (magenta spheres: N, O, S) and with graphite-like sheets (top view).

Due to exchange between different unequal sites, the observed $\Delta\delta$ values are averaged over statistically weighted sites, as discussed in the previous section.

Chemical exchange is discussed in detail by Levitt.[1] When exchange phenomena are discussed, the main emphasis is typically directed towards exchange dynamics which is classified into slow, intermediate and fast exchange. The different sites a water molecule may occupy during the NMR experiment are discussed in the following. The precise type of exchange greatly influences the position of the ^{1}H signal of water.

Different cases of exchange are briefly summarized in Figure 3.10 and will be further discussed in Chapter 6. Intra-pore exchange, as shown in Figure 3.10 a) is one relevant type of exchange. It can occur in pores with a large and small pore radius R and is discussed by Borchard (cf. equations 3.20–3.22). Assuming that the minimal distance ε is nearly constant for a given matrix, R is the limiting parameter for the observed $\Delta\delta$ values. In case of exchange, the obtained $\Delta\delta$ value will be significantly smaller in a pore with a larger pore radius, compared to a smaller pore radius.

The second type of exchange is the inter-pore exchange, where a H_2O molecule changes its position from a small to a larger pore (see Figure 3.10 b)). This exchange averages a large $\Delta\delta$ value of H_2O located in a small pore with a small $\Delta\delta$ value of H_2O located in a larger pore. In case of no exchange or slow exchange, e.g. in a disconnected pore system, two separated NMR signals occur.

A third type of exchange must be considered, when two chemically unequal sites are present in the structure. This is the case when a notable amount of heteroatoms is present, for which additional non-covalent interactions such as hydrogen-bonding must be considered, as illustrated in Figure 3.10 c). It can be assumed that the diamagnetic shift experienced by a water molecule located above (or beneath) the graphite plane is large, while it is basically absent when the molecule is hydrogen-bonded to the heteroatom and therefore located close to the aromatic heteroatoms. Exchange between both sites again averages the position of the NMR line between both pure states. Noteworthy is the fact that hydrogen bonded states (deshielded) often exhibit a line shifted to large ppm values. An exchange with a shielded state then possibly results in a line that is only marginally shifted compared to the lines expected for the cases shown in 3.10 a) and 3.10 b).

Diffusion NMR

As briefly discussed in Chapter 2, the ion diffusivities in (polymer) electrolytes are essential for the understanding of transport properties in these rather complex materials. At this point of discussion diffusion NMR becomes relevant. To measure the diffusion of molecules or ions by NMR, a pulsed field gradient (PFG) spin-echo experiment can be employed.[39] Improved pulse sequences, which compensate convection, eddy currents and suppress the solvent signal have become today's standard.[40, 41, 42]

The pulse sequence shown in Figure 3.11 consists of two radiofrequency pulses ($\pi/2$ and π pulse) separated by the time τ and two gradient pulses separated by the diffusion time Δ. A spin echo is generated after 2τ. The intensity is followed as a function of the gradient strength. In general, the evolution of the spin-echo signal depending on the gradient strength can be described by the Stejskal-Tanner equation:[39]

$$ln[A/A_0] = -D\gamma^2\delta^2 g^2\left(\Delta - \frac{\delta}{3}\right)$$ [3.23]

with the gradient duration δ, the gradient strength g, the self-diffusion coefficient D, the measured echo intensity with and without the implementation of a gradient field, A_0 and A, respectively.
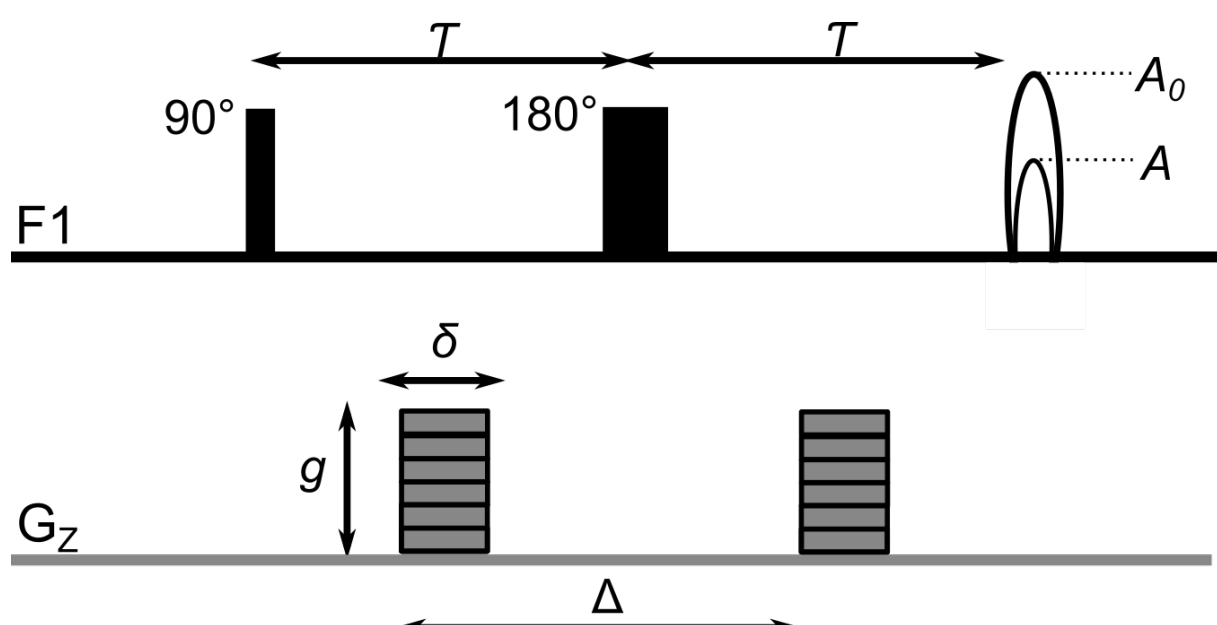
Figure 3.11: Schematic showing the pulsed field gradient (PFG) spin echo pulse sequence e.g. to measure ^{1}H or ^{19}F diffusion. Radiofrequency pulses are present at the F1 channel. Gradient pulses are depicted by grey rectangles. Time τ separates two radiofrequency pulses. The diffusion time is Δ.

The important aspect regarding diffusion NMR is that displacements (mean squared displacement (MSD)) are used to probe molecular or ion diffusivities. The diffusion time Δ is related to a particle's mean squared displacement $\langle r^2(\tau) \rangle$ along one axis (i.e. gradient axis) via:

$$\langle r^2(\tau) \rangle = 2D\Delta \hspace{6cm} [3.24]$$

The mean squared displacement is useful, to estimate the distance over which a particle has diffused in a given time interval.

In Figure 3.12 different random walk trajectories are shown. At longer waiting times τ, particles are able to diffuse over a longer distance r. This is commonly the case for free diffusion as shown in Figure 3.12 a). A log-log plot of the MSD against the waiting time τ would then lead to a straight line with a positive slope. For free "bulk" diffusion, the diffusion coefficients are independent of the diffusion time Δ.

Whenever particles diffuse through a confined medium, the diffusion behavior differs significantly from the case of the free or "bulk" diffusion. Whenever a restricted diffusion is present, the MSD and diffusion coefficient depend significantly on the diffusion time Δ. At very small diffusion times, the particles or molecules may be able to diffuse freely. This would lead to a situation which can be compared to the free diffusion.
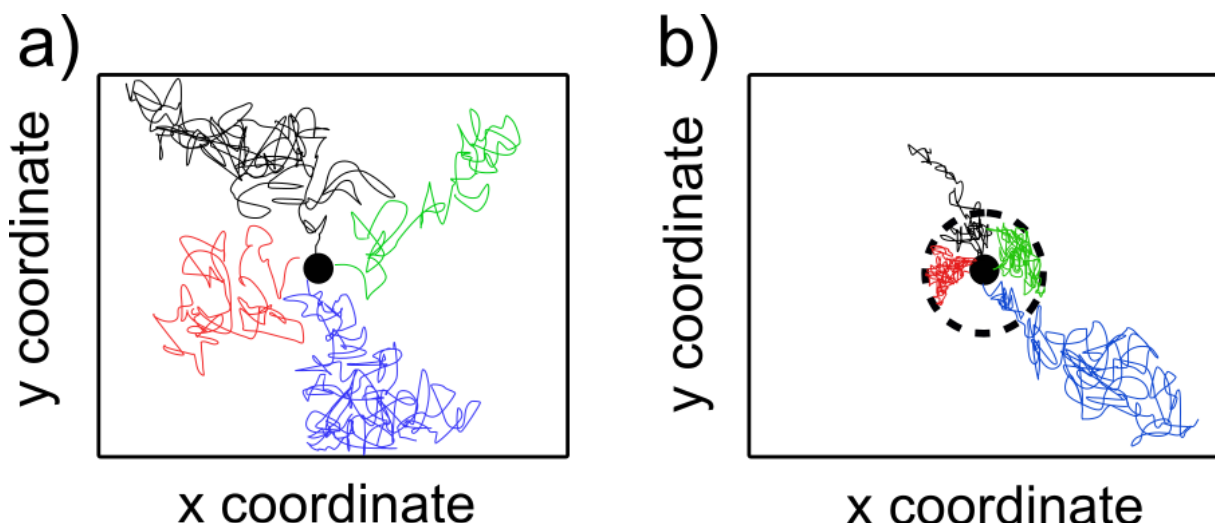
Figure 3.12: (a) Schematic representation of different random walk trajectories for the case of free "bulk" diffusion. (b) Displays different random walk trajectories for the case of diffusion through a confined space. The partially permeable confinement is represented by the dotted circle.

However, by increasing the diffusion time, particles or molecules are not necessarily able to diffuse over longer distances because a confinement prevents these particles from diffusing freely. This is shown in Figure 3.12 b). In this scenario the diffusion coefficient would decrease by increasing the diffusion time Δ. Therefore, a non-linear relation is expected in a log-log plot of the MSD against τ.

How strongly pronounced this effect is, depends on the size of the confinement and how much it restricts the diffusion of the observed nucleus. A so-called confinement parameter $c = \frac{d_{particle}}{l_{confinement}}$ is introduced.[43] This dimensionless parameter is the ratio of the particle's diameter and the confinement length (for cylindrical pores and slit pores). Babayekhorasani and coworkers found that the diffusion coefficient is reduced when the confinement parameter increases.[43]

The isotropic diffusion can be characterized by equation 3.24 and the Stokes-Einstein equation:[44]

$$D = \frac{k_B T}{6\pi\eta R_h} \tag{3.25}$$

with k_B being the Boltzmann constant, T the temperature, η the viscosity of the solvent and R_h the hydrodynamic radius.

By knowing the particle's hydrodynamic radius and the solvent viscosity, the diffusion coefficient can be calculated at a given temperature. For the so-called "anomalous" diffusion ($\alpha \neq 1$), a non-linearity is observed in a log-log plot of the MSD against τ. The relation between the MSD and τ is governed by a power law:

$$\langle r^2(\tau) \rangle \propto \tau^\alpha \tag{3.26}$$

with three cases for the parameter α, namely $\alpha > 1$, $\alpha = 1$ and $\alpha < 1$. The case for which $\alpha > 1$ is called "super-diffusion" (faster than free diffusion) and the case for which $\alpha < 1$ is called "sub-diffusion" (slower than free diffusion).[45, 46]

When the anomalous parameter is $\alpha = 1$, then the normal free diffusion takes place. The anomaly of diffusion can have many different reasons, such as molecular crowding and diffusion through polymer networks.[47]

Another size-related aspect (not related to anomalous diffusion) that needs to be considered is the diffusion of a dissolved salt (A^+B^-) with a cation A^+ larger than B^-. By considering equation 3.25 it can be expected that the cation A^+ diffuses more slowly than the anion due to the larger size. However, materials like ionic liquids may exhibit an opposite behavior, since numerous ion configurations are potentially present in bulk (e.g. ion clusters).[47]

3.3 References

(1) Levitt, M. H. (2013). *Spin dynamics: basics of nuclear magnetic resonance*. John Wiley & Sons.

(2) Abragam, A. (1961). *The principles of nuclear magnetism* (No. 32). Oxford university press.

(3) Keeler, J. (2011). *Understanding NMR spectroscopy*. John Wiley & Sons.

(4) Facelli, J. C. (2004). *Concepts Magn. Reson. A 20*, 42-69.

(5) Ramsey, N. F. (1950). Magnetic shielding of nuclei in molecules. *Physical Review*, *78*(6), 699.

(6) Ramsey, N. F. (1951). Dependence of magnetic shielding of nuclei upon molecular orientation. *Physical Review*, *83*(3), 540.

(7) Widdifield, C. M., & Schurko, R. W. (2009). Understanding chemical shielding tensors using group theory, MO analysis, and modern density-functional theory. *Concepts in Magnetic Resonance Part A: An Educational Journal*, *34*(2), 91-123.

(8) Dahanayake, J. N., Kasireddy, C., Karnes, J. P., Verma, R., Steinert, R. M., Hildebrandt, D., ... & Mitchell-Koch, K. R. (2018). Progress in Our Understanding of 19F Chemical Shifts. *Annual Reports on NMR Spectroscopy*, *93*, 281-365.

(9) Purcell, E. M. (1952). Research in nuclear magnetism, Nobel Lecture. *Physics: l942*.

(10) Morcombe, C. R., & Zilm, K. W. (2003). Chemical shift referencing in MAS solid state NMR. *Journal of Magnetic Resonance*, *162*(2), 479-486.

(11) Anet, F. A., & O'Leary, D. J. (1991). The shielding tensor. Part I: Understanding its symmetry properties. *Concepts in Magnetic Resonance*, *3*(4), 193-214.

(12) Keil, W., Javed, A., Elgabarty, H., Weinberger, C., Tiemann, M., & Schmidt, C. (20xx).

(13) Chapuisat, X. (1991). Exact quantum molecular hamiltonians: II. On the choice of the moving frame of reference. The principal axis system. *Molecular Physics*, *72*(6), 1233-1265.

(14) Young, R. P., Lewis, C. R., Yang, C., Wang, L., Harper, J. K., & Mueller, L. J. (2019). TensorView: A software tool for displaying NMR tensors. *Magnetic Resonance in Chemistry*, *57*(5), 211-223.

(15) Mueller, L. J. (2011). Tensors and rotations in NMR. *Concepts in Magnetic Resonance Part A*, *38*(5), 221-235.

(16) Stejskal, E. O., Schaefer, J., & Waugh, J. S. (1977). Magic-angle spinning and polarization transfer in proton-enhanced NMR. *Journal of Magnetic Resonance (1969)*, *28*(1), 105-112.

(17) Ashbrook, S. E. (2009). Recent advances in solid-state NMR spectroscopy of quadrupolar nuclei. *Physical Chemistry Chemical Physics*, *11*(32), 6892-6905.

(18) NMR of Quadrupolar Nuclei in Solid Materials; Wasylishen, R. E., Ashbrook, S. E., Wimperis, S., Eds.; Encyclopedia of Magnetic Resonance; Wiley: West Sussex, UK, 2012.

(19) Vega, A. J. (2007). Quadrupolar nuclei in solids. *Solid-State NMR Studies of Biopolymers; McDermott, AE; Polenova, T., Eds*, 111-138.

(20) Alemany, L. B. (1993). Critical factors in obtaining meaningful fast MAS NMR spectra of non-integral spin quadrupolar nuclei. A review with particular emphasis on 27 Al MAS NMR of catalysts and minerals. *Applied Magnetic Resonance*, *4*(1-2), 179-201.

(21) Perras, F. A., Widdifield, C. M., & Bryce, D. L. (2012). QUEST—QUadrupolar Exact SofTware: A fast graphical program for the exact simulation of NMR and NQR spectra for quadrupolar nuclei. *Solid state nuclear magnetic resonance*, *45*, 36-44.

(22) Lipsitz, R. S., & Tjandra, N. (2004). Residual dipolar couplings in NMR structure analysis. *Annu. Rev. Biophys. Biomol. Struct.*, *33*, 387-413.

(23) Brunner, E. (2001). Residual dipolar couplings in protein NMR. *Concepts in Magnetic Resonance*, *13*(4), 238-259.

(24) Schenck, J. F. (1996). The role of magnetic susceptibility in magnetic resonance imaging: MRI magnetic compatibility of the first and second kinds. *Medical physics*, *23*(6), 815-850.

(25) VanderHart, D. L. (2007). Magnetic susceptibility and high resolution NMR of liquids and solids. *eMagRes*.

(26) Ulrich, R., Glaser, R. W., & Ulrich, A. S. (2003). Susceptibility corrections in solid state NMR experiments with oriented membrane samples. Part II: theory. *Journal of Magnetic Resonance*, *164*(1), 115-127.

(27) Manning, A. P., Giese, M., Terpstra, A. S., MacLachlan, M. J., Hamad, W. Y., Dong, R. Y., & Michal, C. A. (2014). NMR of guest-host systems: 8CB in chiral nematic porous glasses. *Magnetic Resonance in Chemistry*, *52*(10), 532-539.

(28) Freitas, J. C., Emmerich, F. G., Cernicchiaro, G. R., Sampaio, L. C., & Bonagamba, T. J. (2001). Magnetic susceptibility effects on 13C MAS NMR spectra of carbon materials and graphite. *Solid State Nuclear Magnetic Resonance*, *20*(1-2), 61-73.

(29) Kitajima, S., Matsuda, M., Yamato, M., & Tominaga, Y. (2013). Anisotropic ionic conduction in composite polymer electrolytes filled with clays oriented by a strong magnetic field. *Polymer journal*, *45*(7), 738-743.

(30) Weigend, F., & Ahlrichs, R. (2005). Balanced basis sets of split valence, triple zeta valence and quadruple zeta valence quality for H to Rn: Design and assessment of accuracy. *Physical Chemistry Chemical Physics*, *7*(18), 3297-3305.

(31) Chen, Z., Wannere, C. S., Corminboeuf, C., Puchta, R., & Schleyer, P. V. R. (2005). Nucleus-independent chemical shifts (NICS) as an aromaticity criterion. *Chemical reviews*, *105*(10), 3842-3888.

(32) Schleyer, P. V. R., Manoharan, M., Wang, Z. X., Kiran, B., Jiao, H., Puchta, R., & van Eikema Hommes, N. J. (2001). Dissected nucleus-independent chemical shift analysis of π-aromaticity and antiaromaticity. *Organic Letters*, *3*(16), 2465-2468.

(33) Oth, J. F. M., Woo, E. P., & Sondheimer, F. (1973). Unsaturated macrocyclic compounds. LXXXIX. Dianion of [18] annulene. *Journal of the American Chemical Society*, *95*(22), 7337-7345.

(34) Forse, A. C., Griffin, J. M., Merlet, C., Carretero-Gonzalez, J., Raji, A. R. O., Trease, N. M., & Grey, C. P. (2017). Direct observation of ion dynamics in supercapacitor electrodes using in situ diffusion NMR spectroscopy. *Nature Energy*, *2*(3), 1-7.

(35) Harris, R. K., Thompson, T. V., Norman, P. R., & Pottage, C. (1999). Phosphorus-31 NMR studies of adsorption onto activated carbon. *Carbon*, *37*(9), 1425-1430.

(36) Forse, A. C., Merlet, C., Grey, C. P., & Griffin, J. M. (2021). NMR studies of adsorption and diffusion in porous carbonaceous materials. *Progress in Nuclear Magnetic Resonance Spectroscopy*, *124*, 57-84.

(37) Borchardt, L., Oschatz, M., Paasch, S., Kaskel, S., & Brunner, E. (2013). Interaction of electrolyte molecules with carbon materials of well-defined porosity: characterization by solid-state NMR spectroscopy. *Physical Chemistry Chemical Physics*, *15*(36), 15177-15184.

(38) Báez-Grez, R., Rabanal-León, W. A., Alvarez-Thon, L., Ruiz, L., Tiznado, W., & Pino-Rios, R. (2019). Aromaticity in heterocyclic analogues of benzene: Dissected NICS and current density analysis. *Journal of Physical Organic Chemistry*, *32*(1), e3823.

(39) Stejskal, E. O., & Tanner, J. E. (1965). Spin diffusion measurements: spin echoes in the presence of a time-dependent field gradient. *The journal of chemical physics*, *42*(1), 288-292.

(40) Price, W. S., & Kuchel, P. W. (1991). Effect of nonrectangular field gradient pulses in the Stejskal and Tanner (diffusion) pulse sequence. *Journal of magnetic resonance*, *94*(1), 133-139.

(41) Momot, K. I., & Kuchel, P. W. (2004). Convection-compensating PGSE experiment incorporating excitation-sculpting water suppression (CONVEX). *Journal of magnetic resonance*, *169*(1), 92-101.

(42) Zheng, G., Stait-Gardner, T., Kumar, P. A., Torres, A. M., & Price, W. S. (2008). PGSTE-WATERGATE: An STE-based PGSE NMR sequence with excellent solvent suppression. *Journal of Magnetic Resonance*, *191*(1), 159-163.

(43) Babayekhorasani, F., Dunstan, D. E., Krishnamoorti, R., & Conrad, J. C. (2016). Nanoparticle diffusion in crowded and confined media. *Soft Matter*, *12*(40), 8407-8416.

(44) Einstein, A. (1905). "Über die von der molekularkinetischen Theorie der Wärme geforderte Bewegung von in ruhenden Flüssigkeiten suspendierten Teilchen". *Annalen der Physik* (in German). 322 (8): 549–560.

(45) Molina-Garcia, D., Sandev, T., Safdari, H., Pagnini, G., Chechkin, A., & Metzler, R. (2018). Crossover from anomalous to normal diffusion: truncated power-law noise correlations and applications to dynamics in lipid bilayers. *New Journal of Physics*, *20*(10), 103027.

(46) Metzler, R., & Klafter, J. (2004). The restaurant at the end of the random walk: recent developments in the description of anomalous transport by fractional dynamics. *Journal of Physics A: Mathematical and General*, *37*(31), R161.

(47) Bayles, A. V., Valentine, C. S., Überrück, T., Danielsen, S. P., Han, S., Helgeson, M. E., & Squires, T. M. (2019). Anomalous solute diffusivity in ionic liquids: label-free visualization and physical origins. *Physical Review X*, *9*(1), 011048.

Chapter 4

Electrolyte Materials and Carbonaceous Electrode Materials

This chapter aims to review materials, which are relevant for this work, namely electrolyte systems and their individual components, which are used in lithium ion batteries. Further, carbonaceous materials, used as electrode materials into which ions or molecules can be intercalated are subject of this chapter.

4.1 Electrolytes

A key component of a lithium ion battery is the electrolyte, enabling ion migration from one electrode to the other during charging and discharging of the battery. In particular the charging time, which should be as short as possible, depends to a large extent on the transport properties of the electrolyte. In most cases, the electrolyte is a multi-component system that contains a salt, solvent and further additives. These components are introduced in the following section.

Salts

Lithium salts are an essential part of the electrolytes for lithium-ion batteries and have been intensively studied since the early 70s.[1] One of the main efforts was devoted to stabilize the lithium anode during cycling of the battery and to prevent a too fast cell death. In general, the studied salts, for example $LiBF_4$, $LiPF_6$ or $LiAsF_6$ have in common that the anions were derived from superacids, in the definition of the Brønsted acidity.[2] The idea behind considering Brønsted acids is that the coordination of the anion to the lithium cation is in general weaker, the stronger the acidity is.[3] Weakly coordinating anions are desired in order to obtain a high lithium dissociation. A comprehensive overview of commonly used anions is shown in Figure 4.1.
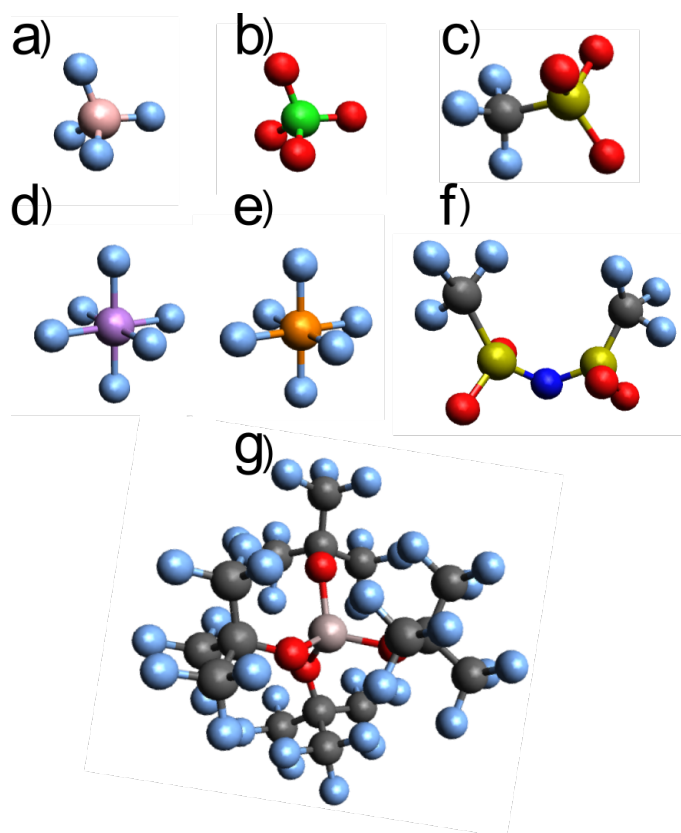
Figure 4.1: Anions commonly used in lithium ion batteries (a-f) and a more advanced anion (g). (a) BF_4^-, (b) ClO_4^-, (c) $SO_3CF_3^-$, (d) PF_6^-, (e) AsF_6^-, (f) $N(SO_2CF_3)_2^-$ (cis conformation) and (g) $[Al(OC(CF_3)_3)_4]^-$ (carbon: grey, fluorine: light blue, nitrogen: dark blue, oxygen: red, sulfur: yellow, chlorine: green, phosphorus: purple, arsenic: orange, aluminum: tan).

Often, the gas-phase acidity is used to estimate the acidity, although the acidity in solution may deviate severely from the latter. For the salts shown in Figure 4.1, two effects have widely been considered. i) the strong acidifying effect of (fluoro)sulfonyl groups, ii) the strong electron withdrawing character of fluorine and highly fluorinated anions in order to achieve a weak association to the lithium cation.[4]

In addition to these two aspects, there are a few more general properties which are crucial for the choice of the lithium salt. The most obvious is that the lithium-ion conductivity should be as high as possible in order to achieve a high-power charging and discharging accompanied with short charging times.[5,6] In more detail, the product of the ion conductivity and the lithium cation transference number t_+ is the decisive transport property, as pointed out in literature.[7] The product of lithium transference number and ion conductivity is in particular important for a reasonable comparison of the lithium ion conductivities in different salts, with varying bulk conductivities. Fast lithium ion transport is needed, since lithium ions are reduced and oxidized

at the surface of the electrodes. The electrochemical reduction and oxidation is a significantly faster process compared to ion migration, which is why the rate-limiting step is largely governed by ion migration. Obviously, the anion in the lithium salt of choice, influences the ion conductivity significantly. This is due to the already mentioned anion coordination and the anion structure. Therefore, a low ion association in combination with a high lithium-ion mobility and lower anion mobility is desirable to meet this goal.

Besides that, the salt's stability is of major importance. A lithium-ion battery operates in a certain potential window of e.g. 0.1 V–3.2 V in case of a $LiFePO_4$-based cell with a graphite anode. Therefore, the salt should show a good stability within this potential window for more than 1000 charge/discharge cycles in order to keep capacity losses small.[8]

On the other hand, it is also desired that the anion decomposes to a certain degree in order to form the so-called solid-electrolyte interphase (SEI). This interphase ideally forms during the first charging. It is composed of salt, solvent and impurities, such as H_2O and O_2. Subsequently, a "passivation layer" is formed, which prevents further salt decomposition and accompanying capacity loss. The desired properties of the SEI are i) good lithium ion conductivity, in order to enable lithium ion transport between the electrode and electrolyte and ii) poor electronic conductivity, in order to prevent further salt or solvent decomposition.[9, 10]

For systems such as PEO-based electrolytes and for binary electrolytes (salts dissolved in ionic liquids), the lithium transference number is no longer independent of the concentration of lithium cations in the electrolyte solution. A possible reason for this may be concentration-dependent changes in the ion conduction mechanism.[11]

For binary electrolytes, a high concentration of lithium salt, just under the precipitation concentration results in higher lithium transference numbers.[12] Solid salt inside the electrolyte solution causes a lowering of the ion conductivity, which is a widely known problem for lithium ion batteries operating at low temperatures. Further relevant aspects are the compatibility of the lithium salt with different parts of a lithium ion battery (electrodes and current collectors) and safety aspects, such as the reaction of the lithium salt with water or oxygen or HF formation (especially for $LiPF_6$).[13, 14, 15]

Recently, anions were specifically synthesized in order to meet the listed needs, for example the [Al(OC(CF$_3$)$_3$)$_4$]$^-$ anion in Figure 4.1 g). These anions with a high fluorine content exhibit often a high ion dissociation in combination with a good oxidative stability, while at the same time lower conductivities were found compared to LiPF$_6$ and other "more classical" lithium salts.[16] The synthesis of new salts may be one key element to realize more customized cells, especially cells operating at very high or low temperatures.

Solvents

In order to enable a good dissociation of the previously discussed lithium salts, appropriate solvents are required. In the last decades, especially carbonates shown in Figure 4.2 and in particular cyclic carbonates have gained attention because of their ability to dissolve large concentrations of the well-established LiPF$_6$ salt.[17] As a result, the so-called LP30 electrolyte (1 M LiPF$_6$ in ethylene carbonate and dimethyl carbonate) has been established which is nowadays as one of the electrolytes used commercially.[18] On the other hand, it is well-known that in particular dimethyl carbonate is able to form highly flammable gases and thus poses a serious safety problem.

Requirements for the choice of a solvent are highly similar with those formulated for the lithium salts. The solvent should i) enable a high ion conductivity and complete dissociation of the lithium salt. ii) exhibit a high electrochemical stability. iii) possess high safety including non-flammability and iv) open up a wide temperature range. Even though, points i), ii) and iv) are (partially) fulfilled for a wide range of carbonates, the safety lack has driven research towards safer solvents.
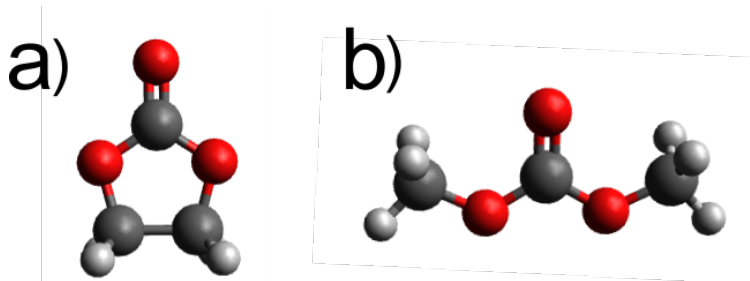

Figure 4.2: Chemical structure of ethylene carbonate (a) and dimethyl carbonate (b).

Ionic Liquids

Recent approaches for finding green solvents focused increasingly on a class of materials called room temperature ionic liquids, which currently replace common organic solvents in a variety of applications.[19] The "green" label can be associated to the low vapor pressure of ionic liquids, which are therefore not released into the environment, different from typical organic solvents. Room temperature ionic liquids are salts exhibiting a low melting point which is far below 100 °C and therefore are in the liquid phase at room temperature. The liquid state is commonly rationalized as one of an associated liquid exhibiting correlated ion motions. The first relevant industrial application of ionic liquids is the BASIL™ process, in which phenyl phosphines are synthesized.[20] Possible future applications are the dissolution of cellulose and applications as electrolytes in lithium-ion batteries.[21, 22]

Further, ionic liquids meet numerous requirements, in particular a high room temperature ion conductivity of c. 2 S/cm^2 (for 1-ethyl-3-methylimidazolium dicyanamide) and a low vapor pressure and thus low flammability.[23]
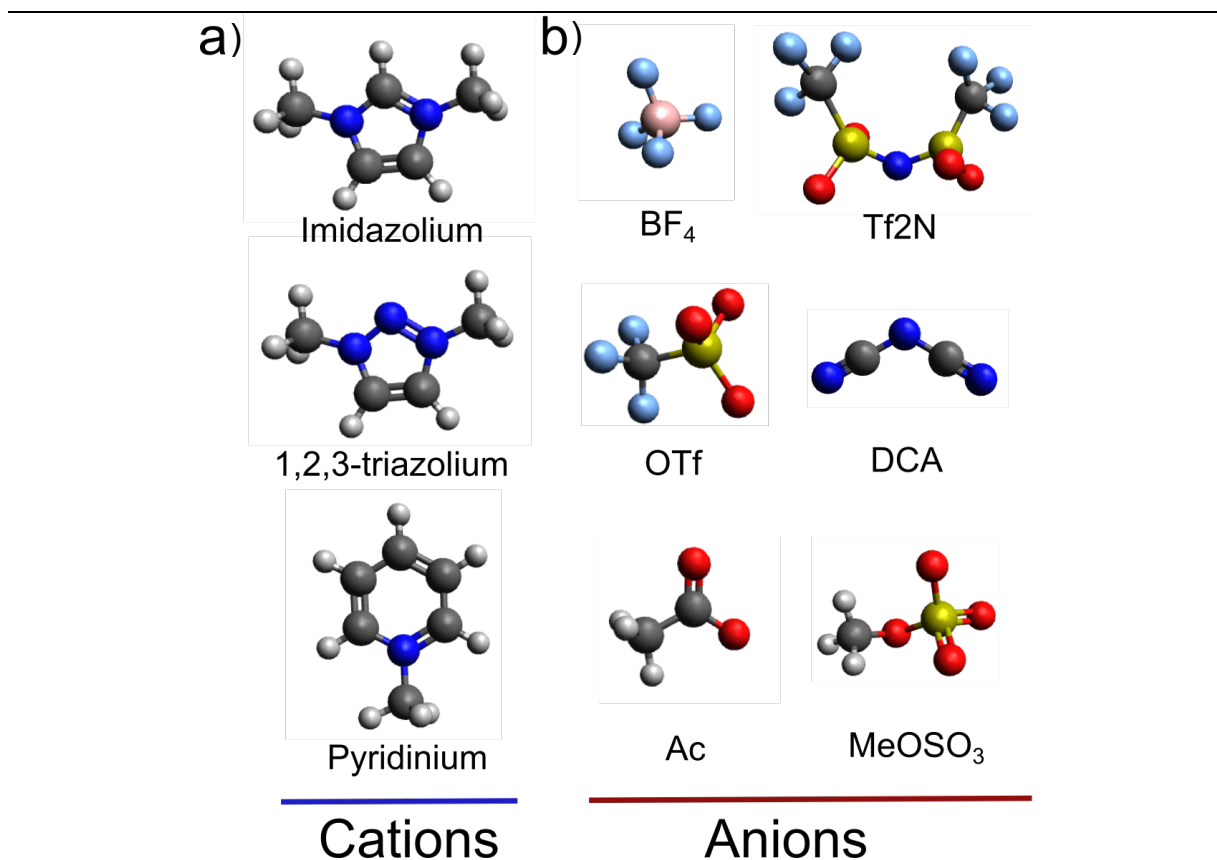

Figure 4.3: Scheme of prominent protic and aprotic cations (a) and fluorinated and non-fluorinated anions (b).

One of the first studies on the physicochemical properties of an ionic liquid was carried out by Walden.[24] He studied the effect of viscosity on the ion conductivity and found a clear deviation from linearity in a plot of ionic conductivity versus viscosity (Walden plot) for the studied ionic liquid. This surprising finding justified further research on the field of ionic liquids. Since then, effort has been invested in the synthesis of novel ionic liquids. Typically, ionic liquids are composed of an organic cation and either an organic or an inorganic anion. Especially, imidazolium or pyridinium-based halides are precursors for a further synthesis of more advanced ionic liquids. An ion exchange reaction can be employed in order to synthesize ions tailored for a special application. In addition to this simple approach, there are endless options for the preparation of advanced ionic liquids.[25]

A further outstanding property of ionic liquids is the wide temperature window in which they exhibit a good stability. Ionic liquids withstand temperatures, well above 100 °C, while organic solvent-based or water-based solvents fail to perform at these elevated temperatures due to their volatile character.[25] At low temperatures, a supercooled liquid phase is present, which is not stable and eventually crystallizes. The high temperature and electrochemical stability of numerous ionic liquids may also be a drawback, in particular of those containing fluorinated groups, once released to the surroundings. Ionic liquids can be classified either as protic or aprotic. The protic or aprotic character of an ionic liquid can easily be altered by changing one of the ions. Some cations and anions are presented in Figure 4.3, while specifically the pyridinium cation is known for its aprotic character.[26] Currently, proton-exchange reactions including ionic liquids are intensively studied, in order to obtain information about unbalanced hydrogen-bonded networks.[27, 28]

Furthermore, other than normal molecular solvents, ionic liquids are known to possess a microstructure which is governed by long range coulombic ion-ion interactions and other interactions such as Van der Waals interactions and H-bonding.[29] In addition, there is evidence of amphiphilic self-assembly of some ionic liquids leading to complex nanostructures and ion configurations such as ion clusters.[30] The concept of ionic liquids being composed of ion pairs is outdated, thus the concept of ion association forming larger structures than a single ion pair turns out to be more accurate.[31, 32] The precise nanostructure of an ionic liquid is decisive for the observed physicochemical properties such as the self-diffusion coefficients of the anion and cation, as well as the solvent properties and conductivity. Diffusion NMR measurements of bulk ionic liquids and of mixtures containing ionic liquids revealed that hydrodynamic radii

differ severely from the ion radii.[33, 34] The latter is explained based on correlated ion motions (cation-cation, anion-cation, anion-anion). In a larger picture, those ion motions contribute to the latter mentioned nanostructure. Still, questions remain concerning the nanostructure and its influence on the diffusion properties and the ion conductivity.

Mixtures of ionic liquids and lithium salts have recently been studied, for which high ion conductivities and good solid electrolyte interphase stabilities were found, especially pronounced for the non-fluorinated dicyanamide (DCA) anion.[35] Furthermore, lithium salt/ ionic liquid mixtures were implemented into a polymer matrix. The product is a so-called polymer electrolyte. This class of electrolytes exhibits numerous promising properties such as a high ion conductivity and is discussed in detail in the following section.

Polymer Electrolytes and Gel Polymer Electrolytes

Due to the issues concerning leakage of liquid electrolytes, a solid-state or solid-like electrolyte would be desirable. Real solid-state electrolytes would entirely be composed of an inorganic solid such as a conductive glass or ceramic.[36, 37] This class of electrolytes currently suffers from poor conductivities, thus polymer electrolytes represent a solid-like alternative which exhibits a significantly higher ion conductivity so far.[37] Further advantages over liquid electrolytes and solid-state electrolytes is a better response of polymer electrolytes to volumetric changes (due to flexibility) at the site of the electrodes which occurs during charging and discharging, simple production and an excellent flexibility which enables the production of a wide range of geometries for lithium ion batteries.[36] Together with a relatively high shear modulus, polymer electrolytes are reported to minimize or suppress the effect of lithium dendrite formation, which is crucial for the implementation of metallic lithium as the anode.[37]

The history of polymer electrolytes can be dated back to the mid 70s, when mixtures of polyethylene oxide (PEO) and alkali metal salts (dry polymer electrolyte) were found to exhibit ion conductivity.[38] Since then, several PEO/lithium salt systems have been studied extensively for their applications in lithium ion batteries.[39] The main principle behind ion dissociation is similar throughout all PEO-based systems, where the lithium cation is coordinated by ether oxygens of PEO, yielding a helical structure of the polymer. However, these all-solid "dry" polymer electrolytes suffer from poor ionic conductivities and from small lithium transference numbers, which limits the application in a "real" cell.[36, 40]

In order to overcome these limitations numerous strategies have been developed, such as the modification of the polymer matrix towards a less crystalline polymer, the implementation of nanoparticles and the incorporation of plasticizer (e.g. solvent molecules or ionic liquids) leading to a new class of the so-called gel polymer electrolytes (GPE).[40, 41] Gel polymer electrolytes exhibit an excellent response to volumetric changes during charging/discharging, a good thermal stability and ion conductivities of c. 10^{-4} S/cm, which are roughly two orders in magnitude larger compared to the dry PEO/LiTFSI system.

These exceptionally high conductivities are obtained due to ion transport in the so-called liquid electrolyte phase in addition to the solvated polymer phase (rich in polymer).[40–42] The existence of these ion phases is evidenced by diffusion NMR experiments showing two differently mobile populations. Due to the liquid electrolyte phase, the ion mobility is partially independent of the segmental motion of the polymer.[43] One consequence is that the ion mobility is depending on the properties of the plasticizer (substance that softens the polymer) and on the nature of the pores in the polymer network. A large number of pores is reducing the amount of active material and should therefore be avoided.

Regarding plasticizers, ionic liquids and other solvents have been mentioned previously. The advantages of neutral low-molar-mass molecules such as carbonates is the increase in ion conductivity and an enhanced ion dissociation. As a disadvantage, the implementation of some small organic molecules can cause a further phase separation because of partial crystallization of the polymer, which decreases the ion conductivity.[44]

The benefits of ionic liquids as plasticizer in gel-polymer electrolytes as an alternative for neutral molecules are higher ion conductivities and excellent coulombic efficiencies, discussed in Chapter 2. As a drawback, the ions of the ionic liquid are migrating during charging and discharging and may therefore decrease the lithium transference number considerably. In many cases the lithium salt/ionic liquid mixtures achieve lithium transference numbers of $t_{Li^+} \approx 0.1$, which is notably smaller compared to other gel-polymer electrolyte systems.[45, 46]

The incorporation of plasticizer into the gel-polymer electrolyte is often accompanied by a severe loss in mechanical strength and interphase stability. A common method to meet these issues is by incorporating inorganic fillers into the gel-polymer electrolyte. Widely used are Al_2O_3, SiO_2 and TiO_2 as nanoparticles in gel-polymer electrolytes, which are found to improve

the mechanical and electrochemical properties. Attention has been addressed to SiO_2 in PVdF-HFP matrices, since in addition to the discussed properties also a tremendous increase in the uptake of electrolyte solutions was found.[47] The reason for the increased electrolyte uptake capability can be found in the porosity of the particles. Numerous reports have shown this behavior for PVdF-HFP/ SiO_2-based systems, while also the influence of particle size on ion conductivities was investigated.[47, 48] It is found that smaller particles boost the ion conductivity particularly well. Furthermore, the ion conduction mechanism may change for gel-polymer electrolytes having inorganic filler incorporated. It is assumed that the ion conductivity is enhanced due to ion migration at the surface boundary of the introduced nanoparticles. Furthermore, mesoporous SBA-15 (pores of c. 10 nm) added to a PVdF-HFP-based polymer electrolyte has shown even higher ion conductivities and larger electrolyte uptake capabilities compared to fumed SiO_2 nanoparticles.[49] However, the introduced nanoparticles tend to form agglomerates over time in gel-polymer electrolytes, which may cause a phase separation and a notable loss in ion conductivity. To overcome these limitations, surface functionalization of the prepared nanoparticles with organophilic groups can be a strategy to further increase the stability of the composite material.[50]

Electrolytes examined in this work (cf. Chapter 5) are polymer based. The statistical co-polymer PVdF-HFP is chosen as the matrix, due to a low crystalline fraction, which is favorable for large electrolyte uptake in the amorphous fraction of the polymer.[51] These membranes have been optimized for applications in rechargeable lithium ion batteries, while the underlying physicochemical principles are often neglected. In particular little is known about the interplay between additives (ionic liquid, lithium salt, filler particles) with the polymer network and how far these interactions may influence electrochemical properties. Reports suggest, that the ion dynamics is only marginally reduced in a PVdF-HFP network, while at the same time a tremendous improvement of the mechanical properties is achieved.[52, 53] Since PVdF-HFP is a neutral polymer, only dispersive interactions are expected between ions and the polymer network, which is reflected in the retained ion dynamics.

Interactions of ions with filler particles are likely to occur, especially when the latter contain polar chemical groups. The focus in this work is directed towards amorphous silica as the filler particles. As discussed in literature, a large filler/ polymer network interphase is desirable in order to boost the ion conductivity and lithium transference number.[53] Therefore, an interpenetrating silica network is used (cf. Sections 5.2 and 5.3) in order to enable a large filler/

polymer network interphase.[54] The *in situ* polymerized silica network is an alternative to the addition of pre-fabricated silica particles, such as amorphous silica or ordered SBA-15.[53] However, there are only few reports about the underlying physicochemical effects present in these complex materials.[55]

NMR studies of these systems are reasonable, since element and ion selective probes are used in a non-invasive way to obtain information about the structure and dynamics of the ionic liquid, lithium salt and the polymer matrix. Detailed information about the ion dynamics ([EMIM][OTf] and LiOTf) can be derived from ^{1}H, ^{7}Li, ^{13}C and ^{19}F NMR spectroscopy. Additional information about changes within the polymer network and the silica network upon changes in electrolyte solution concentration can be monitored. In a step-by step manner, information about the mobility of the single constituents are derived, followed by the complete polymer electrolyte (cf. Section 5.2).

4.2 Electrodes

Porous Carbonaceous Materials

Anodes for lithium ion batteries, as well as other ion/ molecule insertion materials (materials into which ions can be inserted) are typically carbonaceous (e.g. graphite). These materials commonly exhibit large specific surface areas, with excellent electronic conductivity and moderate manufacturing costs.[56] The production employs a variety of possible carbon-bearing precursors, such as coconut shells, sugars, woods and synthetic polymers. Three main fabrication methods can be used. The precursor material is heated directly to high temperatures (> 850 °C) under an inert Ar or N_2 atmosphere. Alternatively, the starting material is pretreated at mild temperatures (150–180 °C) in order to attain a desired structure (e.g. spherical particles), followed by a second heating step reaching temperatures of c. 1000 °C. An example for the latter method is the preparation of saccharide-derived hydrochars.[57] The resulting products typically exhibit pores with a wide pore-size distribution, from micropores (< 2 nm) up to macropores which are larger than 50 nm. Specific surface areas obtained by these methods reach about 400 m^2/g.[57] In addition to these two methods, a salt template or ionic liquid template can be used during the pyrolysis of the precursor, which leads to a tremendous increase in surface area of the obtained product (c. 2000 m^2/g).[58]
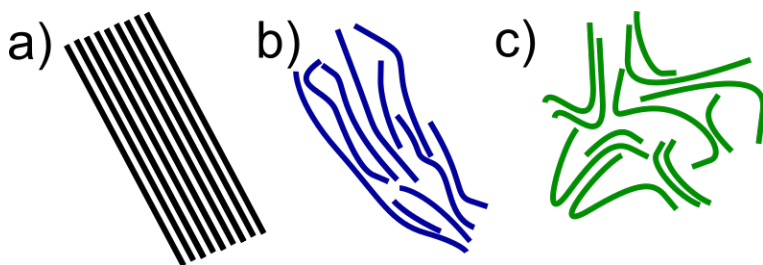
Figure 4.4: Structural scheme of graphite in (a), soft carbon (b) and hard carbon (c).

The general structure of the obtained products may be classified either as graphitic or as non-graphitic, which is shown in Figure 4.4.[59] Next to the highly ordered graphite in Figure 4.4 a), two less ordered structures, namely soft carbon (b) and hard carbon (c) are shown. The question of how far a prepared carbonaceous material is graphitic is typically probed by Raman spectroscopy. Pure graphite serves as a benchmark; it exhibits only the G-band in the Raman spectrum.[60] Many carbonaceous materials further show the additional D-band, which can be related to disordered graphite sheets and possible defects in the carbon sheets. In addition, the full width at half maximum (FWHM) of the D-band gives a measure for the disorder and defects (narrow bands are associated to high order).

A highly graphitic structure is desired in order to be useful as an anode material in lithium ion batteries. Transmission electron microscopy reveals that for graphitic carbon samples a high local order is present (randomly distributed nm-sized sheets), whereas non-graphitic carbon-samples display larger interlayer distances and a higher degree of disorder.[58]

Furthermore, carbonaceous materials containing heteroatoms are an emerging class of materials. One idea behind these materials is that interactions of guest molecules or ions may occur with the heteroatoms (i.e. nitrogen or oxygen). A recent example is the C_1N_1 material, which exhibits a 1:1 stoichiometry of carbon to nitrogen and is prominent to interact with small molecules such as H_2O and CO_2.[61] In particular its remarkable CO_2 adsorption capacity makes this material attractive for gas storage. Also, possible applications as supercapacitor electrodes are currently discussed. Further details are discussed in Chapter 6.

Two different types of carbonaceous materials are scrutinized in chapter 6, namely i) purely saccharide-derived hydrochars prepared from sucrose and trehalose, which are hard-carbon materials and ii) nitrogen-and oxygen containing carbonaceous materials, of which the precise structure is currently investigated.

Both materials have in common that upon carbonization, the formation of (extended) sp^2-hybridized structures is promoted. In this thesis, the carbonization mechanism is studied *ex situ* for different carbonization temperatures of saccharide-derived hydrochars. In particular the chemical transition is investigated for both saccharides, since the carbonization process is often treated in literature as a black box. Temperature-dependent sheet growth and further relevant concepts were derived by means of ^{13}C NMR spectroscopy by Freitas and co-workers and are used in this work.[62] They correlate ^{13}C line widths and ^{13}C chemical shifts to anisotropically growing "graphene-like" sheets (in plane growth). This concept is used to probe structural changes upon pyrolysis of sucrose and trehalose.

Furthermore, the interaction of H_2O with non-polar carbonaceous materials is studied in Section 6.3. Buntkowsky and co-workers, as well as Wu and co-workers explored the latter by means of ^1H NMR. They derived that the observed ^1H chemical shift is reflecting information about the average distance of water molecules from the surface of the matrix.[63, 64] Therefore, an estimate about the average pore size and structure (isolated pores vs. network) can be derived.

Heteroatom-containing carbonaceous materials are commonly prepared by pyrolysis of heteroatom-bearing precursors, such as guanine.[61] In Section 6.2, the chemical structure of polymeric (C_3O_2) (carbon suboxide) is scrutinized, and the carbonization of this well-defined molecule is followed by means of ^{13}C NMR. The second heteroatom-containing material studied in this work is the guanine-derived carbon C_1N_1 which has approximately an equimolar ratio of carbon to nitrogen.[61] Previous attempts to prepare porous carbonaceous materials with high amounts of nitrogen failed.[65] The ability of C_1N_1 to store high amounts of CO_2 is justifying further research on this material. Due to a large specific surface area, C_1N_1 is further expected to be an excellent candidate for a supercapacitor electrode. In order to obtain information about the interaction of small molecules with C_1N_1, H_2O impregnation experiments are performed and followed by ^1H NMR spectroscopy in Section 6.3. So far, very limited insight into similar systems can be found in literature.[66] Heske and co-workers propose a reasonable water uptake for C_2N. They further claim that the absorbed water becomes part of the structure. Therefore, H_2O impregnation experiments with C_1N_1 are useful in order to test their hypothesis.

4.3 References

(1) Dudley, J. T., Wilkinson, D. P., Thomas, G., LeVae, R., Woo, S., Blom, H., ... & Dahn, J. R. (1991). Conductivity of electrolytes for rechargeable lithium batteries. *Journal of power sources*, *35*(1), 59-82.

(2) Akiyama, T. (2007). Stronger brønsted acids. *Chemical Reviews*, *107*(12), 5744-5758.

(3) Krossing, I., & Raabe, I. (2004). Nichtkoordinierende Anionen–Traum oder Wirklichkeit? Eine Übersicht zu möglichen Kandidaten. *Angewandte Chemie*, *116*(16), 2116-2142.

(4) Jow, T. R., Xu, K., Borodin, O., & Ue, M. (Eds.). (2014). *Electrolytes for lithium and lithium-ion batteries* (Vol. 58). New York: Springer.

(5) Xu, K. (2004). Nonaqueous liquid electrolytes for lithium-based rechargeable batteries. *Chemical reviews*, *104*(10), 4303-4418.

(6) Aurbach, D., Talyosef, Y., Markovsky, B., Markevich, E., Zinigrad, E., Asraf, L., ... & Kim, H. J. (2004). Design of electrolyte solutions for Li and Li-ion batteries: a review. *Electrochimica acta*, *50*(2-3), 247-254.

(7) Galluzzo, M. D., Maslyn, J. A., Shah, D. B., & Balsara, N. P. (2019). Ohm's law for ion conduction in lithium and beyond-lithium battery electrolytes. *The Journal of chemical physics*, *151*(2), 020901.

(8) Ryou, M. H., Lee, J. N., Lee, D. J., Kim, W. K., Jeong, Y. K., Choi, J. W., ... & Lee, Y. M. (2012). Effects of lithium salts on thermal stabilities of lithium alkyl carbonates in SEI layer. *Electrochimica acta*, *83*, 259-263.

(9) Cao, C., Pollard, T. P., Borodin, O., Mars, J. E., Tsao, Y., Lukatskaya, M. R., ... & Steinrück, H. G. (2021). Toward Unraveling the Origin of Lithium Fluoride in the Solid Electrolyte Interphase. *Chemistry of Materials*, *33*, 7315-7336.

(10) Verma, P., Maire, P., & Novák, P. (2010). A review of the features and analyses of the solid electrolyte interphase in Li-ion batteries. *Electrochimica Acta*, *55*(22), 6332-6341.

(11) Stolwijk, N. A., Kösters, J., Wiencierz, M., & Schönhoff, M. (2013). On the extraction of ion association data and transference numbers from ionic diffusivity and conductivity data in polymer electrolytes. *Electrochimica Acta*, *102*, 451-458.

(12) Fromling, T., Kunze, M., Schonhoff, M., Sundermeyer, J., & Roling, B. (2008). Enhanced lithium transference numbers in ionic liquid electrolytes. *The Journal of Physical Chemistry B*, *112*(41), 12985-12990.

(13) Iwakura, C., Fukumoto, Y., Inoue, H., Ohashi, S., Kobayashi, S., Tada, H., & Abe, M. (1997). Electrochemical characterization of various metal foils as a current collector of positive electrode for rechargeable lithium batteries. *Journal of power sources*, *68*(2), 301-303.

(14) Lux, S. F., Lucas, I. T., Pollak, E., Passerini, S., Winter, M., & Kostecki, R. (2012). The mechanism of HF formation in LiPF6 based organic carbonate electrolytes. *Electrochemistry Communications*, *14*(1), 47-50.

(15) Tsujioka, S., Nolan, B. G., Takase, H., Fauber, B. P., & Strauss, S. H. (2004). Conductivities and electrochemical stabilities of lithium salts of polyfluoroalkoxyaluminate superweak anions. *Journal of the Electrochemical Society*, *151*(9), A1418.

(16) Rupp, A. B., & Krossing, I. (2015). Ionic Liquids with Weakly Coordinating [MIII (ORF) 4]− Anions. *Accounts of Chemical Research*, *48*(9), 2537-2546.

(17) Dahbi, M., Ghamouss, F., Tran-Van, F., Lemordant, D., & Anouti, M. (2011). Comparative study of EC/DMC LiTFSI and LiPF6 electrolytes for electrochemical storage. *Journal of Power Sources*, *196*(22), 9743-9750.

(18) Zhong, C., Deng, Y., Hu, W., Qiao, J., Zhang, L., & Zhang, J. (2015). A review of electrolyte materials and compositions for electrochemical supercapacitors. *Chemical Society Reviews*, *44*(21), 7484-7539.

(19) Forsyth, S. A., Pringle, J. M., & MacFarlane, D. R. (2004). Ionic liquids—an overview. *Australian Journal of Chemistry*, *57*(2), 113-119.

(20) Maase, M. (2004). Erstes technisches Verfahren mit ionischen Flüssigkeiten. *Chemie in unserer Zeit*, *38*(6), 434-435.

(21) Pinkert, A., Marsh, K. N., Pang, S., & Staiger, M. P. (2009). Ionic liquids and their interaction with cellulose. *Chemical reviews*, *109*(12), 6712-6728.

(22) Lewandowski, A., & Świderska-Mocek, A. (2009). Ionic liquids as electrolytes for Li-ion batteries—An overview of electrochemical studies. *Journal of Power sources*, *194*(2), 601-609.

(23) MacFarlane, D. R., Forsyth, M., Izgorodina, E. I., Abbott, A. P., Annat, G., & Fraser, K. (2009). On the concept of ionicity in ionic liquids. *Physical Chemistry Chemical Physics*, *11*(25), 4962-4967.

(24) Walden, P. (1914). Molecular weights and electrical conductivity of several fused salts. *Bull. Acad. Imper. Sci.(St. Petersburg)*, 1800.

(25) Armand, M., Endres, F., MacFarlane, D. R., Ohno, H., & Scrosati, B. (2011). Ionic-liquid materials for the electrochemical challenges of the future. *Materials for sustainable energy: a collection of peer-reviewed research and review articles from Nature Publishing Group*, 129-137.

(26) Belieres, J. P., & Angell, C. A. (2007). Protic ionic liquids: preparation, characterization, and proton free energy level representation. *The Journal of Physical Chemistry B*, *111*(18), 4926-4937.

(27) Oh, S., Morales-Collazo, O., & Brennecke, J. F. (2019). Cation–Anion Interactions in 1-Ethyl-3-methylimidazolium-Based Ionic Liquids with Aprotic Heterocyclic Anions (AHAs). *The Journal of Physical Chemistry B*, *123*(39), 8274-8284.

(28) Andreeva, D. V., Ip, B., Gurinov, A. A., Tolstoy, P. M., Denisov, G. S., Shenderovich, I. G., & Limbach, H. H. (2006). Geometrical features of hydrogen bonded complexes involving sterically hindered pyridines. *The Journal of Physical Chemistry A*, *110*(37), 10872-10879.

(29) Hayes, R., Warr, G. G., & Atkin, R. (2015). Structure and nanostructure in ionic liquids. *Chemical reviews*, *115*(13), 6357-6426.

(30) Greaves, T. L., & Drummond, C. J. (2013). Solvent nanostructure, the solvophobic effect and amphiphile self-assembly in ionic liquids. *Chemical Society Reviews*, *42*(3), 1096-1120.

(31) Zhao, W., Leroy, F., Heggen, B., Zahn, S., Kirchner, B., Balasubramanian, S., & Müller-Plathe, F. (2009). Are there stable ion-pairs in room-temperature ionic liquids? Molecular dynamics simulations of 1-n-butyl-3-methylimidazolium hexafluorophosphate. *Journal of the American Chemical Society*, *131*(43), 15825-15833.

(32) Kohagen, M., Brehm, M., Thar, J., Zhao, W., Müller-Plathe, F., & Kirchner, B. (2011). Performance of quantum chemically derived charges and persistence of ion cages in ionic

liquids. A molecular dynamics simulations study of 1-n-butyl-3-methylimidazolium bromide. *The Journal of Physical Chemistry B*, *115*(4), 693-702.

(33) Wencka, M., Apih, T., Korošec, R. C., Jenczyk, J., Jarek, M., Szutkowski, K., ... & Dolinšek, J. (2017). Molecular dynamics of 1-ethyl-3-methylimidazolium triflate ionic liquid studied by 1 H and 19 F nuclear magnetic resonances. *Physical Chemistry Chemical Physics*, *19*(23), 15368-15376.

(34) Harris, K. R., & Kanakubo, M. (2016). Self-diffusion coefficients and related transport properties for a number of fragile ionic liquids. *Journal of Chemical & Engineering Data*, *61*(7), 2399-2411.

(35) Karimi, N., Zarrabeitia, M., Mariani, A., Gatti, D., Varzi, A., & Passerini, S. (2021). Nonfluorinated Ionic Liquid Electrolytes for Lithium Metal Batteries: Ionic Conduction, Electrochemistry, and Interphase Formation. *Advanced Energy Materials*, *11*(4), 2003521.

(36) Stephan, A. M., & Nahm, K. S. (2006). Review on composite polymer electrolytes for lithium batteries. *Polymer*, *47*(16), 5952-5964.

(37) Kim, S. H., Choi, K. H., Cho, S. J., Kil, E. H., & Lee, S. Y. (2013). Mechanically compliant and lithium dendrite growth-suppressing composite polymer electrolytes for flexible lithium-ion batteries. *Journal of Materials Chemistry A*, *1*(16), 4949-4955.

(38) Armand, M. (1994). The history of polymer electrolytes. *Solid State Ionics*, *69*(3-4), 309-319.

(39) Jiang, Y., Yan, X., Ma, Z., Mei, P., Xiao, W., You, Q., & Zhang, Y. (2018). Development of the PEO based solid polymer electrolytes for all-solid state lithium ion batteries. *Polymers*, *10*(11), 1237.

(40) Long, L., Wang, S., Xiao, M., & Meng, Y. (2016). Polymer electrolytes for lithium polymer batteries. *Journal of Materials Chemistry A*, *4*(26), 10038-10069.

(41) Popovic, J., Brandell, D., Ohno, S., Hatzell, K. B., Zheng, J., & Hu, Y. Y. (2021). Polymer-based hybrid battery electrolytes: theoretical insights, recent advances and challenges. *Journal of Materials Chemistry A*, *9*(10), 6050-6069.

(42) Richardson, P. M., Voice, A. M., & Ward, I. M. (2016). NMR self diffusion and relaxation time measurements for poly (vinylidene fluoride)(PVDF) based polymer gel electrolytes containing LiBF4 and propylene carbonate. *Polymer*, *97*, 69-79.

(43) Aziz, S. B., Woo, T. J., Kadir, M. F. Z., & Ahmed, H. M. (2018). A conceptual review on polymer electrolytes and ion transport models. *Journal of Science: Advanced Materials and Devices*, *3*(1), 1-17.

(44) Sengwa, R. J., Dhatarwal, P., & Choudhary, S. (2014). Role of preparation methods on the structural and dielectric properties of plasticized polymer blend electrolytes: correlation between ionic conductivity and dielectric parameters. *Electrochimica Acta*, *142*, 359-370.

(45) Xue, Z., He, D., & Xie, X. (2015). Poly (ethylene oxide)-based electrolytes for lithium-ion batteries. *Journal of Materials Chemistry A*, *3*(38), 19218-19253.

(46) Tarascon, J. M., Gozdz, A. S., Schmutz, C., Shokoohi, F., & Warren, P. C. (1996). Performance of Bellcore's plastic rechargeable Li-ion batteries. *Solid State Ionics*, *86*, 49-54.

(47) Yang, C. C., Lian, Z. Y., Lin, S. J., Shih, J. Y., & Chen, W. H. (2014). Preparation and application of PVDF-HFP composite polymer electrolytes in LiNi0. 5Co0. 2Mn0. 3O2 lithium-polymer batteries. *Electrochimica Acta*, *134*, 258-265.

(48) Echelmeyer, T., Meyer, H. W., & van Wüllen, L. (2009). Novel ternary composite electrolytes: Li ion conducting ionic liquids in silica glass. *Chemistry of Materials*, *21*(11), 2280-2285.

(49) Wu, C. G., Lu, M. I., Tsai, C. C., & Chuang, H. J. (2006). PVdF-HFP/metal oxide nanocomposites: the matrices for high-conducting, low-leakage porous polymer electrolytes. *Journal of power sources*, *159*(1), 295-300.

(50) Shin, W. K., Cho, J., Kannan, A. G., Lee, Y. S., & Kim, D. W. (2016). Cross-linked composite gel polymer electrolyte using mesoporous methacrylate-functionalized SiO2 nanoparticles for lithium-ion polymer batteries. *Scientific reports*, *6*(1), 1-10.

(51) Abbrent, S., Plestil, J., Hlavata, D., Lindgren, J., Tegenfeldt, J., & Wendsjö, Å. (2001). Crystallinity and morphology of PVdF–HFP-based gel electrolytes. *Polymer*, *42*(4), 1407-1416.

(52) Ye, H., Huang, J., Xu, J. J., Khalfan, A., & Greenbaum, S. G. (2007). Li ion conducting polymer gel electrolytes based on ionic liquid/PVDF-HFP blends. *Journal of the Electrochemical Society*, *154*(11), A1048.

(53) Ferrari, S., Quartarone, E., Mustarelli, P., Magistris, A., Fagnoni, M., Protti, S., ... & Spinella, A. (2010). Lithium ion conducting PVdF-HFP composite gel electrolytes based on N-methoxyethyl-N-methylpyrrolidinium bis (trifluoromethanesulfonyl)-imide ionic liquid. *journal of Power Sources*, *195*(2), 559-566.

(54) Khurana, S., & Chandra, A. (2019). Ion conducting polymer-silica hybrid ionogels obtained via non-aqueous sol-gel route. *Solid State Ionics*, *340*, 115027.

(55) Echelmeyer, T., Meyer, H. W., & van Wüllen, L. (2009). Novel ternary composite electrolytes: Li ion conducting ionic liquids in silica glass. *Chemistry of Materials*, *21*(11), 2280-2285.

(56) Zhai, Y., Dou, Y., Zhao, D., Fulvio, P. F., Mayes, R. T., & Dai, S. (2011). Carbon materials for chemical capacitive energy storage. *Advanced materials*, *23*(42), 4828-4850.

(57) Wortmann, M., Keil, W., Brockhagen, B., Biedinger, J., Westphal, M., Weinberger, C., ... & Frese, N. (2022). Pyrolysis of sucrose-derived hydrochar. *Journal of Analytical and Applied Pyrolysis*, *161*, 105404.

(58) Fechler, N., Fellinger, T. P., & Antonietti, M. (2013). "Salt templating": a simple and sustainable pathway toward highly porous functional carbons from ionic liquids. *Advanced Materials*, *25*(1), 75-79.

(59) Franklin, R. E. (1951). The structure of graphitic carbons. *Acta crystallographica*, *4*(3), 253-261.

(60) Reich, S., & Thomsen, C. (2004). Raman spectroscopy of graphite. *Philosophical Transactions of the Royal Society of London. Series A: Mathematical, Physical and Engineering Sciences*, *362*(1824), 2271-2288.

(61) Kossmann, J., Piankova, D., Tarakina, N. V., Heske, J., Kühne, T. D., Schmidt, J., ... & López-Salas, N. (2021). Guanine condensates as covalent materials and the concept of cryptopores. *Carbon*, *172*, 497-505.

(62) Freitas, J. C., Emmerich, F. G., Cernicchiaro, G. R., Sampaio, L. C., & Bonagamba, T. J. (2001). Magnetic susceptibility effects on 13C MAS NMR spectra of carbon materials and graphite. *Solid state nuclear magnetic resonance*, *20*(1-2), 61-73.

(63) Wang, H. J., Kleinhammes, A., McNicholas, T. P., Liu, J., & Wu, Y. (2014). Water adsorption in nanoporous carbon characterized by in situ NMR: measurements of pore size and pore size distribution. *The Journal of Physical Chemistry C*, *118*(16), 8474-8480.

(64) Xu, Y., Watermann, T., Limbach, H. H., Gutmann, T., Sebastiani, D., & Buntkowsky, G. (2014). Water and small organic molecules as probes for geometric confinement in well-ordered mesoporous carbon materials. *Physical Chemistry Chemical Physics*, *16*(20), 9327-9336.

(65) Hulicova, D., Yamashita, J., Soneda, Y., Hatori, H., & Kodama, M. (2005). Supercapacitors prepared from melamine-based carbon. *Chemistry of Materials*, *17*(5), 1241-1247.

(66) Heske, J., Walczak, R., Epping, J. D., Youk, S., Sahoo, S. K., Antonietti, M., ... & Oschatz, M. (2021). When water becomes an integral part of carbon–combining theory and experiment to understand the zeolite-like water adsorption properties of porous C 2 N materials. *Journal of Materials Chemistry A*, *9*(39), 22563-22572.

Chapter 5
PVdF-HFP-based Polymer Electrolytes

Scope

In this Chapter polymer electrolytes based on PVdF-HFP as the polymer matrix, an electrolyte solution (lithium salt mixed with an ionic liquid) and silica particles are scrutinized. Within the first Section, two ionic liquids [EMIM][OTf] and [EMIM][BF$_4$] (used as the solvent in this work) are examined for their hydrogen bonding interactions, which are relevant for dissolving the lithium salt. In particular pronounced hydrogen bonding interactions are found for the [OTf]$^-$ anion. In Section 5.2 hybrid polymer electrolytes, which are composed of PVdF-HFP, an electrolyte solution and silica particles (inorganic filler) are studied by means of multi-nuclear NMR spectroscopy. The ^{7}Li ion dynamics is probed and found to correlate almost linearly with previously measured lithium transference numbers. In the following Section (5.3) the diffusion properties of the hybrid polymer electrolytes are studied. Anomalous diffusion is found for ions located in polymer electrolytes, which means that the displacement of the ions is non-linear related to the diffusion time. Polymer electrolytes are implemented in symmetric lithium coin cells in Section 5.4, in order to test their usage in an electrochemical cell. The degradation of the used electrolytes is followed *ex situ*. The last Section (5.5) highlights an effect that occurs during a magic-angle-spinning (MAS) NMR measurement and shows that the measurement itself may has a major impact on the obtained physicochemical properties, i.e. ion conductivity and crystallinity.

5.1 From Hydrogen Bonding to Deuterium Labelling of 1-ethyl-3-methyl-imidazolium trifluoromethanesulfonate [EMIM][OTf] Ionic Liquid
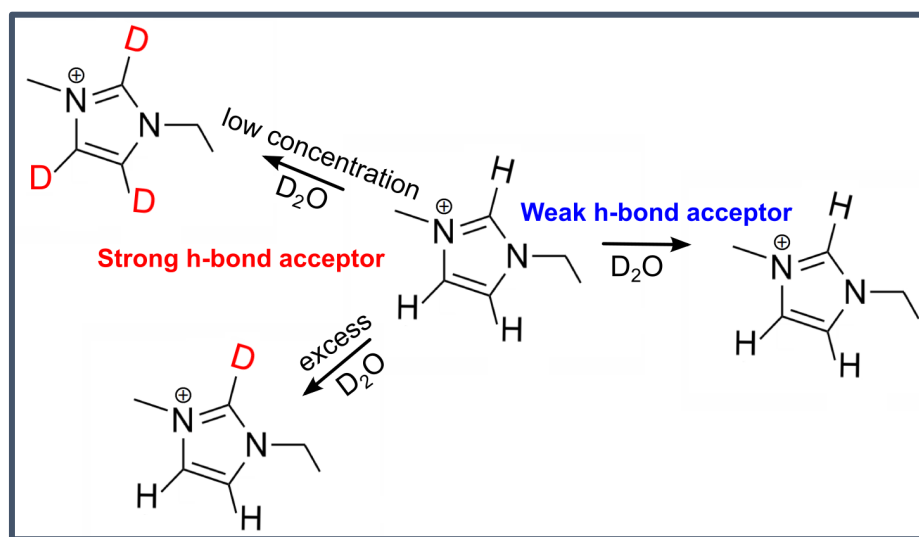
5.1.1 Ionic Liquids and Hydrogen Bonding

As mentioned in Chapter 4.1, protic ionic liquids exhibit next to coulombic interactions also further interactions, such as hydrogen-bonding interactions. The hydrogen-bonding interaction may even lead to well-defined H-bonded networks, which are important in stabilizing ion clusters or other ion configurations.[1,2] A balanced number of acceptor and donor sites present in ionic liquids, is discussed in literature to be a main contribution for their stability.[1,2] However, e.g. in polymer electrolytes there may be additional hydrogen bonding acceptor or donor sites, depending on the used polymer and additives, which may disturb the equilibrium. In order to introduce changes in the donor and acceptor equilibrium, a simpler model system (H_2O/ionic liquid) is often used. This model system results in an unbalanced hydrogen-bonded network.[2] Accompanied by the addition of H_2O or D_2O are changes in the ionic liquid's microstructure. Nevertheless, these changes in the microstructure are not fully understood.[2] In this respect, imidazolium-based ionic liquids are of special interest, since they offer three active hydrogen bond donating sites (C2, C4 and C5) as shown in Figure 5.1.

Whether these positions in the 1-ethyl-3-methyl-imidazolium cation ([EMIM]$^+$) are accessible for a hydrogen bond or even an H/D exchange reaction seems to depend on the anion which is present in the ionic liquid.[3] At the C2 position, a transient carbene occurs during the exchange reaction, in which the anion has the function to stabilize this transient carbene.[3] A typical anion, which is not able to stabilize the transient carbene is the BF_4^- anion.[3,4] Therefore, no H/D exchange reaction can be obtained for simple [EMIM][BF_4]/D_2O mixtures.[10] Also, positions C4 and C5 are slightly acidic and able to perform an H/D exchange reaction, while the precise mechanism is unknown for these positions.

In the context of exchange reactions, the basicity of the anion is considered to be the relevant property.[5,7] But also, the hydrogen bonding of the [EMIM]$^+$ cation to the anion is found to be relevant.[4,5] Due to an insufficient theoretical background, it is difficult to judge, whether the basicity of the anion or the hydrogen bond acceptor properties of the anion are crucial for a H/D exchange reaction. In this section, the working hypothesis is that the hydrogen bond acceptor properties of the anion are decisive for a H/D exchange reaction, while the basicity of the anion in a simple ionic liquid (IL)/ D_2O mixture is assumed to play a less important role. In order to test this hypothesis, mixtures of D_2O and two ionic liquids, namely [EMIM][BF_4] and 1-ethyl-3-methyl-imidazolium trifluoromethanesulfonate ([EMIM][OTf]), will be examined.

5.1.2 Experimental Details

[EMIM][OTf] (>98 % Sigma Aldrich), [EMIM][BF$_4$] (>98 % Sigma Aldrich) and D$_2$O (99.9 % Sigma Aldrich) were used as received. Mixtures of D$_2$O/ IL (IL= [EMIM][OTf], [EMIM][BF$_4$]) were prepared under Schlenk conditions in a single step, with three different reaction conditions: i) The prepared mixtures were stirred with a magnetic stir bar at 40 °C for 24 h. Then, part of the residual H$_2$O/HDO/D$_2$O is removed from the solution by means of a vacuum (10^{-2} mbar). The resulting product contains a molar ratio of $\chi = 0.5$ (n(D$_2$O)/n([EMIM][OTf]). ii) The mixtures were stirred at 100 °C for 24 h and the volatile compounds were removed completely from the solution afterwards. iii) The prepared ionic liquid/ D$_2$O mixtures were stirred at 100 °C for 24 h without removing H$_2$O/HDO/D$_2$O from the solution. Following, ^{1}H and ^{2}H spectra were recorded. ^{1}H kinetic studies were conducted by mixing [EMIM][OTf]/ D$_2$O in a vial and transferring part of the mixture in an NMR tube. The sample is thermally equilibrated for 10 minutes at 40 °C before the measurement started.

## 5.1.3 Balanced and Unbalanced Hydrogen-Bonded Networks
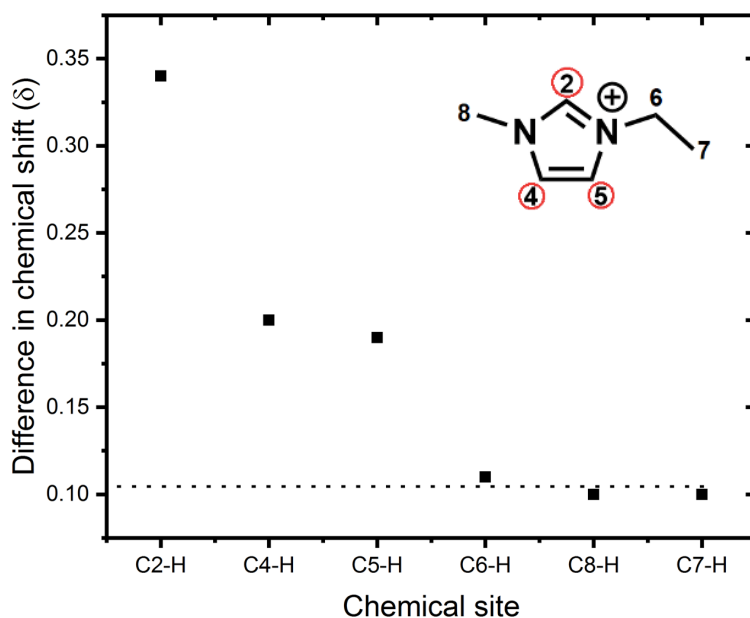
Figure 5.1: Difference in chemical shift for different chemical sites in [EMIM][OTf] and [EMIM][BF$_4$], listed from small (C7-H) to large chemical shifts (C2-H) (see Table 5.1).

Initially, ^{1}H NMR spectra of the pure ionic liquids were recorded, and chemical shifts have been analyzed. The results are presented in Figure 5.1 and in Table 5.1. The differences in chemical shift in Figure 5.1 of [EMIM][OTf] and [EMIM][BF$_4$] show a clear dependence on the chemical site of the considered proton in the [EMIM]$^+$ cation.

Table 5.1: [1]H (700 MHz) chemical shift values for [EMIM][OTf] and [EMIM][BF$_4$] for all individual chemical [EMIM]$^+$ sites measured at 25 °C.

Site	Chemical shift (ppm)		
	[EMIM][OTf]	**[EMIM][BF$_4$]**	**Difference**
C2-H	8.77	8.43	0.34
C4-H	7.58	7.38	0.20
C5-H	7.50	7.31	0.19
C6-H	4.15	4.04	0.11
C8-H	3.84	3.74	0.10
C7-H	1.37	1.27	0.10

Notably, all aliphatic sites display a similar small offset in chemical shift of about 0.1 ppm, while significantly larger differences can be noted for the ring protons C2, C4 and C5 (C2 : 0.34 ppm, C4 : 0.2 ppm and C5 : 0.19 ppm). From Table 5.1 it can additionally be seen that the ring proton shifts of [EMIM][OTf] are larger (downfield shifted) than those found for [EMIM][BF$_4$]. One possible explanation is given by Chen and co-workers, in which ^{1}H chemical shifts for the ring protons of a series of imidazolium-based ionic liquids are correlated with their interionic hydrogen bond strength.[6] Therefore, these differences can be used as a measure for the interionic hydrogen bond strength at positions C2, C4 and C5. The findings from Figure 5.1 suggest that the [OTf]$^-$ anion forms much stronger hydrogen bonds with [EMIM]$^+$ at C4, C5 and C2 than [BF$_4$]$^-$ does.

Further, the basicity of the anions should be considered as an alternative explanation for the observations in Figure 5.1 and Table 5.1. As reported in the literature, the corresponding acid of [BF$_4$]$^-$ exhibits a pK_a value of −0.44,[8] whereas the triflic acid exhibits a pK_a value of −15.[9] That means [BF$_4$]$^-$ is a much stronger base than [OTf]$^-$. Obviously, the significantly weaker base [OTf]$^-$ forms much stronger hydrogen bonds to all three active ring sites. This assumption is backed by chemical shielding DFT calculations of an [EMIM][BF$_4$] and [EMIM][OTf] ion pair (shown in Table A.1 in the appendix) where a notably larger isotropic chemical shift value for the C2−H proton is found for [EMIM][OTf]. Also, the calculated hydrogen bond angle and the H-bond length which are a measure for the H-bond strength (small angles indicate strong hydrogen bonds) support this interpretation. We find a significantly smaller hydrogen bond angle of 1.4 ° in an [EMIM][OTf] ion pair compared to an [EMIM][BF$_4$] ion pair (26.7 °), where the anion is H-bonded to the C2 position. A longer H-bond (2.4 Å) found for [EMIM][OTf], compared to 2 Å for [EMIM][BF$_4$], further supports this interpretation.
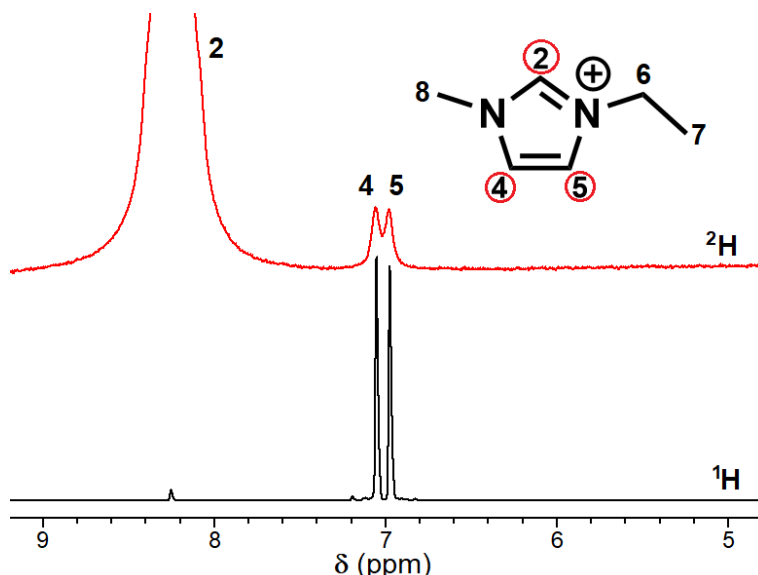
Figure 5.2: Selections of (a) ^{1}H NMR of [EMIM][OTf] treated with D_2O at 40 °C with a partial removal of the volatile compounds and (b) the corresponding ^{2}H NMR spectrum (107.5 MHz). Note, that peak C2 is cropped.

Therefore, it is reasonable to correlate the positions of the ^{1}H signals of [EMIM][BF$_4$] and [EMIM][OTf] (Figure 5.1) to the hydrogen bond acceptor properties of the anion, rather than to the basicity of the anion. This hypothesis is further tested by carrying out H/D exchange reactions. A simple mixing experiment of D_2O/[EMIM][BF$_4$] at 100 °C was performed and no H/D exchange could be observed. On the other hand, mixtures of D_2O/[EMIM][OTf] exhibit H/D exchange reactions, seen in Figure 5.2 and Figure 5.3 The ^{1}H and ^{2}H spectrum of a D_2O/[EMIM][OTf] mixture treated at 40 °C with partial removal of D_2O (molar ratio [EMIM][OTf]:$D_2O \approx$ 2:1) is shown in Figure 5.2. The signal intensity of the C2–H proton is diminished in the ^{1}H spectrum, but intense in the ^{2}H spectrum (Figure 5.2).
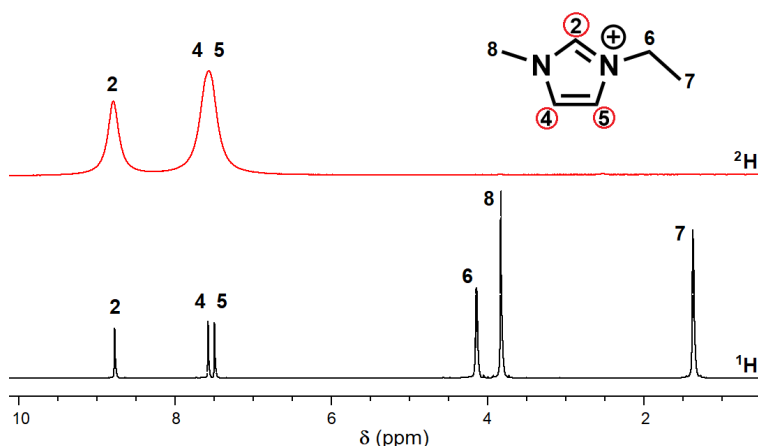

Figure 5.3: ^{1}H NMR spectrum of $\chi \sim 230$ at 100 °C with a complete removal of the volatile compounds and (b) the corresponding ^{2}H NMR spectrum (107.5 MHz) is enlarged.

This means that an almost exclusive H/D exchange can be noted at the C2 position with a deuteration yield of 98 %. A minute amount of the C4/C5 position (c. 1 %) is also deuterated. In Figure 5.3 on the other hand, an equalized deuteration yield of c. 40 % can be seen after the [EMIM][OTf]/D_2O mixture has been stirred at 100 °C with a complete removal of the volatile components. So far, one explanation for these experiments that can already be ruled out is that the basicity of the anion is the key parameter for the H/D exchange reaction, since the much weaker base [OTf]$^-$ enables an H/D exchange, whereas no exchange is observed for the stronger base [BF$_4$]$^-$.

In order to find a possible explanation for these results, a concentration series covering a wide range of molar ratios $\chi = (n(D_2O)/n([EMIM][OTf])$ was prepared and stirred at 100 °C, without the removal of the volatile components. The results are shown in Figure 5.4 and in Table A.2 in the appendix. These experiments have been done in order to maintain a fixed concentration and observe the deuteration yield as a function of the molar ratio. This is important, since changes the ionic liquid/D_2O concentration have occurred in the experiments with the results shown in Figures 5.2 and 5.3. As seen in Figure 5.4, the ^{1}H integrals steadily decrease from a molar ratio of 0.25 up to 10, where the ^{1}H integrals of C2 and C4/C5 positions are nearly the same. At a molar ratio of 10 a minimum is found for the C4/C5 position. This is contrasted at a molar ratio of 230, where position C2 is almost completely deuterated but only a minor fraction of C4/C5 is found to be deuterated.
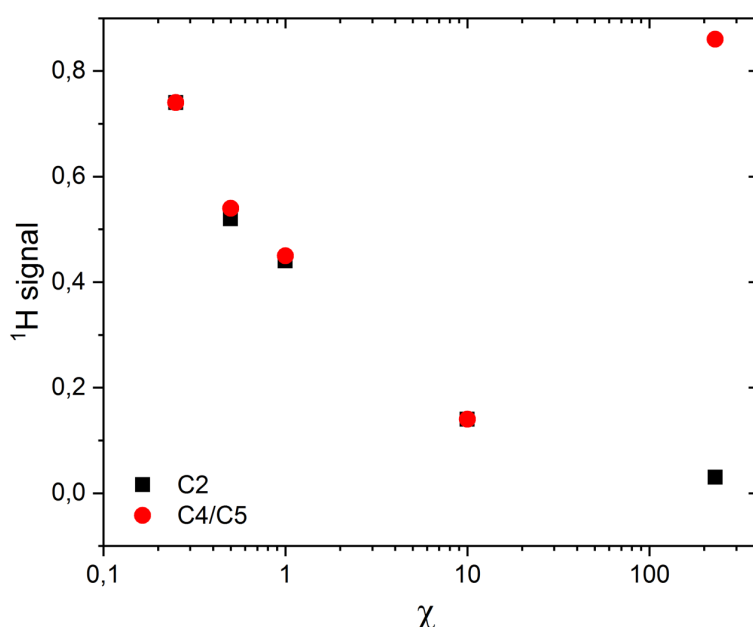

Figure A.5.4: ^{1}H signal intensities of C2 and C4/C5 plotted against the molar ratio. The C4/C5 ^{1}H integral goes through a minimum, while the C2 ^{1}H signal grows steadily upon increasing the [EMIM][OTf] fraction.

This finding shows that there is a significant dependence of the D_2O/[EMIM][OTf] molar ratio on the deuteration yield and selectivity. Only at the largest molar ratio ($\chi{\sim}230$) a "selective" deuteration of the C2 position can be observed. In this context, the dielectric constant of [EMIM][OTf] becomes relevant, which is reported in literature as $16.5{\pm}0.5$.[11] The dielectric constant of water at 20 °C is 80.2.[12] This means that [EMIM][OTf] may fully dissociate only at large D_2O concentrations and changes in the microstructure of the ionic liquid can be expected over the studied concentration range. One possible transition could be that at large [EMIM][OTf] concentrations ion clusters with a complex nanostructure may be present.[13, 14, 15] At moderate molar ratios ($\chi{=}1{-}10$), the water molecules may be part of a rather complex hydrogen bonded network, while at large molar ratios ($\chi{\sim}230$) solvated ions or ion pairs are present. Therefore, Figure 5.4 may possibly be explained by a hydrogen bonded network, which is present at moderate molar ratios, where positions C2, C4/C5 of the [EMIM]+ cation possess an approximately equally strong hydrogen bond to the [OTf]− anion.[15] Therefore, positions C2 and C4/C5 show nearly the same deuteration yield at moderate molar ratios. At larger molar ratios, the ionic liquid may be present as an ion pair, where the [OTf]− anion is mainly located in the vicinity of the C2 position and therefore, a predominantly high deuteration yield is observed at position C2.

In addition, the influence of temperature on the deuteration yield can be seen by comparing Figure 5.4 to Figure 5.2. In either spectrum, a molar ratio of c. 0.5 is present, while the temperatures differed by 60 °C. The deuteration yield at 40 °C is 98 % at C2 and 1 % at C4/C5 while at 100 °C an almost equalized deuteration yield of 52 % at C2 and 54 % at C4/C5 is observed. Therefore, an increased temperature may cause an unspecific deuteration at all three active sites with a deuteration yield of c. 50 %, while a predominant deuteration at C2 is observed at 40 °C.

Further, the kinetics of the deuteration reaction was examined by means of ¹H NMR measurements for $\chi{\sim}230$ and $\chi{=}10$ (both at 40 °C). The reaction profile curves are shown in Figure 5.5. The Figure shows the relative ¹H integrals. An ¹H integral of 1 would match to the expected value (fully protonated) for the C2 or C4/C5 integral, based on integration of the aliphatic [EMIM]+ signals. Time zero is arbitrarily set to the time when the ionic liquid was mixed with D_2O. Both curves show a pseudo first-order reaction profile. For both molar ratios it can be noted that the back reaction must be unfavored, since a steady decrease of the ¹H integral can be seen, while the equilibrium is not yet reached.
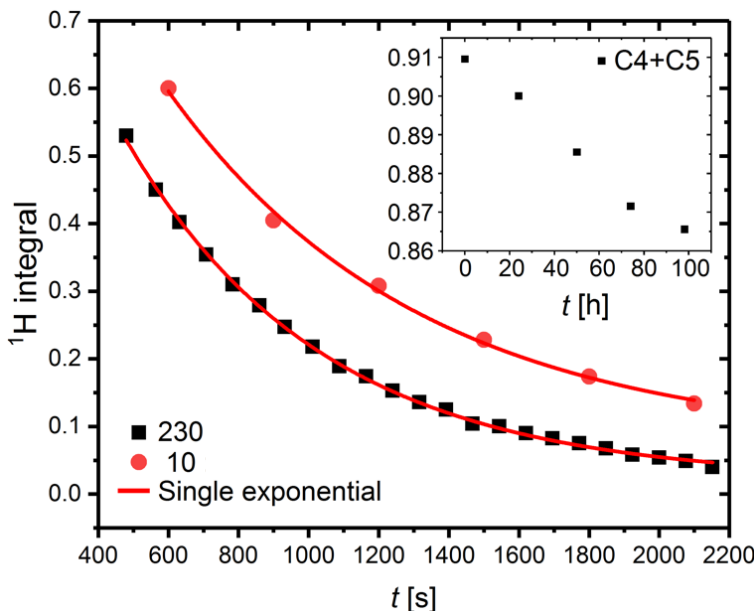
Figure 5.5: Relative ^{1}H integrals (40 °C) of C2-H for $\chi\sim230$ and $\chi=10$ as a function of time. The inset shows the evolution of the relative C4/C5-H integral of the $\chi\sim230$ solution. The $\chi=10$ solution is represented by red circles and the $\chi\sim230$ solution is depicted by black rectangles. Both C2-H curves are fitted by a single exponential (red solid curve).

In addition, it can be noted that the C4/C5 integral is decaying roughly about 1 %/ day. The fitted time constants at C2 of the reactions are $6.4\cdot10^{-4}$ 1/s for $\chi\sim230$ and $4.2\cdot10^{-4}$ 1/s for $\chi=10$. Both time constants differ only by a factor of 1.5, even though the molar ratios differ by a factor of 23. This finding may be an additional hint for the interpretation, that at a molar ratio of 10, the D$_2$O molecules are already well distributed, i.e. in a hydrogen bonded network. This could explain, why the time constants of both molar ratios do not differ severely, when the concentration is increased.

In this work, the deuteration yields are studied as a function of D$_2$O concentration. It is found in Figure 5.4, that equalized deuteration yields at C2, C4/C5 are present for molar ratios up to $\chi=10$. Increasing the molar concentration to $\chi\sim230$ yields a predominant deuteration at the C2 position. Further, it can be deduced from reaction profiles in Figure 5.5 that the C2 position is the kinetic preferred position over C4 and C5 as the exchange rate is notably higher for C2. This finding could possibly be explained by altering ion configurations (depending on concentration), where the C2, C4/C5 positions are equally strongly hydrogen bonded (in a hydrogen bonded network) for molar ratios up to $\chi=10$. The almost exclusive deuteration at C2 ($\chi\sim230$) in Figure 5.4 could possibly be explained by solvated ion pairs, where the anion is predominantly interacting with the C2 position.

More important, this work has highlighted the difference between the hydrogen bond acceptor properties of the anion and its basicity, which should be considered separately from each other. Differences in the hydrogen bond acceptor properties between [OTf]$^-$ and [BF$_4$]$^-$ are decisive, both for a successful H/D exchange reaction (in case of [OTf]$^-$) and for an absence of H/D exchange ([BF$_4$]$^-$). Therefore, this work emphasizes that one must differentiate not only between strong and weak anions, but also between good and bad hydrogen bond acceptors, in order to explain if a H/D exchange occurs.

Regarding the precise abstraction mechanism, in particular for the C4 and C5 sites it can only be speculated that a dual hydrogen bond of the triflate anion with the imidazolium cation may be one possible explanation.[16] In order to obtain additional information about a possible mechanism of the exchange reaction, additional molecular dynamics simulations in combination with e.g. picosecond time-resolved infrared spectroscopy may be useful tools.

5.1.4 References

(1) Hayes, R., Warr, G. G., & Atkin, R. (2015). Structure and nanostructure in ionic liquids. *Chemical reviews*, *115*(13), 6357-6426.

(2) Niedermeyer, H., Hallett, J. P., Villar-Garcia, I. J., Hunt, P. A., & Welton, T. (2012). Mixtures of ionic liquids. *Chemical Society Reviews*, *41*(23), 7780-7802.

(3) Holloczki, O., Gerhard, D., Massone, K., Szarvas, L., Nemeth, B., Veszprémi, T., & Nyulaszi, L. (2010). Carbenes in ionic liquids. *New Journal of Chemistry*, *34*(12), 3004-3009.

(4) Akutsu-Suyama, K., Cagnes, M., Tamura, K., Kanaya, T., & Darwish, T. A. (2019). Controlled deuterium labelling of imidazolium ionic liquids to probe the fine structure of the electrical double layer using neutron reflectometry. *Physical Chemistry Chemical Physics*, *21*(32), 17512-17516.

(5) Oh, S., Morales-Collazo, O., & Brennecke, J. F. (2019). Cation–Anion Interactions in 1-Ethyl-3-methylimidazolium-Based Ionic Liquids with Aprotic Heterocyclic Anions (AHAs). *The Journal of Physical Chemistry B*, *123*(39), 8274-8284.

(6) Chen, S., & Izgorodina, E. I. (2017). Prediction of 1 H NMR chemical shifts for clusters of imidazolium-based ionic liquids. *Physical Chemistry Chemical Physics*, *19*(26), 17411-17425.

(7) Handy, S. T., & Okello, M. (2005). The 2-position of imidazolium ionic liquids: Substitution and exchange. *The Journal of organic chemistry*, *70*(5), 1915-1918.

(8) Friestad, G. K., & Branchaud, B. P. (2001). Tetrafluoroboric acid. *Encyclopedia of Reagents for Organic Synthesis*.

(9) Kütt, A., Selberg, S., Kaljurand, I., Tshepelevitsh, S., Heering, A., Darnell, A., ... & Leito, I. (2018). pKa values in organic chemistry–Making maximum use of the available data. *Tetrahedron Letters*, *59*(42), 3738-3748.

(10) Giernoth, R., & Bankmann, D. (2006). Transition-metal free ring deuteration of imidazolium ionic liquid cations. *Tetrahedron letters*, *47*(25), 4293-4296.

(11) Huang, M. M., Jiang, Y., Sasisanker, P., Driver, G. W., & Weingärtner, H. (2011). Static relative dielectric permittivities of ionic liquids at 25 C. *Journal of Chemical & Engineering Data*, *56*(4), 1494-1499.

(12) Uematsu, M., & Frank, E. U. (1980). Static dielectric constant of water and steam. *Journal of physical and chemical reference data*, *9*(4), 1291-1306.

(13) Kohno, Y., & Ohno, H. (2012). Ionic liquid/water mixtures: from hostility to conciliation. *Chemical Communications*, *48*(57), 7119-7130.

(14) Burba, C. M., Rocher, N. M., & Frech, R. (2009). Hydrogen-Bonding and Ion– Ion Interactions in Solutions of Triflic Acid and 1-Ethyl-3-methylimidazolium Triflate. *The Journal of Physical Chemistry B*, *113*(33), 11453-11458.

(15) Andreeva, D. V., Ip, B., Gurinov, A. A., Tolstoy, P. M., Denisov, G. S., Shenderovich, I. G., & Limbach, H. H. (2006). Geometrical features of hydrogen bonded complexes involving sterically hindered pyridines. *The Journal of Physical Chemistry A*, *110*(37), 10872-10879.

(16) Banik, S. M., Levina, A., Hyde, A. M., & Jacobsen, E. N. (2017). Lewis acid enhancement by hydrogen-bond donors for asymmetric catalysis. *Science*, *358*(6364), 761-764.

5.2 NMR Studies of Hybrid Electrolytes with Confined Electrolyte and *In Situ* Formed Silica
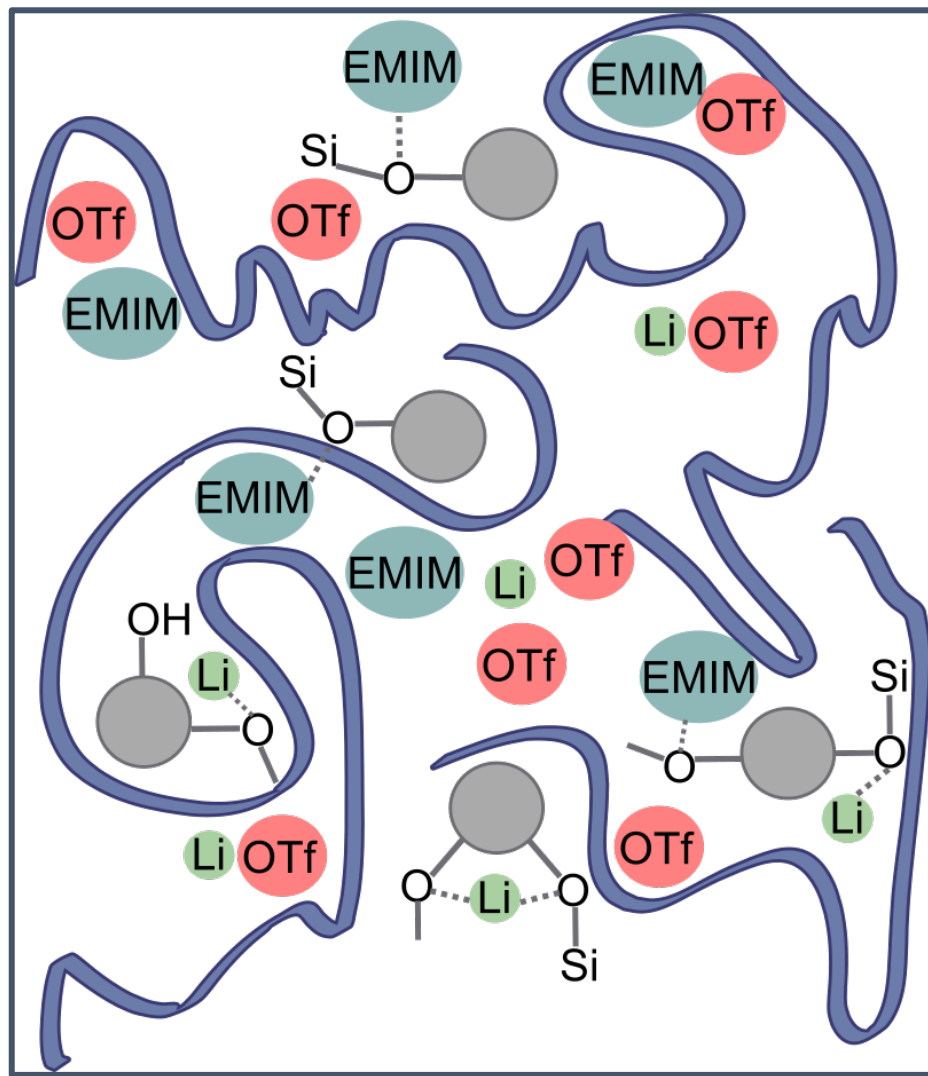
5.2.1 Hybrid Electrolytes

As described in the previous sections, ionic liquid-based polymer electrolytes are currently examined intensively, due to their good safety (low vapor pressure) and high ion conductivity.[1,2] Similar to liquid electrolytes, the crucial aspect is to entrap the ionic liquid in such a way, that the device is not suffering from leakage. Therefore, research has been devoted towards entrapping the liquid electrolyte, for instance in a polymer matrix or in a porous inorganic matrix, such as porous glasses.[3,4] The popularity of the latter is rooted in an increased electrolyte uptake, accompanied with an increase in ion conductivity.[5]

Furthermore, incorporating inorganic particles (SiO_2, TiO_2) into a polymer matrix such as PMMA or PVdF-HFP increases the mechanical properties notably.[6] For many composite systems containing a polymer, an electrolyte solution and inorganic fillers, detailed studies have been carried out. Often, the focus is rather on improving the electrochemical properties, instead of tracing back the physical origin of the observed properties. Partly, this goal has been addressed by a combination of electrochemical studies and IR studies on PVdF-HFP-based ionogels.[7] The latter system exhibits excellent ion conductivities with *in situ* prepared silica particles. Apparently, this preparation method shows benefits over the *ex situ* addition of nanoparticles to the polymer matrix, due to a good dispersibility of the generated particles. In case of the *in situ* generated particles, a connected network may be present enhancing the ion conductivity.[8]

What has been studied in less detail so far is the impact of such an *in situ* generated network on the dynamics of the polymer network. As outlined by Abbrent and co-workers, the addition of different plasticizer decreased the degree of crystallinity in PVdF-HFP-based polymer composites.[9] Besides that, the influence of the electrolyte solution concentration on the ion dynamics, transport phenomena, NMR lineshapes and relaxation times are of special interest, since these properties may be directly linked to ion conductivities and ion transference numbers. Moreover, interactions between the individual constituents, such as hydrogen bonding or ion pairing are likely to occur in these complex systems.[10] Therefore, the following NMR-based work aims to understand the influence of the SiO_2 network on the lithium cation dynamics, [EMIM]$^+$ dynamics and polymer dynamics of a PVdF-HFP-based polymer electrolyte. Furthermore, correlations between NMR-based parameters (line widths) and previously measured electrochemical parameters such as ion transference numbers and ion conductivities will be explored.

5.2.2 Experimental Details

Hybrid organic/inorganic polymer electrolytes were prepared by Shilpa Khurana in the group of Prof. Dr. Amita Chandra in the Delhi University by means of solution casting. A detailed description of the sample preparation can be found in the literature.[7] Initially, poly(vinylidene fluoride-co-hexafluoropropylene) (PVdF-HFP) ($M_w \approx 400.000$ g mol^{-1}, Sigma Aldrich) is dissolved in acetone. Further, an electrolyte solution based on LiOTf (purity > 99 %, Sigma Aldrich) dissolved in 1-ethyl-3methylimidazolium trifluoromethanesulfonate ([EMIM][OTf]) (98 % purity, Sigma Aldrich) is prepared by mixing the salt with [EMIM][OTf], which yields a 0.3 M concentrated electrolyte solution. Subsequently, a defined amount of x wt % electrolyte solution (x = 50, 55, 60 and 65) is added to the dissolved PVdF-HFP. In a further step, tetraethylorthosilicate (TEOS, purity 99 %) is added to the mixture followed by formic acid, which is added dropwise (few drops) to the solution to catalyze the condensation reaction of TEOS molecules yielding silica particles. The mass ratio of PVdF-HFP to TEOS is 3:1. In a last step, the solution is cast in a petri dish, where the acetone is able to evaporate. Opaque films were finally obtained. The precise sample compositions are given in Table 5.2. A reference sample (S3) with no TEOS implemented is used to obtain information about the influence of the silica particles.

The ^{1}H, ^{7}Li and ^{29}Si larmor frequencies were 299.815 MHz, 116.52 MHz and 59.56 MHz respectively. The signal of LiCl in D$_2$O at 0 ppm, the signal of NaCl in D$_2$O at 0 ppm, the Al(H$_2$O)$_6$Cl$_3$ signal at 0 ppm and the OSi(CH$_3$)$_3$ signal of Q$_8$M$_8$ at 11.5 ppm were used as external chemical shift references for ^{7}Li, ^{23}Na, ^{27}Al, and ^{29}Si, respectively. The error of the chemical shifts reported is estimated as ± 0.1 ppm.

Table 5.2: Summary of the sample composition and codes used to label the samples. Numbers are given in wt %.

Samples	Components		
	PVdF-HFP	TEOS	(LiOTf/ EMIMOTf)
S1	100	–	–
S2	75	25	–
S3	35.0	–	65
S4	37.6	12.4	50
S5	34.0	11.0	55
S6	30.0	10.0	60
S7	26.5	8.5	65

5.2.3 Ion Dynamics in Hybrid Electrolytes

Initially, it is of interest to obtain information about the morphology of the samples in order to get insight into the texture of the samples. Therefore, scanning electron microscopy (SEM) in combination with energy dispersive X-ray (EDX) spectroscopy was employed. SEM images of samples S1, S2, S3 and S7 are presented in Figure 5.6. Apparently, the neat polymer exhibits a highly porous structure, seen in Figure 5.6 a). By comparing sample S1 and S2, the influence of the silica is revealed. Obviously, a drastic change in sample morphology can be noted from a highly porous structure (large pore size distribution) being present in S1 towards a smooth and uniform surface in case of sample S2. This finding indicates that the condensed silica is rather present evenly throughout the sample. Even though, few spherical particles with a size of 1 μm can be found for S2 (appendix Figure A.7). An analogous influence of silica may be seen for S3 and S7. While sample S3 exhibits a structure that seems to be composed of small grains which are attached loosely together, sample S7 displays a more compact structure which appears to be rougher compared to S3. Still, it is an open question where precisely the individual constituents are located in the sample.
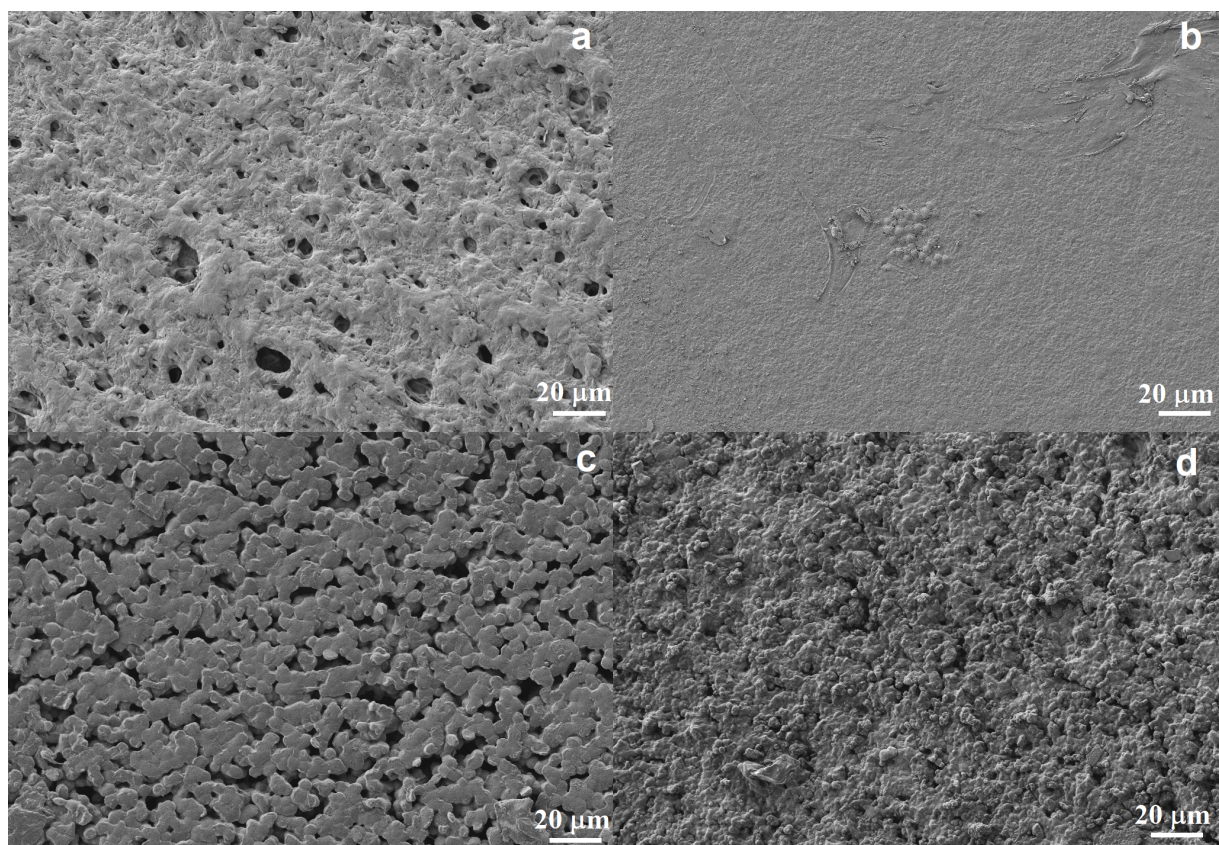

Figure 5.6: SEM top view images of a) PVdF-HFP film (S1), b) PVdF-HFP+TEOS (S2), c) PVdF-HFP+LiOTf/[EMIM][OTf] (S3) and d) PVdF-HFP+TEOS+ LiOTf/[EMIM][OTf] (S7).

The effect of TEOS appears to be that the initially loosely bound structures, as present in Figure 5.6 a) and c) get connected with each other. Pores or either voids in between the grains (Figure 5.6 c)) appear to be filled by an interpenetrating silica network.

In order to obtain further information about the location of the single constituents, EDX maps of sample S6 were presented in Figure 5.7. Additional EDX maps of sample S2 are shown in the appendix. In general, elements probed by EDX such as Si, N and O are sensitive to the individual constituents, since they are unique for the silica network, the imidazolium cation and the triflate anion. The Si map unambiguously reveals that silica is evenly distributed throughout the sample, which supports the interpretation of an interpenetrating silica network. Similar to the Si map, other elemental maps reveal a uniform distribution of the ionic liquid and of the polymer in the ionogel. Note, that the dark spots which appear as pores in the maps of F, C, O, N are not pores but rather depressions, from which only high-energy X-ray radiation (sulfur) can be observed. Therefore, it can be concluded that on the scale of the EDX-map resolution no indication of a phase separation can be probed. A mixing of all individual components is also supported by previously recorded IR spectra.[7]
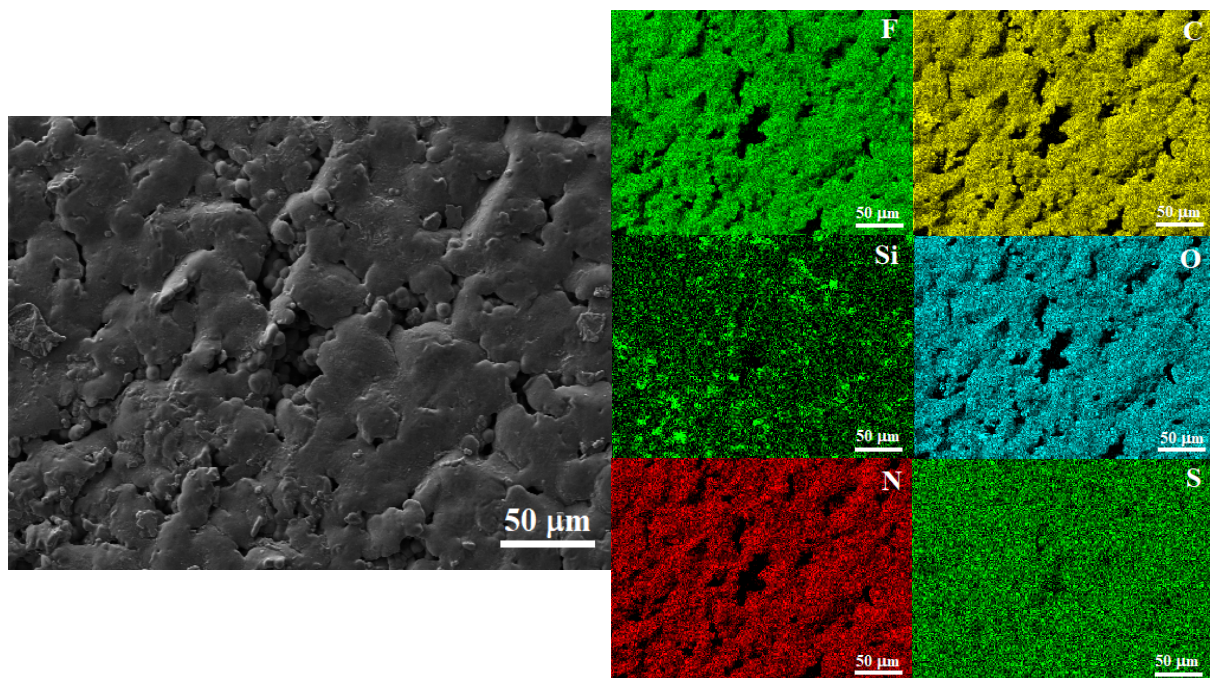

Figure 5.7: SEM micrograph of S6 and corresponding EDX maps of F, C, Si, O, N, S. The scalebar for all micrographs is 50 μm.
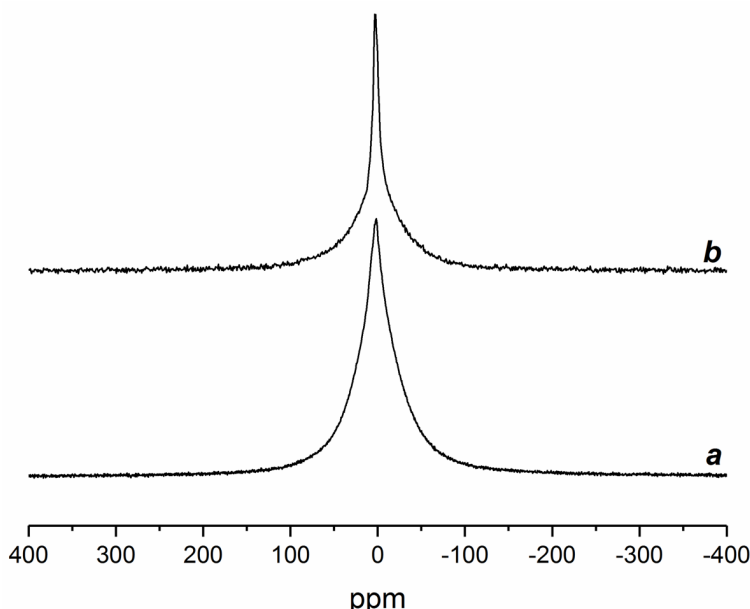
Figure 5.8: Static ^{1}H NMR spectra of the bare PVdF-HFP film (S1) in a) and the PVdF-HFP+TEOS film (S2) in b).

The influence of the silica network on the polymer dynamics can be followed by means of static ^{1}H NMR spectra. The linewidth of a semi-crystalline polymer is significantly depending on homonuclear- and heteronuclear (in this case ^{1}H–^{1}H and ^{1}H–^{19}F dipolar couplings) of the polymer segments.[11, 12] Often, a superposition of narrower and broader lines can be noted corresponding to mobile and less mobile fractions in the polymer, respectively.

Therefore, crystalline polymers tend to exhibit rather broad lines compared to polymers with a high degree of a mobile amorphous phase ($T_g \sim -35$ °C). The silica network is supposed to decrease the amount of the crystalline phases. A comparison of the static ^{1}H NMR spectra between the bare PVdF-HFP film and sample S2 is shown in Figure 5.8. Clearly, Figure 5.8 emphasizes that a tremendous signal narrowing is occurring when the silica matrix is mixed with the polymer matrix, which indicates a reduction in the crystalline polymer fraction. A deconvolution of both lines is given in the appendix (Figure A.89. Overall, the beneficial effect of silica on an increasing amount of amorphous polymer phases could be verified by ^{1}H spectroscopy. Therefore, silica containing electrolytes tend to enhance the ion conductivity in the amorphous polymer region.Furthermore, the ion dynamics and in particular the [EMIM]$^+$ dynamics may be affected by i) the amount of electrolyte solution present in the sample and ii) the presence or absence of silica. Therefore, static and MAS ^{1}H NMR spectra of samples S3−S7 were employed. Static ^{1}H NMR spectra are shown in Figure 5.9.
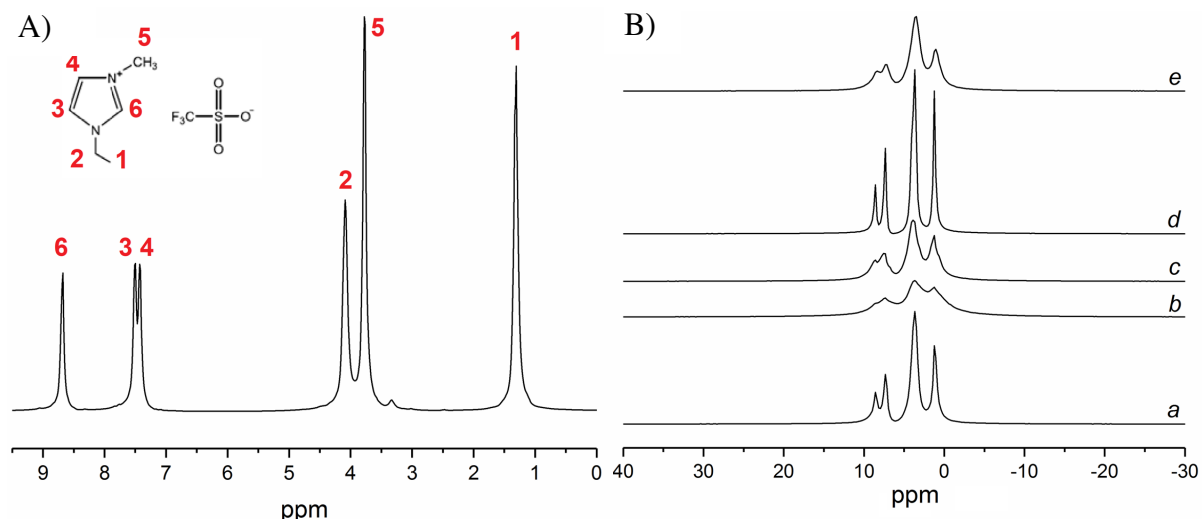
Figure 5.9: ^{1}H NMR spectrum of the electrolyte solution A) and B) hybrid ionogels PVdF-HFP/silica/ES-x with x = 50 b), 55 c), 60 d), and 65 (e) and a) PVdF-HFP/ES-65.

For the neat electrolyte solution in 5.9 A), narrow and well-resolved lines are obtained due to fast molecular tumbling which averages the homonuclear and heteronuclear dipolar interactions and the chemical shift anisotropy. The resolution of the narrow lines remains to a high extent, when the electrolyte solution is incorporated into the polymer matrix. Linewidths of c. 300–400 Hz are present for the polymer electrolytes, which is surprising and indicative for liquid-like dynamics of the polymer electrolyte. The [EMIM]$^+$ dynamics is reduced when the silica network is present in combination with a small amount (50 %) of the electrolyte solution.
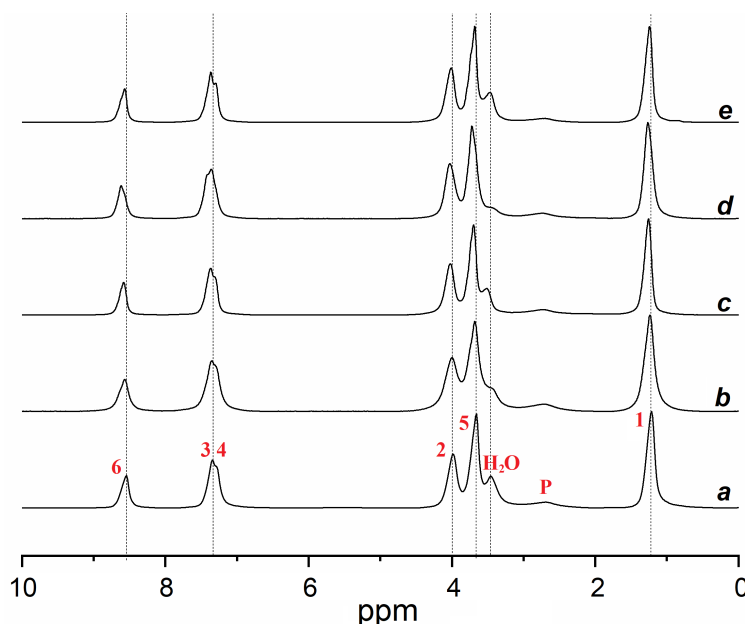

Figure 5.10: ^{1}H NMR spectra of PVdF-HFP/ES-65 (a) and hybrid ionogels PVdF-HFP/silica/ES-x with x = 50 (b), 55 (c), 60 (d), and 65 (e) obtained under 4 kHz MAS. Numeric peak labels refer to the proton sites of EMIM. The peaks labelled H$_2$O (at c. 3.4 ppm) and P (at c. 2.9 ppm) are assigned to water and the mobile fraction of the polymer, respectively.

One explanation for the decrease in mobility (S3 to S4) upon addition of silica is given by Le Bideau and co-workers.[13] They attribute a signal broadening of [EMIM][+] to confinement effects. Le Bideau and co-workers assume that only a marginal decrease in ion dynamics occurs while the distribution of chemical shifts increases.[14] Apparently, this is due to [EMIM][+] experiencing a larger variety of short-range neighboring chemical environments. One possible example is that [EMIM][+] is temporarily hydrogen bonded to a Si–O site of the silica network, yielding another chemical shift compared to the bulk electrolyte. A steady decrease in linewidth from 50 wt% electrolyte solution up to 60 wt% electrolyte solution appears reasonable due to an increasing amount of the liquid-like electrolyte phase. What remains questionable is the increase in linewidth from 60 wt% electrolyte solution up to 65 wt%. Notably, this finding is not in agreement with the diffusion coefficient of the [EMIM][+] cation, discussed in Section 5.3 which shows a larger ion mobility for S7. The explanation for this may be rooted in varying water contents of the sample (seen in Figure 5.10) influencing the static linewidth. In particular Saihara and Bayles show that the ionic liquid reorientation dynamics is strongly affected by the presence of water, which is a further source of the observed line broadening.[15,16] The explanation regarding a distribution of chemical shifts is additionally evidenced by the ^{1}H MAS spectra of all polymer electrolytes presented in Figure 5.10. Even at low spinning rates of 4 kHz, all [EMIM][+] sites could be resolved, while a residual linewidth still remains. Even at higher and lower MAS frequencies (2-8 kHz) (shown in the appendix) no substantial line narrowing is observed, which further supports the hypothesis of a distribution of chemical shifts. Therefore, fast intermediate exchange rates appear more likely than very fast exchange rates.

The lithium cation dynamics is followed by means of [7]Li spectroscopy in order to probe the influence of the silica network on the ion dynamics. A typical example of a [7]Li spectrum recorded under static conditions and under 5 kHz MAS is shown in Figure 5.11. As a spin 3/2 nucleus, [7]Li is expected to exhibit the quadrupolar interaction yielding a quadrupolar broadened line. The static spectrum observed for S4 is rather narrow and featureless, which indicates that homonuclear and heteronuclear dipolar and quadrupolar interactions are mainly averaged due to fast ion motion. Few spinning sidebands which exceed the static linewidth can be found, which are already low in their intensity. According to van Wüllen, this is a strong indication for a reduction in the quadrupolar interaction, again due to fast ion motion.[17] Van Wüllen and co-workers point out, that the number and intensity of the [7]Li spinning sidebands is a measure for the lithium cation mobility, which is crucial for the application in lithium ion batteries. Spinning sidebands of low intensity are indicative for a high ion mobility.
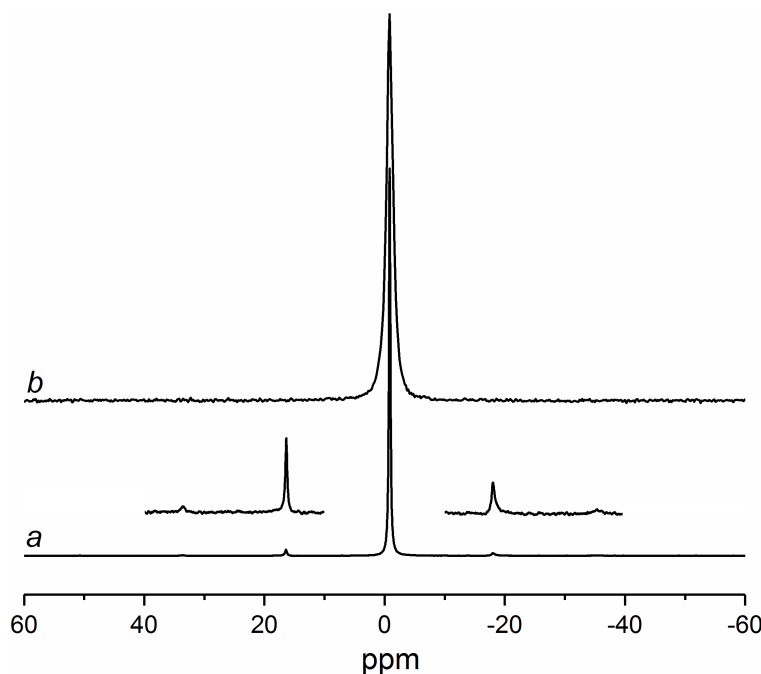
Figure 5.11: a) ^{7}Li MAS NMR spectrum of PVdF-HFP/silica/ES-50 (S4), obtained at a spinning frequency of 2 kHz and b) obtained under static conditions, which is representative for static ^{7}Li spectra of all samples. An exponential apodization of 5 Hz was applied to both spectra.

^{7}Li 2 kHz MAS spectra of the sample series are shown in Figure 5.12. Differences in number and in intensity of the spinning sidebands are noted. In order to compare the spinning sideband intensities, an integration has been carried out for the sidebands and the central line.
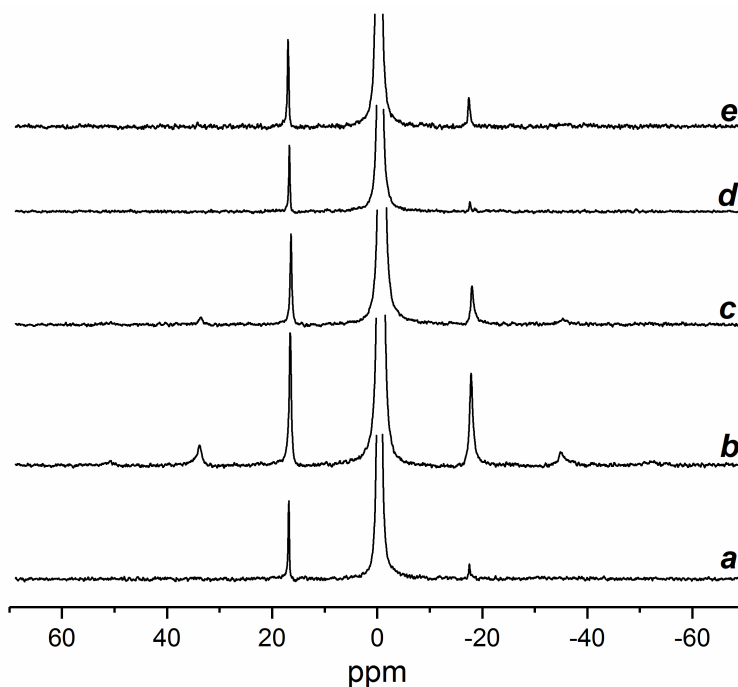
Figure 5.12: ^{7}Li MAS NMR spectra, obtained at a spinning frequency of 2 kHz of a) PVdF-HFP/ES-65 and the hybrid ionogels PVdF-HFP/silica/ES-x with x = 50 b), 55 c), 60 d), and 65 e). 1/20 of the total height is shown for all spectra.

Further, the total fraction of the spinning sideband intensity with respect to the intensity of the central line is obtained and shown in Figure 5.13. A decrease of this ratio is observed upon increasing the amount of electrolyte solution up to 60 wt% while an increase is noted for 65 wt%, as already found for the static ^{1}H linewidths in Figure 5.9. Therefore, a similar trend as found for ^{1}H is found for the ^{7}Li spectra, suggesting equivalent dynamics occurring for both types of ions. This can be confirmed by sample S4, which exhibits the largest number and intensity of spinning sidebands, analogously to the broad static ^{1}H spectrum in Figure 5.26. Both findings may indicate a confinement of the electrolyte solution in the porous silica network.

It appears likely that there exists a correlation between the ^{7}Li fraction of the spinning sideband intensity with respect to the intensity of the central line and the lithium transference numbers, which were measured previously by Khurana and Chandra.[7] The correlation between both parameters is presented in Figure 5.13. Obviously, there is nearly a linear relation between both properties, which emphasizes that they are linked closely to each other. Clearly, sample S4 exhibits the highest fraction of spinning sideband intensity and hence the lowest lithium transference number. Moreover, S6 exhibits a lower ^{7}Li spinning sideband intensity than S7 and therefore a higher lithium transference number. Thus, it seems straightforward that the ion mobility in S7 is higher than in S5 but lower than in S6.
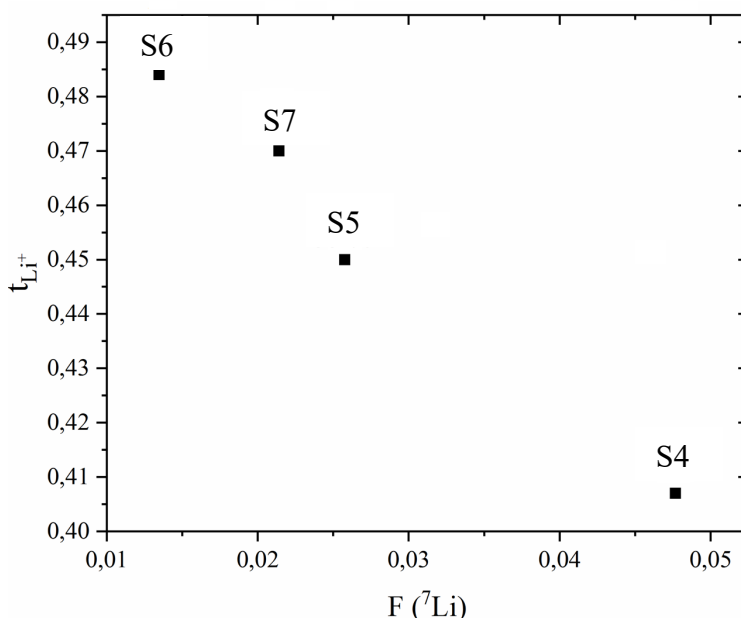

Figure 5.13: Lithium transference numbers t_{Li^+} plotted against the fraction of the ^{7}Li spinning sideband intensity F(^{7}Li).
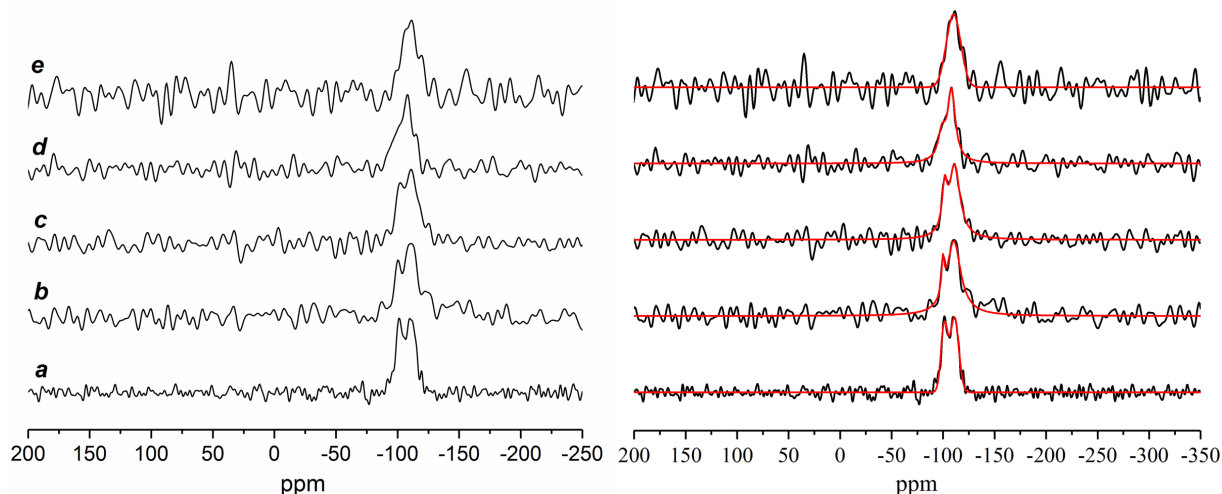
Figure 5.14: ^{29}Si NMR spectra of PVdF-HFP/silica (a), PVdF-HFP/silica/ES-50 (b), PVdF-HFP/silica/ES-55 (c), PVdF-HFP/silica/ES-60 (d), and PVdF-HFP/silica/ES-65 (e) obtained under MAS at 5 kHz and proton decoupling. An exponential apodization with a line broadening of 30 Hz was applied. The red lines are fits with two or one (e) Gaussian/ Lorentzian line(s). The values of the fitted parameters (line position, relative intensity, and full width at half maximum) are shown in Table 5.3.

Finally, the composition of the silica network for the different samples is probed by ^{29}Si NMR spectroscopy. A comparison of ^{29}Si spectra between samples containing the ionic liquid [EMIM][OTf] and the control sample S2 is shown in Figure 5.14. For sake of clarity, a deconvolution of the ^{29}Si signals is added to Figure 5.14. The results are given in Table 5.3.

Unambiguously, it can be seen that the control sample S2 exhibits at least two resolved lines Q^3 and Q^4 at -101.1 ppm and -110.7 ppm, respectively. The common Q^n notation is used for fully condensed Si sites, denoted as Q^4 (Si(OSi)$_4$), and partially condensed Si sites, denoted as Q^3 (Si(OSi)$_3$OH).[19] As ionic liquids are implemented in higher amounts into the samples, the Q^3 site clearly diminishes. This indicates that a more complete condensation indeed occurs for samples containing a notable amount of ionic liquids, as suggested by Karrout and Pierre.[18] They show, that the implementation of ionic liquids into the gelation process results in an acceleration of the hydrolysis and condensation.[18] Therefore, the degree of condensation in the silica network should significantly differ for the control sample S2 and samples containing the ionic liquid. This is found in Figure 5.14 and Table 5.3. One explanation for this finding may be rooted in the acidity of the [EMIM]$^+$ cation, in particular of the C2–H site (discussed in Section 5.1) which additionally catalyzes the condensation reaction.[20] As a result, it can be concluded that the electrolyte solution participates in the condensation reaction in which the silica is formed, yielding a more highly condensed silica network.

Table 5.3: Chemical shift δ, relative intensity I, and full width at half maximum FWHM of the Q^3 and Q^4 peaks obtained by deconvolution of ^{29}Si NMR spectra.

Sample	Assignment	δ (ppm)	I^a	FWHM^b (ppm)
PVdF-HFP/silica	Q^3	-101.1	0.36	6.4
(S2)	Q^4	-110.7	0.64	8.3
PVdF-HFP/silica/ES-50	Q^3	-99.8	0.29	7.4
(S4)	Q^4	-110.5	0.71	14.7
PVdF-HFP/silica/ES-55	Q^3	-102.3	0.42	9.2
(S5)	Q^4	-110.5	0.58	9.9
PVdF-HFP/silica/ES-60	Q^3	-101.6	0.19	9.1
(S6)	Q^4	-108.2	0.81	12.8
PVdF-HFP/silica/ES-65	Q^3	-	-	-
(S7)	Q^4	-110.7	1	16.6

^{a}Relative signal area, error estimated as ± 0.05

^{b}Error estimated as ± 0.2 ppm

Overall, it can be summarized that this work examined the dynamics of (i) the polymer network, (ii) the [EMIM]+ and (iii) the lithium cations in the prepared hydrid ionogels.

In accordance to reports by Abbrent and co-workers, it is found in this work by means of ^1H spectroscopy that the silica network reduces the immobile crystalline polymer fraction notably. Therefore, a higher electrolyte solution content in the amorphous region can be assumed. Further, liquid like dynamics is found for the ionic liquid inside (i) the polymer network and (ii) the hybrid ionogels, which indicates high ion mobilities, close to the bulk electrolyte solution. However, no consistent increase in ^1H ion mobility is found upon increasing the concentration of the electrolyte solution. In addition, a good correlation between the intensity of the ^7Li spinning sidebands and the lithium transference numbers is found. Surprisingly, the ionogel containing 60 wt% electrolyte solution displayed fewer spinning sidebands and a higher lithium transference number than the ionogel with 65 wt% electrolyte solution. This finding resembles the results from ^1H spectroscopy. Lastly, ^{29}Si spectra of the prepared ionogels and a reference sample which does not contain any ions, revealed that the ionic liquid is participating in the silica condensation reaction yielding a more highly condensed silica network. Likely, this

occurs via the acidic C2–H position in the imidazolium cation donating catalytic protons to the condensation reaction.

5.2.4 References

(1) Gray, F. M. (1997). *Polymer electrolytes*. Royal Society of Chemistry.

(2) Long, L., Wang, S., Xiao, M., & Meng, Y. (2016). Polymer electrolytes for lithium polymer batteries. *Journal of Materials Chemistry A*, *4*(26), 10038-10069.

(3) Fuller, J., Breda, A. C., & Carlin, R. T. (1997). Ionic liquid-polymer gel electrolytes. *Journal of the Electrochemical Society*, *144*(4), L67.

(4) Singh, M. P., Singh, R. K., & Chandra, S. (2014). Ionic liquids confined in porous matrices: Physicochemical properties and applications. *Progress in Materials Science*, *64*, 73-120.

(5) Wang, M., Chen, X., Wang, H., Wu, H., Jin, X., & Huang, C. (2017). Improved performances of lithium-ion batteries with a separator based on inorganic fibers. *Journal of Materials Chemistry A*, *5*(1), 311-318.

(6) Gayet, F., Viau, L., Leroux, F., Monge, S., Robin, J. J., & Vioux, A. (2010). Polymer nanocomposite ionogels, high-performance electrolyte membranes. *Journal of Materials Chemistry*, *20*(42), 9456-9462.

(7) Khurana, S., & Chandra, A. (2019). Ion conducting polymer-silica hybrid ionogels obtained via non-aqueous sol-gel route. *Solid State Ionics*, *340*, 115027.

(8) Yao, M., Ruan, Q., Yu, T., Zhang, H., & Zhang, S. (2022). Solid polymer electrolyte with in-situ generated fast Li+ conducting network enable high voltage and dendrite-free lithium metal battery. *Energy Storage Materials*, *44*, 93-103.

(9) Abbrent, S., Plestil, J., Hlavata, D., Lindgren, J., Tegenfeldt, J., & Wendsjö, Å. (2001). Crystallinity and morphology of PVdF–HFP-based gel electrolytes. *Polymer*, *42*(4), 1407-1416.

(10) Suarez, S., Abbrent, S., Greenbaum, S. G., Shin, J. H., & Passerini, S. (2004). Effect of nanosized SiO2 on the transport properties of solventless P (EO) 20LIBETI polymer electrolytes: a solid-state NMR study. *Solid State Ionics*, *166*(3-4), 407-415.

(11) Spiess, H. W. (1991). Structure and dynamics of solid polymers from 2D-and 3D-NMR. *Chemical reviews*, *91*(7), 1321-1338.

(12) Clayden, N. J. (1993). Solid state NMR of synthetic polymers. *Special Applications*, 91-126.

(13) Le Bideau, J., Gaveau, P., Bellayer, S., Neouze, M. A., & Vioux, A. (2007). Effect of confinement on ionic liquids dynamics in monolithic silica ionogels: 1H NMR study. *Physical Chemistry Chemical Physics*, *9*(40), 5419-5422.

(14) Néouze, M. A., Le Bideau, J., Gaveau, P., Bellayer, S., & Vioux, A. (2006). Ionogels, new materials arising from the confinement of ionic liquids within silica-derived networks. *Chemistry of Materials*, *18*(17), 3931-3936.

(15) Bayles, A. V., Valentine, C. S., Überrück, T., Danielsen, S. P., Han, S., Helgeson, M. E., & Squires, T. M. (2019). Anomalous solute diffusivity in ionic liquids: label-free visualization and physical origins. *Physical Review X*, *9*(1), 011048.

(16) Saihara, K., Yoshimura, Y., Ohta, S., & Shimizu, A. (2015). Properties of water confined in ionic liquids. *Scientific reports*, *5*(1), 1-10.

(17) Echelmeyer, T., Meyer, H. W., & van Wüllen, L. (2009). Novel ternary composite electrolytes: Li ion conducting ionic liquids in silica glass. *Chemistry of Materials*, *21*(11), 2280-2285.

(18) Karout, A., & Pierre, A. C. (2009). Silica gelation catalysis by ionic liquids. *Catalysis Communications*, *10*(4), 359-361.

(19) Assink, R. A., & Kay, B. D. (1991). Study of sol-gel chemical reaction kinetics by NMR. *Annual Review of Materials Science*, *21*(1), 491-513.

(20) Noack, K., Schulz, P. S., Paape, N., Kiefer, J., Wasserscheid, P., & Leipertz, A. (2010). The role of the C2 position in interionic interactions of imidazolium based ionic liquids: a vibrational and NMR spectroscopic study. *Physical Chemistry Chemical Physics*, *12*(42), 14153-14161.

5.3 Diffusion NMR in Electrolyte Solutions, PVdF-HFP-Based Polymer Electrolytes and Composite Electrolytes
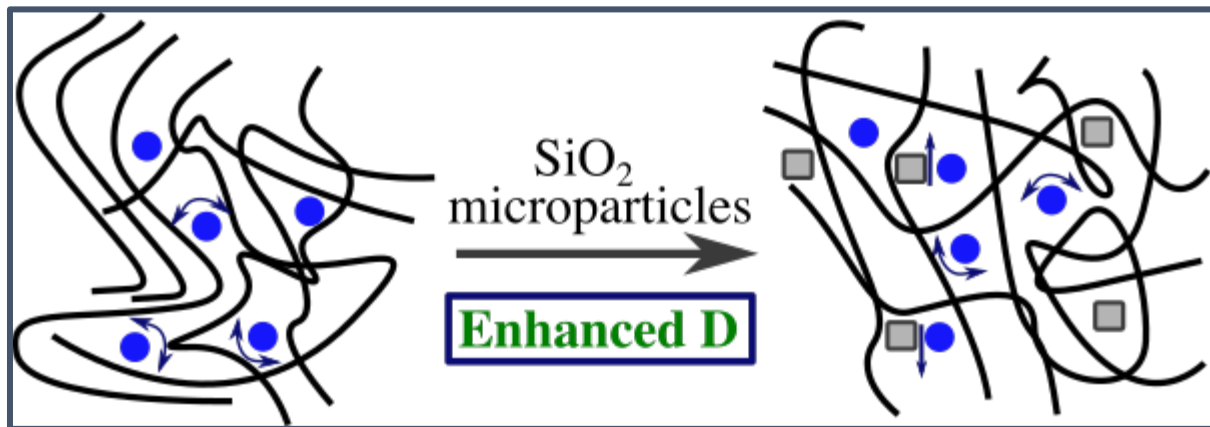
5.3.1 Diffusion NMR of Ionic Liquid-Based Electrolytes

Binary electrolytes, based on a lithium salt dissolved in an ionic liquid have gained attention in the electrochemistry community and were studied by diffusion NMR.[1,2] The popularity of the ionic liquid is rooted in the label "green" solvent, which is aimed to replace the standard organic solvents. Early studies found that the solubility of the lithium salt could be maximized by choosing an ionic liquid which exhibits the same anion as the lithium salt.[3,4] In many cases there is a maximum in ion conductivity which is closely related to the maximum in solubility.[4,5] Recently, binary electrolytes were implemented in a manifold of matrices, such as porous glasses and hybrid organic/inorganic electrolytes, in order to improve the mechanical properties of the electrolyte.[6,7] In hybrid electrolytes, porous silica-microparticles were used as inorganic fillers, enabling an additional electrolyte uptake in the pores. Thereby, an increase of the active electrochemical material could be achieved.

NMR diffusion studies on neat ionic liquids, as well as on electrolyte solutions (lithium salt/ ionic liquid) have been carried out for numerous systems, such as $[EMIM][BF_4]$, $LiBF_4/[EMIM][BF_4]$ and PVdF-based electrolytes containing the latter mixtures.[8−10] A key finding is that the measured diffusion coefficients often strongly deviate from the expected values, based on the Stokes-Einstein relation.[11] More recently PVdF-HFP-based polymer electrolytes have been studied.[12] Richardson and co-workers carried out a PFG diffusion NMR study and found deviations from a single diffusion regime which was assigned to different phases present in the polymer electrolyte.[10] Richardson distinguishes a liquid electrolyte solution phase from a solvated polymer phase (which is rich in polymer). In pursuance of obtaining a better insight into motion phenomena and transport properties in these rather complex materials, multi-nuclear diffusion studies appear well-suited to meet this goal.

Therefore, the diffusion properties of a PVdF-HFP-based polymer electrolyte containing LiOTf (as the lithium salt), [EMIM][OTf] (as the solvent) and a silica network (as the filler) will be scrutinized. The same samples introduced in Chapter 5.2 will be investigated in this section. A benefit of PFG diffusion NMR is that the Li^+, $[EMIM]^+$ and $[OTf]^-$ ion diffusion can be studied separately. In the following section the effect of electrolyte solution concentration and the presence of the silica network on the ion diffusion will be investigated. In particular the effect of the silica network on the ion dynamics is still not well-known and changes in the ion diffusion coefficients can be used to estimate its influence on the ion mobility.

5.3.2 Experimental Details

Hybrid organic/inorganic polymer electrolytes were prepared by Shilpa Khurana in the group of Prof. Dr. Amita Chandra in the Delhi University by means of solution casting. A detailed description of the sample preparation can be found in Section 5.2 and in Table 5.4.

Diffusion NMR experiments were conducted at the Leipzig University in the group of Dr. Muslim Dvoyashkin and at Paderborn University. The diffusion NMR measurements in the liquid state (performed for the electrolyte solution at Paderborn University) were carried out using a 700 MHz Bruker Avance NEO spectrometer equipped with a high resolution cryo-probe (1.5 T/m). The ^{1}H, ^{7}Li and ^{19}F resonance frequencies were 700.130 MHz, 272.09 MHz and 658.78 MHz respectively.

Solid-State diffusion NMR experiments were carried out at Leipzig University and performed by ^{1}H PFG NMR using a home-built NMR spectrometer with a magnetic field of 2.35 T operating with gradients up to 28 T/m. The ^{1}H, ^{7}Li and ^{19}F resonance frequencies were 100.13 MHz, 38.91 MHz and 94.21 MHz respectively. The stimulated echo pulse sequence was used in all of the diffusion experiments. The application of 13-interval pulse sequence was also checked (see appendix). There was no difference in the obtained diffusion decays by 13-interval pulse sequence from the one obtained by the stimulated echo pulse sequence within the experimental uncertainty. Thus, the latter pulse sequence was used. The parameters for diffusion experiments were typically $\Delta = 10$ ms, $\delta = 0.8$ ms, and $\tau = 1.2$ ms, where Δ is the diffusion time, δ is the gradient pulse duration, g is the gradient field strength and τ is the time between the first and second ($\pi/2$) pulses. Further experiments in which Δ is varied are discussed. The diffusion attenuations have been fitted with single-exponential or bi-exponential functions. Furthermore, average diffusion coefficients were fitted by a single exponential, considering the initial decay (first 5-6 data points) of a diffusion curve.

The diffusion coefficients of a single exponential and a bi-exponential decay are obtained by fitting the data to Equation 5.1 and 5.2, respectively:

$$A = A_1 \exp\left(-D(\gamma\delta g)^2\left(\Delta - \frac{\delta}{3}\right)\right) \tag{5.1}$$

$$A = A_1 \exp\left(-D_1(\gamma\delta g)^2\left(\Delta - \frac{\delta}{3}\right)\right) + A_2 \exp\left(-D_2(\gamma\delta g)^2\left(\Delta - \frac{\delta}{3}\right)\right) \tag{5.2}$$

with signal fractions A_x, self-diffusion coefficients D, the gyromagnetic ratio γ, the diffusion time Δ, the gradient duration δ and the gradient strength g.

Table 5.4: Summary of the sample composition and codes used to label the samples. Numbers are given in wt %. The ratio of PVdF-HFP/TEOS is 3:1. S3 is a reference sample without silica.

Samples	Components		
	PVdF-HFP	**TEOS**	**(LiOTf/ EMIMOTf) (ES)**
S3	35.0	–	65
S4	37.6	12.4	50
S5	34.0	11.0	55
S6	30.0	10.0	60
S7	26.5	8.5	65

5.3.3 Ion Diffusion in Electrolytes

Initially, in order to estimate possible experimental errors of the diffusion NMR measurements the diffusion curves measured at Paderborn University and at Leipzig University should be compared. One example of a ^{1}H diffusion measurement of [EMIM][OTf] carried out at 298 K is presented in Figure 5.15.

The comparison between both diffusion curves in Figure 5.15 shows an excellent agreement within the experimental error. The diffusion curve measured at the University Paderborn is not decaying to the same intensities as the diffusion curve from Leipzig, due to smaller gradient strengths available in the Paderborn University. Nevertheless, both curves perfectly match up to an intensity of c. 10 %, while only minor deviations can be noted at an intensity of c. 3 %. The minor deviation from a single exponential (black curve) at low intensities is assigned to an experimental error, likely associated to the gradient pulses. The diffusion coefficient of the [EMIM]$^+$ cation of [EMIM][OTf] obtained from our data (University Paderborn) is $4.2 \cdot 10^{-11} \pm 0.2$ m^2/s, which resembles the data from Brennecke and co-workers and shows that the measured data are indeed valid.[13]

Additionally, the diffusion coefficients of the [OTf]$^-$ anion and the [EMIM]$^+$ cation are compared for the sample series. One example of the neat ionic liquid is shown in Figure 5.16.
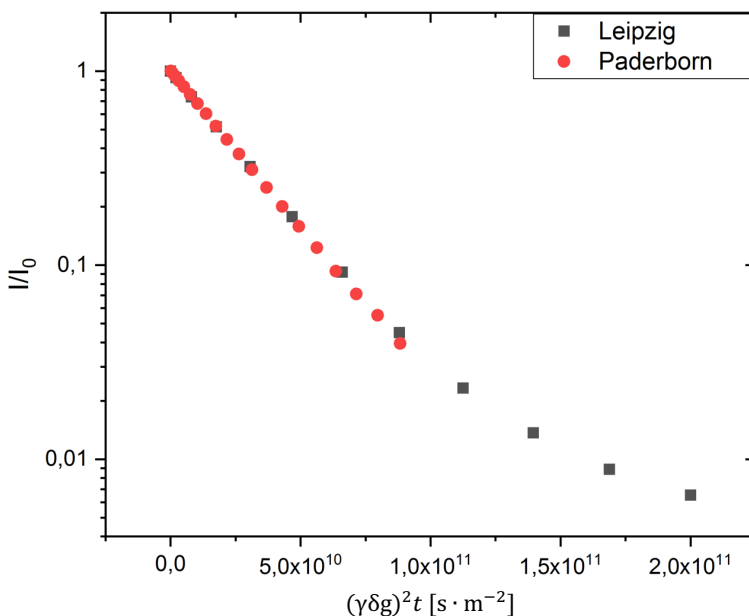
Figure 5.15: Diffusion curve of the [EMIM]+ cation of [EMIM][OTf] (298 K) measured at the University Paderborn and at the Leipzig University.

Clearly visible in Figure 5.16 is the faster ^{1}H diffusion (black curve) compared to the ^{19}F diffusion (red curve). The same trend is observed for all hybride electrolytes studied in this section (shown in the appendix). This means that the larger [EMIM]+ cation (c. 7.6 Å diameter) diffuses faster than the smaller [OTf]− anion (c. 3.9 Å). This feature was earlier found by Wencka et al. for the neat ionic liquid ([EMIM][OTf]) and labelled as "anomalous diffusion",[11] a term which is not used in this work to describe the slower anion diffusion.
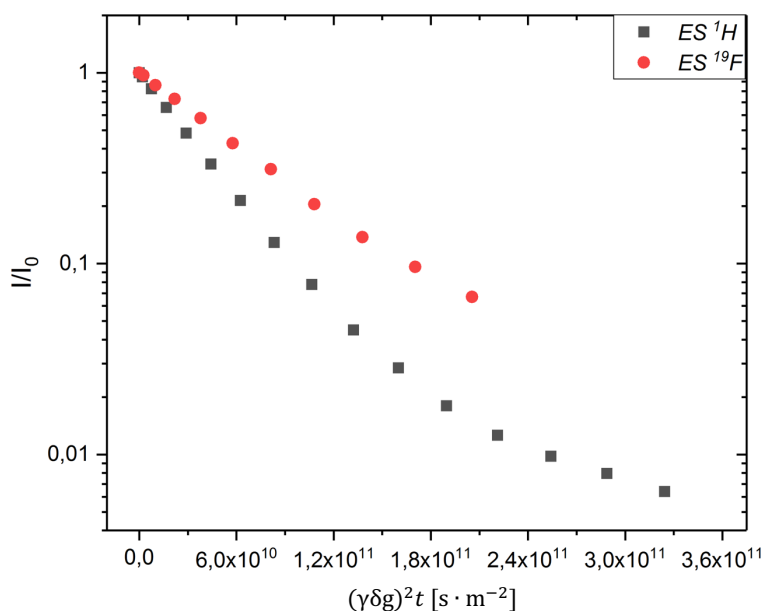
Figure 5.16: An example of ^{1}H and ^{19}F diffusion curves of the electrolyte solution (ES), measured at 2.35 T and 298 K. For all samples fast ^{1}H diffusion ([EMIM]+) is observed and significantly slower ^{19}F diffusion ([OTf]−).

This finding appears contradicting, since the smaller anion (c. 3.9 Å diameter) is diffusing more slowly than the larger [EMIM] cation (c. 7.6 Å diameter), which may be explained by anion-rich clusters and additional correlated anion-anion motions.[11, 14]

The average ^{1}H and ^{19}F diffusion coefficients are presented in Figure 5.17. The influence of the polymer, of the silica network and of the electrolyte solution (ES) concentration on the ^{1}H and ^{19}F diffusion coefficients can be seen. Firstly, the addition of the polymer (PVdF-HFP) can be followed by comparing ES and S3. Clearly, a reduction of both ^{1}H and ^{19}F diffusion coefficients can be seen from ES to S3. This reduction may be explained by a restricted diffusion present in the polymer electrolyte, which can be related to the grain-like structure seen in the SEM images in Section 5.2 (Figure 5.7).

Also, the ratio of the diffusion coefficients of cation/anion D_+/D_- (indicated by dotted lines) changes in Figure 5.17. The D_+/D_- ratios are shown in Figure 5.18. Nevertheless, the data are too scattered in order to derive any clear information. The D_+/D_- ratios are explained by Harris and co-worker to indicate differences in ion velocity correlations and distinct ion diffusivities. The latter may vary substantially for [EMIM]$^+$–[EMIM]$^+$, [EMIM]$^+$–[OTf]$^-$ and for [OTf]$^-$–[OTf]$^-$ motional correlations.
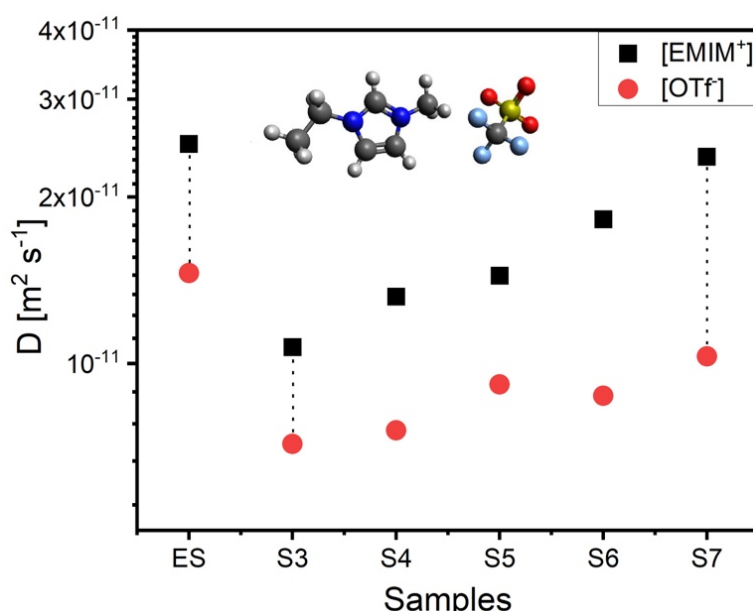

Figure 5.17: Average diffusion coefficients for ^{1}H and ^{19}F for the sample series obtained at 288 K. As the amount of electrolyte solution increases, the fraction of the slow diffusing component decreases which unambiguously shows that the fraction of the "liquid-like" electrolyte phase increases.

Indeed, an earlier study by Harris revealed that the cation-anion velocity correlations are low in magnitude, while the anion-anion velocity correlations are found to be just marginally larger.[14, 16] One result from these considerations is that anions are more restricted in their mobility, unable to diffuse as individual species, whereas this is more likely to be the case for the [EMIM] cations. Harris and co-workers report a D_+/D_- value for bare [EMIM][OTf] to be nearly 1.4, while we find a value of $D_+/D_- = 1.5$ for the electrolyte solution which shows, that the addition of LiOTf to the ionic liquid does not change the motion of the anion and cation significantly.

In addition, the beneficial influence of the silica matrix on the diffusion coefficients of [EMIM]$^+$ and [OTf]$^-$ can be seen in Figure 5.17. Comparing the ^{1}H and ^{19}F diffusion coefficients of sample S3 (without silica) with sample S7 (with silica), it becomes clear that both ion diffusivities significantly increase. The [EMIM]$^+$ diffusion coefficient in sample S7 nearly resembles the one of the ES, while the diffusion coefficient of the [OTf]$^-$ anion is clearly smaller compared to the ES. One possible explanation are non-covalent interactions between the fluorine rich polymer and the fluorinated anion, decreasing the anion diffusivity.

The ^{1}H and ^{19}F diffusion curves are examined in more detail in Figure 5.19. One observation for both ^{1}H and ^{19}F diffusion curves is that nearly a single exponential decay can be noted for the neat ES, while a multi exponential decay is present for the polymer electrolytes S3 and S7.
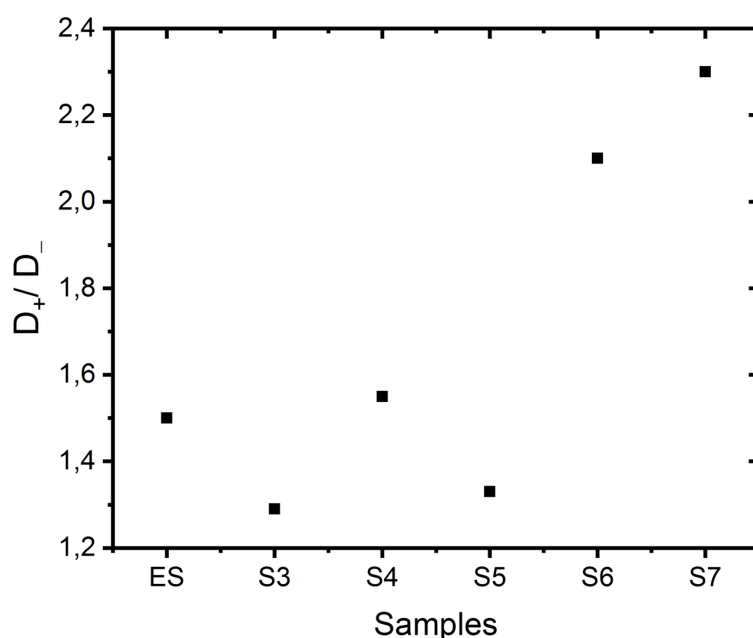

Figure 5.18: D_+/D_- ratios of the average diffusion coefficients shown in Figure 5.8.
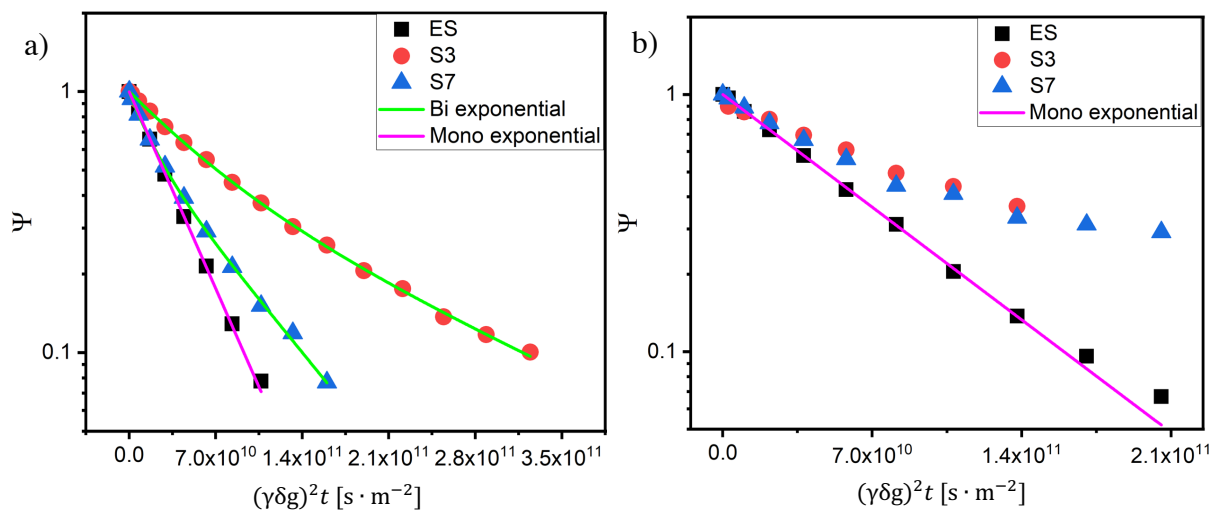
Figure 5.19: a) ^1H diffusion curves for bare ES, sample S3 and S7, b) corresponding ^{19}F diffusion curves, both obtained at 288 K.

In order to fit the ^1H diffusion data of the polymer electrolytes, a simple bi-exponential fit is used, shown in Equation 5.2. The fit results are given in Table 5.5 and the fractions of the slow and fast diffusing species are shown in Figure 5.20. The bi-exponential fit reasonably describes the data points, seen in Figure 5.19 a). However, the ^{19}F diffusion data in Figure 5.19 b) could not be fitted by a bi-exponential fit, which may be due to the fact that the two-population model is oversimplified in case of ^{19}F. In case of slow exchange, anion-rich clusters of different sizes would yield a broad distribution of diffusion coefficients, rather than two well-defined diffusion regimes. Therefore, in case of ^{19}F (and ^7Li) only the average diffusion coefficient is considered which is derived from a linear fit to the first few data points yielding an average diffusion value over all diffusing species. Figure 5.19 a) further shows a trend that was discussed earlier, namely that the implementation of the ES into PVdF-HFP (S3) decreases the ^1H diffusivity, while the addition of the silica matrix (S7) clearly increases the diffusivity.

Table 5.5: ^1H diffusion coefficients and fractions of the fast and slow diffusing component.

Sample	Diffusion ($\times 10^{-11}$ m^{2}s^{-1})[a]		Fraction (%)	
	D_{Fast}	D_{Slow}	A_{Fast}	A_{Slow}
ES	6.0[b]	-	1	0
S3	1.60	0.51	51	49
S4	1.65	1.15	12	88
S5	4.48	1.05	22	78
S6	4.12	1.29	28	72
S7	5.37	1.33	36	64

[a]Error of the diffusion coefficient estimated as ± 0.2 m^{2}s^{-1}

[b]Obtained from Figure 5.21
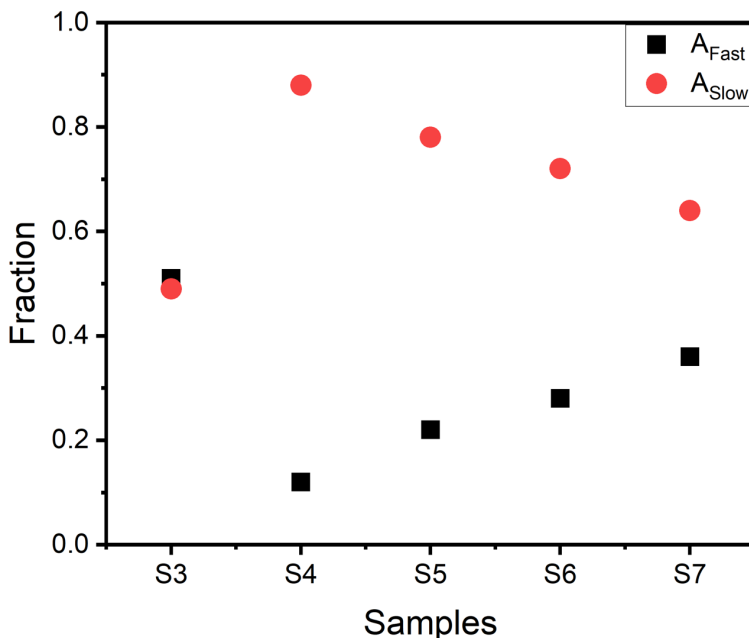
Figure 5.20: Intensity fractions of the ^{1}H fast and slow diffusing component obtained at 288 K.

Figure 5.20 further reveals that the two fractions (slow and fast diffusing) of the [EMIM]$^+$ cation constantly change over the sample series. Adding silica to the polymer electrolyte, visibly increases the amount of slowly diffusing [EMIM]$^+$ cations. From S4 to S7 the amount of electrolyte solution is increased, which leads to a decrease of slowly diffusing [EMIM]$^+$ cations. A reasonable explanation for the presence of a slow and fast diffusing ion species was presented by Richardson and co-workers.[10] According to them, the physical meaning of these two populations is rooted in two distinguishable phases, namely the so-called liquid electrolyte phase (rich in electrolyte) which exhibits faster diffusion and the solvated polymer electrolyte phase (rich in polymer) in which ions may diffuse more slowly.[10] Connecting the explanation by Richardson to the observations from Figure 5.20, it appears plausible that the silica matrix (present in S4-S7) increases the amount of the mobile ion fraction (liquid electrolyte).

In order to derive further information about restricted ion diffusion due to the polymer matrix, it is useful to perform ^{1}H diffusion NMR experiments in which the diffusion time Δ is varied. An example of the ^{1}H diffusion curves is given for the neat ES and the sample S3 in Figure 5.21. As expected for the electrolyte solution in bulk phase, a variation of the diffusion time from 10 ms to 80 ms does not change the observed diffusion curve, as seen in Figure 5.21 a). This expectation is based on the normal Fickian diffusion behavior for a liquid in bulk phase. No indication of restricted diffusion is seen. At large gradient strengths and low signal intensities, a deviation from a single exponential decay is found in Figure 5.21 a) which can be explained by possible deviations in the actual gradient strength.
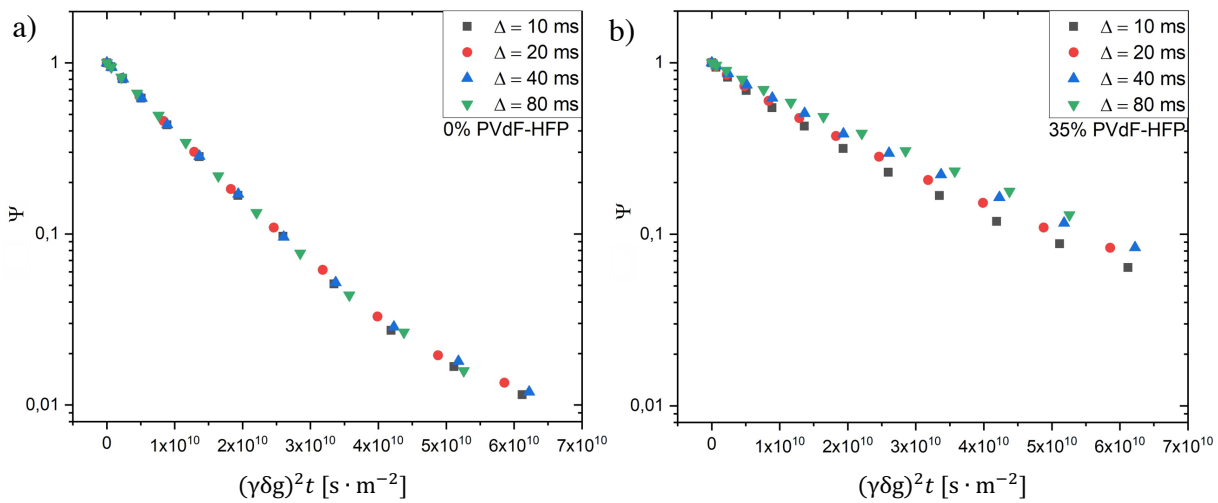
Figure 5.21: Intensity decay curves for the ^{1}H diffusion measurements of [EMIM[+]] in the bulk ES in a) and in sample S3 in b), measured at 328 K.

However, Δ-dependent changes of the ^{1}H diffusion curves of S3 (electrolyte solution + PVdF-HFP) can be observed in Figure 5.21 b). Slower diffusion of the [EMIM][+] cation is seen for longer diffusion times (80 ms). This behavior is indicating that a restricted diffusion is present for the [EMIM][+] cation and likely also for the other ions. This type of diffusion is typically observed for molecules in a confined space, such as a polymer network or inside cells.[15] Therefore, the diffusion curves seen in Figure 5.21 b) (polymer electrolyte) are dominated by two effects; i) the confinement effect which reduces ion displacements for longer diffusion times and ii) the effect of ions being located in at least two phases yielding "slow" and "fast" diffusing populations and therefore slowly decaying diffusion curves and rapidly decaying diffusion curves, respectively.

In particular the confinement effect can be even better visualized by observing the mean squared displacement $\langle r^2(\tau)\rangle$ $(\tau = \Delta)$(MSD), derived from the diffusion coefficients obtained in Figure 5.21. The MSD as a function of diffusion time of samples ES and S3 is presented in Figure 5.22. The basic theory can be found in Chapter 3.2. The [EMIM][+] diffusion in bulk electrolyte solution yields a MSD trace that is linear with respect to the diffusion time. As a result, the distances over which an [EMIM][+] cation diffuses can be seen. On the other hand, the [EMIM][+] diffusion in sample S3 is clearly deviating from linearity. The deviation is below the normal diffusion and therefore may be called sub-diffusion for which $\langle r^2(\tau)\rangle \propto \tau^\alpha$, $\alpha < 1$. However, based on the limited diffusion time variations it remains difficult to closer quantify α and judge about how strongly confined the [EMIM][+] cation is.
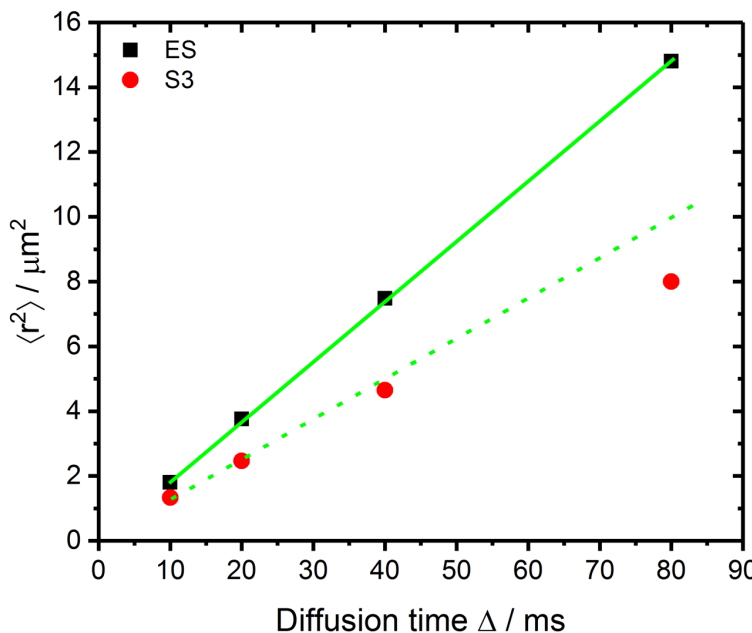
**Figure 5.22:** MSD as a function of diffusion time Δ of [EMIM]⁺ in bulk ES and in sample S3 (using the average D value given in the appendix) at 328 K. The straight lines denote a linear fit.

Arrhenius plots for all ions of the electrolyte solution and of sample S3 are compared in Figure 5.23 (results shown in the appendix). Within the presented temperature range, all data points of the electrolyte solution can be fitted by a linear fit, which indicates an Arrhenius-type temperature dependence. However, as shown by Wencka and co-workers ionic liquids rather exhibit an VTF-type temperature dependence which is revealed in a wider temperature region and in particular for lower temperatures, where a supercooled liquid phase is present.[11]
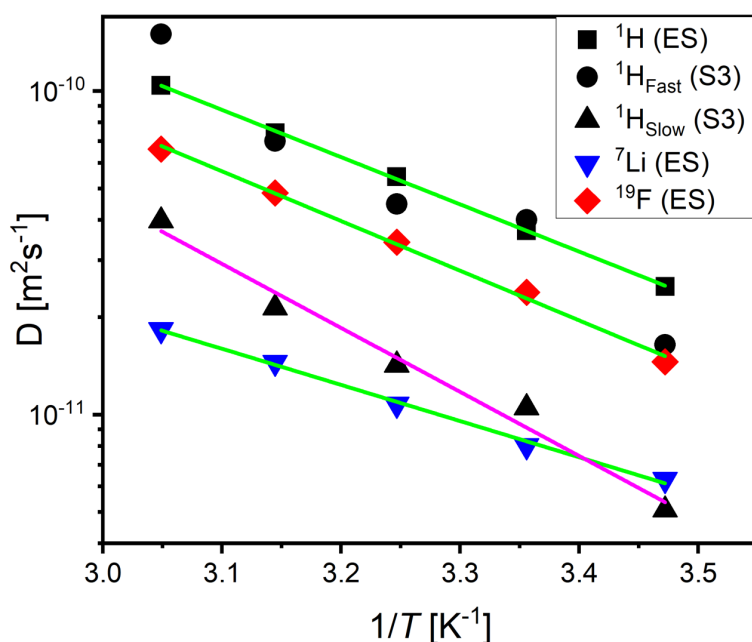
Figure 5.23: ¹H, ⁷Li and ¹⁹F temperature dependent diffusion coefficients for the neat electrolyte solution and ¹H diffusion coefficients of the slow and fast diffusing species for S3.

Fit results of the activation energies are given in the appendix. It can be seen in Figure 5.23 that for the electrolyte solution the $[EMIM]^+$, $[OTf]^-$ and Li^+ activation energies are nearly the same, a trend that is expected for ions in solution. For the $[EMIM]^+$ cation in sample S3, an activation energy almost twice as high can be noted. This finding may be explained by the influence of the polymer segmental motion on the motion of the ions. Therefore, the idea of a solvated polymer phase may be reasonable in the light of the results shown in Figure 5.23. For the fast diffusing species of $[EMIM]^+$ in sample S3, the data points are extremely scattered. The latter makes it difficult to carry out a linear fit.

Furthermore, NMR or "apparent" transference numbers can be derived from diffusion data in order to estimate the individual contribution of each ion to the total charge transported by all ions. The apparent transference numbers are calculated according to Price,[1] which were discussed in detail in Chapter 2.2.The apparent transference numbers presented in Figure 5.24 should always be treated with special caution since the ion activity parameter is not considered for the calculation of these numbers.[2, 17] The ion activity parameter is the ratio of the ion conductivity and the apparent transference number. If the ion activity parameter is equal 1, then all ions in the solution are dissociated and may actively participate in ion transport. In Figure 5.24 an apparent lithium transference number of c. 0.02 % is found for the both samples, which is in the range of the one found for the $LiBF_4$/ $EMIMBF_4$ system by Price.[1]
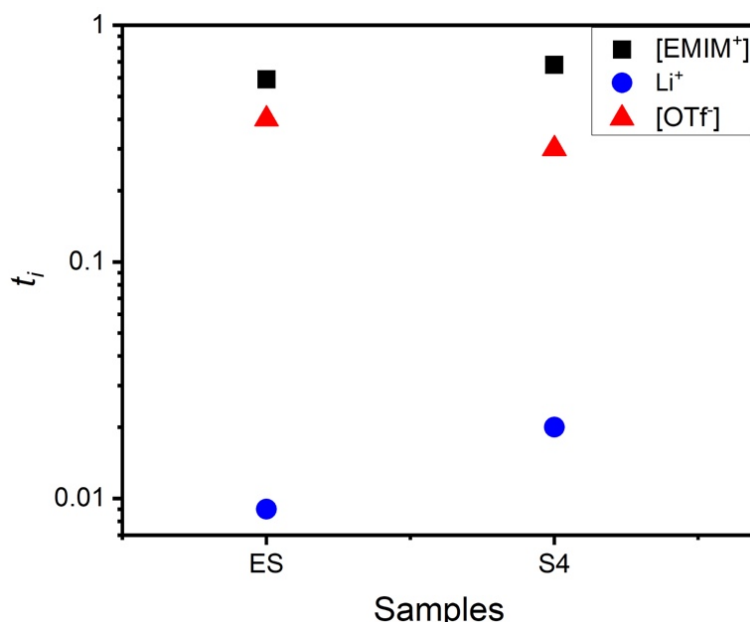

Figure 5.24: Apparent ion transference numbers for bulk ES and sample S4, calculated with diffusion coefficients measured at 298 K.

The explanation for this rather low apparent ion transference number is that the sample is composed completely of ions, which means that [EMIM]$^+$ and [OTf]$^-$ have a major contribution because the molar concentration of 0.3 M (LiOTf) is rather low, yielding a low apparent transference number. The apparent transference numbers calculated for the electrolyte solution are 0.59, 0.4 and 0.01 for [EMIM]$^+$, [OTf]$^-$ and Li$^+$, respectively. For sample S4, a clear reduction of the [OTf]$^-$ transference number (to 0.03) is obtained, because of a drastic decrease in [OTf]$^-$ diffusivity, seen in Figure 5.17.

Overall, it can be concluded that all polymer electrolyte samples including the neat electrolyte solution exhibit a diffusion in which the smaller anion diffuses more slowly than the larger [EMIM]$^+$ cation. The polymer matrix decreases the ion diffusion coefficients significantly. The reason for this may be correlated ion velocities leading to a situation where anion-anion motional correlations are favored over cation-cation motional correlations.

Further, it could be shown that the ^{1}H diffusion curves of the polymer electrolyte samples exhibit a bi-exponential decay, which is explained by two different electrolyte phases, namely a solvated polymer phase and a liquid electrolyte solution phase. The diffusion of the [OTf]$^-$ anion is multi-exponential but cannot be fitted by two populations, which has two possible reasons: i) anion clusters of different sizes for which a slow exchange is present or non-covalent interactions with the fluorinated polymer.

In addition, it could be shown that the ion diffusion in the polymer electrolyte is restricted, which means that ions are not able to diffuse freely in the polymer electrolytes. Lastly, the impact of the silica microparticles has been found to enhance the ion diffusivities significantly and therefore improves the mobility of the ions. This finding is highlighting the benefit of implementing the silica network into the polymer electrolyte samples.

5.3.4 References

(1) Hayamizu, K., Aihara, Y., Nakagawa, H., Nukuda, T., & Price, W. S. (2004). Ionic conduction and ion diffusion in binary room-temperature ionic liquids composed of [emim][BF4] and LiBF4. *The Journal of Physical Chemistry B*, *108*(50), 19527-19532.

(2) Fromling, T., Kunze, M., Schönhoff, M., Sundermeyer, J., & Roling, B. (2008). Enhanced lithium transference numbers in ionic liquid electrolytes. *The Journal of Physical Chemistry B*, *112*(41), 12985-12990.

(3) Long, L., Wang, S., Xiao, M., & Meng, Y. (2016). Polymer electrolytes for lithium polymer batteries. *Journal of Materials Chemistry A*, *4*(26), 10038-10069.

(4) Rosol, Z. P., German, N. J., & Gross, S. M. (2009). Solubility, ionic conductivity and viscosity of lithium salts in room temperature ionic liquids. *Green Chemistry*, *11*(9), 1453-1457.

(5) Pereiro, A. B., Araújo, J. M. M., Oliveira, F. S., Esperança, J. M. S. S., Lopes, J. C., Marrucho, I. M., & Rebelo, L. P. N. (2012). Solubility of inorganic salts in pure ionic liquids. *The Journal of Chemical Thermodynamics*, *55*, 29-36.

(6) Echelmeyer, T., Meyer, H. W., & van Wüllen, L. (2009). Novel ternary composite electrolytes: Li ion conducting ionic liquids in silica glass. *Chemistry of Materials*, *21*(11), 2280-2285.

(7) Khurana, S., & Chandra, A. (2019). Ion conducting polymer-silica hybrid ionogels obtained via non-aqueous sol-gel route. *Solid State Ionics*, *340*, 115027.

(8) Brookes, R., Davies, A., Ketwaroo, G., & Madden, P. A. (2005). Diffusion coefficients in ionic liquids: relationship to the viscosity. *The Journal of Physical Chemistry B*, *109*(14), 6485-6490.

(9) Kaintz, A., Baker, G., Benesi, A., & Maroncelli, M. (2013). Solute diffusion in ionic liquids, NMR measurements and comparisons to conventional solvents. *The Journal of Physical Chemistry B*, *117*(39), 11697-11708.

(10) Richardson, P. M., Voice, A. M., & Ward, I. M. (2016). NMR self diffusion and relaxation time measurements for poly (vinylidene fluoride)(PVDF) based polymer gel electrolytes containing LiBF4 and propylene carbonate. *Polymer*, *97*, 69-79.

(11) Wencka, M., Apih, T., Korošec, R. C., Jenczyk, J., Jarek, M., Szutkowski, K., ... & Dolinšek, J. (2017). Molecular dynamics of 1-ethyl-3-methylimidazolium triflate ionic liquid studied by 1 H and 19 F nuclear magnetic resonances. *Physical Chemistry Chemical Physics*, *19*(23), 15368-15376.

(12) Miao, R., Liu, B., Zhu, Z., Liu, Y., Li, J., Wang, X., & Li, Q. (2008). PVDF-HFP-based porous polymer electrolyte membranes for lithium-ion batteries. *Journal of Power Sources*, *184*(2), 420-426.

(13) Menjoge, A., Dixon, J., Brennecke, J. F., Maginn, E. J., & Vasenkov, S. (2009). Influence of water on diffusion in imidazolium-based ionic liquids: A pulsed field gradient NMR study. *The Journal of Physical Chemistry B*, *113*(18), 6353-6359.

(14) Harris, K. R., & Kanakubo, M. (2016). Self-diffusion coefficients and related transport properties for a number of fragile ionic liquids. *Journal of Chemical & Engineering Data*, *61*(7), 2399-2411.

(15) Wong, I. Y., Gardel, M. L., Reichman, D. R., Weeks, E. R., Valentine, M. T., Bausch, A. R., & Weitz, D. A. (2004). Anomalous diffusion probes microstructure dynamics of entangled F-actin networks. *Physical review letters*, *92*(17), 178101.

(16) Harris, K. R., & Kanakubo, M. (2012). High pressure studies of the transport properties of ionic liquids. *Faraday discussions*, *154*, 425-438.

(17) Zhao, J., Wang, L., He, X., Wan, C., & Jiang, C. (2008). Determination of lithium-ion transference numbers in LiPF6–PC solutions based on electrochemical polarization and NMR measurements. *Journal of The Electrochemical Society*, *155*(4), A292.

5.4 Combining Electrochemical and *Ex Situ* NMR Studies to Reveal the Performance of a Polymer Electrolyte in a Symmetric Cell
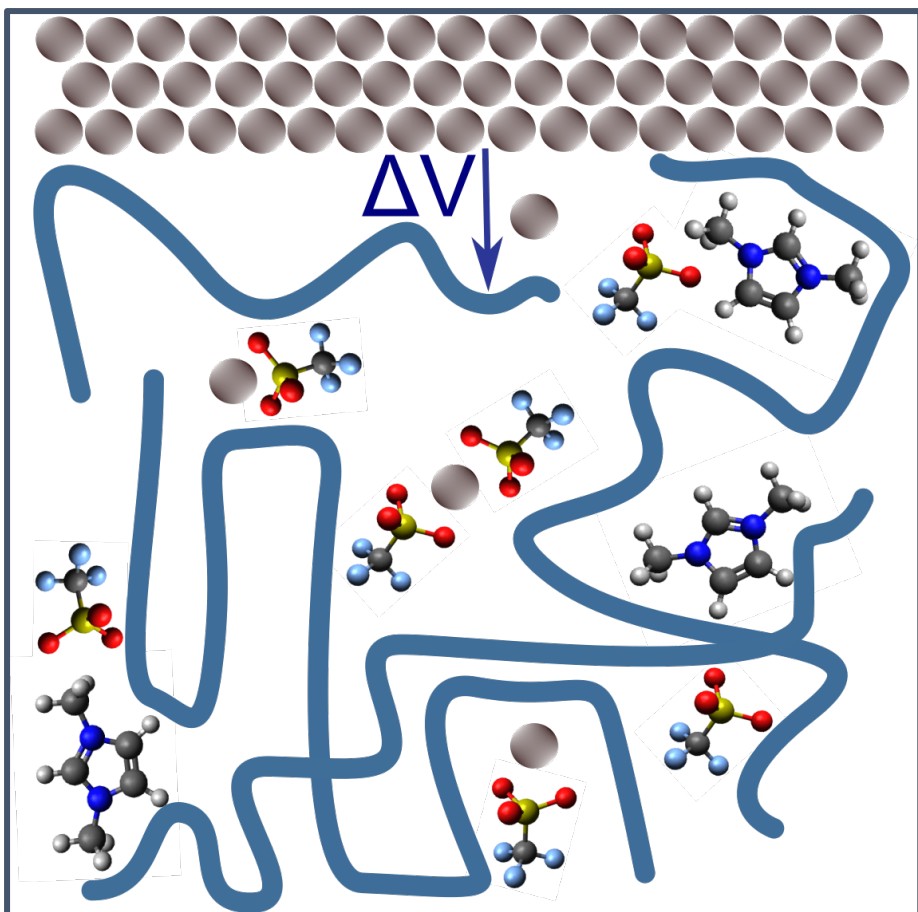
5.4.1 NMR and Electrochemistry

As shown in Chapter 5.2, there are some correlations between information obtained by NMR and by electrochemical measurements, i.e. the ^{7}Li spinning sidebands and the lithium transference number. Since the electrolytes studied in Chapter 5 may potentially be used in a lithium ion battery, it is useful to test these materials in a symmetric lithium cell with non-blocking lithium electrodes. As pointed out in literature, electrochemical parameters such as the ion conductivity may have a different outcome, depending on whether blocking or non-blocking electrodes are used in the setup.[1, 2] As proposed in literature, it is reasonable to use non-blocking electrodes (lithium metal in case of lithium ion electrolytes/ sodium in case of sodium ion electrolytes) to achieve a successful measurement of the lithium transference numbers of different lithium electrolytes.[3–5] As shown by Hu and co-workers, *ex situ* NMR studies are suitable to detect changes in the electrolyte upon cycling a lithium ion battery, even though *in situ* NMR is the method of choice if the required probes are available.[6] In addition to the electrolyte performance can be probed by impedance spectroscopy, which further gives insight into the interfacial resistance.[7] In The following, a PVdF-HFP-based polymer electrolyte containing an electrolyte solution (LiOTf/ [EMIM][OTF]) will be studied. As discussed by Sun and co-workers, the PVdF-HFP polymer exhibits a particular good interfacial stability which will be studied by comparing the latter matrix with a glass separator.[8]

5.4.2 Experimental Details

Two steps of preparation are carried out, (i) the preparation of the polymer electrolytes and (ii) the manufacturing of symmetric cells. For the preparation of the polymer electrolytes, x molal electrolyte solutions (x = 0.1, 0.3 and 0.5) were prepared by mixing vacuum dried lithium trifluoromethanesulfonate (purity > 99 %, Sigma Aldrich) with 1-ethyl-3methylimidazolium trifluoromethanesulfonate ([EMIM][OTf]) (98 % purity, Sigma Aldrich) in an Ar-glovebox. Furthermore, the electrolyte solution is mixed with PVdF-HFP ($M_w \approx 400.000$ g mol^{-1}, Sigma Aldrich) in a mass ratio of 60 % electrolyte solution and 40 % polymer. Additionally, 2 mL anhydrous acetone is added to the mixture, which is stirred by a magnetic stir bar at 30 °C for 24 h in order to fully dissolve the polymer. After 24 h a transparent single-phased solution is obtained. In a last step, acetone is evaporated leaving behind a transparent film of the polymer electrolyte film which is further used. A second reference sample is prepared for which a Whatman® glass separator is initially dried at c. 10^{-2} mbar and 110 °C over night. Then, this filter is soaked in the 0.3 m electrolyte solution for 4 h prior further use.
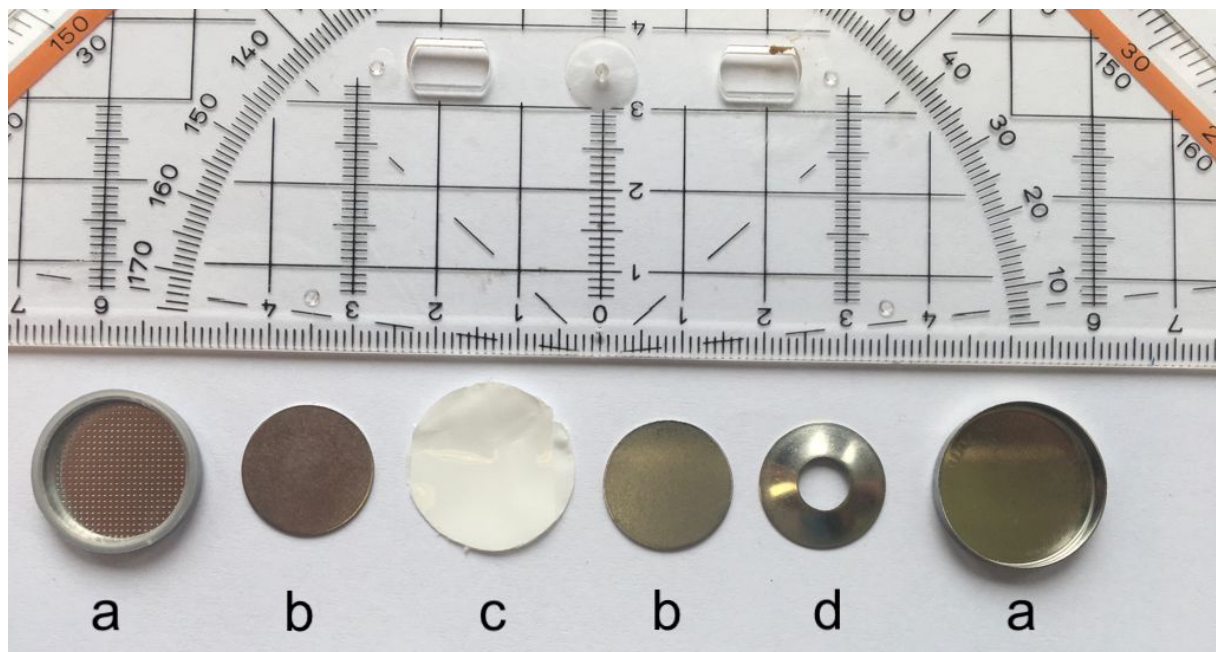
Figure 5.25: Photograph of parts of a coin cell. a) is the cell casing, b) are spacer on which the metallic lithium (diameter 15 mm) is placed. c) is a separator, which is our case replaced by the polymer electrolyte and d) is a spring.

Either the polymer electrolyte film or the soaked Whatman® filter was used as the separator and as the electrolyte at the same time. The individual components of the symmetric cell are shown in Figure 5.25. From both membranes, discs of 16 mm diameter were punched out to cover the 15 mm electrode surface and prevent a short circuit. The components in the order as shown in Figure 5.25 were assembled and pressed with a coin cell press (Cambridge Energy Solutions) to obtain a sealed coin cell. For *ex situ* measurements, the coin cells were transferred into the Ar-glovebox and disassembled. Electrochemical data are acquired following an experiment protocol, provided by Dr. Michael Galluzzo which is presented in the appendix A.5.

5.4.3 Electrolyte Degradation

Impedance spectra of polymer electrolytes containing different molal concentrations of LiOTf are shown in Figure 5.26. It should be pointed out that the 0.5 m LiOTf electrolyte solution contains insoluble solid salt particles. As pointed out by Roling and co-workers, increasing the salt concentration above the solubility limit results in a decrease in ion conductivity since part of the electrolyte is composed of "neutral" salt.[9] In particular this effect can be seen for the 0.5 m polymer electrolyte in the Nyquist plot in Figure 5.26, showing a lower conductivity compared to the 0.3 m sample, seen from the high frequency semi-circle.
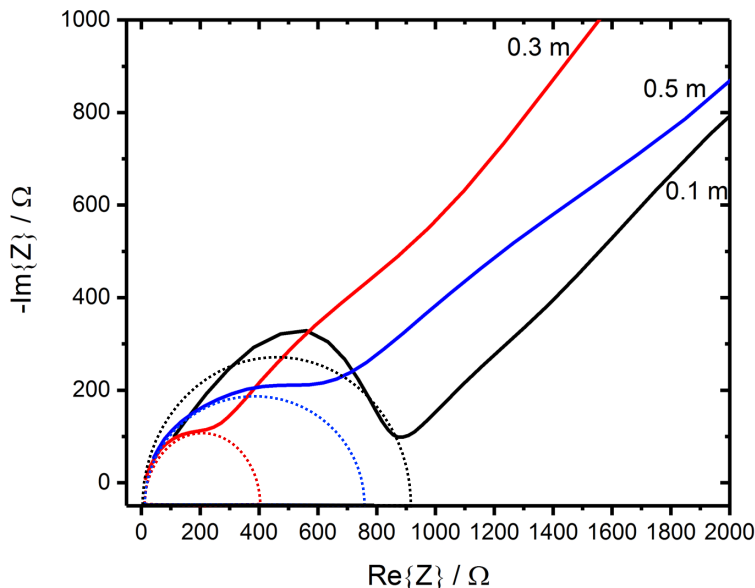
Figure 5.26: Nyquist plot for three polymer electrolytes (PVdF-HFP+ electrolyte solution) containing a 0.1 m, 0.3 m and 0.5 m electrolyte solution. Semi-circles represent no fitting results, but approximately indicate the electrolyte resistance (corresponding to RE in Fig. 2.7) values (σ: 0.3 m > 0.5 m > 0.1 m).

Notably, the 0.3 m polymer electrolyte exhibits the highest electrolyte conductivity (smallest Re{Z} value) among the polymer electrolyte samples. This is the reason for further using this sample. The findings presented in Figure 5.26 are in accord to conductivity data given by Chandra and co-workers, who found a maximum in conductivity for the 0.3 m electrolyte solution.[10] Furthermore, the electrolyte conductivity in the 0.3 m polymer electrolyte should be compared to the 0.3 m Whatman® reference sample, in order to evaluate the influence of the matrix on the ion conductivity. The corresponding Nyquist plots are presented in Figure 5.27.
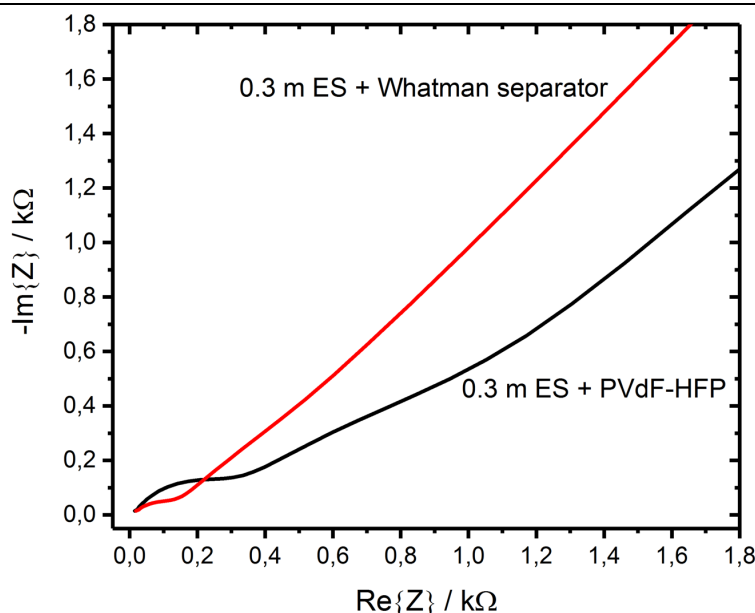

Figure 5.27: Nyquist plots of the 0.3 m polymer electrolyte and for the 0.3 m Whatman® reference membrane, showing the high frequency region.

Clearly, the electrolyte conductivity is higher in the Whatman® reference membrane compared to the 0.3 m polymer electrolyte. This finding is indicative of a higher electrolyte conductivity being present in the liquid electrolyte phase over the solvated polymer phase. Nevertheless, both ion conductivities (Whatman, polymer electrolyte) are of similar order. Also, Balsara makes use of this explanation to derive differences in ion conductivity in a series of polymer electrolytes.[11]

The stability of the electrolyte upon cycling the cell can be obtained by means of ^{1}H NMR spectroscopy at three different stages, (i) the pristine electrolyte solution, (ii) the electrolyte solution embedded in either matrix and (iii) the membranes after 1000 charge/discharge cycles. The corresponding ^{1}H spectra for the Whatman® reference membrane are shown in Figure 5.28. Obviously, the incorporation of the electrolyte solution into the Whatman® glass membrane (pore diameter 1.6 μm) causes an increase in linewidth. A further increase in linewidth can be noted after the symmetric cell has been cycled 1000 times. A small signal broadening after incorporation may be explained by [EMIM]$^+$ cations which are restricted in their dynamics due to the confinement by the glass fiber. A broadening after cycling may be due to dimerization of [EMIM]$^+$. The situation appears different in case of the polymer electrolyte sample presented in Figure 5.29. Initially, the incorporation of the electrolyte solution into the PVdF-HFP matrix again increases the static ^{1}H linewidth. A marginally broader static ^{1}H linewidth can be observed compared to the electrolyte solution incorporated into the Whatman® separator.
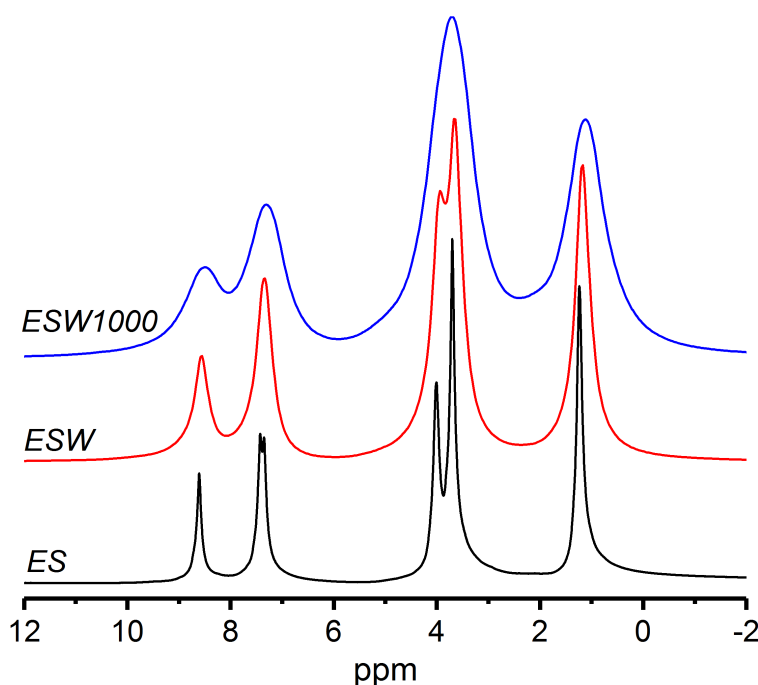

Figure 5.28: Static ^{1}H NMR spectra of the neat electrolyte solution (ES), the Whatman® glass membrane soaked in the electrolyte solution (ESW) and the latter after 1000 charge discharge cycles.
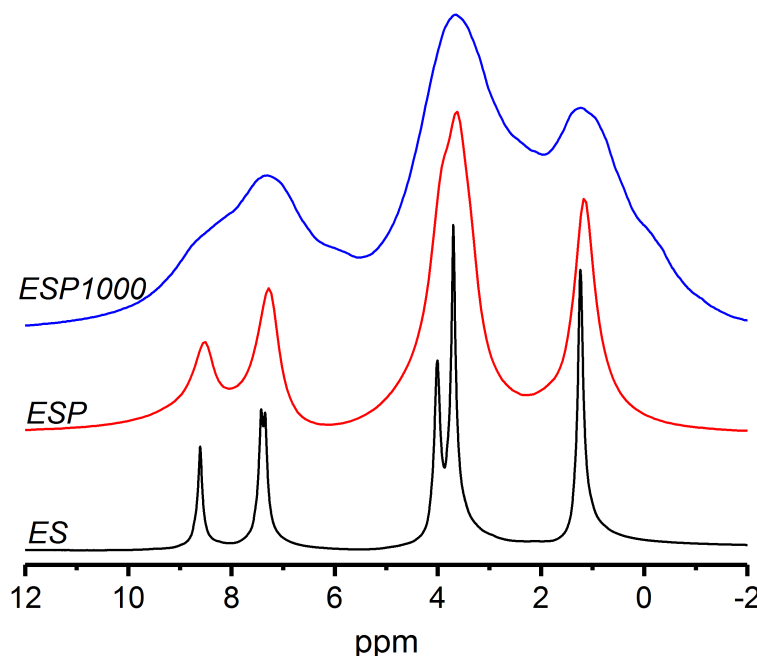
Figure 5.29: Static ^{1}H NMR spectra of the neat electrolyte solution (ES), the polymer electrolyte (ESP) and the polymer electrolyte after 1000 charge discharge cycles (ESP1000).

This may be due to the solvated polymer electrolyte phase in which ion dynamics may be reduced compared to the liquid electrolyte phase, as discussed by Richardson in their diffusion NMR study.[12] Following 1000 charge/discharge cycles, the static ^{1}H linewidth increases notably, compared to the pristine polymer electrolyte. One possible reason could be the onset of a chemical degradation of the [EMIM][+] cation, seen in the extra signals at 6 ppm and 0 ppm.
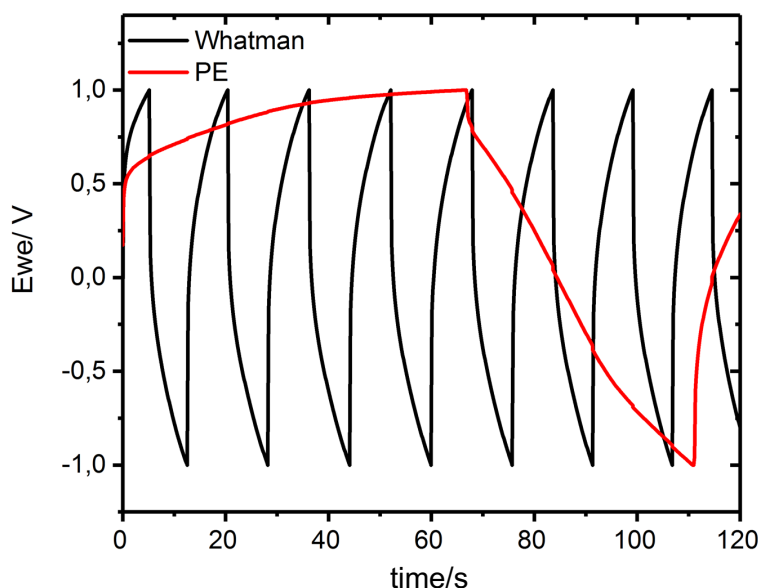

Figure 5.30: Charge discharge curves for symmetric lithium cells with the Whatman® glass membrane soaked in the electrolyte solution and of the polymer electrolyte (PE). Cycling is performed to a limit of $1/{-1}$ V and $+10/{-10}$ mA constant current, corresponds to a current density of 5.65 mA/cm^2.

Besides the electrolyte dynamics, also the solid-electrolyte-interphase plays an important role in the symmetric cell.[13] The potential limit of 1 V/−1 V is reached significantly faster for the Whatman® membrane compared to the polymer electrolyte. The significantly shorter time to perform a full charge/discharge cycle in case of the Whatman® membrane (16 s for the first cycle) compared to the polymer electrolyte (110 s) reflects a capacity loss due to SEI formation[13, 14]. For the polymer electrolyte (red curve) in Figure 5.30 an additional feature can be seen after the first +1 V charging step. The rapid decay of the voltage after 1 V is reached is the so-called Ohmic drop, which corresponds to the internal resistance of the cell,[15] which is maintained for all 1000 charge discharge cycles.

Additional charge discharge cycles are presented in Figure 5.31. They show a reduction in the time to reach the potential limit for the polymer electrolyte and the Whatman® separator, which is possibly due to the growth of the SEI or to a concentration polarization. Accompanied by SEI growth is a further reduction in the electrolyte capacity. For even more charge/discharge cycles (close to 1000), the times required to reach the potential limit nearly equalizes for both membranes (7 s for the Whatman® membrane vs. 7.7 s for the polymer electrolyte). Further charge/discharge plots showing up to 1000 cycles are presented in the appendix. The findings from Figures 5.30 and 5.31 and the presented interpretation are further analyzed by plotting the cycle number with respect to the cycle duration. The corresponding graph is shown in Figure 5.32.
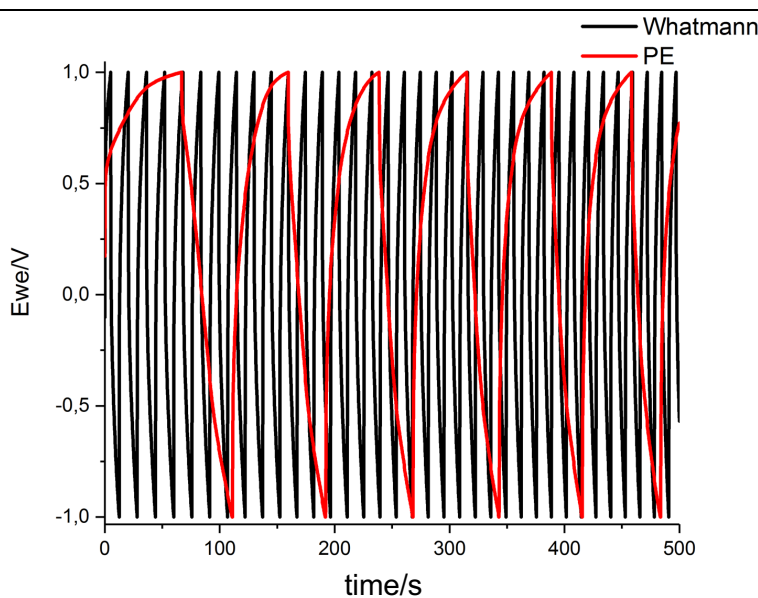

Figure 5.31: First six charge/discharge cycles of the polymer electrolyte sample compared to 29 cycles of the Whatman® membrane.
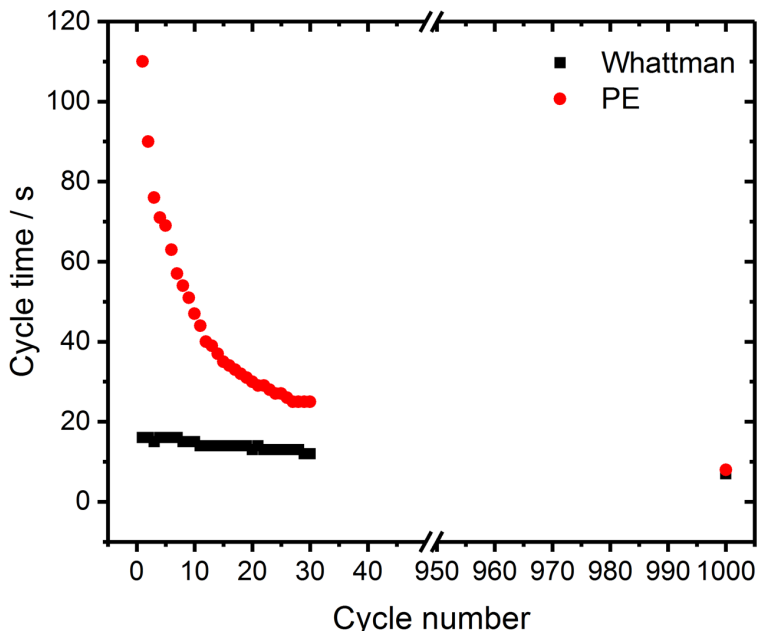
Figure 5.32: Evolution of the cycle time with respect to the cycle number for the polymer electrolyte and the Whatman separator. A strong decay is found for the polymer electrolyte.

As seen in Figure 5.32, a strong decay of the cycle time is found for the polymer electrolyte upon increasing the cycle number. This finding fits in well with the extremely broadened static ^{1}H spectra of the polymer electrolyte (Figure 5.29) and may indicate an electrolyte degradation.

The interfacial resistance at different conditioning stages of the symmetric cell can be probed by EIS. The impedance spectra of both samples are shown in Figure 5.33, where two different semi-circles can be found, one at small Re{Z} values (inset) and one at larger Re{Z} values.
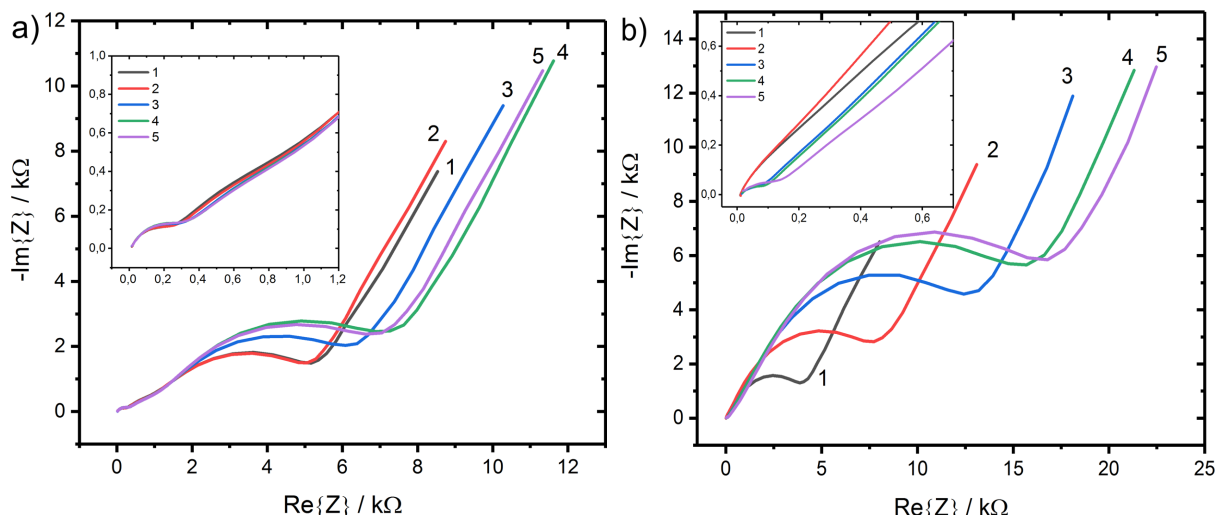

Figure 5.33: Impedance spectra of five different stages of cell conditioning with a) the polymer electrolyte and b) the Whatman® membrane. The semi-circle at larger Re{Z} values is assigned to the interfacial resistance.

The first simi-circle at small Re{Z} values is assigned to the electrolyte resistance, while the second semi-circle is assigned to the interfacial resistance. A clear increase of the latter can be found for both materials. As discussed in literature, the PVdF-HFP matrix exhibits good interfacial stability and prevents a severe growth of the SEI, also apart from lithium ion batteries.[16, 17] The findings from Figure 5.33 show a less pronounced SEI growth compared for the polymer electrolyte compared to the Whatman® separator and therefore support the literature reports. One possible explanation may be considered, namely that the fluorine-rich polymer becomes an integral part of the fluorine donating source and therefore plays an important role in the degradation mechanism.

To summarize, this chapter scrutinized the performance of PVdF-HFP-based polymer electrolytes in a symmetric lithium cell. The results are summarized in Table 5.6. Electrolyte dynamics and degradation, as seen by ^{1}H NMR is severely different in the PVdF-HFP-based polymer electrolyte and the electrolyte solution incorporated into the Whatman® glass fiber. Moreover, electrolyte conductivities obtained from impedance spectra suggest a similar ion conductivity for both materials. Further, charge/discharge curves together with impedance spectra suggested that a strong growth of the SEI occurs in case of the Whatman® glass fiber, while the SEI growth is significantly hampered in case of the PVdF-HFP-based polymer electrolyte. Furthermore, a notably higher electrolyte degradation is found in case of the polymer electrolyte compared to the Whatman® glass fiber by means of cycling experiments. Overall, these findings show that the PVdF-HFP matrix may be directly involved in the electrolyte degradation. Further ^{13}C and ^{19}F experiments are useful, in order to obtain additional information about the possible degradation of the PVdF-HFP polymer.

**Table 5.6:** Electrolyte and interface stability under cell cycling

Method	Polymer Electrolyte	Whatman
NMR	Severe change after cycling	Moderate change after cycling
Cycle Time	Significant decay	Small decay
Impedance Spectra	Minor change after cycling	Severe changes after cycling

5.4.4 References

(1) Yusuf, S. N. F., Yusof, S. Z., Kufian, M. Z., & Teo, L. P. (2019). Preparation and electrical characterization of polymer electrolytes: A review. *Materials Today: Proceedings*, *17*, 446-458.

(2) Galluzzo, M. D., Maslyn, J. A., Shah, D. B., & Balsara, N. P. (2019). Ohm's law for ion conduction in lithium and beyond-lithium battery electrolytes. *The Journal of chemical physics*, *151*(2), 020901.

(3) Evans, J., Vincent, C. A., & Bruce, P. G. (1987). Electrochemical measurement of transference numbers in polymer electrolytes. *Polymer*, *28*(13), 2324-2328.

(4) Sørensen, P. R., & Jacobsen, T. (1982). Conductivity, charge transfer and transport number — an ac-investigation of the polymer electrolyte LiSCN-poly (ethyleneoxide). *Electrochimica acta*, *27*(12), 1671-1675.

(5) MacDonald, J. R. (1973). Theory of space-charge polarization and electrode-discharge effects. *The Journal of Chemical Physics*, *58*(11), 4982-5001.

(6) Hu, J. Z., Jaegers, N. R., Hu, M. Y., & Mueller, K. T. (2018). In situ and ex situ NMR for battery research. *Journal of Physics: Condensed Matter*, *30*(46), 463001.

(7) Lu, P., Li, C., Schneider, E. W., & Harris, S. J. (2014). Chemistry, impedance, and morphology evolution in solid electrolyte interphase films during formation in lithium ion batteries. *The Journal of Physical Chemistry C*, *118*(2), 896-903.

(8) Jie, J., Liu, Y., Cong, L., Zhang, B., Lu, W., Zhang, X., ... & Sun, L. (2020). High-performance PVDF-HFP based gel polymer electrolyte with a safe solvent in Li metal polymer battery. *Journal of Energy Chemistry*, *49*, 80-88.

(9) Fromling, T., Kunze, M., Schonhoff, M., Sundermeyer, J., & Roling, B. (2008). Enhanced lithium transference numbers in ionic liquid electrolytes. *The Journal of Physical Chemistry B*, *112*(41), 12985-12990.

(10) Khurana, S., & Chandra, A. (2019). Ion conducting polymer-silica hybrid ionogels obtained via non-aqueous sol-gel route. *Solid State Ionics*, *340*, 115027.

(11) Hallinan Jr, D. T., & Balsara, N. P. (2013). Polymer electrolytes. *Annual review of materials research*, *43*, 503-525.

(12) Richardson, P. M., Voice, A. M., & Ward, I. M. (2016). NMR self diffusion and relaxation time measurements for poly (vinylidene fluoride)(PVDF) based polymer gel electrolytes containing LiBF4 and propylene carbonate. *Polymer*, *97*, 69-79.

(13) Balbuena, P. B., & Wang, Y. X. (Eds.). (2004). *Lithium-ion batteries: solid-electrolyte interphase*. World Scientific.

(14) Markevich, E., Salitra, G., Rosenman, A., Talyosef, Y., Chesneau, F., & Aurbach, D. (2015). The effect of a solid electrolyte interphase on the mechanism of operation of lithium–sulfur batteries. *Journal of Materials Chemistry A*, *3*(39), 19873-19883.

(15) Gao, J., Shi, S. Q., & Li, H. (2015). Brief overview of electrochemical potential in lithium ion batteries. *Chinese Physics B*, *25*(1), 018210.

(16) Zhu, M., Wu, J., Liu, B., Zhong, W. H., Lan, J., Yang, X., & Sui, G. (2019). Multifunctional polymer electrolyte improving stability of electrode-electrolyte interface in lithium metal battery under high voltage. *Journal of Membrane Science*, *588*, 117194.

(17) Tang, X., Muchakayala, R., Song, S., Zhang, Z., & Polu, A. R. (2016). A study of structural, electrical and electrochemical properties of PVdF-HFP gel polymer electrolyte films

for magnesium ion battery applications. *Journal of Industrial and Engineering Chemistry*, *37*, 67-74.

5.5 Magic-Angle-Spinning and its Effect on the Ion Conductivity, Sample Crystallinity and Morphology of a PVdF-HFP-Based Polymer Electrolyte
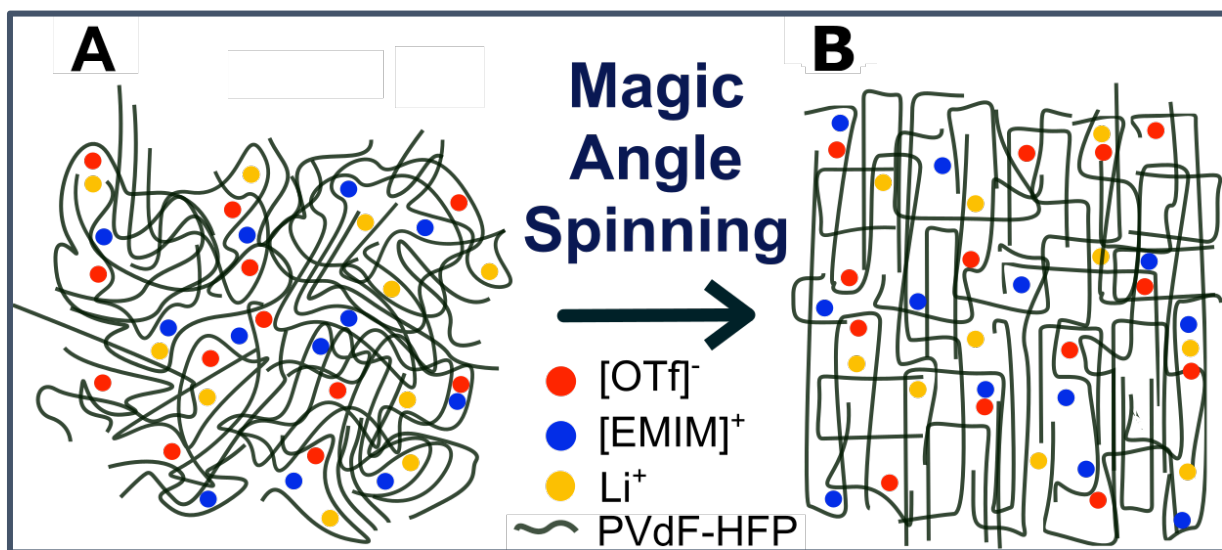
5.5.1 MAS and Polymer Electrolytes

The polyethylene oxide and lithium bis (trifluoromethanesulfonyl)imide (PEO/LiTFSI) system is one of the most studied polymer electrolyte system so far and has been investigated by numerous methods, including XRD and NMR.[1, 2] In particular modifications, including the incorporation of inorganic (nano)-particles has been examined.[3] While studying the PEO/LiTFSI system under magic-angle-spinning (MAS) at moderate spinning frequencies (c. 10 kHz) Messinger and co-workers noted drastic changes within the lineshapes of ^{1}H, ^{7}Li and ^{19}F after their polymer electrolyte has been spun under MAS.[4] Further reports show similar observations made for a variety of samples (membranes, natural rubber).[5, 6, 7] All these materials have in common, that they exhibit a certain pliability, where MAS effects a distortion of the lineshape which is sometimes accompanied with line shifts.[6, 7]

Furthermore, Golodnitsky and co-workers examined PEO-based lithium polymer electrolytes and find that these samples show changes in lineshape upon drawing the polymer electrolyte.[8, 9, 10] Golodnistky assigns changes in lineshape to originate from anisotropic magnetic susceptibility effects which are present in the polymer electrolyte after stretching. In a microscopic picture, the stretching creates a polymer chain alignment and therefore induces an additional crystalline phase in the materials. Surprisingly, Golodnitsky and Goldberg find that their stretched polymer electrolytes exhibit a significantly larger ion conductivity (one order in magnitude) compared to the pristine polymer electrolytes.

Clearly, one remaining question is whether MAS may induce a comparable crystalline polymer phase in the polymer electrolyte samples. Messinger and co-workers assumed this, based on their NMR results, without providing additional experimental evidence.

Even though, this seems unexpected, there are methods to probe the presence of a crystalline polymer phase such as DSC and XRD. In order to examine this effect for a new PVdF-HFP-based polymer electrolyte, we prepare polymer electrolytes which are spun under MAS and further analyzed by DSC and impedance spectroscopy. The goal is to evaluate the influence of spinning the polymer electrolyte under MAS, on the degree of crystalline phases and on the ion conductivity. This may answer the question, whether line distortions seen by Messinger, Kitamura and others are comparable to the stretching effects noted by Golodnitsky and co-workers. Further, this approach may open up the possibility to discuss stretching (and MAS) as methods to improve the ion conductivity of polymer electrolytes.

5.5.2 Experimental Details

Polymer electrolytes were prepared with the same precursor materials analogously to the solution casting approach in Section 5.2. All materials were either handled in an Ar-glovebox or at the Schlenk line. For the polymer electrolyte film, poly(vinylidene fluoride-co-hexafluoropropylene) (PVdF-HFP) and a 1 molar solution of LiOTf in 1-ethyl-3-methyl-imidazolium trifluoromethanesulfonate ([EMIM][OTf]) were added to a 5 mL vial (60 wt% electrolyte solution, 40 wt % PVdF-HFP) which is placed in a Schlenk vessel. The used [EMIM][OTf] is a deuterated product (deuteration yield c. 40 % at C2, C4 and C5) which is obtained by method (ii) in Section 5.1. Once this vessel is connected to the Schlenk line, 2 mL of anhydrous acetone were added to the mixture and stirred with a magnetic stir bar for 24 h. After 24 h a transparent single-phase solution was obtained. Furthermore, the evaporation of acetone was carried out under argon counterflow for 12 h until a transparent film was obtained. In a last step, the remaining volatile compounds were removed by a vacuum-cold trap (nominal pressure 10^{-2} mbar) for 1 h. The prepared sample is treated as the "reference" sample.

An additional sample is prepared ("polymer electrolyte after MAS"), by cutting the reference sample into c. 1x1 mm² pieces and packing these into a 4 mm zirconia MAS rotor. The latter is spun under 7 kHz MAS at 40 °C for 12 h. Afterwards, the rotor is disassembled in an Ar-glovebox, while the individual pieces are fused together and formed a compact hollow cylinder as shown in Figure 5.13 a). This sample is further examined. Photographs of the reference sample and of the polymer electrolyte after MAS are added to the appendix. Electrochemical measurements were carried out by Dr. Ali Javed in the working group of Prof. Dr. Michael Tiemann (Paderborn University). DFT calculations were carried out by Dr. Hossam Elgabarty in the working group of Prof. Dr. Thomas Kühne (Paderborn University).

5.5.3 Morphology, Conductivity and NMR Spectra after MAS

In order to enable a clear definition of axis systems, including sample system and molecular axis system, a clear definition has to be stated. This definition is carried out in Figure 5.34. Here, a) shows the axis system of the samples and b) the axis system of the 1-ethyl-3-methyl-imidazolium cation. It should be noted that NMR experiments, as well as DSC, XRD and impedance studies were carried out using a cutting from the hollow cylinder obtained after MAS. The axis system of the sample can be converted into the molecular axis system, which is relevant for the nuclear shielding tensor calculations.
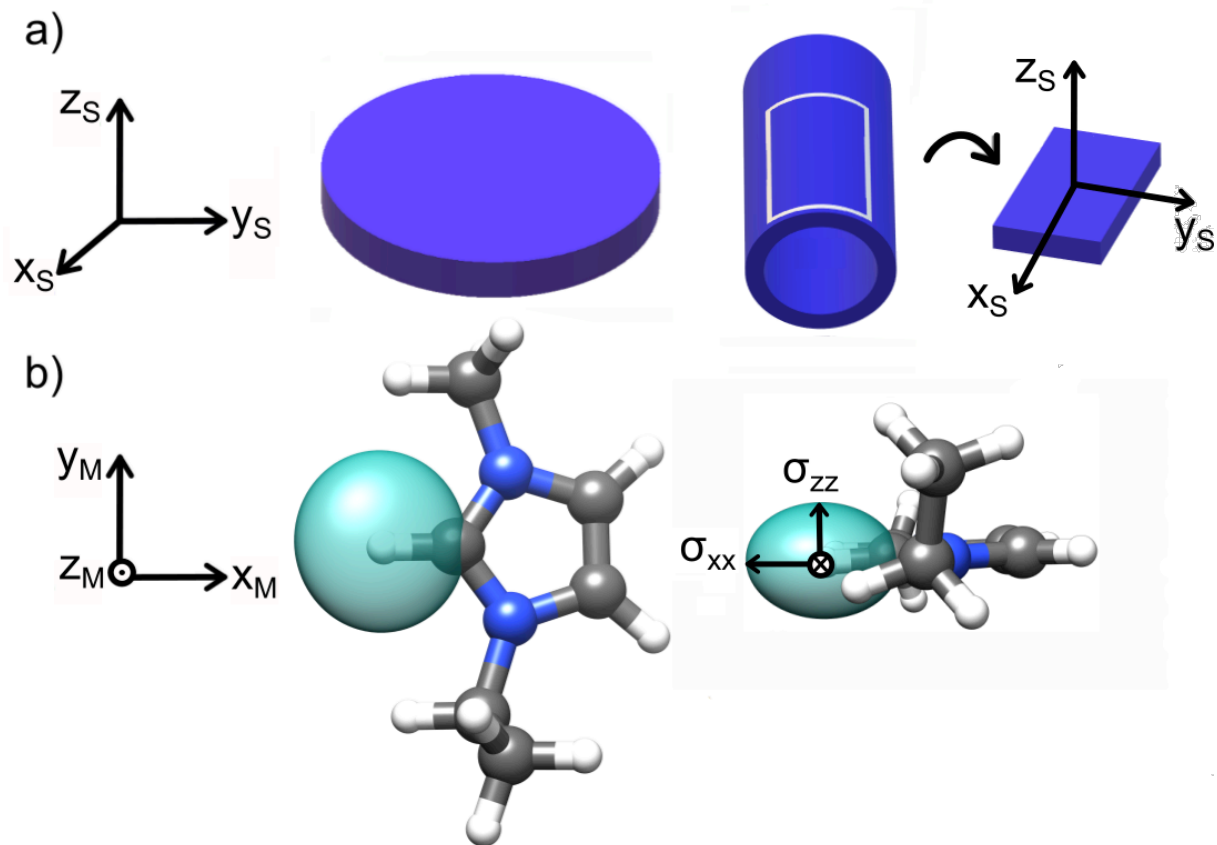
Figure 5.34: a) shows the axis system of the studied samples with the disc-shaped reference sample, the polymer electrolyte after MAS as a hollow cylinder and a cutting from the hollow cylinder as a plane rectangle. b) defines the molecular axis system of the [EMIM] cation with the chemical shielding tensor in green (schematically shown for the C2−H nucleus from top and side-view).

Further, it should be verified if spectra similar to Messinger and Golodnitsky can be found analogously for the PVdF-HFP/ electrolyte solution system studied in this work. Therefore, ^{7}Li static and MAS spectra were acquired and shown in Figure 5.35. Spectra a) and b) were recorded under 7 kHz MAS, whereas c), d) and e) are static spectra. Spectrum a) is acquired at incipient MAS and thus exhibits a Lorentzian line falling close to −0.1 ppm, which is expected for solvated lithium cations. Apparently, the peak shape changes from a single Lorentzian line to a doublet-like peak in b). Doublet-like peaks under MAS are found by Chen and co-workers for natural rubber at an increase of the crystalline phase which is formed under MAS.[11] Therefore, it can be assumed that the appearance of the additional upfield shifted signal can be attributed to the formation of a crystalline phase in the material. The corresponding static spectrum after MAS changes from a broad Lorentzian line in c) towards a broad smeared out doublet, which can be attributed to an anisotropic magnetic susceptibility within the sample.[6, 7, 12]
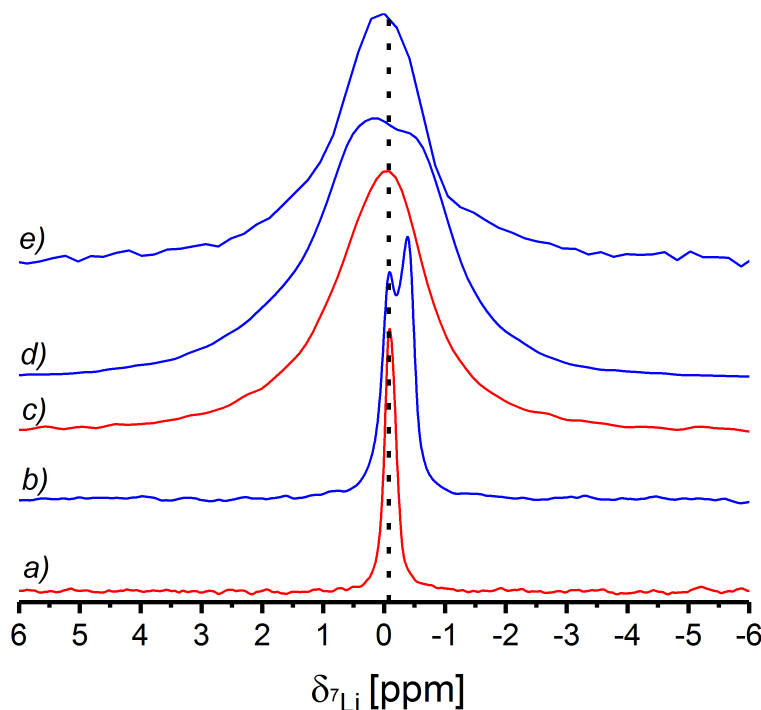
Figure 5.35: ^{7}Li NMR spectra of the pristine polymer electrolyte, under 7 kHz MAS in a) and static in c). ^{7}Li spectra of the polymer electrolyte after MAS, 7 kHz MAS in b) and under static conditions in d). Spectrum e) shows a static ^{7}Li spectrum of 1x1 mm^2 cuttings of the polymer electrolyte film after MAS.

Spectrum e) shows a static ^{7}Li spectrum of the polymer electrolyte after MAS, for which the hollow cylinder was cut back into pieces of c. 1x1 mm^2 and placed back into the rotor. Obviously a nearly Lorentzian line could be retained. This finding on the other hand, is indicating that the previously found doublet results from anisotropic magnetic susceptibility, since it shows a dependence on sample geometry. In this respect, Golodnitsky and co-workers report, that the high conducting crystalline phase may last only up to 300 h.[8, 13] Therefore, the crystalline phase may disintegrate after a certain time. As a result, both effects discussed in literature are found, namely (i) the anisotropic bulk magnetic susceptibility effect resulting from sample shape, as well as (ii) a crystalline polymer phase which is formed during MAS and for which a clearly distinguishable chemical environment is present.

In addition, Kitamura and co-workers employed angle-dependent ^{13}C measurements, in order to derive information about the presence of a crystalline polymer phase in natural rubber. Due to the fact that the studied materials exhibit only 40 wt% polymer and ^{13}C nuclei typically show long spin-lattice relaxation times (T_1), makes ^{13}C angle-dependent measurements unattractive. Instead, we make use of the deuterium labelling of the ionic liquid in order to perform ^{2}H-angle-dependent measurements, which are not limited by long T_1 relaxation times.
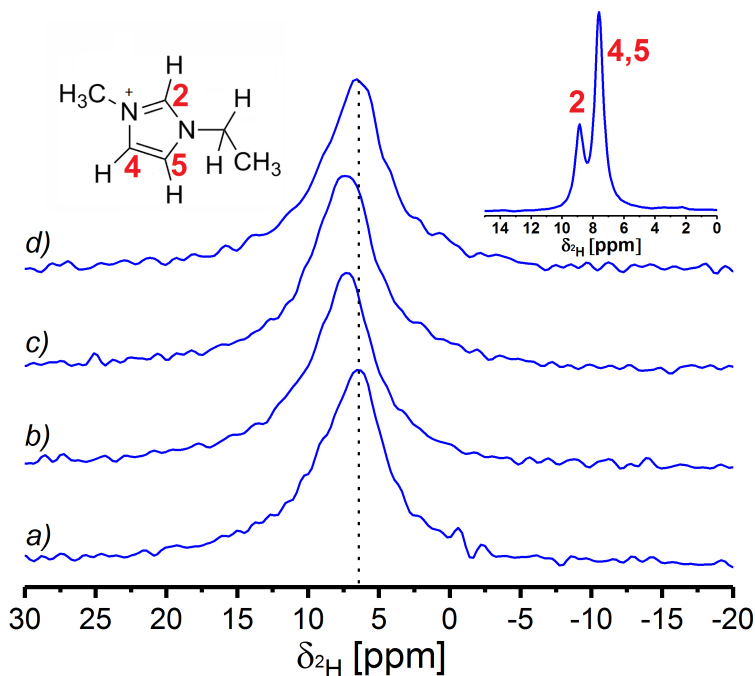
Figure 5.36: [2]H spectra of the polymer electrolyte film after MAS positioned with the y_S-axis parallel to the magnetic field. This starting position is labelled as 0° in a). Further the sample is rotated around the x_S-axis at 45° in b), at 90° in c) and at 180° in d). The largest shift is obtained for 90°. The inset shows a ^{2}H MAS spectrum of the polymer electrolyte acquired under 7 kHz.

Different ^{2}H spectra are recorded either under MAS or with a home-build goniometer probe are shown in Figure 5.36. ^{2}H NMR spectra are typically governed by quadrupolar interactions, since deuterons exhibit a spin quantum number of $I = 1$. The first order quadrupolar interaction is relevant, which can be averaged in case of fast isotropic molecular tumbling. The quadrupolar splitting is defined as:

$$\Delta v = \left(\frac{3}{4}\right) \delta \left(3 \cos^2 \beta - 1\right)$$ [5.3]

with $\delta = e^2 qQ/h$ as the quadrupolar coupling constant and the angle between the director and the external magnetic field is labelled as β.

As reported by Jelinski, the quadrupole coupling constant for a rigid C–D bond is in the order of 125 kHz.[14] However, the linewidths found in Figure 5.36 are in the order of 260 Hz. As a result, the residual quadrupolar interaction is smaller than 260 Hz. From this value, the order parameter S can be calculated.[15] The order parameter calculated for the spectra in Figure 5.125 is $\sim 2 \cdot 10^{-3}$ and therefore a highly disordered system is present. Considering, that the span of ^{2}H chemical shift is as small as 10 ppm, it is possible to estimate the motional averaged chemical shift anisotropy (CSA) to be as small as 0.02 ppm.
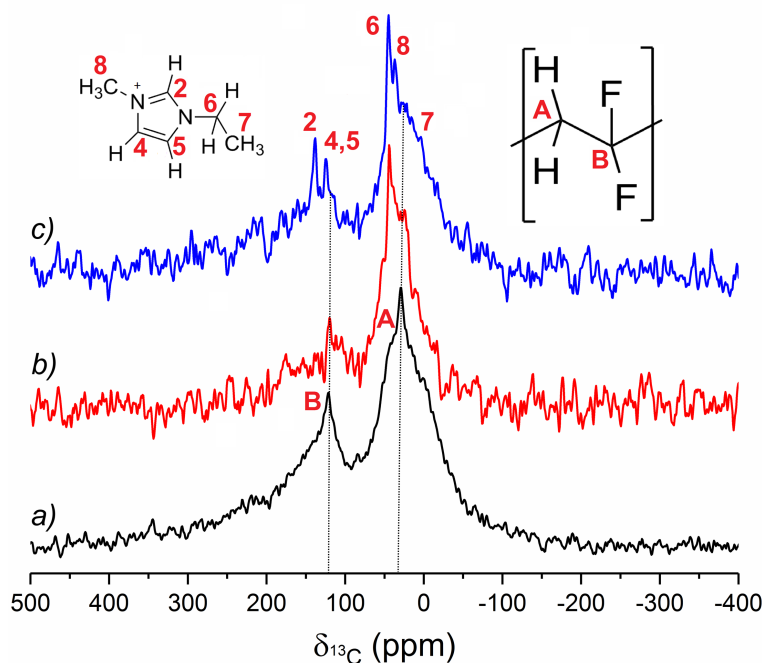
Figure 5.37: Static ^{13}C–CP spectra of a) PVdF-HFP, b) polymer electrolyte before MAS and c) small pieces of the polymer electrolyte after MAS.

However, the observed difference in chemical shift upon rotation is c. 1.5 ppm which exaggerates the motional averaged CSA. Hence, it is possible to exclude CSA to be responsible for the observable line shift. Additional information about calculations of the chemical shielding tensors C2, C4 and C5 are given in the appendix.

Further, ^{13}C–CP spectra were employed and shown in Figure 5.37 to estimate the amount of rigid (crystalline) fractions for the three samples. This is because CP suppresses mobile components, while only ^1H–^{13}C sites with a residual dipolar coupling are predominantly excited. Therefore, the relative amount of crystalline fractions can be estimated. The neat PVdF-HFP film in Figure 5.16 a) displays a typical ^{13}C spectrum found for a semi-crystalline polymer, which is composed of a superposition of narrow and broad peaks. As reported in literature, the main contributions arise from the methylene carbon sites (A) at 28.5 ppm and the CF_2 carbon sites (B) at 120.8 ppm (both from the PVdF unit).[16] Signals of the HFP-unit on the other hand are unresolved by CP. Clearly, the spectrum of the polymer electrolyte before MAS in b) exhibits a notable signal reduction compared to the PVdF-HFP spectrum in a). This indicates a reduction in the crystalline fraction, which is consistent with findings from XRD and DSC as further discussed. For the polymer electrolyte after MAS in c), all [EMIM]$^+$ signals can be found. These signals are also present for the neat polymer electrolyte, thus having a

lower S/N ratio. Overall, a slight increase in signal intensity may be noted from b) to c) which would be in agreement with the formation of a crystalline phase under MAS.

Furthermore, we tried to follow possible morphological changes of the polymer electrolyte spun under MAS, by means of scanning electron microscopy (SEM). In particular top-view (along z_S-axis) and side-view (along y_S-axis) SEM images were employed and shown in Figure 5.38 to trace back the effect of MAS. Additional SEM images of the neat PVdF-HFP film are given in the appendix. To begin with the unspun polymer electrolyte in a) and b), it can be seen that a rather smooth surface topology is present. Furthermore, an absence of large pores can be noted, while few pores (marked in green) with a pore diameter of 1 µm can be found. Nevertheless, this is a surface topology which is expected for a low evaporation rate. Obviously, the outer and inner topology of the polymer electrolyte spun under MAS appears significantly different compared to the neat polymer electrolyte. The top view presented in Figure 5.38 c) shows an imprinted structure with stripe-like pattern. This feature is obviously absent for the neat polymer electrolyte film.
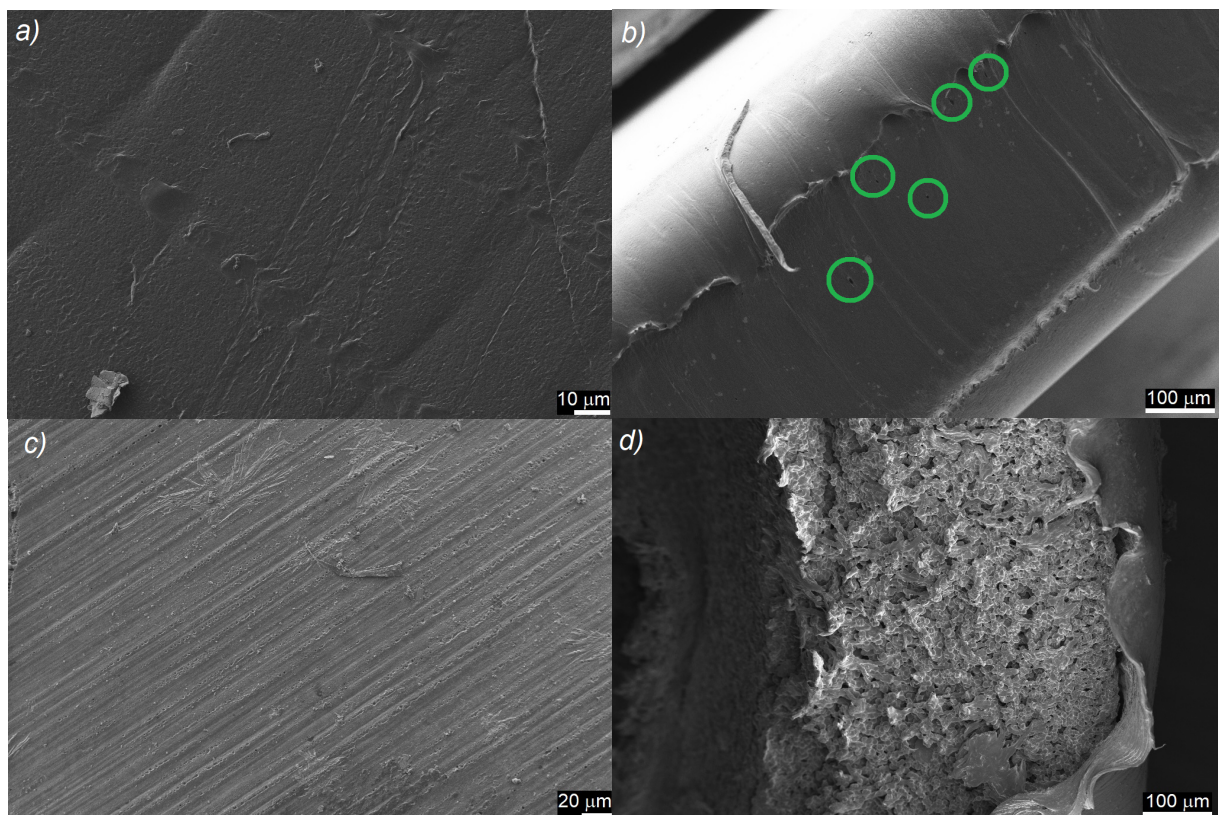

Figure 5.38: SEM images Polymer electrolyte before MAS top view (along z_S) in a) and side view (along y_S) in b) and polymer electrolyte after MAS top view c) side view d). In order to obtain side-view SEM images, the samples were cut with a scissor inside an Ar-glovebox. Pores are marked with green circles.

One explanation for this finding is that the individual pieces of c. 1x1 mm² fused to a compact film, where the outer surface is fused into the notches of the inner rotor walls. Therefore, we have acquired SEM images of the inner rotor wall and indeed found notches which fit to the found topology at the polymer electrolyte spun under MAS. SEM micrographs of the inner rotor wall are added to the appendix. As a result, the inner rotor walls act as a template for the polymer electrolyte. The corresponding side-view image (along the y_S-axis) is shown in d). The inner structure seems to be composed of a complex three-dimensional grain-like structure. One explanation for this structure is that the polymer electrolyte partially melts at 40 °C, while during cooling a rearrangement occurs to the sample, yielding the observed structure.

In order to gain a deeper insight into the crystallinity of the three samples, XRD and DSC measurements were employed. Regarding XRD, numerous experiments were carried out for neat PVdF and PVdF-HFP and for polymer electrolytes based on these polymers.[18, 19, 20] For neat PVdF five crystalline polymorphs are reported so far, namely α, β, γ ,δ and ε.[21] The powder X-ray diffractograms of the three samples are shown in Figure 5.39. The diffractogram of the neat PVdF-HFP film in a) exhibits diffraction peaks at 2θ values of 18.4° ([0 2 0]), 39.4° ([0 0 2]) which are assigned to α signals and 20.2° ([1 0 1]), 26.8° ([0 2 2]) which can be assigned to γ signals.[18−21]
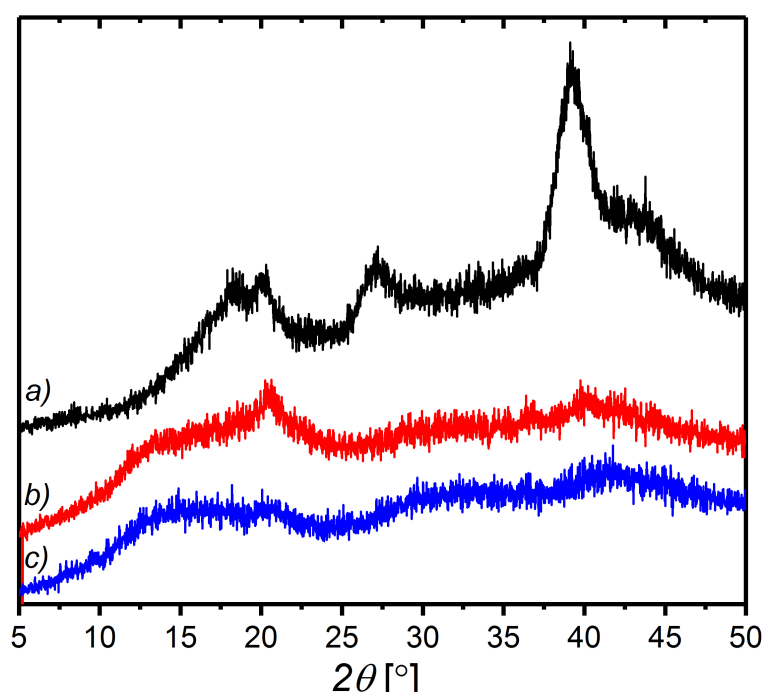

Figure 5.39: Powder XRD patterns of PVdF-HFP polymer film in a), the polymer electrolyte film before MAS in b) and after MAS in c).

Notably, the addition of the electrolyte solution to the polymer reduces the amount of crystalline phases clearly, which is in accordance to literature.[23] XRD pattern of the polymer electrolyte after MAS are basically absent, since only the background signal of the sample holder can be observed here. In particular for the polymer electrolyte spun under MAS, the size of the sample holder is exceeding the size of the sample. Therefore, these unfavorable measurement conditions make it impossible to distinguish between the pristine polymer electrolyte and the polymer electrolyte after MAS.

However, further results can be obtained in case of differential scanning calorimetry (DSC). The DSC thermograms in the temperature range from −55 °C to 160 °C of the first two heating cycles are presented in Figure 5.40. The neat PVdF-HFP film displays two broad endothermic signals. These two signals have their maxima around 52 °C and 144 °C and a shoulder at c. 130 °C. In literature, the signal at 52 °C is assigned to a reorientation of α crystals.[22] The signal region at 144 °C is assigned to the melting point of α and γ crystals. The glass transition temperature is found at −34 °C and is in particular well-resolved for the cooling curves, which are shown in the appendix. Clearly, the addition of the electrolyte solution decreases the area of the endothermic peaks compared to the bare PVdF-HFP film. Furthermore, a change in the peak position can be found for both endothermic signals. Obviously, a depression of the melting temperature occurs, which shifts the peak from 144 °C for bare PVdF-HFP to 115.8 °C for the polymer electrolyte. The second endothermic signal, which can be found at 52 °C for bare PVdF-HFP, is found at 54 °C for the polymer electrolyte. Besides that, the glass transition temperature shifts from −33 °C for bare PVdF-HFP to −36 °C for the polymer electrolyte as seen in particular for the cooling curves in the appendix.
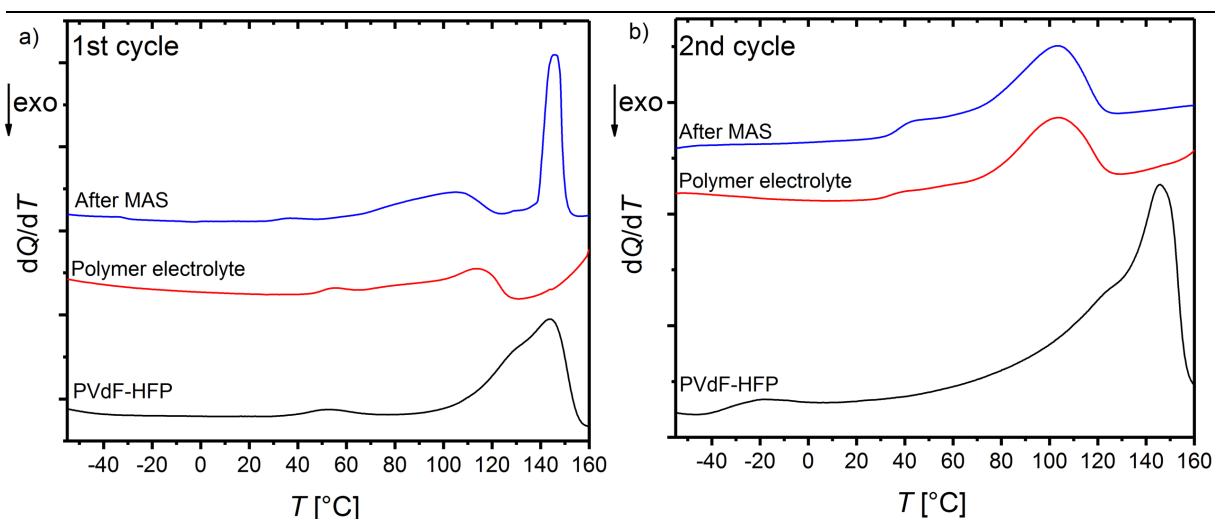

Figure 5.40: DSC thermograms for the PVdF-HFP film, the polymer electrolyte and the polymer electrolyte after MAS. The first two heating cycles are shown.

In addition, the glass transition temperature for the polymer electrolyte spun under MAS is fond at −33.4 °C. This endothermic signal that was previously found at 52 °C and 54 °C for PVdF-HFP and the polymer electrolyte respectively, is now found at 35 °C for the polymer electrolyte spun under MAS. It can readily be noted, that the DSC thermograms of the polymer electrolyte and the polymer electrolyte after MAS appear similar up to 125 °C, while above this an additional endothermic signal can be found at 146.3 °C. Clearly, this endothermic peak is absent for the pristine polymer electrolyte, but present for the polymer electrolyte spun under MAS. The FWHM of this signal (∼6 °C) is rather narrow compared to the other signals found, which suggests that this is a rather well-defined crystalline phase. The second heating cycle reveals that this crystalline phase must have been generated under MAS, because it is not retained for the second heating cycle. Therefore, this phase does not form spontaneously from melt but must have been induced by MAS. As a result, MAS is able to induce a crystalline phase in the polymer electrolyte, which degrades once the melting point is reached. Overall, this observation is in good agreement with reports by Messinger and co-workers, which indicate that heating the polymer electrolyte after MAS, leads to a lineshape almost resembling the one of the pristine polymer electrolyte.[4]

So far, the findings indicate that similar to the PEO/LiTFSI system, a well-ordered crystalline polymer phase could be obtained. It is of special interest to clarify whether this effect is substantially consistent with the stretching experiments performed by Golodnitsky. Therefore, impedance spectroscopy is employed to obtain information about the influence of MAS on the transport properties of the polymer electrolyte.[24, 25, 26] The electrochemical response of the sample is reduced to a capacitor with an area A and the sample thickness t. Properties which are relevant for the later discussion are impedance Z^*, permittivity ε^* and the AC-conductivity σ^* which are defined as:

$$C_0 = \varepsilon_0 \frac{A}{t} \tag{5.4}$$

$$\varepsilon^* = \varepsilon' - i\varepsilon'' \tag{5.5}$$

$$Z^* = Z' + iZ'' = \frac{1}{i\omega C_0 \varepsilon^*} \tag{5.6}$$

$$\varepsilon' = -\frac{Z''}{\omega C_0 (Z'^2 + Z''^2)} \tag{5.7}$$

$$\varepsilon'' = \frac{Z'}{\omega C_0 \left(Z'^2 + Z''^2\right)} \qquad \text{[5.8]}$$

$$\sigma' = \omega \, \varepsilon_0 \, \varepsilon'' \qquad \text{[5.9]}$$

$$\sigma'' = \omega \, \varepsilon_0 \, \varepsilon' \qquad \text{[5.10]}$$

X' and X'' denote the real and imaginary parts, respectively, of a complex function X^* (note the different sign conventions for ε^* and Z^*, C_0 is the vacuum capacitance, $\varepsilon_0 = 8.85 \cdot 10^{-12}$ F/m is the permittivity of free space, $\omega = 2\pi f$ is the angular frequency, and f is the frequency of the applied field.[27, 28]

Nyquist plots for the pristine polymer electrolyte and the polymer electrolyte spun under MAS are shown in the appendix. Typically, two semi-circles should be seen, one at high frequencies which can be correlated to the electrolyte resistance and one at lower frequencies which is assigned to electrolyte electrode interphase dynamics. However, clear semi-circles at high frequencies are only visible at –40 °C. We find that the high-frequency semicircle cannot be resolved properly due to resolution limitations of the instrument, which is assigned to a low electrolyte resistance as reported in literature.[29]

Therefore, frequency dependent ion conductivities were measured and shown in Figure 5.41. The precise conductivities at different characteristic frequencies are presented in the appendix. The plots shown in Figure 5.41 clearly exhibit two distinct regions.
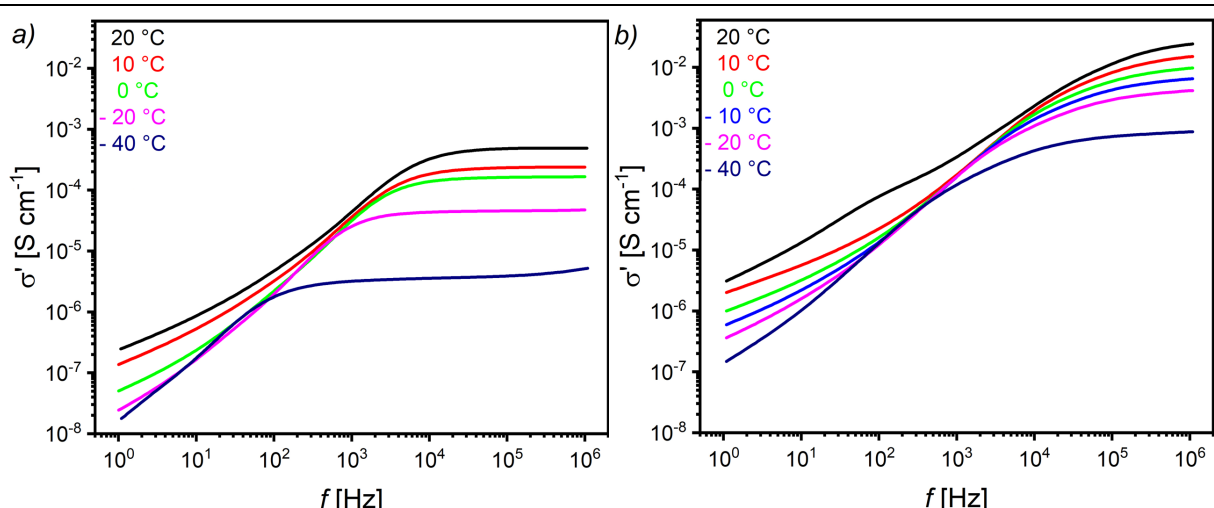

Figure 5.41: Frequency dependent conductivity of the pristine polymer electrolyte in a) and the polymer electrolyte spun under MAS in b).

Firstly, all curves in 5.41 exhibit a plateau, which is assigned to the materials DC conductivity, while the initial tail at low frequencies is originating from electrode polarization. Clearly, the polymer electrolyte spun under MAS shows a higher conductivity compared to the pristine polymer electrolyte. A possible explanation for this finding can be derived from observations made by Golodnitsky.[8–10] Under MAS, the individual pieces of c. 1x1 mm^2 fused together to a continuous membrane, while these pieces experience the centripetal force. This force mimics the stretching force in the Golodnitsky reports, creating a high conductive crystalline polymer phase. Furthermore, an additional hump can be found for the 20 °C curve in Figure 5.41 b), which is even more pronounced for the frequency-dependent permittivity data in Figure 5.42 b). The decrease in permittivity at low frequencies is due to the electrode polarization, while the high frequency is dominated by charge carrier accumulation and relaxation peaks. An additional relaxation peak is found for the 20 °C curve in Figure 5.42 b). In turn, this signal must result from an additional relaxation process, as possibly present for ions in the induced crystalline phase. In general, the relaxation peaks shift towards higher frequencies while increasing temperature. From the position of the maximum, so-called Cole-Cole plots (imaginary part vs. real part of the permittivity) are determined which provide the relaxation times τ.[30, 31] Based on the ion relaxation times, the activation energies can be calculated according to the Vogel-Tamman-Fulcher (VTF) equation:

$$\tau = \tau_0 T^{-1/2} \exp\left(-\frac{E_\tau}{k_B(T - T_0)}\right) \qquad [5.11]$$

with temperature T, testing temperature T_0 which corresponds to T_g– 50 K (T_g is used from DSC data), a pre-exponential factor τ_0 and the Boltzmann constant is k_B.
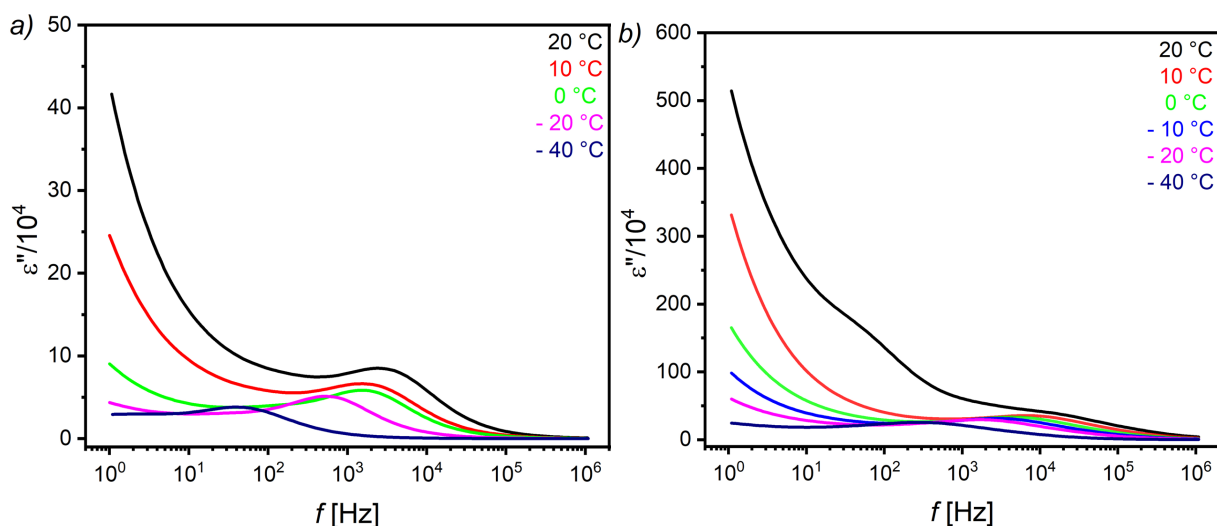

Figure 5.42: Frequency dependent imaginary part of the permittivity for the polymer electrolyte in a) and for the polymer electrolyte after MAS in b).
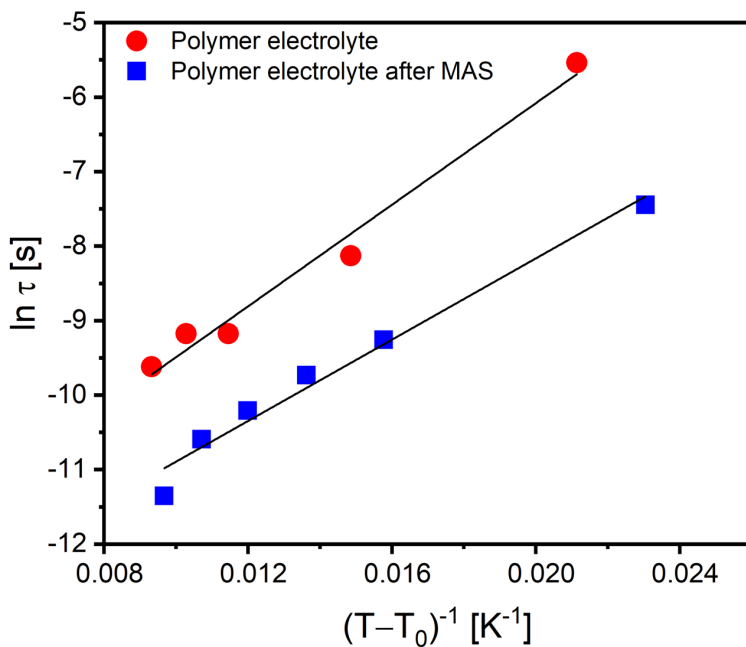
Figure 5.43: VTF plots for the pristine polymer electrolyte and for the polymer electrolyte spun under MAS. The black lines denote linear fits.

Classical Arrhenius activities are present in case of neat liquid electrolytes. On the other hand, for ionic liquids and in particular for polymer electrolytes where ion motions are correlated to segmental motions of the polymer chains, the VTF model is more accurate due to correlated motions.[32, 33] The corresponding VTF plot for the polymer electrolyte and the polymer electrolyte spun under MAS is shown in Figure 5.43. An almost linear relationship between $(T - T_0)^{-1}$ and $\ln(\tau)$ can be found. Furthermore, activation energies of 0.028 eV and 0.022 eV are found for the polymer electrolyte and the polymer electrolyte spun under MAS (fitting error ± 0.002 eV). The calculated activation energies are in perfect agreement with activation energies presented by Romero for a PVdF-HFP-based polymer electrolyte, ranging from 0.02 eV up to 0.03 eV.[34] Even though, the system studied in this work exhibits other types of ions compared the report by Romero, we find almost identical activation energies. This finding suggests, that the activation energies depend strongly on the used polymer.

To summarize, in this work we investigated the influence of magic-angle-spinning (MAS) on a PVdF-HFP-based polymer electrolyte and find that upon spinning, the individual pieces of c. 1x1 mm² fuse together and form a continues hollow cylinder. The fusion occurs at high pressures of 0.0166 MPa at 7 kHz MAS. Furthermore, we were able to show by means of DSC that a crystalline polymer phase is induced by MAS. Similar to findings by Messinger, we observe ^{7}Li NMR line distortions and deviations which are explained by the anisotropic bulk magnetic susceptibility arising from sample shape and ordered polymer domains. Overall, we

have identified similarities between polymer electrolytes which have been stretched previously and polymer electrolytes spun under MAS, since both samples exhibit a tremendous increase in ion conductivity. Therefore, MAS and sample stretching can be used as general tools to increase the ion conductivity.

5.5.4 References

(1) Paul, P. P., McShane, E. J., Colclasure, A. M., Balsara, N., Brown, D. E., Cao, C., ... & Nelson Weker, J. (2021). A Review of Existing and Emerging Methods for Lithium Detection and Characterization in Li-Ion and Li-Metal Batteries. *Advanced Energy Materials*, *11*(17), 2100372.

(2) Stephan, A. M. (2006). Review on gel polymer electrolytes for lithium batteries. *European polymer journal*, *42*(1), 21-42.

(3) Zhu, X., Wang, K., Xu, Y., Zhang, G., Li, S., Li, C., ... & Ma, Y. (2021). Strategies to Boost Ionic Conductivity and Interface Compatibility of Inorganic-Organic Solid Composite Electrolytes. *Energy Storage Materials*.

(4) Messinger, R. J., Vu Huynh, T., Bouchet, R., Sarou-Kanian, V., & Deschamps, M. (2020). Magic-angle-spinning-induced local ordering in polymer electrolytes and its effects on solid-state diffusion and relaxation NMR measurements. *Magnetic Resonance in Chemistry*, *58*(11), 1118-1129.

(5) Kimura, H., Dohi, H., Kotani, M., Matsunaga, T., Yamauchi, K., Kaji, H., ... & Asakura, T. (2010). Molecular dynamics and orientation of stretched rubber by solid-state 13 C NMR. *Polymer journal*, *42*(1), 25-30.

(6) Kitamura, M., Hata, Y., Yasuoka, H., Kurotsu, T., & Asano, A. (2012). Strain-induced 13 C chemical shift change of natural rubber. *Polymer journal*, *44*(8), 778-785.

(7) Kawamura, I., Degawa, Y., Yamaguchi, S., Nishimura, K., Tuzi, S., Saitô, H., & Naito, A. (2007). Pressure-induced Isomerization of Retinal on Bacteriorhodopsin as Disclosed by Fast Magic Angle Spinning NMR. *Photochemistry and photobiology*, *83*(2), 346-350.

(8) Golodnitsky, D., Livshits, E., Rosenberg, Y., Peled, E., Chung, S. H., Wang, Y., ... & Greenbaum, S. G. (2000). A new approach to the understanding of ion transport in semicrystalline polymer electrolytes. *Journal of Electroanalytical Chemistry*, *491*(1-2), 203-210.

(9) Golodnitsky, D., Livshits, E., Ulus, A., Barkay, Z., Lapides, I., Peled, E., ... & Greenbaum, S. (2001). Fast ion transport phenomena in oriented semicrystalline LiI– P (EO) n-based polymer electrolytes. *The Journal of Physical Chemistry A*, *105*(44), 10098-10106.

(10) Golodnitsky, D., Livshits, E., Kovarsky, R., Peled, E., Chung, S. H., Suarez, S., & Greenbaum, S. G. (2004). New generation of ordered polymer electrolytes for lithium batteries. *Electrochemical and Solid State Letters*, *7*(11), A412.

(11) Lin, W., Bian, M., Yang, G., & Chen, Q. (2004). Strain-induced crystallization of natural rubber as studied by high-resolution solid-state 13C NMR spectroscopy. *Polymer*, *45*(14), 4939-4943.

(12) VanderHart, D. L. (2007). Magnetic susceptibility and high resolution NMR of liquids and solids. *eMagRes*.

(13) Golodnitsky, D., Strauss, E., Peled, E., & Greenbaum, S. (2015). On order and disorder in polymer electrolytes. *Journal of The Electrochemical Society*, *162*(14), A2551.

(14) Jelinski, L. W. (1986). Deuterium NMR of solid polymers. *VCH Verlagsgesellschaft, High Resolution NMR Spectroscopy of Synthetic Polymers in Bulk,* 335-364.

(15) Higgs, T. P., & MacKay, A. L. (1977). Determination of the complete order parameter tensor for a lipid methylene group from 1H-and 2H-NMR spin labels. *Chemistry and Physics of Lipids*, *20*(2), 105-114.

(16) Hucher, C., Beaume, F., Eustache, R. P., & Tekely, P. (2005). Probing phase structure and location of reverse units in poly (vinylidene fluoride) by solid-state NMR. *Macromolecules*, *38*(5), 1789-1796.

(17) Li, M., Katsouras, I., Piliego, C., Glasser, G., Lieberwirth, I., Blom, P. W., & de Leeuw, D. M. (2013). Controlling the microstructure of poly (vinylidene-fluoride)(PVDF) thin films for microelectronics. *Journal of Materials Chemistry C*, *1*(46), 7695-7702.

(18) Martins, P., Lopes, A. C., & Lanceros-Mendez, S. (2014). Electroactive phases of poly (vinylidene fluoride): Determination, processing and applications. *Progress in polymer science*, *39*(4), 683-706.

(19) Ruan, L., Yao, X., Chang, Y., Zhou, L., Qin, G., & Zhang, X. (2018). Properties and applications of the β phase poly (vinylidene fluoride). *Polymers*, *10*(3), 228.

(20) Lee, S. (2011). Crystal structure and thermal properties of poly (vinylidene fluoridehexafluoropropylene) films prepared by various processing conditions. *Fibers and Polymers*, *12*(8), 1030-1036.

(21) Cai, X., Lei, T., Sun, D., & Lin, L. (2017). A critical analysis of the α, β and γ phases in poly (vinylidene fluoride) using FTIR. *RSC advances*, *7*(25), 15382-15389.

(22) Merlini, C., Barra, G. M. O., Araujo, T. M., & Pegoretti, A. (2014). Electrically pressure sensitive poly (vinylidene fluoride)/polypyrrole electrospun mats. *Rsc Advances*, *4*(30), 15749-15758.

(23) Abbrent, S., Plestil, J., Hlavata, D., Lindgren, J., Tegenfeldt, J., & Wendsjö, Å. (2001). Crystallinity and morphology of PVdF–HFP-based gel electrolytes. *Polymer*, *42*(4), 1407-1416.

(24) Stavrinidou, E., Sessolo, M., Winther-Jensen, B., Sanaur, S., & Malliaras, G. G. (2014). A physical interpretation of impedance at conducting polymer/electrolyte junctions. *AIP Advances*, *4*(1), 017127.

(25) Chan, C. H., & Kammer, H. W. (2017). Impedance spectra of polymer electrolytes. *Ionics*, *23*(9), 2327-2337.

(26) Sharon, D., Bennington, P., Liu, C., Kambe, Y., Dong, B. X., Burnett, V. F., ... & Nealey, P. F. (2018). Interrogation of electrochemical properties of polymer electrolyte thin films with interdigitated electrodes. *Journal of The Electrochemical Society*, *165*(16), H1028.

(27) Careem, M. A., Noor, I. S. M., & Arof, A. K. (2020). Impedance Spectroscopy in Polymer Electrolyte Characterization. *Polymer Electrolytes: Characterization Techniques and Energy Applications*, 23-64.

(28) Schönhals, A. (2003). Molecular dynamics in polymer model systems. In *Broadband dielectric spectroscopy* (pp. 225-293). Springer, Berlin, Heidelberg.

(29) Yuan, C., Zhu, X., Su, L., Yang, D., Wang, Y., Yang, K., & Cheng, X. (2015). Preparation and characterization of a novel ionic conducting foam-type polymeric gel based on polymer PVdF-HFP and ionic liquid [EMIM][TFSI]. *Colloid and Polymer Science*, *293*(7), 1945-1952.

(30) M Hadi, J., B Aziz, S., M Nofal, M., Hussein, S. A., Hafiz, M. H., Brza, M. A., ... & Woo, H. J. (2020). Electrical, dielectric property and electrochemical performances of plasticized silver ion-conducting chitosan-based polymer nanocomposites. *Membranes*, *10*(7), 151.

(31) Javid Iqbal, M., Nadeem, M., & Hassan, M. M. (2013). Low temperature AC electrical study of Pr0. 5− xLaxCa0. 5MnO3 (x= 0.0–0.4) ceramics by employing impedance spectroscopy. *Journal of Applied Physics*, *114*(11), 113708.

(32) Aziz, S. B., Woo, T. J., Kadir, M. F. Z., & Ahmed, H. M. (2018). A conceptual review on polymer electrolytes and ion transport models. *Journal of Science: Advanced Materials and Devices*, *3*(1), 1-17.

(33) Guisao, J. P. T., & Romero, A. J. F. (2015). Interaction between Zn2+ cations and n-methyl-2-pyrrolidone in ionic liquid-based Gel Polymer Electrolytes for Zn batteries. *Electrochimica Acta*, *176*, 1447-1453.

(34) Tafur, J. P., & Romero, A. J. F. (2014). Electrical and spectroscopic characterization of PVdF-HFP and TFSI—ionic liquids-based gel polymer electrolyte membranes. Influence of ZnTf2 salt. *Journal of Membrane Science*, *469*, 499-506.

Chapter 6

Porous Carbonaceous Materials

Scope

In Chapter 6 three substantially different carbonaceous materials are scrutinized. The outcome of pyrolysis for two different saccharide-derived hydrochars is followed by means of ^{13}C NMR spectroscopy in Section 6.1. During pyrolysis a lateral sheet growth of aromatic domains is found to occur. The structure of the two carbonized saccharide-derived hydrochars is highly similar, whereas the macroscopic structure differs substantially. The structure of polymeric (C_3O_2) (carbonsuboxide) is explored in Section 6.2. This heteroatom containing polymeric carbon is found to exhibit unique bonding environments. By post carbonization, this material is transformed into a highly aromatic material, similar to the saccharide-derived hydrochars. In the last section (6.3), the interaction of water with the nitrogen containing carbon C_1N_1 and all carbonaceous materials studied in this work is investigated. Unlike for materials (almost) entirely composed of carbon, the pore walls of C_1N_1 are expected to be polar and therefore strongly interact with H_2O. For the carbonized materials studied in Sections 6.1 and 6.2, water molecules are able to enter the pores of these materials, whereas a notable entry of water in the polar pores of C_1N_1 is not observed. Based on this surprising finding, a water repelling character is attributed to C_1N_1.

6.1 Pyrolysis of Saccharide-Derived Hydrochars
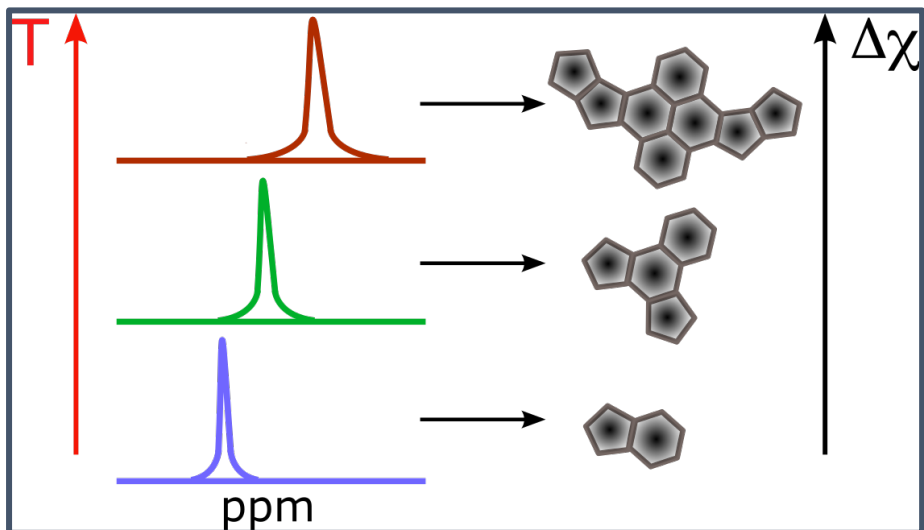
6.1.1 Hard Carbon Spheres

One of the most abundant and renewable precursor materials for the preparation of hard carbon spheres is sucrose, which can be found in numerous plants. Other saccharides, such as glucose, fructose, starch and other organic precursor materials are also commonly used to prepare hard carbon spheres.[1,2,3] After hydrothermal treatment of the saccharide precursor at circa 150–180 °C monodisperse spherical particles are produced in most cases.[4,5] In order to obtain graphite-like structures, into which lithium or sodium ions can be intercalated, a post carbonization is carried out under inert atmosphere.[6,7,8]

There are several studies on sucrose-derived hard carbon spheres. For example, Wang and co-workers studied the porosity and electrochemical discharge capacities for sucrose-derived hard carbon spheres, which were obtained exclusively at temperatures of 1000 °C and above.[9,10] However, as this example and many other literature reports show, the pyrolysis process itself is still only little understood and mostly a "black box". Differences in the outcome of the pyrolysis between different precursor materials is another aspect which remains poorly understood.

The temperature dependent pyrolysis of two different saccharides using ^{1}H and ^{13}C NMR spectroscopy is studied in the following section. For this purpose, sucrose-derived hydrochars were post-carbonized at various temperatures, and afterwards the chemical and morphological transitions of the products were investigated by NMR spectroscopy. In addition, sucrose-derived hydrochars were compared to trehalose-derived hydrochars (both carbonized at 1000 °C), in order to evaluate the influence of the precursor on the carbonized material.

The natural disaccharides sucrose and trehalose occur in numerous plants, fungi and animals and are therefore easy to access.[11] Sucrose is composed of a glucose monomer connected to a fructose monomer via a α,β-1,2-glycosidic linkage, shown in Figure 6.1 a). The popularity of trehalose is rooted in its high chemical stability, of the stronger α,α-1,1-glycosidic linkage between two glucose monomers, as shown in Figure 6.1 b). Hence, trehalose is more heat-stable compared to other sugars, more resistant against hydrolysis and stable in a large pH window.[12] Keeping these properties in mind is useful to evaluate the results of hydrothermal treatment, as well as carbonization.
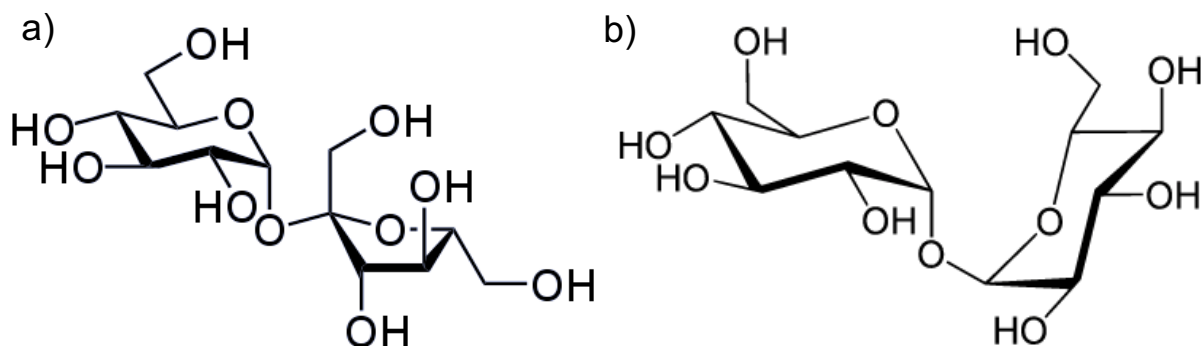
Figure 6.1: Molecular structures of sucrose a) and of trehalose b).

6.1.2 Experimental Details

Samples were provided by Dr. Martin Wortmann (Bielefeld University, Department of Physics). Experimental details for the sample preparation have been reported in the literature.[5, 13] Sucrose and trehalose were hydrothermally carbonized in a 0.5 M aqueous solution for 24 h in an autoclave at 150 °C (sucrose) and at 180 °C (trehalose). Sucrose-derived hydrochar was post carbonized at temperatures of 400 °C, 550 °C, 700 °C, 850 °C and 1000 °C under inert nitrogen gas flow (purity > 99.999 %). A constant heat rate of 10 K/min and a constant gas flow of 150 mL/min was chosen for all samples. Trehalose-derived hydrochar was post carbonized at 1000 °C. ^{13}C MAS time-domain data were obtained by the use of direct excitation (DE) or cross polarization (CP) from ^{1}H with a contact time of 2 ms and with ^{1}H decoupling. CP excitation curves for contact times between 10 μs and 8 ms are shown in the appendix (Section A.7). For ^{13}C NMR measurements a spectral width of ± 100 kHz, a pulse duration of 3.5 μs, 8192 time-domain data points, a recycling delay of 3 s for CP and 5 s for DE and typically 4096 scans were used. An exponential apodization corresponding to a line width of 100 Hz was applied to the ^{13}C time-domain data to smoothen the spectra. ^{13}C spectra were externally referenced to the methine carbon signal of adamantane at 29.5 ppm.

6.1.3 Relationship Between Pyrolysis and Structure

Changes in composition after post-carbonization at different temperatures can be followed by means of ^{13}C NMR spectroscopy for sucrose-derived hydrochars. Two types of ^{13}C spectra are presented in Figure 6.2, namely DE and CP spectra. If a large number of ^{1}H dipolarly coupled to ^{13}C are present in the sample, CP is the method of choice due to the increase in signal intensity. DE on the other hand, excites all ^{13}C nuclei in the same way and is used to probe the chemical environment of all ^{13}C nuclei.
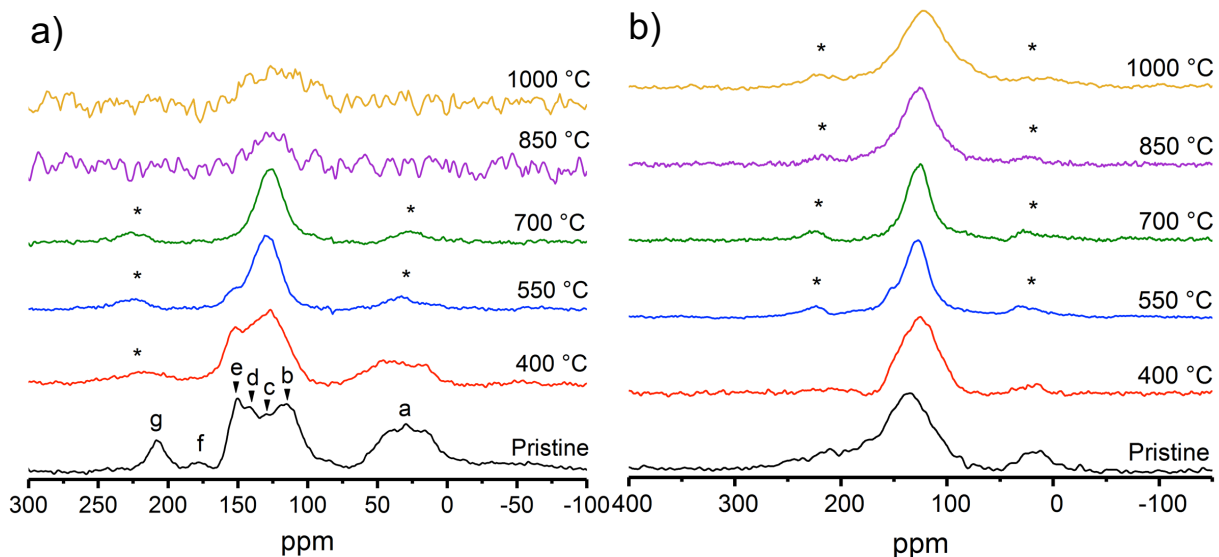
Figure 6.2: ^{13}C 7 kHz MAS spectra of sucrose-derived hydrochars at different post-carbonization temperatures. a) measured under CP and b) DE. The pristine sample is hydrothermally treated (150°C) sucrose. Spinning sidebands are denoted with asterisks. Peak positions are given in the appendix (A.7).

In order to obtain more information about the ^{13}C signals, CP spectra were acquired in addition to DE spectra. CP spectra can give indirect information about the mobility of a given ^{13}C site and the presence or absence of dipolarly coupled ^{1}H nuclei can be derived. Signal intensities in CP spectra depend strongly on the chosen contact time and on $T_{1\rho}$. One common issue with DE spectra are long longitudinal relaxation times T_{1}, especially of rigid ^{13}C sites. Therefore, partially relaxed spectra are obtained (for insufficient recycling delays), from which no quantitative intensity ratios are obtained. This problem can be solved by employing long relaxation delays ($5 \cdot T_{1}$).
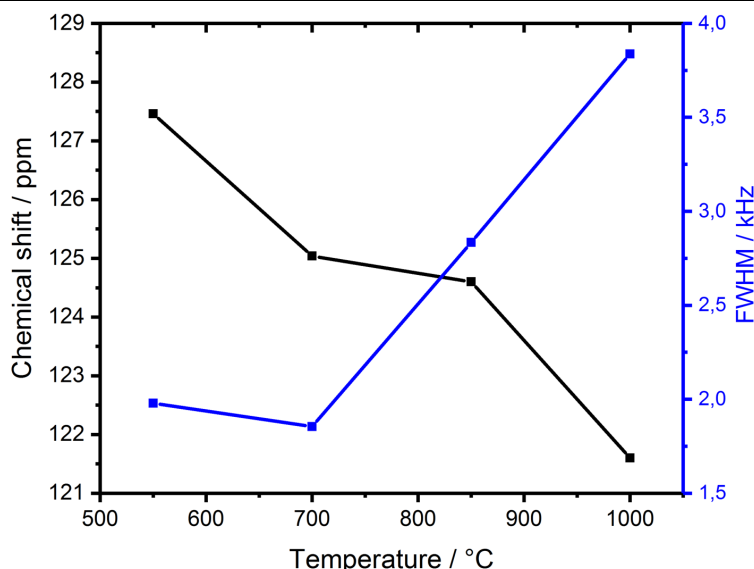

Figure 6.3: Variation of the ^{13}C DE-MAS chemical shift (center of the largest signal) and FWHM as a function of post-carbonization temperature.

The longitudinal relaxation time in the rotating frame $T_{1\rho}$, as well as the optimum in contact time largely differs for different ^{13}C sites. The optimum in contact time differs for the ^{13}C signals in Figure 6.2, as shown in Figure A.26 in the appendix. Therefore, no quantitative intensity ratios can be derived from CP spectra. DE spectra with a good S/N ratio and CP spectra with a bad S/N ratio were shown by Buntkowsky and co-workers for carbonized materials, in which case the absence of a reasonable signal is interpreted as a low abundance of ^{1}H nuclei in the structure.[14] The pristine spectrum shown in Figure 6.2 a) is in a good agreement with spectra of sucrose and glucose-derived hydrochars reported in the literature.[15, 16, 17] The pristine sample in Figure 6.2 is hydrothermally carbonized (150 °C) sucrose.

Paine and co-workers carried out a detailed study on the pyrolysis of glucose and glucose/fructose in air and followed their chemical transition. They showed that transient hydroxymethylfurfural species occur during pyrolysis, which is also expected to be the relevant intermediate species for hydrothermally treated sucrose.[18] Baccile and co-workers have carried out a detailed NMR study on the hydrothermal carbonization of glucose and assigned all relevant signals in their work.[17] The signal assignment serves as the basis for the signal assignment in Figure 6.2 a) and in Table A.6 and A.7 in the appendix.

Three groups of signals can be identified: (i) The group of signals in the aliphatic region (a) which can be found below 70 ppm with a maximum at 29.5 ppm. This set of signals corresponds to mobile and rigid sp^3-carbon sites, typically found for CH_3, CH_2 and CH groups. (ii) Signals found in the region from 100–160 ppm correspond to different sp^2-carbon sites. According to Baccile, the signal at 114.5 ppm (b) corresponds to carbon sites in the β-position of furan rings. Furthermore, signals at 141.2 ppm (d) and 150.1 ppm (e) originate from the α-positions (2 and 5) of the furan rings. In addition, the peak at 129.9 ppm (c) is characteristic for graphene-like carbon sites, which are present in small quantities. (iii) Two further peaks belong to the last set of signals found above 160 ppm. The signal at 177.7 ppm (f) is related to aldehyde groups, while the more intense signal at 208.4 ppm (8) originates from ketone groups.

Due to the high similarity between the pristine spectrum shown in Figure 6.2 a) and the results presented by Baccile, a similar structure between sucrose- and glucose-derived hydrochars can be assumed. Therefore, the most probable structure for the glucose-derived product as well as for the sucrose-derived hydrochar is a complex network of randomly connected furan rings which results from transient hydroxymethylfurfural species. Taking into account the low

intensity of the graphite-like signals (c), these groups appear only as byproducts during hydrothermal carbonization at the rather low temperature of 150 °C. Comparing the DE spectrum (Figure 6.2 b)) of the pristine material with the CP spectrum, it is evident that the direct polarized spectrum is composed entirely of a broad signal in the region (ii), which means that CP indeed enhances the signal intensity.

After incipient pyrolysis at mild temperatures of 400 °C, it can readily be noted that there are strong similarities in the region between 100–160 ppm of the ^{13}C CP NMR spectrum compared to the ^{13}C CP spectrum of the pristine material. Changes that occurred upon heating to 400 °C are evident in the signal reduction of the aliphatic carbon sites and in the absence of carbonyl signals.

The DE spectrum is dominated by a broad signal around 129.9 ppm which results from sp^2-carbon sites with a large chemical shift anisotropy (CSA). The large CSA causes a severe broadening of the static linewidth, which is the reason why two spinning sidebands (denoted by asterisks) become visible under magic-angle-spinning.

Increasing the post-carbonization temperature up to 550 °C causes a signal narrowing for the CP and DE spectrum, due to the fact that a smaller variety of sp^2-carbon sites remain. Increasing the post-carbonization temperature even further (700 °C) leads to a disappearance of all signals except one signal at 125 ppm. At 700 °C a cross polarization spectrum can still be acquired which means that a notable amount of ^{1}H is present in the sample. The gradual changes are in agreement with a transition from a furane-dominated structure towards a graphite-like structure. Similar changes can also be found in the DE ^{13}C spectrum, in which also only one signal at 125 ppm can be found.

Additional changes can be found above 700 °C. Clearly, the CP intensity is lost for samples treated at 850 °C and 1000 °C, whereas the DE spectra exhibit a continuous broadening. The signal broadening as a function of post-carbonization temperature is shown in Figure 6.3. DE spectra of similar width as those presented in Figure 6.2 are found for carbon nanotubes and graphene.[19, 20] Therefore, it seems likely that a further graphitization occurs at these elevated temperatures. At temperatures up to 700 °C functional groups such as aliphatic groups and carbonyl groups combust predominantly, while above 700 °C structural hydrogen is lost leading to an aromatic sheet growth.

Furthermore, in the case of high post-carbonization temperatures above 700 °C the line-broadening is accompanied with an up-field shift of the signal towards lower ppm values. The chemical shift, as well as signal width as a function of post-carbonization temperature is shown in Figure 6.3. One interpretation for the signal shift towards lower ppm values at increasing post-carbonization temperatures is the increasing anisotropy of the magnetic susceptibility for larger extended aromatic structures. The latter is in line by XRD results, shown elsewhere.[5] Vanderhart discussed the influence of the magnetic susceptibility on chemical shift.[21] He points out that anisotropy in the magnetic susceptibility may be understood as an additional field, acting at the site of the nucleus. Therefore equation 3.1 (in Chapter 3) is modified:

$$\omega_0 = -\gamma \mathbf{B_0} + \mathbf{B_S} \qquad\qquad [6.1]$$

with the demagnetizing field $\mathbf{B_S} = \alpha\,\kappa\,\mathbf{B_0}$. The susceptibility tensor is κ and α is the Osborne factor (depending on the macroscopic sample shape).

It can be assumed that α remains constant for all samples, while the susceptibility tensor differs. Changes of the chemical shift towards lower ppm values (stronger shielding) is observed in Figure 6.3, from which an increasing demagnetizing field with an increasing post-carbonization temperature can be deduced. This interpretation fits in well with laterally growing aromatic domains, possessing π-currents. The latter are purely diamagnetic in nature and therefore contribute to a net demagnetizing field below and above the aromatic rings.
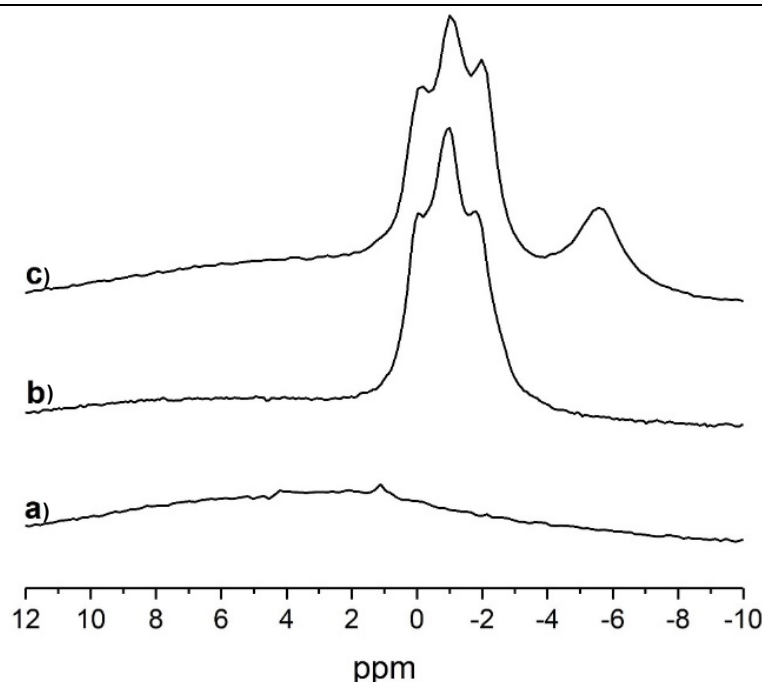

Figure 6.4: [1]H spectra of the sucrose-derived hydrochar treated at 850 °C, measured under 7 kHz MAS. Spectrum a) oven dried sample (140 °C for 48 h), b) received hydrochar (transported under ambient conditions), c) hydrochar exposed to ambient laboratory atmosphere for two weeks.

In order to additionally support the presence of a demagnetizing field for the carbonized samples, ^{1}H spectra were employed. The corresponding ^{1}H spectra of the sucrose-derived hydrochar treated at 850 °C are presented in Figure 6.4. Further, the ^{1}H NMR spectra of hydrochars and other carbonaceous materials are discussed in more detail in Section 6.3. The spectrum a) in Figure 6.4 shows one broad and featureless band and a narrow weak signal, located at 1.1 ppm. While the broad line corresponds to remaining structural hydrogen atoms, the small and narrow signal of low intensity can be assigned to freely rotating water molecules.[14]

On the other hand, additional and more intense signals appear in b) and c) after the sample has been exposed to ambient conditions. Even though the material is designated as hydrophobic, this finding clearly shows that water molecules enter the pores. Spectrum b) shows three narrow signals at 0 ppm, −1 ppm and −1.9 ppm. For c) even an additional peak at −5.6 ppm can be noted. For organic materials, signals in the vicinity of 0 ppm rarely occur, for example in case of tetramethylsilane (TMS). Thus, negative chemical shift values are not often observed. The explanation for this finding is that water molecules entering the pores interact with the magnetic field induced by the aromatic ring currents.[14] This effect was also observed by Xu and co-workers, who studied the interaction of water with mesoporous carbon materials and found negative chemical shifts.[22] Wu and co-workers also obtained similar ^{1}H NMR spectra for microporous activated carbon.[14] These literature reports support the interpretation that a demagnetizing field through π-currents is also observed in the case of the carbonized samples studied in this work. Further details on the NMR spectroscopy of water in carbonaceous host matrices are discussed in Chapter 6.3.

Overall, the process of pyrolysis at lower carbonization temperatures (400 °C–550 °C) can be rationalized as a combustion of functional groups. Upon increasing the post-carbonization temperature, a lateral sheet growth is induced, leading towards local graphite-like structures, in which functional groups are no longer present, i.e. at least not in detectable quantities. Globally, a semi-crystalline carbonaceous material could be obtained which exhibits randomly oriented sheets and as a consequence a non-graphitic character, as previously discussed in Chapter 4. Therefore, this material may exhibit a rather high tortuosity, which could be a disadvantage for the use in lithium ion batteries.[24] Furthermore, ^{13}C NMR spectra shown in Figure 6.2 revealed that an increasing lateral sheet growth and an accompanying increased anisotropy of the magnetic susceptibility shifts and broadens the ^{13}C line (Figure 6.3) at increasing post-carbonization temperatures.

In the following, the outcome of pyrolysis for sucrose-derived hydrochars is compared to trehalose-derived hydrochar.

Comparing the structure of both saccharide-derived products is useful, in order to estimate the influence of the precursor structure on the final product. A first insight into the chemical transition upon hydrothermal carbonization at 180 °C can be gathered by means of the ^{13}C CP spectrum presented in Figure 6.5. Sucrose on the other hand was hydrothermally carbonized at 150 °C, which may influence the comparability of further results. Even though both precursor materials (sucrose and trehalose) have the chemical formula $C_{12}H_{22}O_{11}$, they differ in their structure, since sucrose exhibits a 5-membered fructose ring, that is absent for trehalose, but trehalose has a second glucose ring.

From the perspective of the ^{13}C CP spectra in Figure 6.5, both materials are highly similar, since all signals present for sucrose-derived hydrochar can also be found for trehalose-derived hydrochar. The precise chemical shift values of signals obtained for trehalose-derived hydrochar are shown in the Table A.6 and A.7 in the appendix. Nevertheless, the intensity ratios of signals b–e differ between the trehalose-derived hydrochar and sucrose-derived hydrochar. Baccile and others assign signal (b) at 114.5 ppm to the β-position of furan rings (C–$\underline{C}$=C), while signals at 141.2 ppm (d) and 150.1 ppm (e) originate from the α-positions (2 and 5) of the furan rings (C=$\underline{C}$–O).[16, 17, 18]
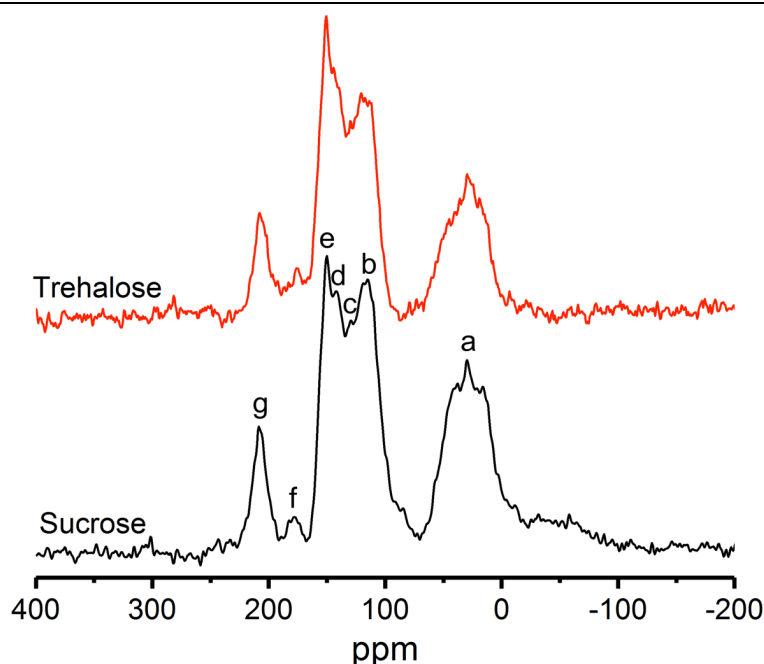

Figure 6.5: ^{13}C CP MAS NMR spectrum of sucrose-derived hydrochar (7 kHz) and trehalose-derived hyadrochar (10 kHz).

For sucrose-derived hydrochar the intensity of signals (b)+(c) and (d)+(e) are nearly similar, while the intensity clearly changes for trehalose-derived hydrochar. The integral of signals (b)+(c) is clearly smaller compared to the integral of (d)+(e) for trehalose-derived hydrochar. Therefore, this finding suggests that for trehalose-derived hydrochar a higher number of sp^2-carbon sites bonded to one oxygen is present. This may be caused by a higher chemical stability of the α,α-1,1-glycosidic linkage in trehalose over the α,β-1,2-glycosidic linkage in sucrose.[24, 25] As stipulated by Grigera and Cremer, water molecules play a crucial role in further stabilizing the α,α-1,1-glycosidic linkage, which likely seems to be the case for the hydrothermal treatment of trehalose in water.[24, 25] This interpretation backed by EDX and XPS is presented elsewhere.[14]

Finally, the carbonized product of trehalose-derived hydrochar (1000 °C) is compared to the one derived from sucrose (1000 °C) by means of ^{13}C DE spectra, shown in Figure 6.6 For sucrose-derived hydrochar carbonized at 1000 °C only a single signal located at 121.5 ppm with several shoulders can be found. For carbonized trehalose-derived hydrochar a similar spectrum can be obtained, with a signal at 122 ppm. Both spectra exhibit two spinning sidebands of similar intensity, which is indicative for both static linewidths being of similar width. The similar width of both MAS lines of c. 3.7 kHz as well as the chemical shifts point to a similar magnetic anisotropy of the aromatic sheets in both materials.[26]
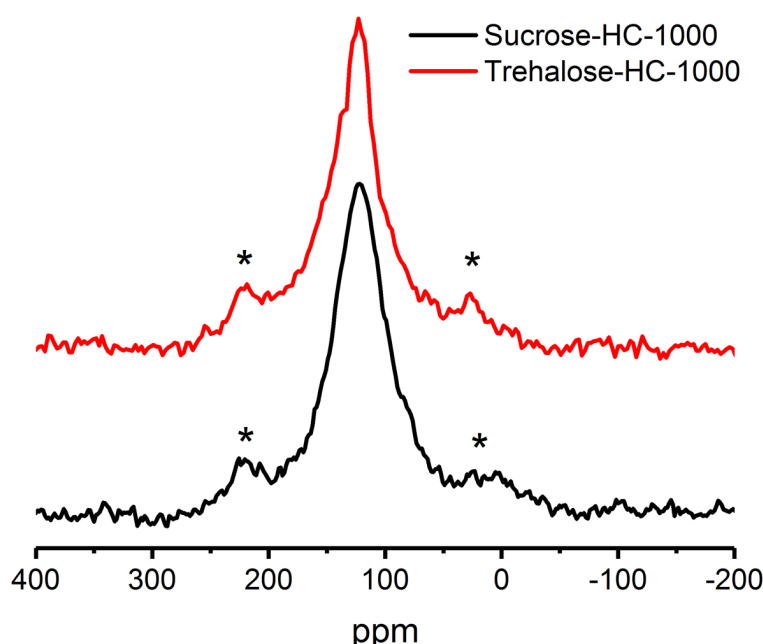

Figure 6.6: ^{13}C DE NMR spectra of post-carbonized sucrose-derived hydrochar and trehalose-derived hydrochar spun under 7 kHz MAS. Both materials were carbonized at 1000 °C. Spinning sidebands are marked by asterisks.

Overall, this section explored the impact of the pyrolysis temperature and precursor material on the structure of the obtained hydrochars. At elevated temperatures of 1000 °C, increasing linewidths and signal shifts are observed, indicating a lateral growth of aromatic sheets. The signal shifts and broadening is explained by an increase in the anisotropy of the magnetic susceptibility. Furthermore, two different precursor materials, namely sucrose and trehalose (chemical formula $C_{12}H_{22}O_{11}$) were used to show that the resulting hydrochars exhibit clear differences in chemical composition. The pyrolyzed products exhibit NMR spectra which are very similar and therefore prevent any detailed differentiation. In particular the trehalose-derived hydrochar appears to maintain a higher oxygen content, compared to the sucrose-derived hydrochar. It remains unclear, whether this observation is directly related to the stronger glycosidic linkage in trehalose, or whether differences in the hydrothermal carbonization temperature (150 °C for sucrose and 180 °C for trehalose) are more decisive.

Future experiments including the trehalose-derived hydrochar may implement this material as an active electrode material in a coin cell. Hard carbon materials have gained certain attention, in particular in Na-ion batteries, which is why this novel synthesized trehalose-derived hydrochar may be a promising candidate.[27]

6.1.4 References

(1) Mi, Y., Hu, W., Dan, Y., & Liu, Y. (2008). Synthesis of carbon micro-spheres by a glucose hydrothermal method. *Materials Letters*, *62*(8-9), 1194-1196.

(2) Cheng, Y., Yang, M., Fang, C., Chen, J., Bai, M., & Su, J. (2017). Controllable morphologies of carbon microspheres via green hydrothermal method using fructose and xylose. *Chemistry Letters*, *46*(9), 1400-1402.

(3) Haibo, O., Cuiyan, L., JianFeng, H., & Jie, F. (2014). Synthesis of carbon/carbon composites by hydrothermal carbonization using starch as carbon source. *RSC Advances*, *4*(24), 12586-12589.

(4) Hu, B., Wang, K., Wu, L., Yu, S. H., Antonietti, M., & Titirici, M. M. (2010). Engineering carbon materials from the hydrothermal carbonization process of biomass. Advanced materials, 22(7), 813-828.

(5) Wortmann, M., Keil, W., Brockhagen B., Biedinger, J., Westphal, M., Weinberger, C., Diestelhorst, E., Hachmann, W., Zhao, Y., Tiemann, M., Reiss, G., Hüsgen, B., Schmidt, C., Sattler, K., Frese, N. (2022). Pyrolysis of sucrose-derived hydrochar. *Journal of Analytical and Applied Pyrolysis*, 161, 105404.

(6) Jian, Z., Xing, Z., Bommier, C., Li, Z., & Ji, X. (2016). Hard carbon microspheres: potassium-ion anode versus sodium-ion anode. Advanced Energy Materials, 6(3), 1501874.

(7) Tang, K., White, R. J., Mu, X., Titirici, M. M., van Aken, P. A., & Maier, J. (2012). Hollow carbon nanospheres with a high rate capability for lithium-based batteries. ChemSusChem, 5(2), 400-403.

(8) Wang, Q., Li, H., Chen, L., & Huang, X. (2002). Novel spherical microporous carbon as anode material for Li-ion batteries. Solid State Ionics, 152, 43-50.

(9) Wang, Q., Li, H., Chen, L., & Huang, X. (2001). Monodispersed hard carbon spherules with uniform nanopores. *Carbon*, *39*(14), 2211-2214.

(10) Wang, Q., Li, H., Chen, L., & Huang, X. (2002). Novel spherical microporous carbon as anode material for Li-ion batteries. *Solid State Ionics*, *152*, 43-50.

(11) Elbein, A. D., Pan, Y. T., Pastuszak, I., & Carroll, D. (2003). New insights on trehalose: a multifunctional molecule. *Glycobiology*, *13*(4), 17R-27R.

(12) Richards, A. B., Krakowka, S., Dexter, L. B., Schmid, H., Wolterbeek, A. P. M., Waalkens-Berendsen, D. H., ... & Kurimoto, M. (2002). Trehalose: a review of properties, history of use and human tolerance, and results of multiple safety studies. Food and chemical toxicology, 40(7), 871-898.

(13) Wortmann, M., Keil, W., Westphal, M., Diestelhorst, E., Brockhagen, B., Biedinger, J., Weinberger, C., Bandzio, L., Tiemann, M., Hütten, A., Schmidt, C., Reiss, G., Sattler, K., Frese, N. (20XX). Synthesis of Carbon Microspheres with Binary Size Distribution via Hydrothermal Carbonization of Trehalose. *To be submitted*.

(14) Xu, Y., Watermann, T., Limbach, H. H., Gutmann, T., Sebastiani, D., & Buntkowsky, G. (2014). Water and small organic molecules as probes for geometric confinement in well-ordered mesoporous carbon materials. *Physical Chemistry Chemical Physics*, *16*(20), 9327-9336.

(15) Zhong, R., Liao, Y., Shu, R., Ma, L., & Sels, B. F. (2018). Vapor-phase assisted hydrothermal carbon from sucrose and its application in acid catalysis. *Green Chemistry*, *20*(6), 1345-1353.

(16) Titirici, M. M., Antonietti, M., & Baccile, N. (2008). Hydrothermal carbon from biomass: a comparison of the local structure from poly-to monosaccharides and pentoses/hexoses. *Green Chemistry*, *10*(11), 1204-1212.

(17) Baccile, N., Laurent, G., Babonneau, F., Fayon, F., Titirici, M. M., & Antonietti, M. (2009). Structural characterization of hydrothermal carbon spheres by advanced solid-state MAS 13C NMR investigations. *The Journal of Physical Chemistry C*, *113*(22), 9644-9654.

(18) Paine III, J. B., Pithawalla, Y. B., & Naworal, J. D. (2008). Carbohydrate pyrolysis mechanisms from isotopic labeling: Part 4. The pyrolysis of d-glucose: The formation of furans. *Journal of analytical and applied pyrolysis*, *83*(1), 37-63.

(19) Worsley, M. A., Kucheyev, S. O., Mason, H. E., Merrill, M. D., Mayer, B. P., Lewicki, J., ... & Baumann, T. F. (2012). Mechanically robust 3D graphene macroassembly with high surface area. *Chemical Communications*, *48*(67), 8428-8430.

(20) Bac, C. G., Bernier, P., Latil, S., Jourdain, V., Rubio, A., Jhang, S. H., ... & Hirsch, A. (2001). 13C NMR investigation of carbon nanotubes and derivatives. *Current Applied Physics*, *1*(2-3), 149-155.

(21) VanderHart, D. L. (2007). Magnetic susceptibility and high-resolution NMR of liquids and solids. *eMagRes*.

(22) Song, Y., Chong, Y., Raghavan, A., Xing, Y., Ling, Y., Kleinhammes, A., & Wu, Y. (2017). Nucleation and growth process of water adsorption in micropores of activated carbon revealed by NMR. *The Journal of Physical Chemistry C*, *121*(15), 8504-8509.

(23) Chen, H., Pei, A., Wan, J., Lin, D., Vilá, R., Wang, H., ... & Cui, Y. (2020). Tortuosity effects in lithium-metal host anodes. *Joule*, *4*(4), 938-952.

(24) Donnamaria, M. C., Howard, E. I., & Grigera, J. R. (1994). Interaction of water with α, α-trehalose in solution: molecular dynamics simulation approach. *Journal of the Chemical Society, Faraday Transactions*, *90*(18), 2731-2735.

(25) Albertorio, F., Chapa, V. A., Chen, X., Diaz, A. J., & Cremer, P. S. (2007). The α, α-(1→1) linkage of trehalose is key to anhydrobiotic preservation. *Journal of the american chemical society*, *129*(34), 10567-10574.

(26) Freitas, J. C., Cipriano, D. F., Zucolotto, C. G., Cunha, A. G., & Emmerich, F. G. (2016). Solid-State 13C NMR Spectroscopy Applied to the Study of Carbon Blacks and Carbon Deposits Obtained by Plasma Pyrolysis of Natural Gas. *Journal of Spectroscopy*, *2016*.

(27) Zhao, L. F., Hu, Z., Lai, W. H., Tao, Y., Peng, J., Miao, Z. C., ... & Dou, S. X. (2021). Hard carbon anodes: fundamental understanding and commercial perspectives for Na-ion batteries beyond Li-ion and K-ion counterparts. *Advanced Energy Materials*, *11*(1), 2002704.

6.2 Red Carbon: From Rediscovery to Post-Carbonization
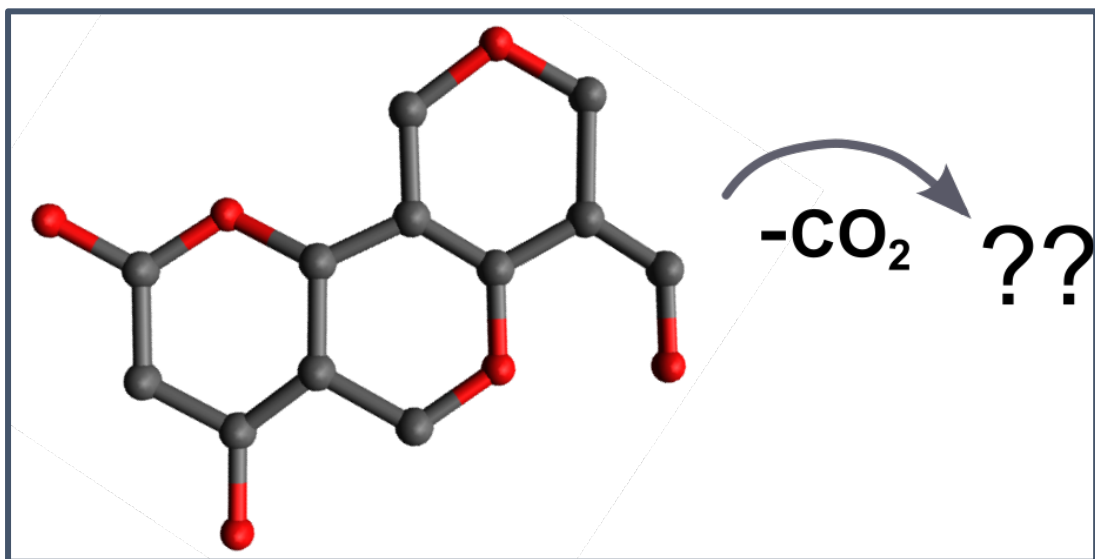
6.2.1 The History of Red Carbon

The post-carbonization of many organic precursor materials at high temperatures is a process which leads to properties difficult to control. The choice of precursors for the preparation of carbonaceous materials is crucial for the obtained properties, while not very pronounced for sucrose and trehalose.[1, 2] Ideas to prepare carbonaceous materials with well-defined properties are (i) either the implementation of new precursors yielding well-defined products or (ii) the use of mild temperatures and smarter condensation reaction routes. First experiments resulting in nitrogen containing carbon nitride C_3N_4 were carried out by Liebig in 1834. This material has been rediscovered in the late 20th century.[3]

Seminal work on the related carbon suboxide (C_3O_2), was carried out in 1874 by Brodie who observed CO condensation to C_3O_2 in an induction tube.[4] The material Brodie obtained was a red-colored polymeric material, from which the name "red carbon" is derived. In the 1960s this material has further been studied in terms of structure and applications.[5] However, there has been a decline in interest in this material afterwards.

The alternative synthesis of carbon suboxide from acetic anhydride and malonic acid benefit from the rather mild reaction conditions of 140 °C. In the first step a condensation of malonic acid and acetic anhydride occurs, where a mixed anhydride is obtained. In a second step a polymerization at room temperature results in the formation of a dark-colored solid.[5] However, the reported properties of the product material differ, depending on the polymerization temperature and time. Again, the precise properties are highly sensitive to the reaction conditions, as briefly discussed for the saccharide-derived hydrochars. The structure of the red carbon material is described in the literature to be a ladder structure, illustrated in Figures 6.7 and 6.8.[6]

The following work firstly examines the structure of poly(carbon suboxide), which is synthesized in liquid-phase. The obtained poly(carbon suboxide) is used as a precursor material for post-carbonization. Poly(carbon suboxide) as a precursor exhibits a well-defined structure and a single mechanism to release leaving groups (CO_2). Therefore, the latter is a good candidate for a carbonization model system which is comprised of a highly ordered precursor. The outcome of carbonization is then compared to the previously carbonized saccharides (see Chapter 6.1).
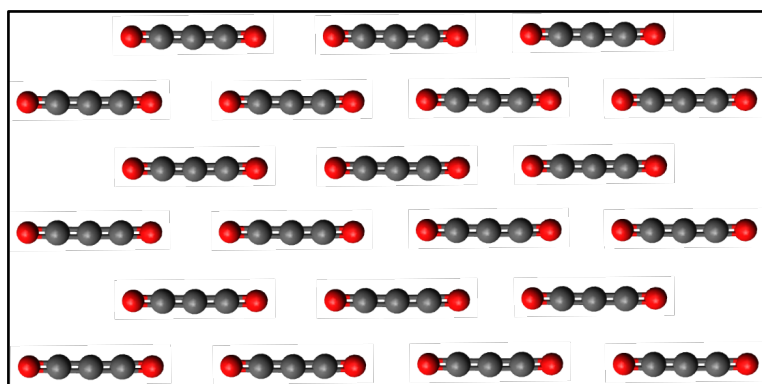
Figure 6.7: Side-view of the A−B stacking order of polymeric C_3O_2 sheets.[7]

6.2.2 Experimental Details

The red carbon and its carbonized product were synthesized at the Max-Planck Institute for Colloids and Interfaces in Potsdam by Dr. Mateusz Odziomek in the group of Prof. Dr. Markus Antonietti. The precise synthetic route is published elsewhere.[7] This material is used as the precursor for post-carbonization. Equivalently to Chapter 6.1, poly(carbon suboxide) was post-carbonized in an inert nitrogen atmosphere, using a heat ramp of 100 °C/h up to 800 °C. Further information regarding experimental details are again presented elsewhere.[7,8] A scheme of the stacking order of the red carbon is shown in Figure 6.7. The proposed reaction mechanism for the formation of red carbon is shown in Figure 6.8.
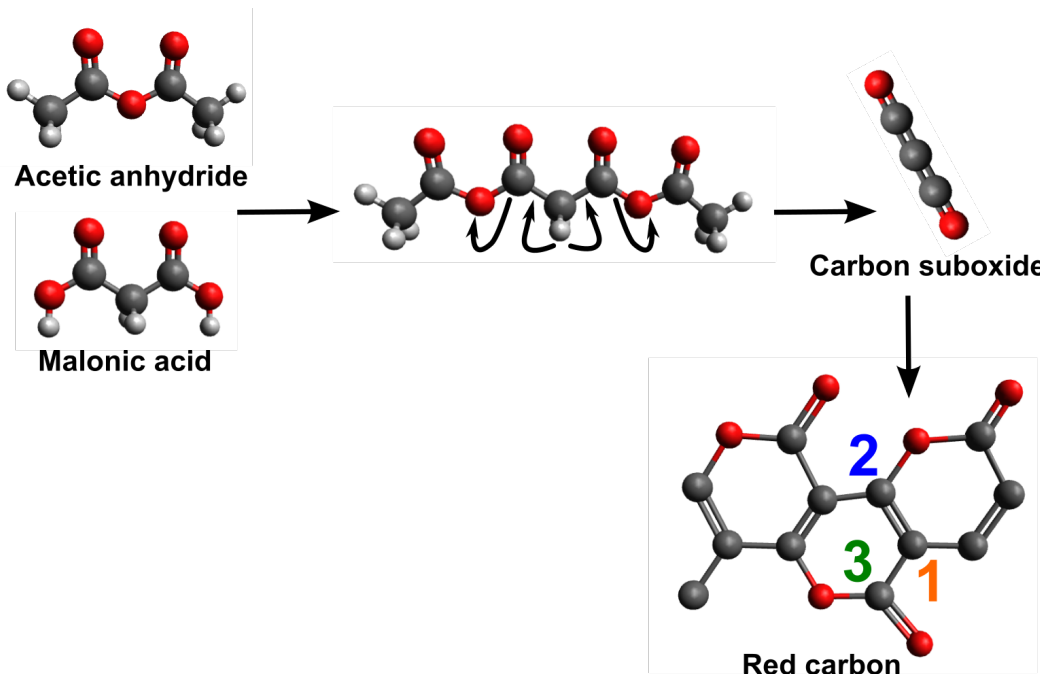

Figure 6.8: Scheme of the proposed reaction mechanism from activation of malonic acid towards the formation of the mixed anhydride with acetic acid. Two equivalents of formic acid are released to obtain linear carbon suboxide which subsequently polymerizes to the red carbon.[7]

## 6.2.3 Chemical Structure and Carbonization of Red Carbon
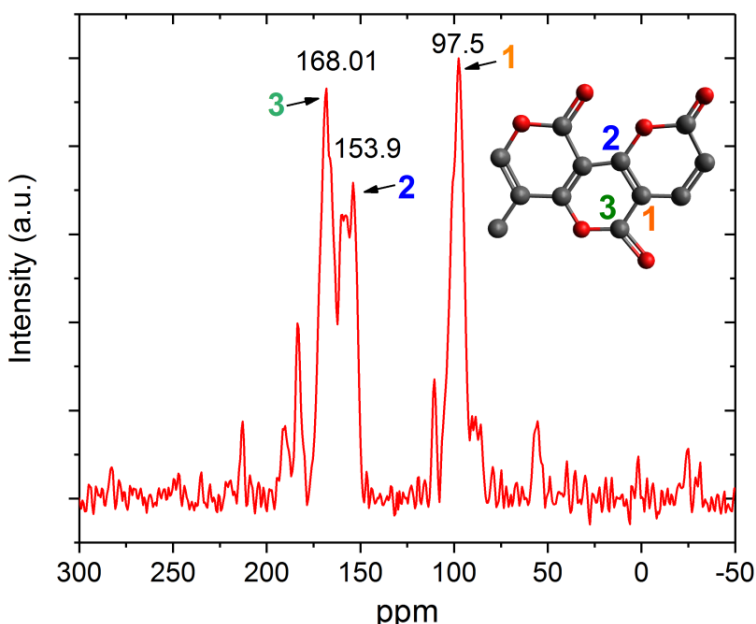
Figure 6.9: [13]C 10 kHz DE MAS spectrum of the red carbon sample. The peak assignment is based on a literature report.[6] The ^{13}C spectrum suggests the presence of polypyrone units as shown in the depicted structure.

Relevant information regarding the chemical structure of the prepared poly(carbon suboxide) can be obtained by means of ^{13}C NMR. A detailed NMR study on carbon suboxide was carried out by Schmedt auf der Günne and co-workers, who assigned the signals of all relevant ^{13}C sites.[6]

The direct excitation (DE) [13]C 10 kHz MAS spectrum of the poly(carbon suboxide) product of this work is shown in Figure 6.9 and confirms that it is mainly composed of sp^2-hybridized carbon atoms, since signals are present above 90 ppm exclusively. The intensity ratios of the ^{13}C DE spectrum seen in Figure 6.9 are not quantitative, due to extremely long T_1 relaxation times of the rigid sp^2 carbon sites, as pointed out by Schmedt auf der Günne.[6] The most intense signals (1–3) found in Figure 6.9 can be correlated to the three different carbon sites in the polymer. Signal (1) at 97.5 ppm is assigned to the C–$\underline{C}$=C carbon sites which are not attached to any heteroatom, representing an electron rich aromatic site. Carbon sites, which are similarly electron-rich, typically exhibit chemical shift values at around 128 ppm (for benzene).[9] The peaks at 168.1 ppm (3) and 153.9 ppm (2) are assigned to carbonyl carbons from the lactone group (O–$\underline{C}$=O) and from a carbon site connected to one oxygen atom (O–$\underline{C}$=C). The additional signals at 182.3 and 190.8 ppm likely originate from carboxylic groups which are present either

as end groups of the polymer or as impurities.[9] Ketone groups, which are associated with side-reaction products are found at 212.8 ppm. A signal of low intensity at 110.5 ppm may indicate an onset of thermal degradation of the red carbon towards a graphite-like structure. Using cross-polarization (CP) measurements on the other hand, did not yield a reasonable signal, even after sampling of 8192 scans. This finding confirms that ^{1}H atoms are basically absent in the structure. Taking into account the results from X-ray diffraction and density functional theory studies of poly(carbon suboxide), an A−B stacking of single C_3O_2 sheets seems likely.[7]

Further insight into the unique properties of the prepared polymeric C_3O_2 can be gained by ^{1}H NMR spectroscopy, as shown in Figure 6.10. For polymeric C_3O_2 stored under ambient conditions four signals together with a shoulder at 0 ppm can be seen. The most intense peak at 2 ppm may be assigned to structural protons, since no large changes in intensity are observed upon heating the material. The peak at 5.8 ppm apparently results from water, since drying the material at 80 °C causes a decrease in signal intensity, accompanied by the presence of a signal at 1.1 ppm which is assigned to gas-like single water molecules.[10] The larger shift downfield, compared to bulk water (4.7 ppm) indicates stronger hydrogen bonding than in the bulk water phase.[11] Likely, this is due to water molecules forming strong hydrogen bonds, either to the carboxylic group or to the ether group of C_3O_2.
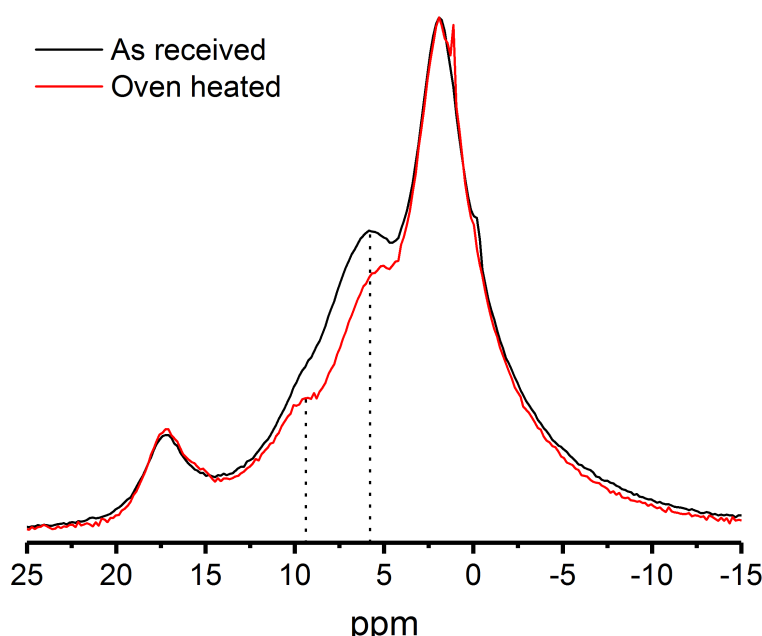

Figure 6.10: ^{1}H 10 kHz MAS spectrum of polymeric C_3O_2, as received (exposed to ambient atmosphere) and oven dried for 4 h at 80 °C. Signals at 5.8 ppm and 9.4 ppm are marked by dotted lines. Absolute signal intensities are shown.

The origin of the signal at 9.4 ppm, as well as the signal at 17.3 ppm cannot be unequivocally explained at this point. One possible explanation for the signal at 17.3 ppm may be the presence of largely extended aromatic ring currents, creating a large deshielded region present at the edges of the molecular plane (Figure 3.9). For an already downfield shifted signal, such as that of an aldehyde group, a strongly downfield shifted signal would be expected. Still, this finding is exceptional for organic compounds and indicates the presence of an aromatic network with unique bonding environments.

Since it can be assumed that the produced polymeric C_2O_3 is highly ordered, a follow-up question is which structural changes occur during an oxygen reduction reaction (post-carbonization). As discussed in the previous sections, precursor materials used to produce highly carbonized materials are often small monomers or oligomers. The carbonization of larger oligomers/polymers has been carried out in the past for cellulose and polymer blends such as poly(acrylonitrile) and poly(vinylidenfluoride) but is still a field of ongoing research.[12, 13] One typical disadvantage of carbonization of some precursors is the poor electric conductivity accompanied with a high degree of disorder. A highly conductive and certainly ordered carbonaceous material is desirable for numerous applications. Therefore, polymeric C_3O_2 served as a precursor material for post-carbonization. The relevant decomposition mechanism, as probed by TGA-MS is the decomposition of polymeric C_3O_2 into CO_2:

$$(C_3O_2)_x \rightarrow C_{2x} + xCO_2 \qquad [6.2]$$
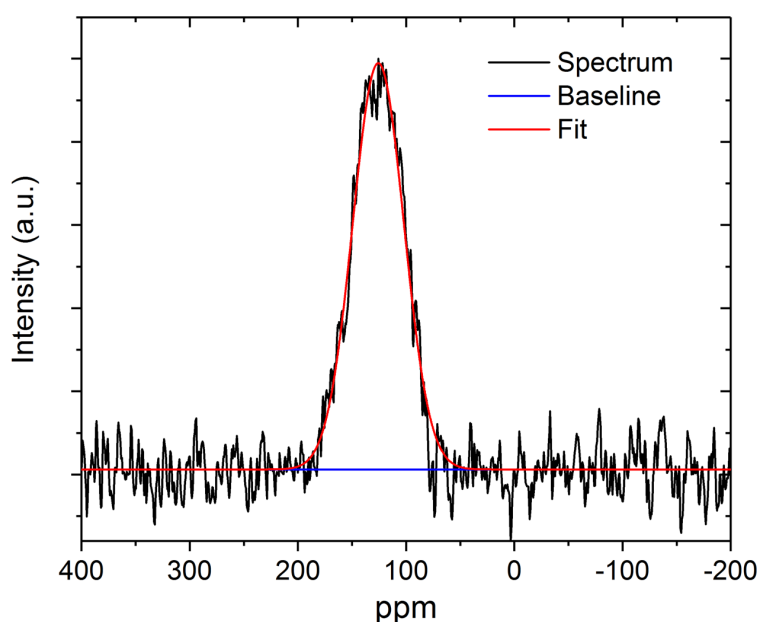
Figure 6.11: [13]C DE 10 kHz MAS spectrum of poly(carbon suboxide) carbonized at 800 °C. A single gaussian fit is carried out.

Although negligible traces of CO were detected by mass spectroscopy coupled to the TGA, still the main combustion mechanism remains the one shown in equation 6.2.[7]

The ^{13}C DE NMR spectrum is shown in Figure 6.11. No ^{13}C CP spectrum could be acquired due to the low amount of protons in the structure. The ^{13}C signal for the material post-carbonized at 800 °C displays a single broad peak (FWHM c. 4 kHz) without additional spinning sidebands at 10 kHz. The width of the ^{13}C signal is similar to the sucrose-derived hydrochars (c. 3.8 kHz at 1000 °C) which is typical for sp^2-carbon sites exhibiting a large anisotropy in their magnetic susceptibility.[14] This is due to the lateral extension of aromatic sheets.[15] Also the position of the signal at 127 ppm is commonly found for sp^2-carbon sites in numerous carbonized materials, as reported by Freitas.[16]

To summarize, this chapter scrutinized polymeric C_3O_2 and its structural changes after post-carbonization. A unique structure of polymeric C_3O_2 could be confirmed by means of ^1H and ^{13}C NMR spectroscopy. Carbonization of this rather unusual precursor at 800 °C resulted in an amorphous material with locally arranged aromatic domains. The latter is entirely composed of sp^2-carbon sites, which is backed by ^{13}C NMR spectroscopy. As shown by means of ^1H spectroscopy, the obtained line shift is smaller compared to sucrose-derived carbons, which will be an object of discussion in Chapter 6.3. Further experiments of water added to porous carbonaceous materials are needed in order to understand these phenomena in more detail. Therefore, an additional heteroatom containing carbonaceous material and its interaction with H_2O is scrutinized in the following section.

6.2.4 References

(1) Wortmann, M., Keil, W., Brockhagen B., Biedinger, J., Westphal, M., Weinberger, C., Diestelhorst, E., Hachmann, W., Zhao, Y., Tiemann, M., Reiss, G., Hüsgen, B., Schmidt, C., Sattler, K., Frese, N. (2022). Pyrolysis of sucrose-derived hydrochar. Journal of Analytical and Applied Pyrolysis, 161, 105404.

(2) Wortmann, M., Keil, W., Westphal, M., Diestelhorst, E., Brockhagen, B., Biedinger, J., Weinberger, C., Bandzio, L., Tiemann, M., Hütten, A., Schmidt, C., Reiss, G., Sattler, K., Frese, N. (20XX). Synthesis of Carbon Microspheres with Binary Size Distribution via Hydrothermal Carbonization of Trehalose. *To be submitted*.

(3) Liebig, J. (1834). Über einige Stickstoff-Verbindungen. *Annalen der Pharmacie*, *10*(1), 1-47.

(4) Brodie, B. C. (1874). IV. On the action of electricity on gases.—II. On the electric decomposition of carbonic-acid gas. *Philosophical Transactions of the Royal Society of London*, (164), 83-103.

(5) Smith, R. N., Young, D. A., Smith, E. N., & Carter, C. C. (1963). The structure and properties of carbon suboxide polymer. *Inorganic Chemistry*, *2*(4), 829-838.

(6) auf der Günne, J. S., Beck, J., Hoffbauer, W., & Krieger-Beck, P. (2005). The structure of poly (carbonsuboxide) on the atomic scale: a solid-state NMR study. *Chem. Eur. J*, *11*(15), 4429-4440.

(7) Odziomek, M., Giusto, P., Kossmann, J., Tarakina, N. V., Heske, J., Rivadeneira, S. M., Keil, W., Schmidt, C., Mazzanti, S., Savateev, A., Kühne, T. D., Antonietti, M., López-Salas, N. (2022). "Red carbon": A rediscovered polymeric, crystalline semiconductor. *Submitted*.

(8) Odziomek, M., Zheng, X., Zschiesche H., Tarakina, N. V., Keil, W., Schmidt, C., Antonietti, M., Lopez-Salas, N. (2022). From carbon suboxide to processable porous carbons. *To be submitted*.

(9) Baccile, N., Laurent, G., Babonneau, F., Fayon, F., Titirici, M. M., & Antonietti, M. (2009). Structural characterization of hydrothermal carbon spheres by advanced solid-state MAS 13C NMR investigations. *The Journal of Physical Chemistry C*, *113*(22), 9644-9654.

(10) Grünberg, B., Emmler, T., Gedat, E., Shenderovich, I., Findenegg, G. H., Limbach, H. H., & Buntkowsky, G. (2004). Hydrogen bonding of water confined in mesoporous silica MCM-41 and SBA-15 studied by 1H solid-state NMR. *Chemistry–A European Journal*, *10*(22), 5689-5696.

(11) Elgabarty, H., Khaliullin, R. Z., & Kühne, T. D. (2015). Covalency of hydrogen bonds in liquid water can be probed by proton nuclear magnetic resonance experiments. *Nature communications*, *6*(1), 1-6.

(12) Sevilla, M., & Fuertes, A. B. (2009). The production of carbon materials by hydrothermal carbonization of cellulose. *Carbon*, *47*(9), 2281-2289.

(13) Wortmann, M., Frese, N., Mamun, A., Trabelsi, M., Keil, W., Büker, B., ... & Sabantina, L. (2020). Chemical and morphological transition of poly (Acrylonitrile)/poly (vinylidene fluoride) blend nanofibers during oxidative stabilization and incipient carbonization. *Nanomaterials*, *10*(6), 1210.

(14) Mazur, A. S., Vovk, M. A., & Tolstoy, P. M. (2020). Solid-state 13C NMR of carbon nanostructures (milled graphite, graphene, carbon nanotubes, nanodiamonds, fullerenes) in

2000–2019: a mini-review. *Fullerenes, Nanotubes and Carbon Nanostructures*, *28*(3), 202-213.

(15) VanderHart, D. L. (2007). Magnetic susceptibility and high resolution NMR of liquids and solids. *eMagRes*.

(16) Freitas, J. C., Cipriano, D. F., Zucolotto, C. G., Cunha, A. G., & Emmerich, F. G. (2016). Solid-State 13C NMR Spectroscopy Applied to the Study of Carbon Blacks and Carbon Deposits Obtained by Plasma Pyrolysis of Natural Gas. *Journal of Spectroscopy*, *2016*.

(17) Gershoni-Poranne, R., & Stanger, A. (2015). Magnetic criteria of aromaticity. *Chemical Society Reviews*, *44*(18), 6597-6615.

(18) Cyrański, M. K., Havenith, R. W., Dobrowolski, M. A., Gray, B. R., Krygowski, T. M., Fowler, P. W., & Jenneskens, L. W. (2007). The phenalenyl motif: a magnetic chameleon. *Chemistry–A European Journal*, *13*(8), 2201-2207.

(19) Chen, Z., Wannere, C. S., Corminboeuf, C., Puchta, R., & Schleyer, P. V. R. (2005). Nucleus-independent chemical shifts (NICS) as an aromaticity criterion. *Chemical reviews*, *105*(10), 3842-3888.

6.3 The Interaction of Water with Carbonaceous Materials
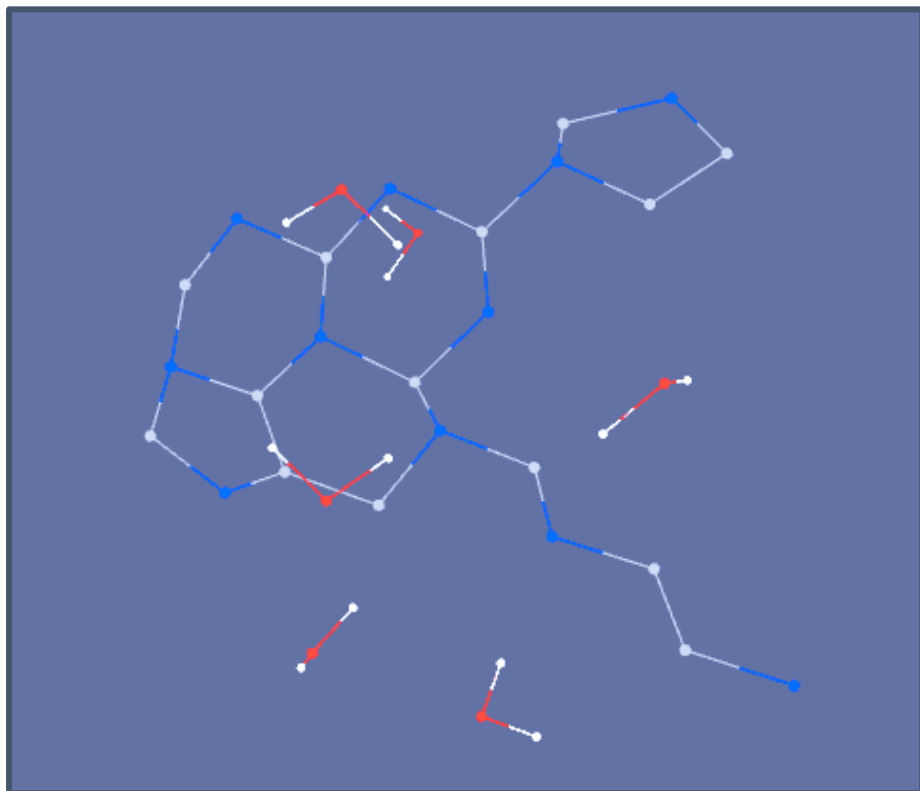
6.3.1 C_1N_1

Over the past 20 years, the interactions of adsorbates with numerous organic and inorganic host matrices, particularly with porous carbonaceous materials, have been studied by a manifold of methods.[1–4] Especially NMR spectroscopy has proven to be a versatile tool, able to probe local adsorbate environments in host matrices.[5] The adsorbate dynamics can be analyzed by solid- and liquid-state NMR spectroscopy, although the interpretation of the data is not trivial at all, due to different contribution. Interactions, which cannot be directly probed by NMR, are the surface roughness of the matrix and its impact on the adsorbate, but also the coupling between electronic excitations of the matrix and of the adsorbate.[6]

Besides doped carbonaceous materials, other heteroatom rich materials such as C_3O_2, C_3N_4, and C_1N_1 have gained attention due to their promising applications in CO_2 capturing or energy storage in supercapacitors.[7, 8, 9] From the perspective of NMR spectroscopy, so far only very little is known about the adsorption of water into the nitrogen-rich material C_2N.[10] Other nitrogen-bearing carbonaceous materials with potential hydrogen bonding sites such as C_1N_1 are currently being studied.[8, 11] Particularly, aqueous electrolytes are expected to enter the pores of the polar C_1N_1 matrix. The predominant interactions depend on both the host matrix and the guest molecules. In this work water molecules are used as a probe for the pore size, the pore size distribution, the chemical structure and possible hydrogen-bonding interactions.

An important contribution of the carbonaceous matrix on NMR spectra is originating from the ring current effect, discussed in detail in Chapter 3.2, which is present whenever π-electrons (within conjugated carbon rings) interact with an external magnetic field.[12]

Different effects, namely the π-currents, the hydrogen-bonding, the pore size distribution and the chemical structure are expected to influence the position of the proton signal of the adsorbed water in C_1N_1. In the following section the interaction of water with C_1N_1 is studied by means of ^{1}H NMR spectroscopy. The pores of C_1N_1 are expected to be polar and thus it can be expected that water molecules should be able to enter these. In addition, the adsorption of water into the previously discussed saccharide-derived hydrochars (Section 6.1) and the pyrolyzed red carbon, introduced in Section 6.2, is discussed in more detail. They exhibit non-polar pore walls and therefore could be compared with the polar pore walls of C_1N_1 in order to derive possible differences.

6.3.2 Experimental Details

The preparation of C_1N_1 (cG@700 and cG@700-SZ10) was carried out at the Max-Planck Institute for Colloids and Interfaces in Potsdam by the Group of Prof. Dr. Markus Antonietti and Dr. Nieves Lopez-Salas. The synthesis is reported in detail in the literature.[8, 11] The sample composition is shown in Table 6.1.

[1]H time-domain signals were recorded after single pulse excitation, while cross polarization (CP) experiments were employed for ^{13}C NMR measurements. In order to carry out ^{1}H NMR measurements, a recycling delay of 5 s, an excitation pulse length of 3.5 μs and 32 scans were employed. [1]H spectra were externally referenced to the water signal (25 °C) at 4.7 ppm.

Table 6.1: Overview of the sample composition and specific surface areas of cG@700,[8] cG@700-SZ10,[11] p-C_3O_2 and C800,[9] Sucrose-HC[20] and Trehalose-HC[21].

| Sample | EDX/ECA composition [at. %] | | | | S_{BET} | V_{BET} |
	C	N	O	H	m^2g^{-1}	cm^3g^{-1}
cG@700-SZ10	46.6	42.4	4.4	n.d.[a]	812	0.4
cG@700	54.5/ 59.8	41.8/28.9	3.7/ 5.1	1.6	212	0.17
p-C_3O_2	52.95	0.06	n.d.	2.09	85	n.d.
C800	94.26/ 96.5	n.d.	2.89/ 3.5	0.6	533	n.d.
Trehalose HC (1000 °C)	91.7	n.d.	8.3	n.d.	505	0.34
Sucrose HC (850 °C)	96.5	n.d.	3.5	n.d.	480	n.d.
Sucrose HC (1000 °C)	96.4	n.d.	3.6	n.d.	470	n.d.

n.d.: not determined

^{13}C CP NMR measurements were recorded using a recycling delay of 3 s, an excitation pulse length of 3.5 μs and a contact time of 1 ms. The time domain signals were averaged over 4096 scans. [13]C spectra were externally referenced to the methine carbon signal of adamantane at

29.5 ppm. The chemical shifts reported have an error of ± 0.1 ppm. Samples were packed into 4 mm ZrO rotors and degassed at 250 °C for 24 or 48 h at a nominal pressure of 10^{-3} mbar. After degassing, defined amounts of deionized water were added to the samples with an Eppendorf single channel pipette (0.1–2.5 µL or 0.5–10 µL pipette size). The time of water addition was set as time zero for the subsequent time-dependent ^{1}H MAS NMR measurements.

6.3.3 Water in Polar and Non-Polar Pores

Two fundamental requirements must be considered before the adsorption of water into both C_1N_1 materials cG@700 and cG@700-SZ10 (different pore sizes and pore volumes, see Table 6.1) is explored: Namely that i) both C_1N_1 materials should be chemically similar and ii) in order to accurately interpret different H_2O resonances, structural hydrogens (^{1}H from the carbon matrix) must be identified, in order to distinguish the structural ^{1}H signals from water signals. In order to answer the question regarding chemical similarity i), ^{13}C CP MAS measurements of both samples were employed and presented in Figure 6.12. Indeed, both spectra are highly similar in shape within the observed signal-to-noise ratio, which means that cG@700 and cG@700-SZ10 can be described as chemically analogous. Therefore, these observations support the findings from elemental analysis, which indicate a similar chemical structure for both C_1N_1 samples (see Table 6.1).
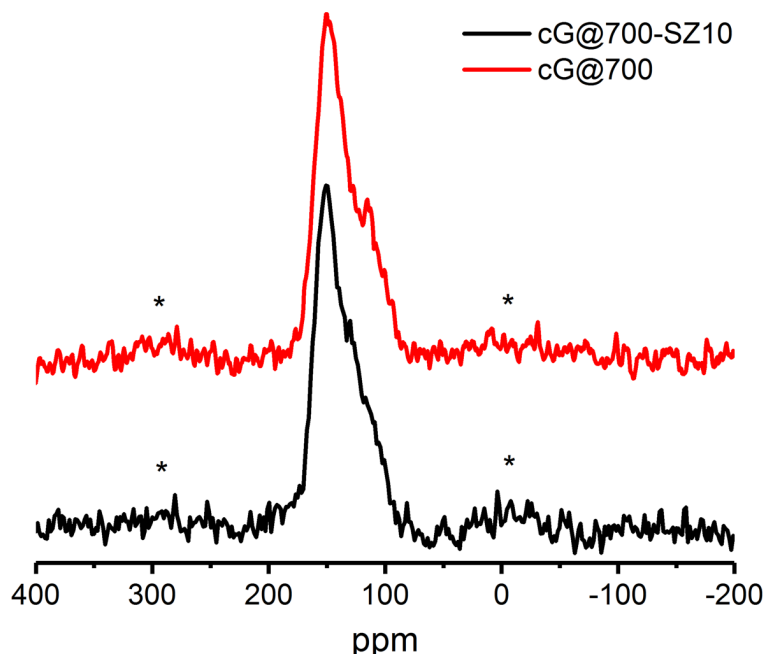

Figure 6.12: ^{13}C CP 10 kHz MAS spectra of cG@700 and cG@700-SZ10. Spinning sidebands are denoted by asterisks.

As found by deconvolution (shown for cG@700 in Figure A.27 in the appendix), two main signals are present, exhibiting characteristic chemical shift values of 149.3 ppm and 117.9 ppm. Both signals are characteristic for sp^2-hybridized carbon sites.[22] While the dominant signal at 149.3 ppm can be assigned to the α-position of a pyridine-type structure, the signal at 117.9 ppm originates from C=$\underline{C}$−C carbon sites which are present for example at the γ-position in a pyridine-type structure. [22,23,24] It is noteworthy that no signals below 100 ppm can be found, indicating that aliphatic groups, if present at all, exist only in marginal quantities.

Furthermore, structural proton signals can be distinguished from water signals by comparing ^{1}H MAS spectra of cG@700 and cG@700-SZ10 (as received), which have been exposed to ambient atmosphere for an undefined period, with both materials dried for 48 h prior to measurement. The corresponding ^{1}H MAS spectra are presented in Figure 6.13. [1]H chemical shifts are presented in Table 6.2.

There are many similarities between the spectra of "dried" and "as received". To begin with cG@700, two main sets of peaks can be found for the "as received" sample, located at c. 1 ppm and 10 ppm. Both signals exhibit notable changes upon drying, indicated by the diminishing signal at 8.6 ppm and 1.4 ppm. The signal at 10.2 ppm is barely affected and is therefore assigned to structural protons, likely originating from pyridine-type structures. All the other signals can be assigned to water adsorbed to C_1N_1. Surprisingly, three different water sites can be resolved, which are shifted either downfield or upfield from the typical bulk water signal at 4.7 ppm.[25]
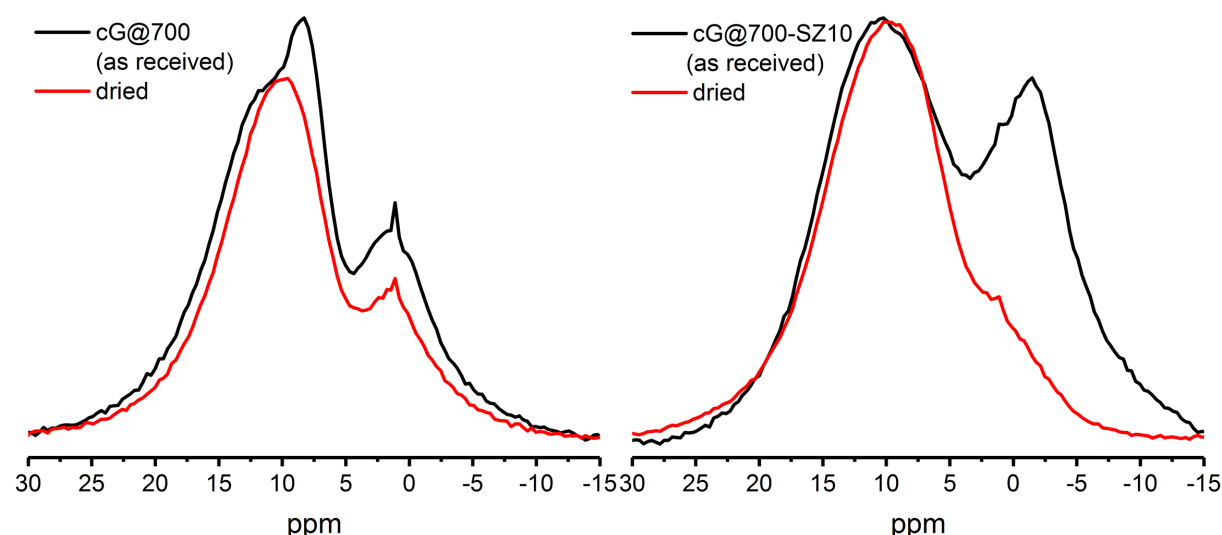

Figure 6.13: [1]H 10 kHz MAS spectra of cG@700 and cG@700-SZ10, normalized to the signal of the structural protons at c. 10 ppm.

Table 6.2: [1]H chemical shifts and $\Delta\delta$ values derived from drying and H_2O impregnating experiments.

cG@700			cG@700-SZ10		
Assignment	**δ/ ppm**	**$\Delta\delta$/ ppm**	**Assignment**	**δ/ ppm**	**$\Delta\delta$/ ppm**
Structural [1]H	10.2	-	structural [1]H	10.2	-
Hydrogen-bonded H_2O[a]	8.6	-	Hydrogen-bonded H_2O[a]	8.5	-
H_2O Monomers	1.1	-	H_2O Monomers	1.1	-
Shielded H_2O	1.4	−3.6[b]	Shielded H_2O	−1.5	−6.2[b]

a: determined from H_2O impregnating experiments

b: relative to the bulk water signal at 4.7 ppm

The first water signal occurs at 1.4 ppm. The position of this upfield shifted water signal is reflecting the presence of π-currents in the material. Ring currents are reported for the nitrogen-rich C_2N material,[10] which are also expected for C_1N_1 to occur. This signal is reduced in intensity upon drying the material. Therefore, it is reasonable to assign this signal to water molecules at positions where the local shielding field is large, i.e. close to a pore wall.[26]

Superimposed on the broad signal at 1.4 ppm is the second water peak, an extremely small and narrow peak (total spectral intensity smaller than 1 %) at 1.1 ppm. The position and the narrowness of this water signal are characteristic for non-hydrogen bonded water, i.e. single water molecules which are able to rotate freely and therefore yield an extremely narrow line.[27, 28] Important to note is that this non-hydrogen bonded water is also found in other purely carbon-based materials, where the same chemical shift of 1.1 ppm is detected.[27] As seen in Table 6.2 and in the literature, the chemical shift of this signal is largely independent of the carbonaceous matrix.

The third signal which is assigned to H_2O is found downfield at 8.6 ppm. The position of the signal indicates that this water site experiences strong hydrogen bonding.[29] One obvious interpretation is that this signal originates from H_2O hydrogen-bonded to nitrogen atoms of the C_1N_1 matrix. Literature on the interaction of H_2O with pyridine-type nitrogen sites supports this interpretation.[29]

Overall, three substantially different water sites could be detected for cG@700, namely H_2O hydrogen bonded to nitrogen of C_1N_1 (8.6 ppm), water in the vicinity of a local shielding field

(1.4 ppm) and very small amounts of isolated water monomers which are not hydrogen bonded (1.1 ppm). The observed variety of different water sites in cG@700 is remarkable, and rarely seen for carbonaceous materials.

Drying experiments performed on cG@700-SZ10 reveal the presence of a more downfield shifted signal (−1.5 ppm), compared to cG@700 (1.4 ppm). From the latter chemical shift values the diamagnetic shifts $\Delta\delta$ are calculated by equation 3.18, taking the bulk water signal at 4.7 ppm as the reference value. According to Forse and co-workers, both resulting $\Delta\delta$ values (−3.6 ppm for cG@700 and −6.2 ppm for cG@700-SZ10) are found for some adsorbed liquids in porous carbonaceous materials.[5] The difference between both values is large, for which the following possible explanation appears plausible.

As discussed in Chapter 3.2 and in the corresponding literature, differences in the observed $\Delta\delta$ values correlate well with varying average distances of the studied nucleus from the pore wall.[30] Therefore, nuclei located closer to the pore wall (i.e. located inside a smaller pore) exhibit larger $\Delta\delta$ values. The larger $\Delta\delta$ value observed for cG@700-SZ10 reflects the higher fraction of micropores present in this sample. The cG@700 sample, on the other hand exhibits a larger fraction of mesopores and therefore a considerably lower $\Delta\delta$ value.

No well resolved signal around 8.6 ppm can be found for cG@700-SZ10 (Figure 6.13), while the broadness of the signal around 10 ppm indicates the presence of this water signal. The presence of a hydrogen-bonded H_2O signal is verified and discussed for the water impregnation experiments below. For the impregnation experiments not the absolute amounts of the added water are relevant, but the pore saturation factor. The pore saturation factors, i. e. the ratios of the added amount of water with respect to the pore volume of the material (V_{Water}/ V_{Pore}), are given in Table 6.3. The pore volume was determined via N_2 sorption experiments.[8, 11]

Before proceeding to the C_1N_1 water impregnation experiments, the water impregnation experiments for a purely carbon-based matrix are presented. The time-resolved ^{1}H NMR spectra of hydrothermally carbonized (1000 °C) trehalose (Section 6.1) are presented in Figure 6.14 and 6.15. Figure 6.14 shows that the bulk water signal (4.7 ppm) steadily diminishes in intensity as a function of time, while the intensity of two upfield shifted signals, located at −3 ppm and −6.5 ppm steadily increases.
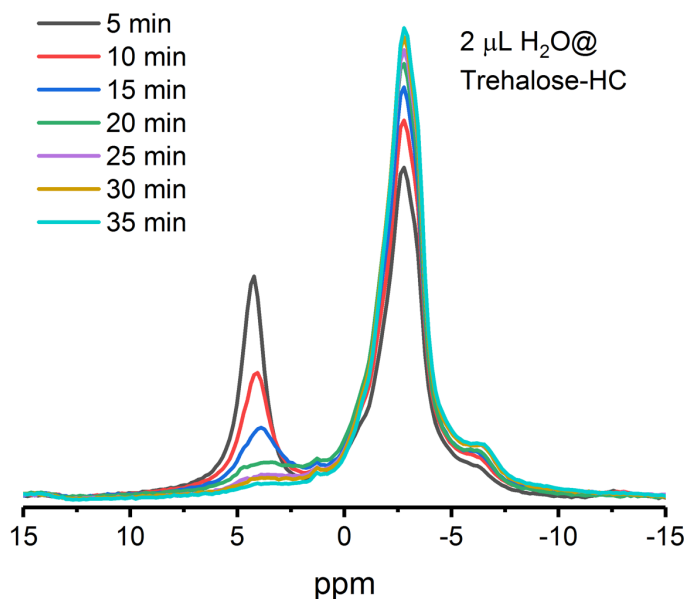
Figure 6.14: Time-dependent ^1H 5 kHz MAS spectra of 2 μL H_2O added to hydrothermally carbonized trehalose. The pore saturation factor is 20 %.

Again, the two upfield shifted signals are interpreted as "in-pore" H_2O, while the signal at 4.7 ppm is assigned to the bulk water phase. The presence of the two different upfield shifted signals and several shoulders indicates a distribution of pore sizes, ranging from pores with a diameter of a few nm to extremely small pores (less than 1 nm).[18, 32] This is also reflected in the large Δδ values of −11.2 ppm and −7.7 ppm. Large Δδ values of c. −10 ppm were typically found for intercalated ions or molecules in graphene layers.[33] Therefore, the signal at −6.5 ppm can be assigned to H_2O intercalated between two graphitic layers.
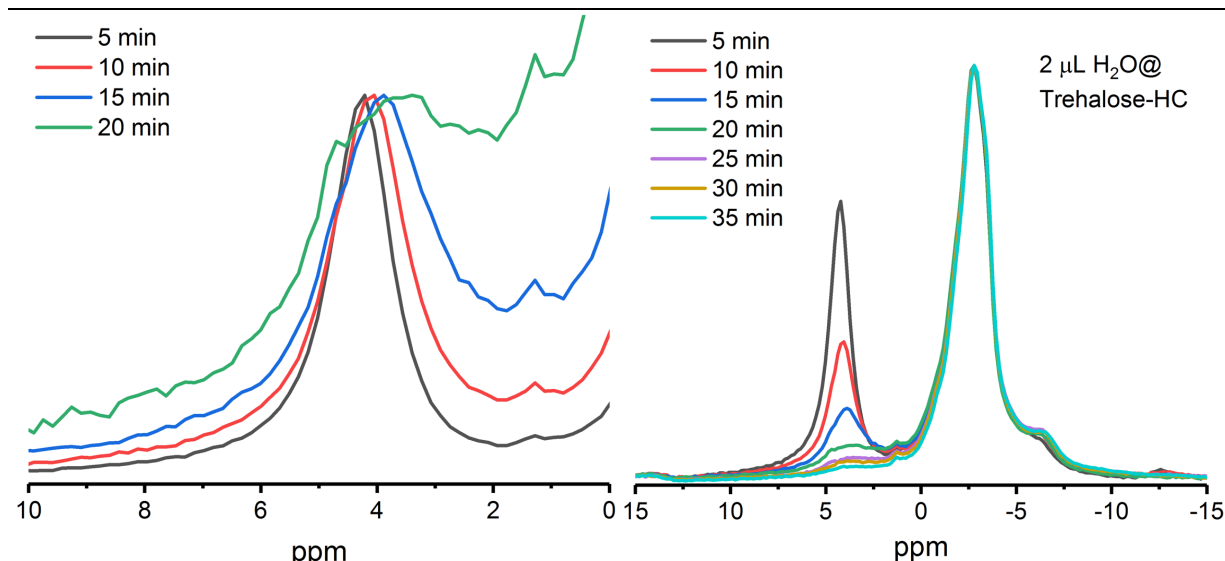
Figure 6.15: Normalized ^1H MAS spectra of 2 μL water added to hydrothermally carbonized trehalose shown in Figure 6.14 but scaled to the bulk water signal, while the right spectra are normalized to the in-pore water signal.
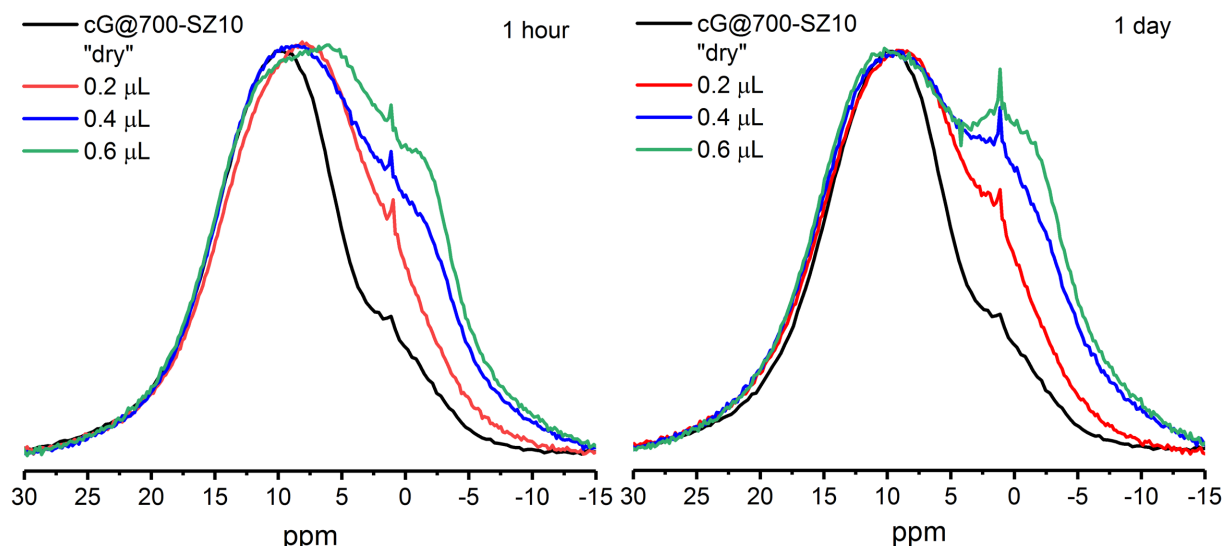
Figure 6.16: [1]H 10 kHz MAS spectra of cG@700-SZ10, impregnated with different amounts of H_2O. Spectra were collected after one hour and one day and normalized to the mass of cG@700-SZ10.

Furthermore, the same time-dependent ^{1}H MAS spectra (scaled to same hight of the bulk water peak) of hydrothermally carbonized trehalose in Figure 6.15 reveal a shift of the bulk water signal to lower ppm values, accompanied by a line broadening. This observation can be explained by an exchange between ex-pore water and in-pore water, which is located in the vicinity of the aromatic surface.[34] This is clear evidence of an exchange between the bulk water reservoir and the in-pore water, until the bulk water is adsorbed completely into the inner pores from the surface. The in-pore water signal nearly maintains its width, which indicates that there is no notable exchange from the in-pore water to the bulk water reservoir.
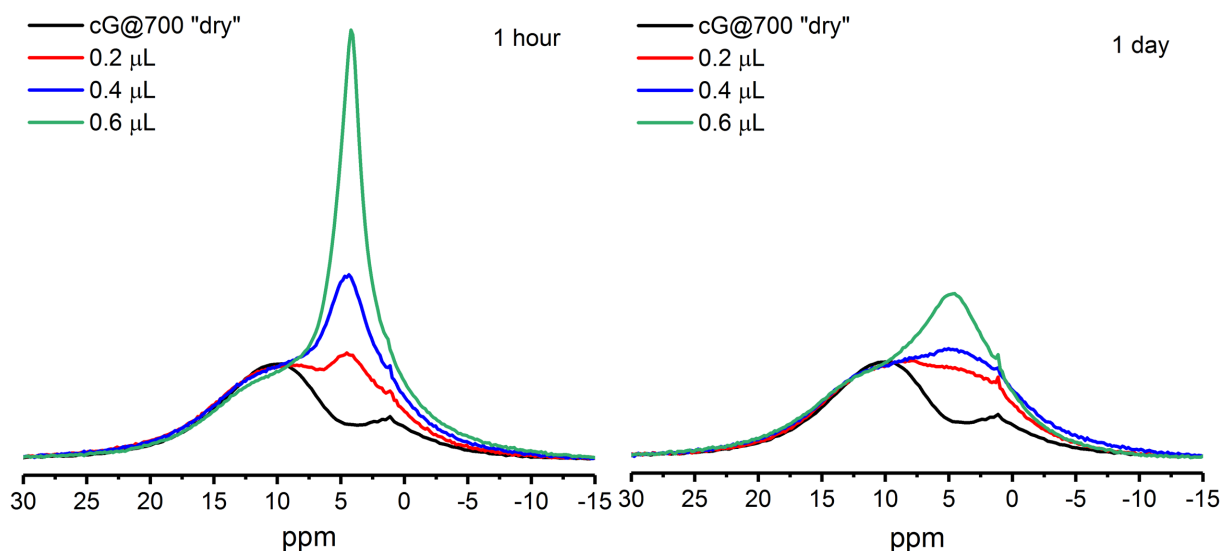
Figure 6.17: [1]H 10 kHz MAS spectra of cG@700, impregnated with different amounts of H_2O. Spectra were collected after one hour and one day and normalized to the amount of cG@700.

^{1}H NMR studies of H_2O impregnated cG@700-SZ10 and cG@700 are presented in Figure 6.16 and Figure 6.17. The $\Delta\delta$ values found for both C_1N_1 samples are smaller compared to the ones of hydrothermally carbonized trehalose. One possible explanation is the difference in the chemistry of the surface which yields different $\Delta\delta$(max) values. Another explanation could be rooted in larger pores of both C_1N_1 samples. However, the low accessibility is most likely not rooted in a too small pore size, since even pores smaller than 0.8 nm are accessible for H_2O molecules.[32] This means, that either i) the pores in both C_1N_1 samples are considerably smaller than 0.8 nm or ii) there are further non-covalent interactions i.e. hydrogen bonding, which act between H_2O and the C_1N_1 matrix and prevent H_2O from entering the pores.

Possible explanations for the small $\Delta\delta$ values of both C_1N_1 materials can be derived from Figures 6.16 and 6.17. Several aspects are revealed by Figure 6.16. Hydrogen-bonded H_2O with a signal at 8.6 ppm is seen in all cases, independent of the added amount of H_2O. Therefore, both samples cG@700 and cG@700-SZ10 contain hydrogen-bonded water. Moreover, the redistribution of H_2O from ex-pore (4.7 ppm) into both reservoirs, hydrogen-bonded (8.6 ppm) and shielded H_2O (−1.5 ppm) can be seen. Clearly visible in Figure 6.17 for cG@700 is the loss of signal intensity of bulk water, without a redistribution to "in-pore" water, as seen for hydrothermally carbonized trehalose (Figure 6.14). In order to verify if there is indeed a loss of water with time instead of a redistribution, the total intensity of the spectra were analyzed as a function of time.
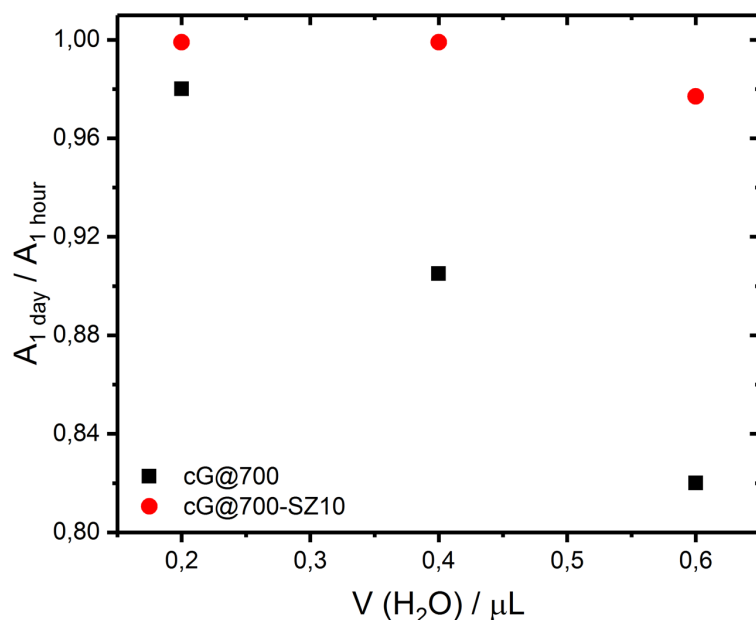

Figure 6.18: Evolution of the ratio of volume specific integrals (integral of 1 day/ 1 hour) for cG@700 and cG@700-SZ10.

Table 6.3: Volumes of H_2O used for impregnating experiments and calculated saturation levels (based on pore volumes derived from N_2 sorption experiments).[8, 11]

| | cG@700 | | cG@700-SZ10 | |
	Volume H_2O/ μL	Saturation / %	Volume H_2O/ μL	Saturation / %
	0.2	1.8	0.2	1.1
	0.4	3.5	0.4	2.1
	0.6	5.2	0.6	3.2
	-	-	2	10.5
	-	-	5	26.6

The integrals for cG@700-SZ10 and cG@700 are shown in Figure 6.18. Taking into account an integration error of 1 %, it becomes clear that no significant signal loss can be detected within the chosen small amounts of H_2O in the case of cG@700-SZ10. For cG@700, there is evidence that a loss of signal intensity occurs, which is more pronounced for larger amounts of H_2O. The signal loss could be explained by evaporation of H_2O during MAS (stream of dry air is used). Another reason may be the presence of so-called cryptopores, which are inaccessible for water molecules.[11] One may conclude, the bulk water did not occupy the pores of cG@700, at least not in notable quantities. Larger amounts of H_2O were added to cG@700-SZ10 in order to test whether a similar trend as for cG@700 can be obtained. 2 μL and 5 μL H_2O were added to cG@700-SZ10 (Figure 6.19), in order to test this hypothesis.
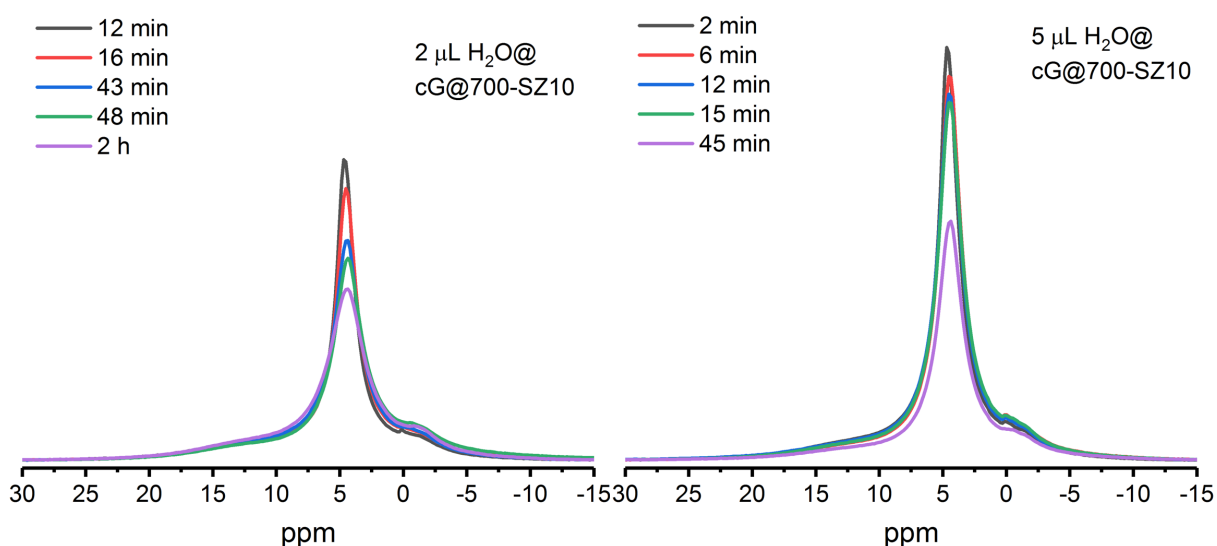

Figure 6.19: Time-resolved ^{1}H 10 kHz MAS spectra of cG@700-SZ10, impregnated with different amounts of H_2O (2 μL and 5 μL) corresponding to a pore saturation factor of 10.5 % and 26.6 %.
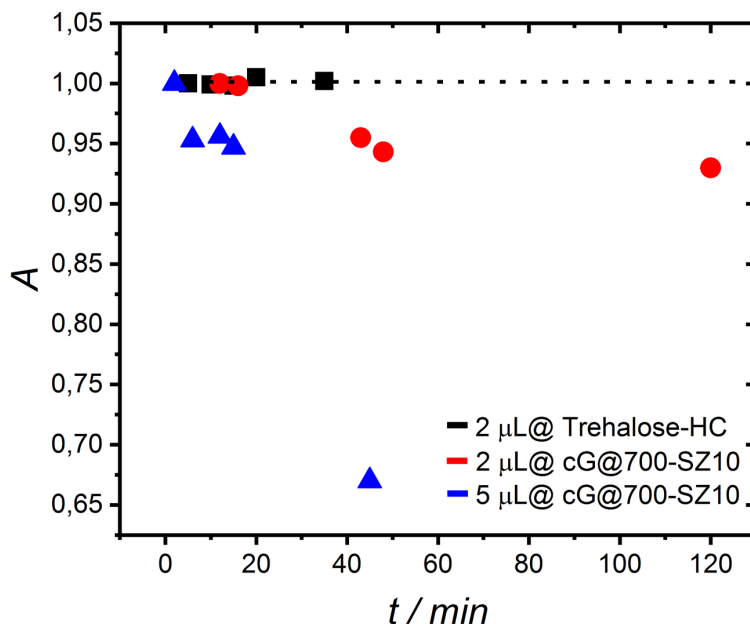
Figure 6.20: Time-dependent integrals of cG@700-SZ10 with 2 µL and 5 µL added H$_2$O (corresponding to pore saturation factors of 10.5 % and 26.6 %) and of hydrothermally carbonized trehalose with a pore saturation factor of 20 %.

The time-dependent integrals of cG@700-SZ10 and for comparison, Trehalose-HC are presented in Figure 6.20. Figures 6.19 and 6.20 show a similar trend as seen for cG@700, (1 hour/ 1 day) in which case the integral reduces over the time of the experiment. This leads to the interpretation that only a very limited fraction of the added water is accessing the pores. Independent of the added amount of water, no major increase in signal intensity of the "in-pore" water (deshielded and hydrogen bonded) can be obtained, which is backed by the clear signal loss shown in Figure 6.20. This loss of the total signal (up to 33 %) is now clearly beyond the integration error and again supports the hypothesis that the added water slowly evaporates, instead of entering the pores, opposed to that is seen for Trehalose-HC in Figure 6.14. For the latter the integral remains nearly unchanged within the integration error, that can be seen in Figure 6.20. Both aspects, namely a nearly constant integral and a significant redistribution from bulk water to in-pore water could not be observed for cG@700 and cG@700-SZ10.

Overall, the performed NMR experiments demonstrated the water repelling character of C$_1$N$_1$. This counterintuitive observation is remarkable, since a rapid adsorption of liquid H$_2$O is shown for a non-polar matrix (hydrothermally carbonized trehalose) but does not occur for both polar matrices, cG@700 and cG@700-SZ10. Two possible explanations can be rationalized. i) Cryptopores, are present for both C$_1$N$_1$ materials, which are inaccessible for guest molecules.[11] Then, a larger fraction of cryptopores is present in cG@700 compared to cG@700-SZ, which

is expressed in a smaller water uptake for cG@700. ii) The C_1N_1 samples exhibit an overall water repelling character and exhibit only few water adsorption sites. The role of non-covalent interactions, such as hydrogen bonding remains the subject of ongoing research. The influence of pore polarity on the adsorption of liquid water cannot be answered with the scope of experiments performed in this work. Further NMR studies on the interaction of polar and non-polar matrices with guest molecules would be needed to answer this question.

6.3.4 Pore Structure of Non-Polar Porous Carbons

Further information about the non-polar pores of saccharide-derived hard carbon spheres and C800 (carbonized red carbon) can be derived from water impregnation experiments followed by ^{1}H NMR spectroscopy. Two relevant aspects can be derived from the ^{1}H NMR spectra, namely (i) the chemical shift(s) and (ii) the presence or absence of several water signals. As introduced in Chapter 3.2, the chemical shift is in first approximation directly proportional to the pore radius of a spherical pore (for a given surface chemistry). Therefore, signals shifted to more negative ppm values indicate that a larger fraction of water molecules is located more closely at the aromatic surface, i.e. in a small pore. Exchange between different sites (discussed in Chapter 3.2) is strongly linked to the number of signals found in the ^{1}H NMR spectrum. The trivial reason of a single signal, which is the presence of only one site is highly unlikely and not considered. The presence of a single signal indicates that different sites have been averaged during the NMR experiment, which is the case for both the intra-pore exchange and the inter-pore exchange.[33] On the other hand, pore structures which exhibit disconnected pores of different size, often yield several signals. Both aspects will be scrutinized in the following section.

Table 6.4: Overview of the $\delta\Delta$ values obtained for all carbonaceous materials studied.

| Sample	$\delta\Delta$ [ppm]	S_{BET} [m^{2}g^{-1}]
cG@700-SZ10	−6.2	812
cG@700	−3.6	212
p-C_3O_2	n.d.	85
C800 (p-C_3O_2)	−6.5	533
Trehalose HC (1000 °C)	−7.5/ −11.5	505
Sucrose HC (850 °C)	−5.7/−10.2	480
Sucrose HC (1000 °C)	−10.1	470

n.d.: not determined
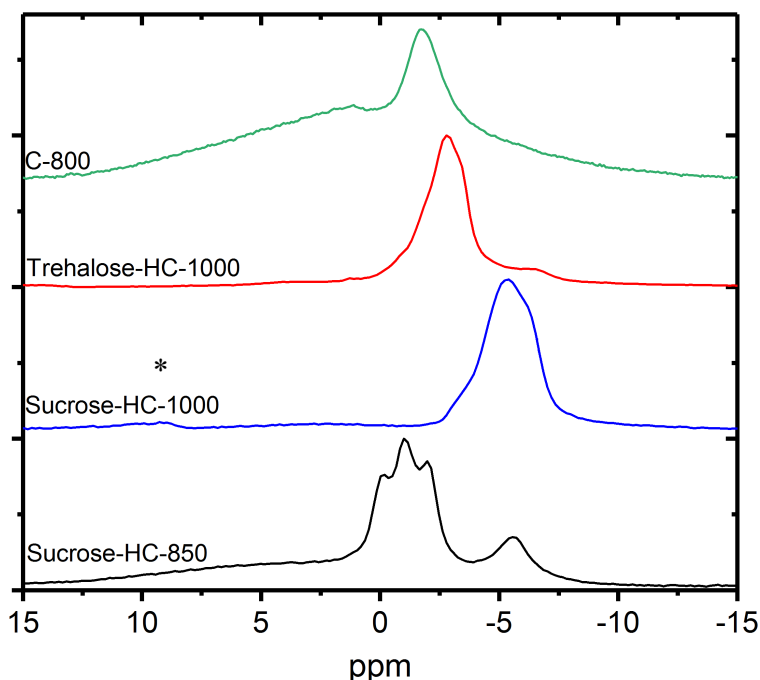
Figure 6.21: ^{1}H MAS spectra of all mainly carbon-based materials studied in Chapter 6. C800, Sucrose-HC-850 and Trehalose-HC-1000 were spun at a MAS rate of 10 kHz, while Sucrose-HC-1000 was spun at 5 kHz (spinning sideband at 10 ppm).

In the previous section 6.3.3 the water adsorption properties of C_1N_1 have been discussed in detail. The ^{1}H NMR spectra of the purely carbon-based materials (shown in Figure 6.21) are analyzed in the following. The pore filling factors of the samples besides Trehalose-HC-1000 (20 %) are unknown. An overview of the $\delta\Delta$ values of all scrutinized carbonaceous materials is given in Table 6.4. Even though the materials studied in this section are all entirely carbon-based, their ^{1}H MAS spectra differ notably. One or several up-field shifted signals can be seen, whose chemical shift values also differ significantly.

First, both sucrose-HC spectra shown in Figure 6.21 are discussed. For Sucrose-HC-850 a signal at -5.6 ppm is seen, accompanied by three signals centered at -1 ppm. For Sucrose-HC-1000 only one broad signal, which consists of superimposed peaks, is found at -5.4 ppm. One possible interpretation for the separated peaks of sucrose-HC-850 °C are not interconnected pores, which means that there are smaller pores isolated from larger pores. Therefore, no inter-pore exchange occurs between both types of pores, resulting in two signals. At elevated temperatures (1000 °C) the smaller and larger pores become connected and an inter-pore exchange becomes possible. As a result, the lines merge together. However, the merged peak is not found at the expected position, which can be explained by a smaller average pore size of Sucrose-HC-1000 compared to Sucrose-HC-850. This is backed by N_2 sorption experiments,

for which a larger fraction of micropores is reported in the case of Sucrose-HC-1000 (93 % micropores) compared to Sucrose-HC-850 (81 % micropores).[20, 21]

Trehalose-HC-1000, similar to sucrose-HC-1000 exhibits one main signal, which is composed of several individual peakscentered at −2.8 ppm. The signal at −2.8 ppm may originate from H_2O molecules located in pores with a larger pore diameter compared to Sucrose-HC-1000. An additional small shoulder can be seen for Trehalose-HC-1000 at −6.8 ppm. Again, this indicates the presence of water in a minor fraction of extremely small pores which are not connected to the majority of larger pores. It appears likely that higher carbonization temperatures are required for trehalose and sucrose to create a connected porous network.

The last sample C800, exhibits one broad line from structural ^1H atoms and a narrow line which is assigned to water, located at −1.8 ppm. This upfield shifted water signal compared to the other purely carbon-based materials is explained by a large fraction of mesopores (68 %) for which intra-pore exchange averages the observed chemical shift towards larger (upfield shifted) values.

Furthermore, a possible pore filling mechanism can be deduced from Figure 6.22, where time-resolved ^1H MAS spectra of water impregnated Sucrose-HC-1000 are shown.
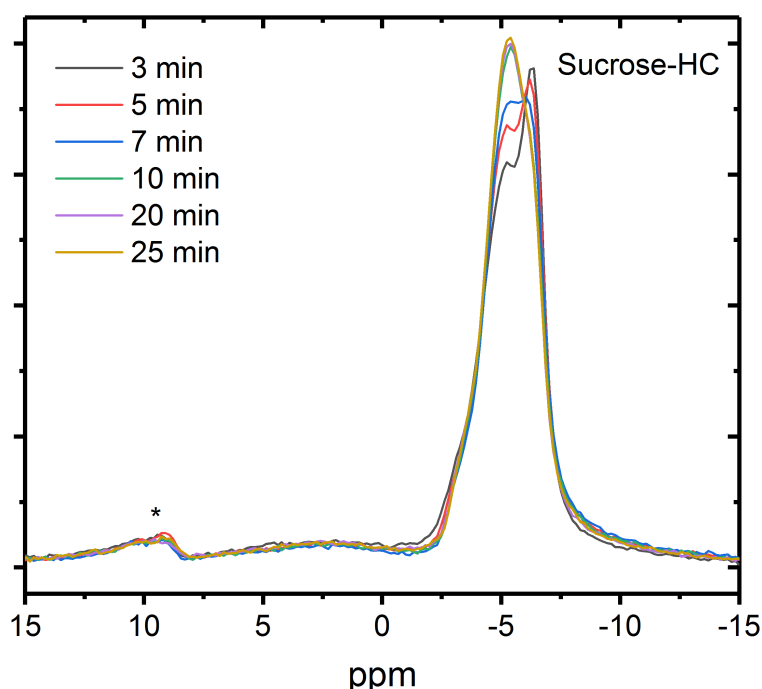

Figure 6.22: Time-resolved ^1H 5kHz MAS spectra of Sucrose-HC-1000 to which 2 μL H_2O were added. One of the spinning sidebands is denoted by an asterisk.

At an early stage (3 min), a signal located at -6.4 ppm is steadily decreasing in intensity, while after 20 minutes the center of the most intense peak is found at -5.1 ppm. At an initial stage (3 min), the surface positions are occupied with H_2O molecules, which yields an upfield shifted line (-6.4 ppm). In the following a steady deposition of water molecules further distanced from the pore walls occurs, accompanied by intra-pore exchange, which yields a less up-field shifted signal (-5.1 ppm). This shows that a slow redistribution of H_2O occurs in the pore system.

The findings of this section are summarized in Figure 6.23. As shown in Section 6.3.4, the number of upfield shifted signals is indicative of the presence of an interconnected pore system or of disconnected pores, where no inter-pore exchange can occur. The diamagnetic shift can further be used to estimate the average position of exchanging water molecules from the pore wall. A severe upfield shift can be associated to water in pores with a small pore diameter, i.e. micropores, while a less upfield shifted signal is related to water molecules in larger pores.
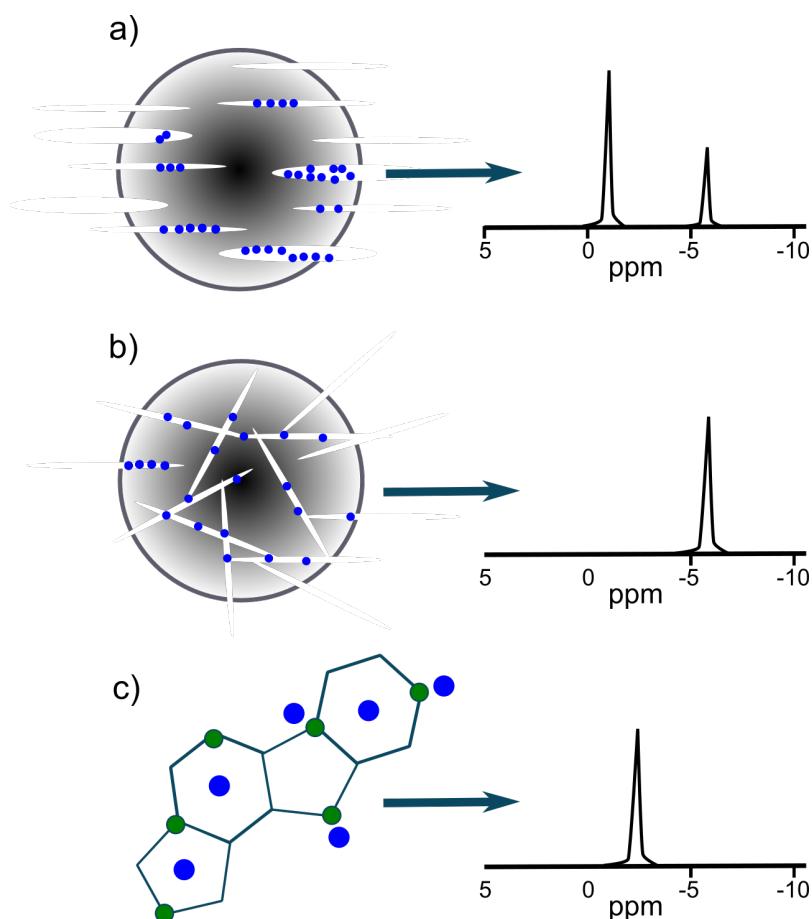
Figure 6.23: Schematic representation of the relationship between pore connectivity, H_2O adsorption sites and ^1H signals in different pore systems. Blue spheres represent water molecules, green spheres nitrogen atoms. (a) Micropores and mesopores which are not connected. (b) Connected microporous network. (c) Two-site exchange in C_1N_1.

In Figure 6.23 a), a pore system that exhibits micro- and mesopores which are not interconnected with each other is shown (e.g. Sucrose-HC-850), where two sets of isolated signals for pores of different size are observed. If the pores of different size were connected, a single peak at an average position would be observed. From this observation it can be concluded that no exchange of H_2O between the two different sites occurs. If the pores of different size were connected, a single peak at an average position would be observed. A pore system of interconnected micropores (e.g. Sucrose-HC-1000), for which a single signal can be observed is shown in 6.23 b). Figure 6.23 c) represents the case of heterocyclic aromatic structures, in the case for C_1N_1. The result of an exchange between two different sites, one of which has a heteroatom for strong hydrogen bonding, yields a signal that is less upfield shifted compared to signals found for the purely carbon-based materials in a) and b).

Overall, ^{1}H NMR spectroscopy on water in polar and non-polar pores of carbonaceous materials has proven to be a sensitive tool to probe i) the local pore structure, ii) exchange phenomena and iii) non-covalent interactions such as hydrogen bonding. Besides that, the general affinity of water to enter either pores could be revealed within this work. Future work may consider a broader pore saturation region (i.e. 10–100 % pore saturation), in order to have a measure for the pores which are accessible for water molecules. Including these experiments would be useful, in order to get an impression for the actual amount of cryptopores in the C_1N_1 materials. Additional relaxation (T_1, T_2) measurements are useful, in order to obtain information about the dynamics of a certain water signal. Further ^{1}H experiments using non-polar organic molecules such as toluene (as the guest molecule) appear useful, in order to estimate whether hydrogen-bonding and further non-covalent interactions are a main source of the water repelling properties of C_1N_1.

6.3.5 References

(1) Wang, Y., Song, Y., & Xia, Y. (2016). Electrochemical capacitors: mechanism, materials, systems, characterization and applications. *Chemical Society Reviews*, *45*(21), 5925-5950.

(2) Yang, M., & Zhou, Z. (2017). Recent breakthroughs in supercapacitors boosted by nitrogen-rich porous carbon materials. *Advanced Science*, *4*(8), 1600408.

(3) Perovic, M., Qin, Q., & Oschatz, M. (2020). From molecular precursors to nanoparticles—tailoring the adsorption properties of porous carbon materials by controlled chemical functionalization. *Advanced Functional Materials*, *30*(41), 1908371.

(4) Weinberger, C., Heckel, T., Schnippering, P., Schmitz, M., Guo, A., Keil, W., ... & Wilhelm, R. (2019). Straightforward immobilization of phosphonic acids and phosphoric acid esters on mesoporous silica and their application in an asymmetric aldol reaction. *Nanomaterials*, *9*(2), 249.

(5) Forse, A. C., Merlet, C., Grey, C. P., & Griffin, J. M. (2021). NMR studies of adsorption and diffusion in porous carbonaceous materials. *Progress in Nuclear Magnetic Resonance Spectroscopy*, *124*, 57-84.

(6) Kavokine, N., Bocquet, M. L., & Bocquet, L. (2022). Fluctuation-induced quantum friction in nanoscale water flows. *Nature*, *602*(7895), 84-90.

(7) Ong, W. J., Tan, L. L., Ng, Y. H., Yong, S. T., & Chai, S. P. (2016). Graphitic carbon nitride (g-C3N4)-based photocatalysts for artificial photosynthesis and environmental remediation: are we a step closer to achieving sustainability?. *Chemical reviews*, *116*(12), 7159-7329.

(8) Kossmann, J., Heil, T., Antonietti, M., & López-Salas, N. (2020). Guanine-Derived Porous Carbonaceous Materials: Towards C1N1. *ChemSusChem*, *13*(24), 6643.

(9) Odziomek, M., Giusto, P., Kossmann, J., Tarakina, N. V., Heske, J., Rivadeneira, S. M., Keil, W., Schmidt, C., Mazzanti, S., Savateev, A., Kühne, T. D., Antonietti, M., López-Salas, N. (2022). "Red carbon": A rediscovered polymeric, crystalline semiconductor. *Submitted*.

(10) Heske, J., Walczak, R., Epping, J. D., Youk, S., Sahoo, S. K., Antonietti, M., ... & Oschatz, M. (2021). When water becomes an integral part of carbon–combining theory and experiment to understand the zeolite-like water adsorption properties of porous C 2 N materials. *Journal of Materials Chemistry A*, *9*(39), 22563-22572.

(11) Kossmann, J., Piankova, D., Tarakina, N. V., Heske, J., Kühne, T. D., Schmidt, J., ... & López-Salas, N. (2021). Guanine condensates as covalent materials and the concept of cryptopores. *Carbon*, *172*, 497-505.

(12) Haigh, C. W., & Mallion, R. B. (1979). Ring current theories in nuclear magnetic resonance. *Progress in nuclear magnetic resonance spectroscopy*, *13*(4), 303-344.

(13) Pople, J. A. (1956). Proton magnetic resonance of hydrocarbons. *The Journal of Chemical Physics*, *24*(5), 1111-1111.

(14) Oth, J. F. M., Woo, E. P., & Sondheimer, F. (1973). Unsaturated macrocyclic compounds. LXXXIX. Dianion of [18] annulene. *Journal of the American Chemical Society*, *95*(22), 7337-7345.

(15) Harris, R. K., Thompson, T. V., Norman, P. R., & Pottage, C. (1999). Phosphorus-31 NMR studies of adsorption onto activated carbon. *Carbon*, *37*(9), 1425-1430.

(16) Schleyer, P. V. R., Manoharan, M., Wang, Z. X., Kiran, B., Jiao, H., Puchta, R., & van Eikema Hommes, N. J. (2001). Dissected nucleus-independent chemical shift analysis of π-aromaticity and antiaromaticity. *Organic Letters*, *3*(16), 2465-2468.

(17) Chen, Z., Wannere, C. S., Corminboeuf, C., Puchta, R., & Schleyer, P. V. R. (2005). Nucleus-independent chemical shifts (NICS) as an aromaticity criterion. *Chemical reviews*, *105*(10), 3842-3888.

(18) Borchardt, L., Oschatz, M., Paasch, S., Kaskel, S., & Brunner, E. (2013). Interaction of electrolyte molecules with carbon materials of well-defined porosity: characterization by solid-state NMR spectroscopy. *Physical Chemistry Chemical Physics*, *15*(36), 15177-15184.

(19) Báez-Grez, R., Rabanal-León, W. A., Alvarez-Thon, L., Ruiz, L., Tiznado, W., & Pino-Rios, R. (2019). Aromaticity in heterocyclic analogues of benzene: Dissected NICS and current density analysis. *Journal of Physical Organic Chemistry*, *32*(1), e3823.

(20) Wortmann, M., Keil, W., Brockhagen B., Biedinger, J., Westphal, M., Weinberger, C., Diestelhorst, E., Hachmann, W., Zhao, Y., Tiemann, M., Reiss, G., Hüsgen, B., Schmidt, C., Sattler, K., Frese, N. (2022). Pyrolysis of sucrose-derived hydrochar. *Journal of Analytical and Applied Pyrolysis*, 161, 105404.

(21) Wortmann, M., Keil, W., Westphal, M., Diestelhorst, E., Brockhagen, B., Biedinger, J., Weinberger, C., Bandzio, L., Tiemann, M., Hütten, A., Schmidt, C., Reiss, G., Sattler, K., Frese, N. (20XX). Synthesis of Carbon Microspheres with Binary Size Distribution via Hydrothermal Carbonization of Trehalose. *To be submitted*.

(22) Baccile, N., Laurent, G., Babonneau, F., Fayon, F., Titirici, M. M., & Antonietti, M. (2009). Structural characterization of hydrothermal carbon spheres by advanced solid-state MAS 13C NMR investigations. *The Journal of Physical Chemistry C*, *113*(22), 9644-9654.

(23) Hansen, M., & Jakobsen, H. J. (1973). High-resolution 13C NMR spectra and long-range 13C–1H spin coupling constants in pyridine and 2-bromopyridine. *Journal of Magnetic Resonance (1969)*, *10*(1), 74-84.

(24) Kawashima, H., Yamashita, Y., & Saito, I. (1997). Solid-state 13C NMR of pyridine-swollen coal. *Energy & fuels*, *11*(3), 709-715.

(25) Babij, N. R., McCusker, E. O., Whiteker, G. T., Canturk, B., Choy, N., Creemer, L. C., ... & Yang, Q. (2016). NMR chemical shifts of trace impurities: Industrially preferred solvents used in process and green chemistry. *Organic process research & development*, *20*(3), 661-667.

(26) Song, Y., Chong, Y., Raghavan, A., Xing, Y., Ling, Y., Kleinhammes, A., & Wu, Y. (2017). Nucleation and growth process of water adsorption in micropores of activated carbon revealed by NMR. *The Journal of Physical Chemistry C*, *121*(15), 8504-8509.

(27) Xu, Y., Watermann, T., Limbach, H. H., Gutmann, T., Sebastiani, D., & Buntkowsky, G. (2014). Water and small organic molecules as probes for geometric confinement in well-ordered mesoporous carbon materials. *Physical Chemistry Chemical Physics*, *16*(20), 9327-9336.

(28) Grünberg, B., Emmler, T., Gedat, E., Shenderovich, I., Findenegg, G. H., Limbach, H. H., & Buntkowsky, G. (2004). Hydrogen bonding of water confined in mesoporous silica MCM-41 and SBA-15 studied by 1H solid-state NMR. *Chemistry–A European Journal*, *10*(22), 5689-5696.

(29) Balevicius, V., Aidas, K., Tamuliene, J., & Fuess, H. (2005). 1H NMR and DFT study of proton exchange in heterogeneous structures of pyridine-N-oxide/HCl/DCl/H2O. *Spectrochimica Acta Part A: Molecular and Biomolecular Spectroscopy*, *61*(5), 835-839.

(30) Cervini, L., Lynes, O. D., Akien, G. R., Kerridge, A., Barrow, N. S., & Griffin, J. M. (2019). Factors affecting the nucleus-independent chemical shift in NMR studies of microporous carbon electrode materials. *Energy Storage Materials*, *21*, 335-346.

(31) Anderson, R. J., McNicholas, T. P., Kleinhammes, A., Wang, A., Liu, J., & Wu, Y. (2010). NMR methods for characterizing the pore structures and hydrogen storage properties of microporous carbons. *Journal of the American Chemical Society*, *132*(25), 8618-8626.

(32) Cervini, L., Lynes, O. D., Akien, G. R., Kerridge, A., Barrow, N. S., & Griffin, J. M. (2019). Factors affecting the nucleus-independent chemical shift in NMR studies of microporous carbon electrode materials. *Energy Storage Materials*, *21*, 335-346.

(33) Li, K., Bo, Z., Yan, J., & Cen, K. (2016). Solid-state NMR study of ion adsorption and charge storage in graphene film supercapacitor electrodes. *Scientific Reports*, *6*(1), 1-9.

(34) Levitt, M. H. (2013). *Spin dynamics: basics of nuclear magnetic resonance*. John Wiley & Sons

Chapter 7

Summary & Outlook

Two main topics have been scrutinized within this work, namely electrolytes and carbonaceous electrodes.
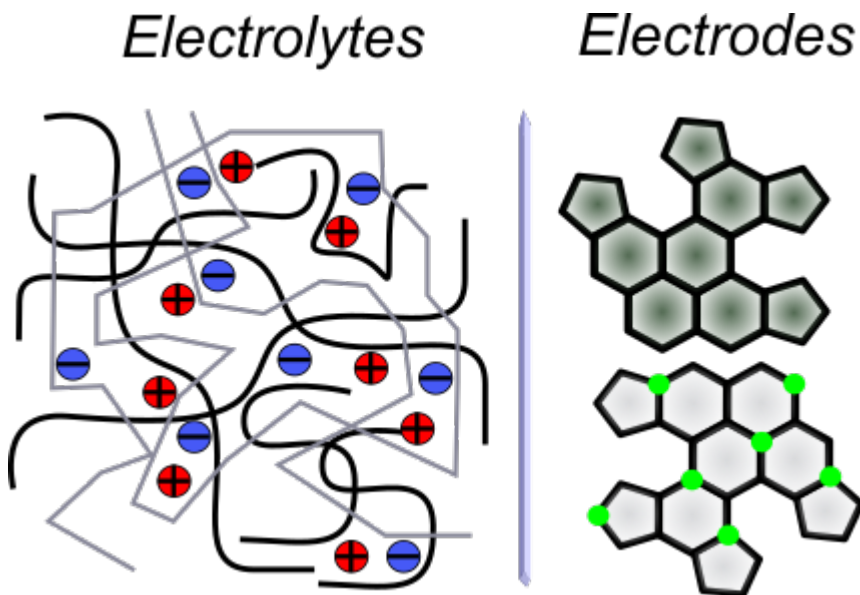
Figure S.1: Schematic representations of polymer electrolytes (left, discussed in Chapter 5) and carbonaceous electrode materials (right, discussed in Chapter 6).

Hydrogen bonding properties of the ionic liquid [EMIM][OTf], which is the solvent of the gel polymer electrolyte in this work, were investigated in **Section 5.1**. We find that the [OTf]$^-$ anion forms strong intermolecular hydrogen bonds to the [EMIM]$^+$ cation, which activate the acidic C–H protons of [EMIM]$^+$ and enable H/D exchange reactions under relatively mild conditions. In addition, the deuteration yield is highly sensitive to the molar ratio of D$_2$O/[EMIM][OTf], which is explained by altered ion configurations (ion cluster, ion pairs) for varying molar fractions. In addition, the performed experiments suggest that the hydrogen bonding acceptor properties of the [OTf]$^-$ anion are more relevant than the anion basicity for a H/D exchange reaction. These findings may pave the way to the synthesis of advanced ionic liquids, starting from [EMIM]$^+$, which is activated at the C2 position or equally at C2, C4 and C5. Using selectively deuterated imidazolium-based ionic liquids would be desirable, in order to study site-specific exchange reactions and further reactions with ionic liquids by means of NMR. One possible field of application would be electrochemical reactions of imidazolium-based ionic liquids, such as the electrochemical gating (metallization of an insulator).[1]

Dynamic aspects of hybrid ionogels are discussed in **Section 5.2**. Liquid-like ion dynamics of the [EMIM]$^+$ and Li$^+$ could be seen from ^{1}H and ^{7}Li MAS experiments, which indicate that the polymer matrix and the silica network slow down the ion dynamics. The advantage of the silica network in the polymer electrolyte, further examined in Section 5.3, is explained by a decrease of the crystalline polymer fraction. Additionally, the experiments show a good correlation between the intensity of the ^{7}Li spinning sidebands and the lithium transference number. This is explained by spinning sidebands indicating the fraction of immobilized lithium cations, which leads to a decrease of the ion transference number.

The ion diffusion (Li$^+$, [EMIM]$^+$ and [OTf]$^-$) inside of PVdF-HFP-based polymer electrolytes is discussed in **Section 5.3**. Anomalous ion diffusion is found for all studied polymer electrolytes (and hybrid electrolytes), which means that the mean squared displacement of a particle is non-linearly related to its diffusion time. This can be explained by a restricted ion diffusion caused by the polymer matrix. Additionally, we find that the significantly smaller [OTf]$^-$ anion (compared to the [EMIM]$^+$ cation) exhibits a smaller diffusion coefficient, which is not expected based on the Stokes-Einstein equation. This phenomenon is likely to be caused by correlated anion-anion motions. In addition, the *in situ* generated silica network in combination with a high electrolyte concentration increases the ion diffusivity in the polymer electrolyte significantly.

The studied PVdF-HFP-based polymer electrolytes were implemented into symmetric lithium cells and tested for their electrochemical performance in comparison to a cell, in which the polymer film was replaced by a Whatman® (glass fiber) membrane (**Section 5.4**). It could be shown that cycling a symmetric lithium cell containing the PVdF-HFP-based polymer electrolyte results in a SEI formation and a degradation of the polymer electrolyte. Additional experiments, e.g Coulombic efficiency need to be carried out in order to judge whether the prepared polymer electrolytes can potentially be used in lithium ion batteries.

The influence of MAS experiments on ion conductivity and NMR spectra of PVdF-HFP-based polymer electrolytes is discussed in **Section 5.5**. It could be shown that under MAS the pristine polymer electrolyte changes its shape and deforms towards a hollow-cylinder shaped membrane. This is accompanied by a significant increase in the ion conductivity which is explained by the formation of elongated polymer segments under the pressure of the MAS conditions. The latter should be verified by future mechanical stretching experiments of

polymer electrolytes, which would possibly show an analogous behavior compared to the material deformation under MAS conditions. These results ultimately show that the ion conductivity can be enhanced by aligning the polymer network. In the future, XRD experiments on mechanically stretched PVdF-HFP polymer electrolyte films should be carried out, in order to have additional insight into possible changes in the crystallinity of the polymer, i.e. changes of the crystal polymorph, as seen for PEO-based polymer electrolytes earlier.[2, 3]

Different carbonaceous electrode materials were investigated in Chapter 6. In **Section 6.1** the pyrolysis of saccharide-derived hydrochars (hard carbon) was scrutinized. The temperature-resolved chemical transition of sucrose-derived hydrochars was followed by means of ^{13}C NMR spectroscopy, from which a transition from a furane-dominated towards a graphite-like structure could be deduced. Anisotropic aromatic domains grow during the process of pyrolysis and cause a line shift accompanied by a broadening, which is seen for sucrose-derived hydrochars. Selecting trehalose as a second precursor for hydrothermal carbonization resulted in a similar chemical structure. Judging from the information of the ^{13}C DE and CP spectra, there is only a minor influence of the precursor (sucrose, trehalose) on the overall chemical structure of the carbonized product.

The chemical structure of polymeric carbon suboxide (C_3O_2) and its carbonized product were analyzed in **Section 6.2**. Using ^{13}C NMR spectroscopy the chemical structure of polymeric C_3O_2 could be revealed as being composed of polypyrone units. Further insight into the aromatic network could be obtained by ^1H NMR spectroscopy, which points to unique bonding properties associated with an extremely downfield shifted signal at 17.3 ppm. Carbonization of polymeric C_3O_2 results in the formation of aromatic sp^2-carbon domains, which is seen by a broad and featureless ^{13}C signal. The width of this signal of c. 4 kHz is similar to the ones found for the saccharide-derived hydrochars (Section 6.1), which indicates that a similar anisotropy of the magnetic susceptibility is present for these materials.

Finally, in **Section 6.3** the interaction of water with all carbonaceous matrices was elucidated. In particular, the material C_1N_1, which is assumed to possess polar pores, and its adsorption of water was scrutinized. Signals originating from water molecules inside of an aromatic network and outside of an aromatic network (in-pore, ex-pore) could be distinguished by means of ^1H NMR spectroscopy. It was shown that water molecules can easily access the pores of a non-polar matrix (hydrothermally carbonized trehalose). However, only a very limited accessibility

of liquid water in the polar pores of two differently prepared C_1N_1 materials could be observed. This unexpected observation indicates a water repelling character of the two C_1N_1 samples. One possible explanation for this observation could be that both C_1N_1 samples exhibit so-called cryptopores, which are inaccessible for water molecules and therefore remain unoccupied.[4] Still, the role of pore polarity in the adsorption of liquid water in C_1N_1 is not fully understood and needs to be specified in further experiments. Also, impregnation experiments including simple non-polar solvents, i.e. toluene may be useful, in order to estimate the influence of non-covalent interactions on the adsorption.

In a second part, the interaction of water with exclusively carbon-based materials was analyzed. From time-resolved ^{1}H spectra information about exchanging or non-exchanging water molecules and therefore about the pore structure of the carbon-based materials was obtained. Single highly upfield shifted signals are associated with an interconnected porous network, in which water molecules can partake in inter- and intra-pore exchange. On the other hand, the presence of two or more separated upfield shifted signals was related to disconnected pores, for which the main exchange mechanism is the intra-pore exchange. Future NMR experiments may involve commercial electrolytes used for lithium ion batteries or sodium ion batteries in order to obtain information e.g. about the average distance of a specific ion from the carbon surface.

Overall, this work has highlighted the potential of NMR spectroscopy as a tool to study energy storage materials (electrolytes and electrodes). The scrutinized materials show a potential as sustainable and renewable energy storage materials, for which this work has made a contribution. The study on polymer electrolytes has linked fundamental physicochemical properties to a manifold of NMR spectra and diffusion data and is therefore a relevant contribution for a better understanding of this new class of materials. In particular the ion dynamics could be probed by NMR spectroscopy and therefore opens up an alternative perspective on polymer electrolytes in addition to electrochemical measurements. The studied electrode materials have potential use as electrodes for metal ion batteries (saccharide-derived hydrochars) and supercapacitor electrodes (C_1N_1). Again, NMR spectroscopy has proven to be a versatile tool to study the adsorption of guest molecules into carbonaceous host matrices. Specifically, the high sensitivity of the chemical shift towards in-pore and ex-pore guest molecules shows that NMR spectroscopy is an inevitable tool for the understanding of these rather complex adsorption mechanisms.

References

(1) Hope, M. A., Griffith, K. J., Cui, B., Gao, F., Dutton, S. E., Parkin, S. S., & Grey, C. P. (2018). The role of ionic liquid breakdown in the electrochemical metallization of VO2: An NMR study of gating mechanisms and VO2 reduction. *Journal of the American Chemical Society*, *140*(48), 16685-16696.

(2) Golodnitsky, D., Livshits, E., Ulus, A., Barkay, Z., Lapides, I., Peled, E., ... & Greenbaum, S. (2001). Fast ion transport phenomena in oriented semicrystalline LiI– P (EO) n-based polymer electrolytes. *The Journal of Physical Chemistry A*, *105*(44), 10098-10106.

(3) Golodnitsky, D., Livshits, E., Kovarsky, R., Peled, E., Chung, S. H., Suarez, S., & Greenbaum, S. G. (2004). New generation of ordered polymer electrolytes for lithium batteries. *Electrochemical and Solid State Letters*, *7*(11), A412.

(4) Kossmann, J., Piankova, D., Tarakina, N. V., Heske, J., Kühne, T. D., Schmidt, J., ... & López-Salas, N. (2021). Guanine condensates as covalent materials and the concept of cryptopores. *Carbon*, *172*, 497-505.

Appendix

A1. General Experimental Remarks

All solid-state NMR experiments discussed in this work were conducted on an Apollo Tecmag spectrometer equipped with a 7.1 T Oxford magnet. The corresponding [1]H Larmor frequency is 299.8145 MHz. Standard MAS probes for 4 mm and 7 mm ZrO rotors were used. The pulse sequences used, are given in the corresponding sections.

Liquid state NMR measurements were carried out using a 700 MHz Bruker Avance NEO spectrometer equipped with a high resolution cryo-probe.

In order to acquire SEM images, samples were coated with a thin layer of gold (c. 1 nm) at a nominal pressure of 10^{-2} mbar using a Leica EM SCD500 sputter coater. SEM images were recorded with a Zeiss Neon 40 scanning electron microscope, using the in-lense detector and the Everhart-Thornley (SE2) detector. Typically, an acceleration voltage of 2 kV and magnifications of 2000–5000 were used. EDX images were recorded at an acceleration voltage of 5 kV and an aperture size of 120 μm. The high-current mode was used to obtain EDX images.

The heat flux in DSC measurements was recorded in the temperature range from −70 to 170 °C using a Netzsch DSC 204 F1 Phoenix differential scanning calorimeter. Typical heating rates of 10 K/min and 20 K/min were used.

Powder X-ray diffractograms were obtained with a Bruker AXS D8 Advance diffractometer using monochromatic Cu Kα1 radiation with 40 kV and 40 mA. The goniometer step size was 0.02° for 2θ angles from 5–50°. A standard powder specimen holder (poly(methyl methacrylate)) was used which exhibits a circular notch, into which the samples were placed for XRD measurements.

A.2 Supplementary Material for Section 5.1

The presented ^{1}H and ^{2}H NMR spectra were recorded using a 700 MHz Bruker Avance NEO spectrometer equipped with a high resolution cryo-probe. The ^{1}H and ^{2}H resonance frequencies were 700.130 MHz and 107.474 MHz, respectively. Time dependent ^{1}H spectra were collected by preparing a D_2O/ [EMIM][OTf] mixture, inserting it as fast as possible into an NMR tube and recording spectra in given time intervals. Isotropic values of the nuclear magnetic shielding tensors were calculated at the RI-MP2 level of theory, using the def2/TZVP basis set.[1] The molecular geometry of each ion pair was pre-optimized in vacuum using the B3LYP DFT functional. All calculations were performed in Orca version 4.2.1.[2] The calculated isotropic chemical shielding values were used to calculate the NMR chemical shift as following:

$$\delta_i = \frac{\nu_i - \nu_{Ref}}{\nu_{Ref}} = \frac{\sigma_{Ref} - \sigma_i}{1 - \sigma_{Ref}} \approx \sigma_{Ref} - \sigma_i \qquad [A.1]$$

with ν_i, ν_{Ref}, as the reference σ_i and σ_{Ref} being assigned to the resonance frequencies and shielding parameters of sample i and of the reference sample (tetramethylsilane).

The isotropic chemical shielding of tetramethylsilane is assigned to 30.84 ppm.[3] We note that the hydrogen bond distance is shorter in [EMIM][BF$_4$] (2.0 Å) compared to [EMIM][OTf] (2.4 Å). Even though, [EMIM][OTf] exhibits a longer hydrogen bond distance, the overall strength of the hydrogen bond is larger for [EMIM][OTf]. We explain this by strong interactions of oxygen atoms of [OTf]⁻ with C2–H versus weak interactions of fluorine atoms of [BF$_4$]⁻ with C2–H. The calculated molecular arrangements of [EMIM][BF$_4$] and [EMIM][OTf] are depicted in Figure A.1. The corresponding shielding values are given in Table A.1

Distance: 2.4 Å   Distance: 2.0 Å
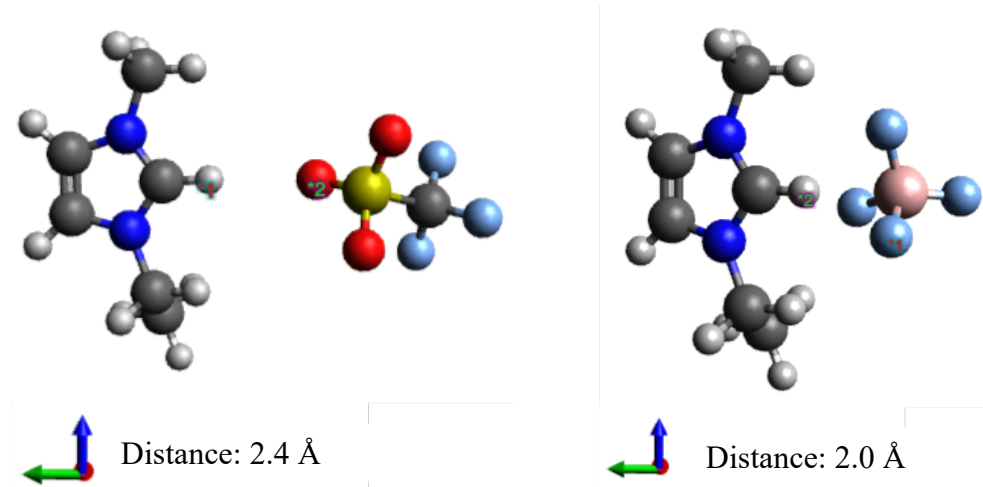
Figure A.1: Calculated molecular arrangements of [EMIM][OTf] and [EMIM][BF$_4$]. Atoms with the closest interatomic distance (1 and 2) are marked.

Table A.1: Calculated isotropic chemical shift values in ppm for an ion pair of [EMIM][BF$_4$] and [EMIM][OTf].

Ionic Liquid	C2-H	C4-H	C5-H
[EMIM][OTf]	10.35	6.18	6.23
[EMIM][BF$_4$]	9.22	6.12	6.19
Difference	1.13	0.06	0.04

Furthermore, Figures A.2-A.6 show the ^{1}H NMR spectra of different mixtures of D$_2$O and [EMIM][OTf]. Based on these results the integration of Table A.2 is carried out. The H$_2$O signal (marked with an asterisk) shifts upfield by increasing the ionic liquid concentration. This is due to H$_2$O participating in a hydrogen-bonded network.
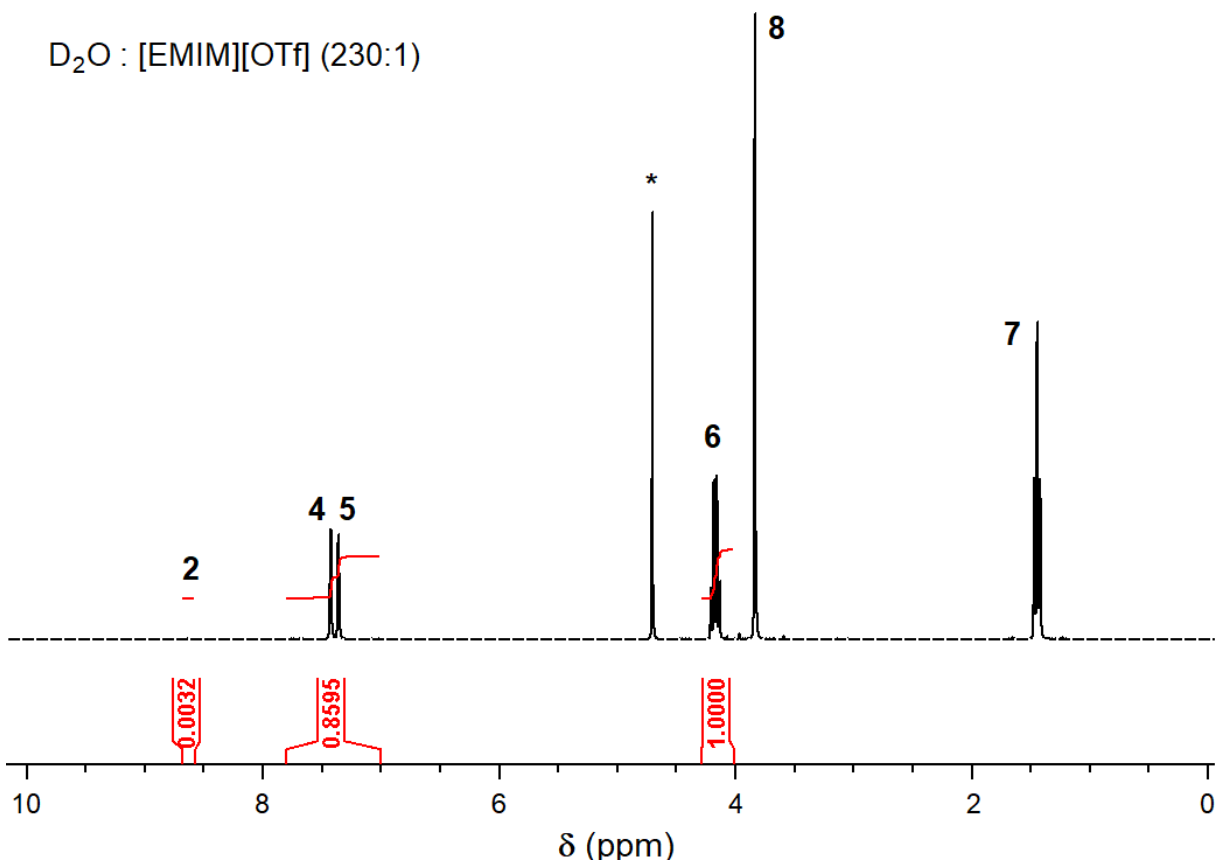
Figure A.2: ^{1}H NMR spectrum of D$_2$O/[EMIM][OTf] (230:1). The H$_2$O signal is marked with an asterisk.
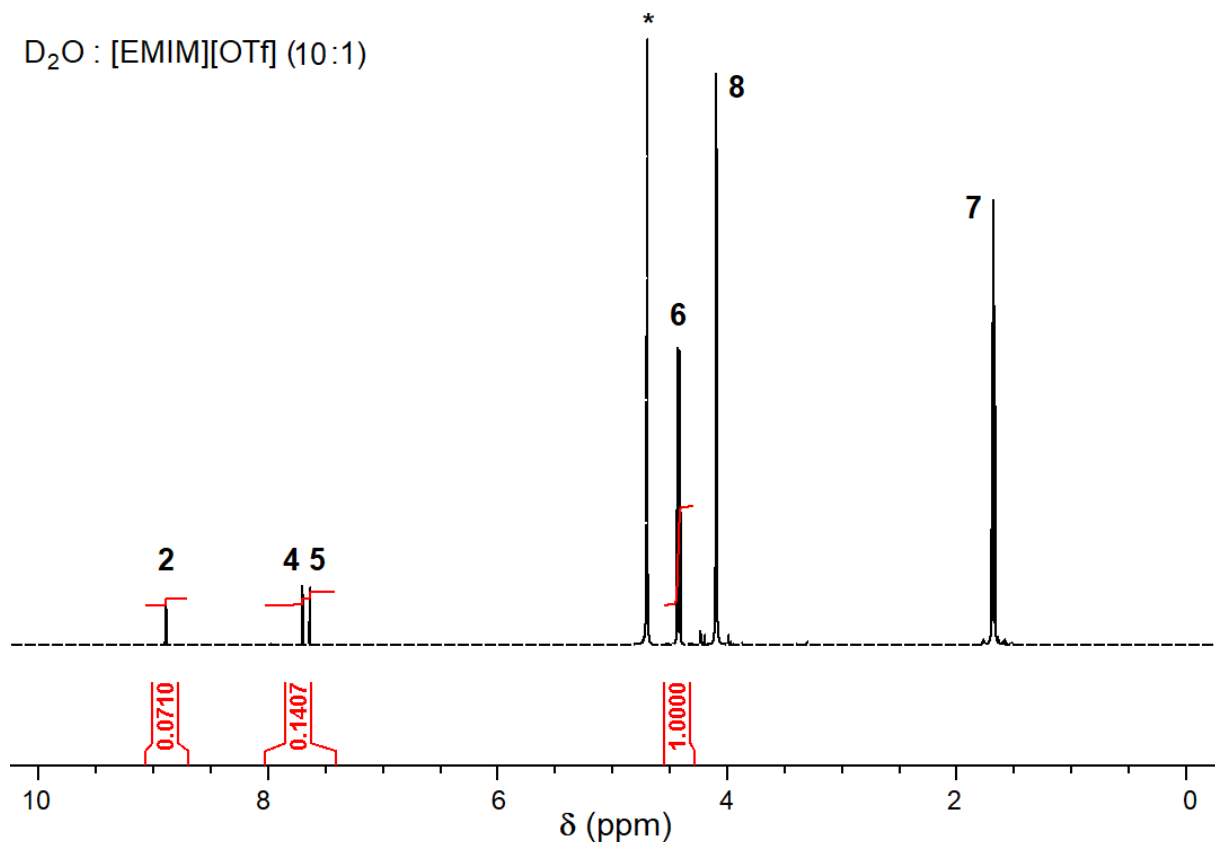
Figure A.3: ^{1}H NMR spectrum of D_2O/[EMIM][OTf] (10:1). The H_2O signal at 4.7 ppm is marked with an asterisk.
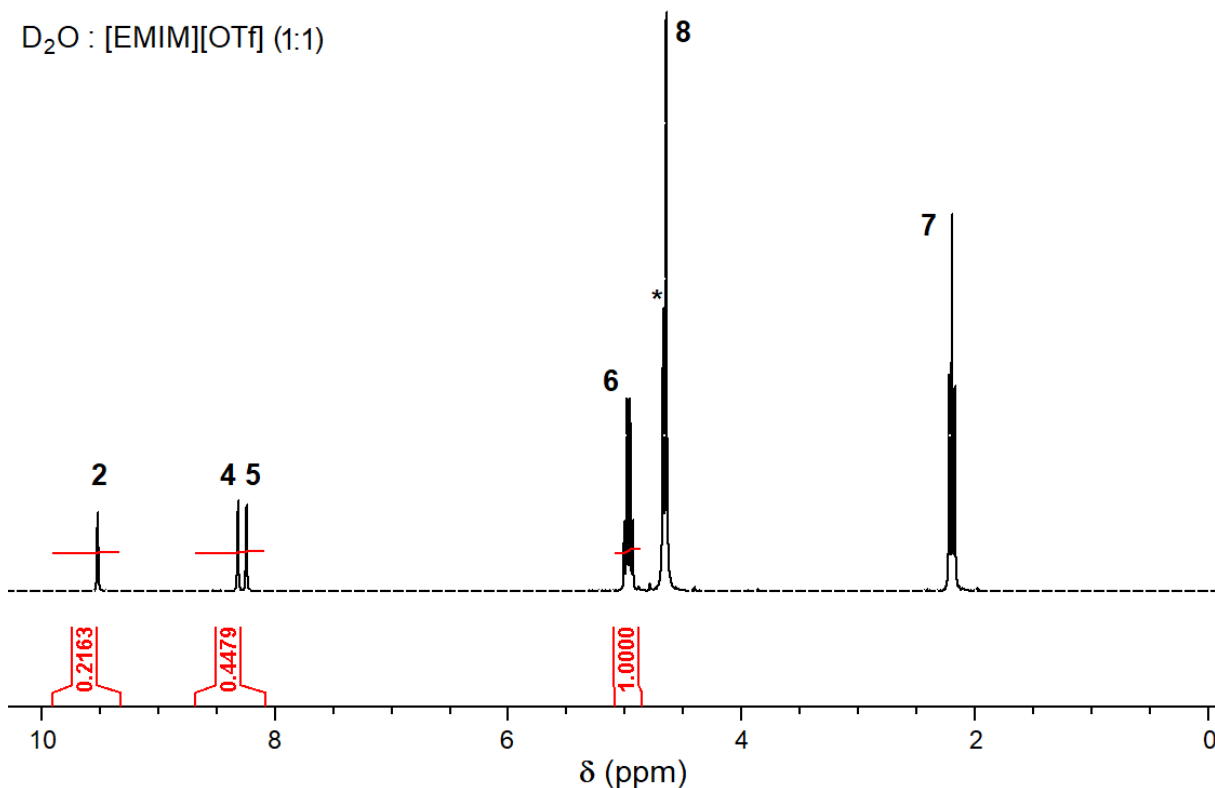
Figure A.4: ^{1}H NMR spectrum of D_2O/[EMIM][OTf] (1:1). Note that the H_2O signal shifts towards lower ppm while the absolute H_2O concentration decreases, which is reported in detail elsewhere.[4]
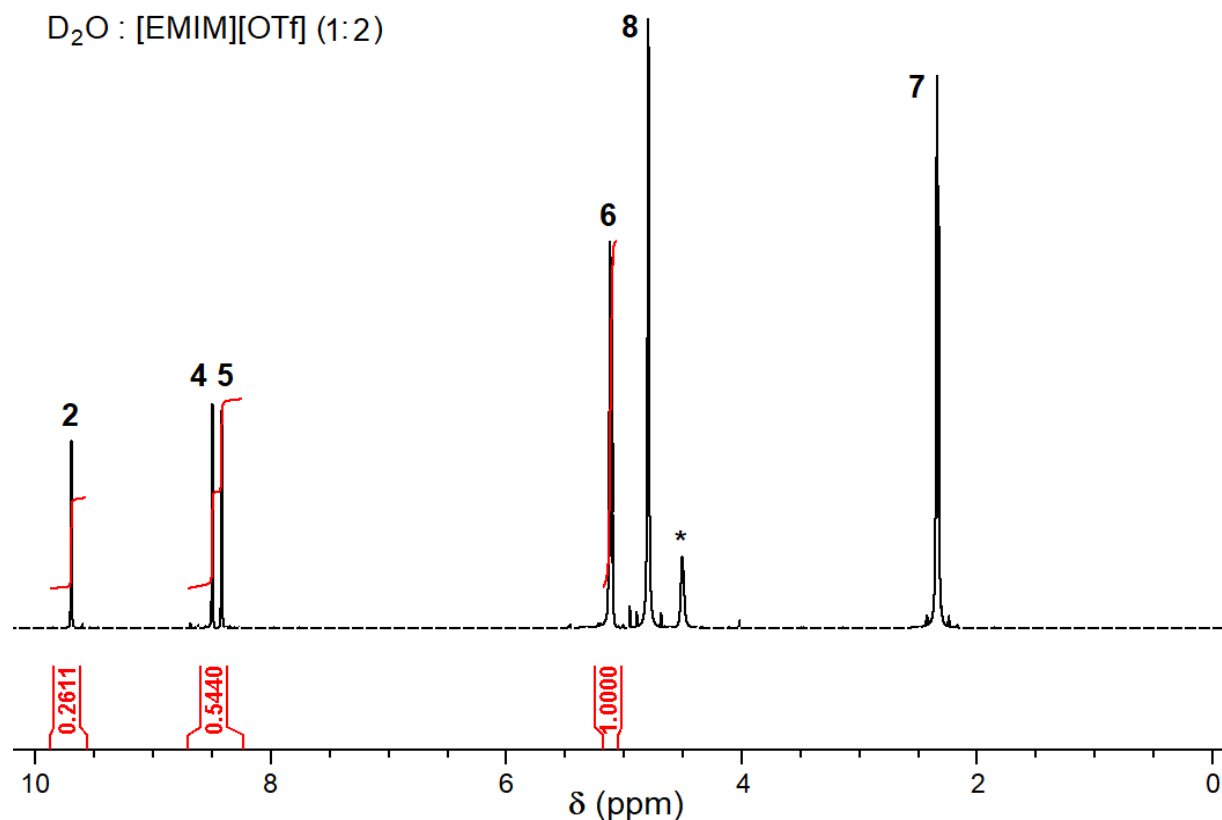
D$_2$O : [EMIM][OTf] (1:2)

Figure A.5: ^{1}H NMR spectrum of D$_2$O/[EMIM][OTf] (1:2). The H$_2$O signal is marked with an asterisk.
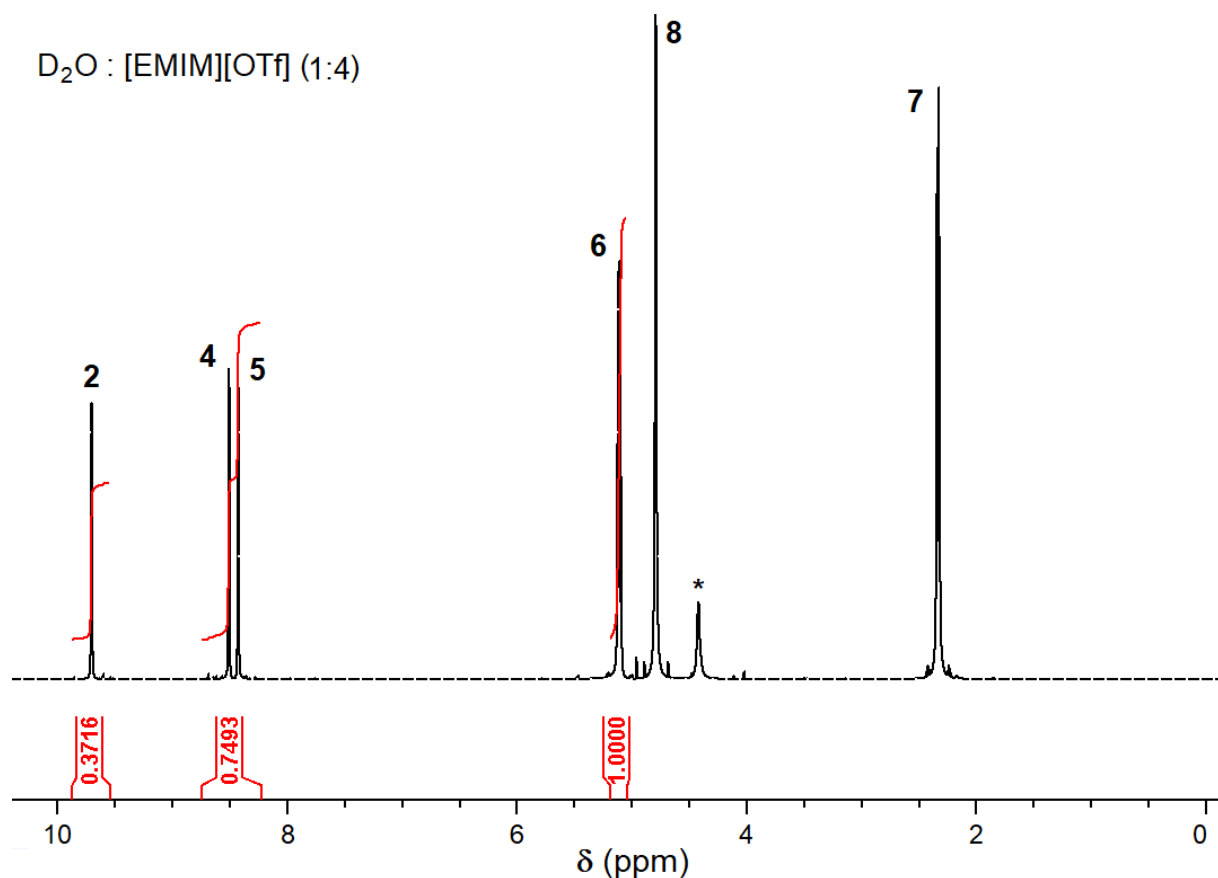
D$_2$O : [EMIM][OTf] (1:4)

Figure A.6: ^{1}H NMR spectrum of D$_2$O/[EMIM][OTf] (1:4). The H$_2$O signal is marked with an asterisk.

Table A.2: Overview of the ^{1}H integrals for a variety of mixtures of [EMIM][OTf] and D_2O treated at condition 100 °C without the removal of the volatile compounds.

^{1}H integral	c (n(D_2O)/n([EMIM][OTf]))[a]				
	230:1	**10:1**	**1:1**	**1:2**	**1:4**
C2-H	0.3%	14%	44%	52%	74%
C4+C5-H[b]	86%	14%	45%	54%	74%

[a] Based on the assumption of the densities being approximately 1.387 g cm^{-3} for [EMIM][OTf] and 1.107 g cm^{-3} for D_2O at 25°C.
[b] The sum of proton signals from C4-H and C5-H are considered due to partial signal overlapping, seen in Figure 5.3.

References

(1) Saihara, K., Yoshimura, Y., Ohta, S., & Shimizu, A. (2015). Properties of water confined in ionic liquids. *Scientific reports*, *5*(1), 1-10.
(2) Weigend, F., & Ahlrichs, R. (2005). Balanced basis sets of split valence, triple zeta valence and quadruple zeta valence quality for H to Rn: Design and assessment of accuracy. *Physical Chemistry Chemical Physics*, *7*(18), 3297-3305.
(3) Neese, F. (2018). Software update: the ORCA program system, version 4.0. *Wiley Interdisciplinary Reviews: Computational Molecular Science*, *8*(1), e1327.
(4) Makulski, W., & Jackowski, K. (2020). 1H, 13C and 29Si magnetic shielding in gaseous and liquid tetramethylsilane. *Journal of Magnetic Resonance*, *313*, 106716.

A.3 Supplementary Material for Section 5.2

SEM and EDX images of sample S2 are shown in Figure A.7. They support the interpretation made in Section 5.2, that a silica network is present in the sample. Nevertheless, Figure A.7 also shows the presence of few µm-sized silica particles, which can be found at different spots in the sample.
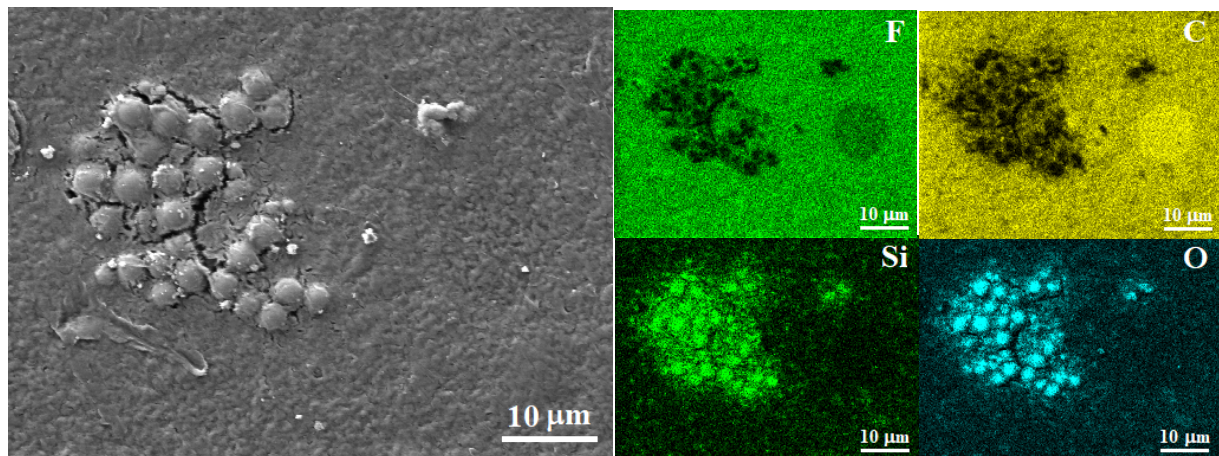

Figure A.7: SEM image and EDX (F, C, Si and O) maps of sample S2. The scanning electron microscopy reveals the presence of 1–4 µm sized spheres. As evidenced by EDX maps, these spherical particles are condensed silica particles. Next to these particles, a silica network is revealed by EDX, showing that silica is present throughout the sample.

The effect of the silica matrix on the polymer mobility is further supported by the deconvolution of the ^{1}H spectra (Figure 5.8) presented in Figure A.8. Clearly, the fraction of broad ^{1}H signals is reduced by implementing the silica matrix.
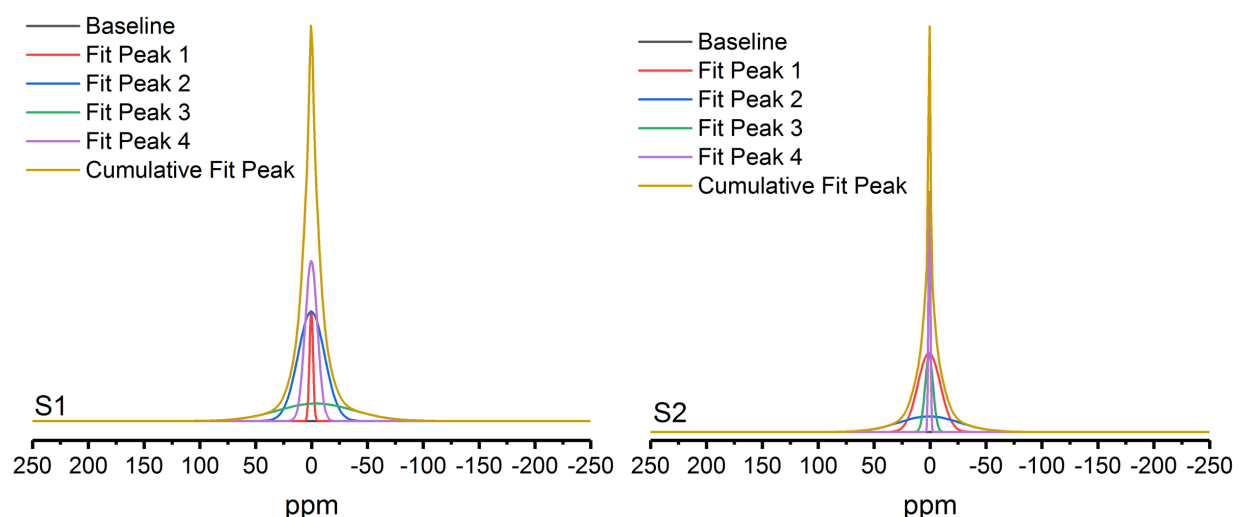
Figure A.8: Static ^{1}H spectra and deconvolutions of sample S1 and S2. The fraction of broad signals is reduced for S2, due to the silica network increasing the amount of the mobile amorphous fraction.

The effect of MAS on the ^{1}H linewidth is shown in Figure A.9. By increasing MAS frequency, no notable line narrowing can be observed, which supports the interpretation of van Wüllen of a distribution of isotropic chemical shifts.[1] The limiting linewidth of the instrument is c. 10 Hz.
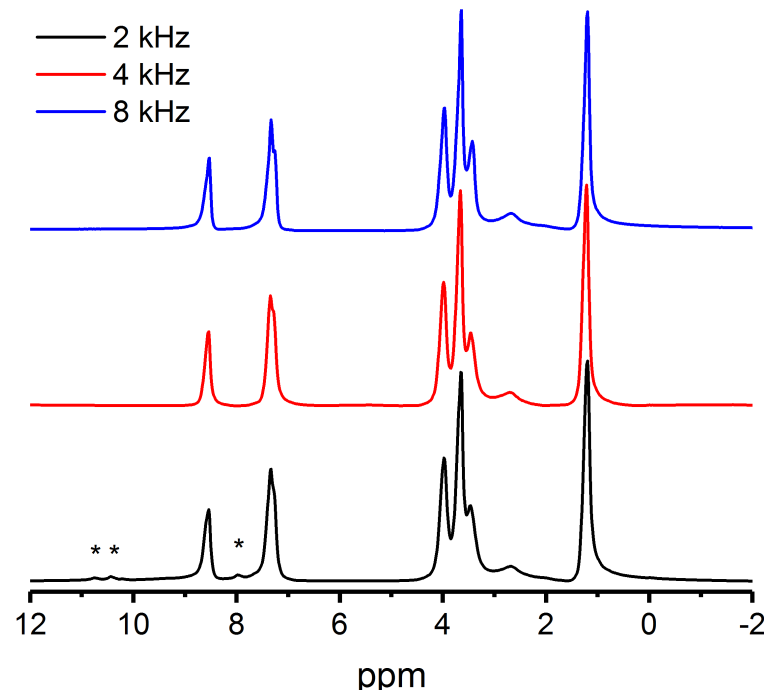

Figure A.9: Example of ^{1}H MAS spectra of sample S3, which are equivalent for the sample series. Obviously, the increase in MAS frequency does not yield a notable decrease in linewidth.

References

(1) Echelmeyer, T., Meyer, H. W., & van Wüllen, L. (2009). Novel ternary composite electrolytes: Li ion conducting ionic liquids in silica glass. *Chemistry of Materials*, *21*(11), 2280-2285.

A.4 Supplementary Material for Section 5.3

The Cotts-13 pulse sequence was tested for diffusion experiments carried out at Leipzig University, yielding the same results as for the stimulated-echo pulse sequence.[1] ^{1}H and ^{19}F diffusion curves are presented in Figures A10-A13. All of them show a slower anion diffusion compared to the [EMIM]$^+$ cation diffusion.
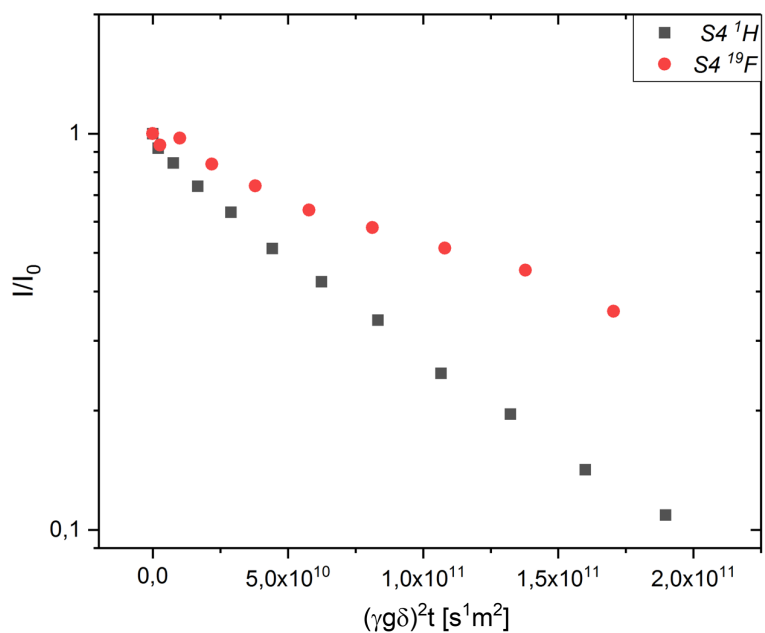
Figure A.10: ^{1}H and ^{19}F diffusion curves of sample S4, measured at 288 K.
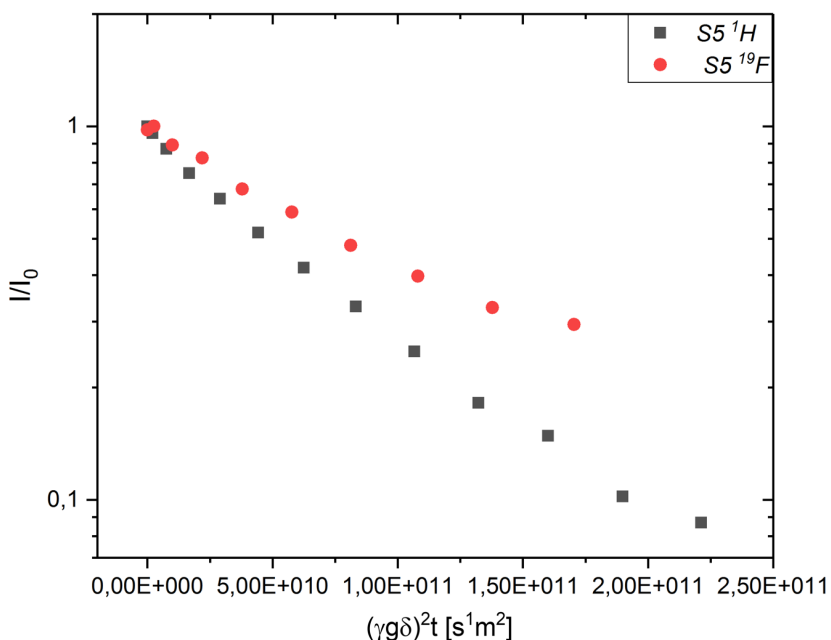
Figure A.11: ^{1}H and ^{19}F diffusion curves of sample S5, measured at 288 K.
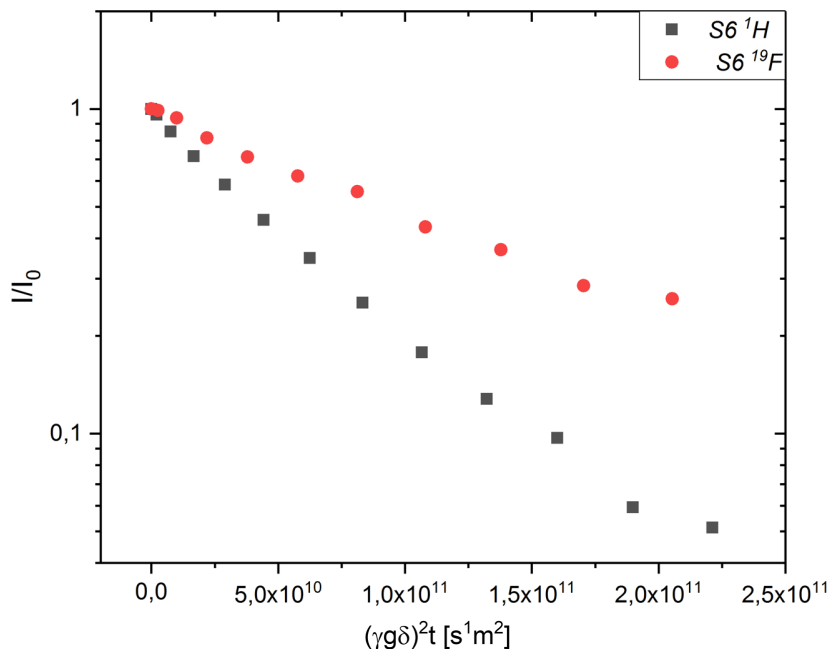
Figure A.12: [1]H and ^{19}F diffusion curves of sample S6, measured at 288 K.
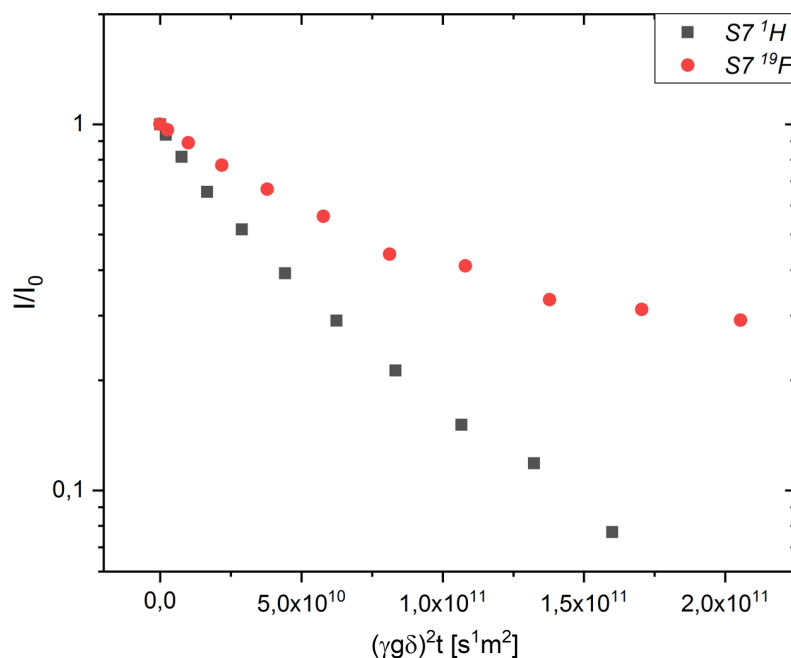
Figure A.13: [1]H and ^{19}F diffusion curves of sample S7, measured at 288 K.

The fit results of the activation energies (electrolyte solution) yield 12.1 ± 0.1 kJ/mol, 12.7 ± 0.4 kJ/mol and 9.3 ± 0.4 kJ/mol for $[EMIM]^+$, $[OTf]^-$ and Li^+. The $[EMIM]^+$ activation energy in S3 is 20.0 ± 1 kJ/mol and therefore almost twice as high as in the bulk electrolyte solution.
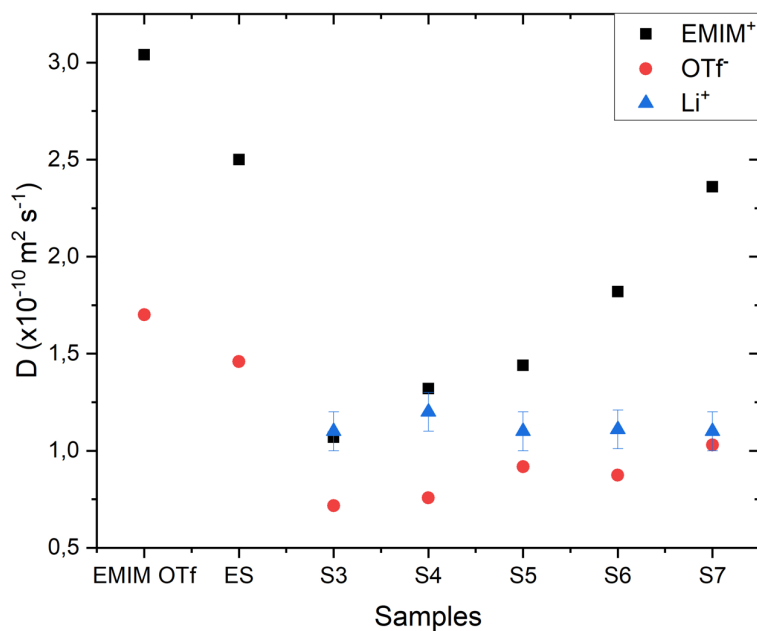
Figure A.14: [1]H, [7]Li and [19]F Diffusion coefficients, measured at 15 °C for the complete sample series including the neat ionic liquid [EMIM][OTf].

The severe measurement error of the [7]Li diffusion must be considered, in order to categorize the results from Figure A.14. Therefore, in Figure A.15 the [7]Li diffusion curves of S3 and S5 are shown, which exhibit a severe scattering. Based on them, no clear differences in the [7]Li diffusion coefficients can be derived for the sample series.
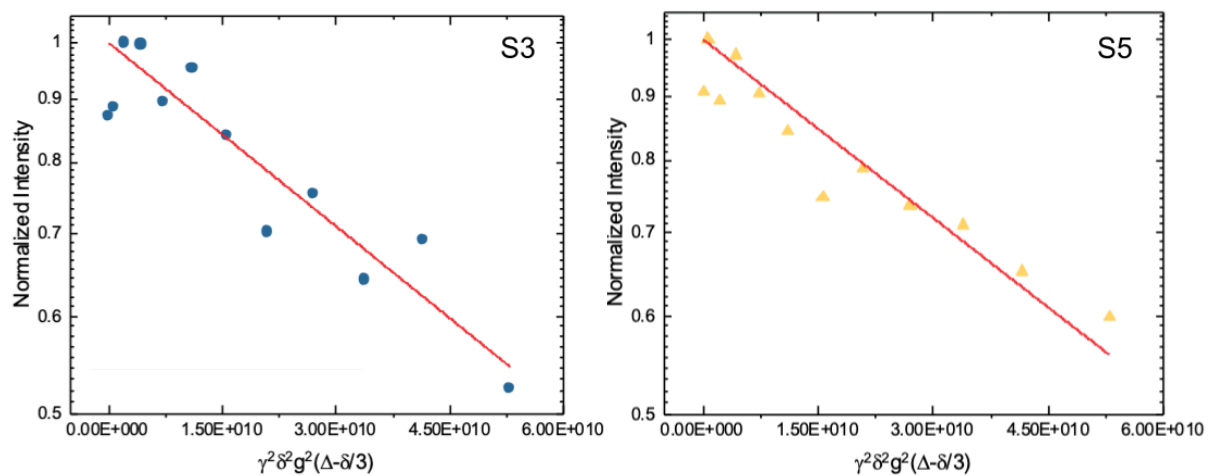

Figure A.15: [7]Li Stejskal-Tanner plots of sample S3 (D= $1.1 \cdot 10^{-11}$ m^2/s) and S5 (D= $1.1 \cdot 10^{-11}$ m^2/s).

References

(1) Acevedo, N. C., MacMillan, B., Newling, B., & Marangoni, A. G. (2017). Shear effects on the diffusive movement of oil in triacylglycerol networks. *RSC advances*, *7*(3), 1634-1642.

A.5 Supplementary Material for Section 5.4

An electrochemical measurement protocol was used in order to perform cell conditioning. The 18-step protocol is shown in Table A.3.

Table A.3: Electrochemical cell conditioning protocol

Nr.	Method	Nr.	Method
1	OCV	10	PEIS
2	PEIS	11	OCV
3	OCV	12	CA
4	CA	13	CA
5	CA	14	PEIS
6	PEIS	15	OCV
7	OCV	16	CA
8	CA	17	OCV
9	OCV	18	PEIS

Chronoamperometry (CA) measurements were carried out at different stages in the conditioning protocol. A current of ± 10 mA is applied in the E range of -2.5-2.5 V (100 μV resolution). This corresponds to a current density of 5.6 mA/cm^2. PEIS (Potentiostatic electrochemical impedance spectroscopy) was carried out in the frequency window 100 mHz-7 MHz, using a sinus input signal of 80 mV (E range: -2.5-2.5 V and 100 μV resolution). Open-circuit-voltage (OCV) was measured for the symmetric Li-cells. Here, no external load is connected to the symmetric cell. OCV probes the potential difference between both electrodes.
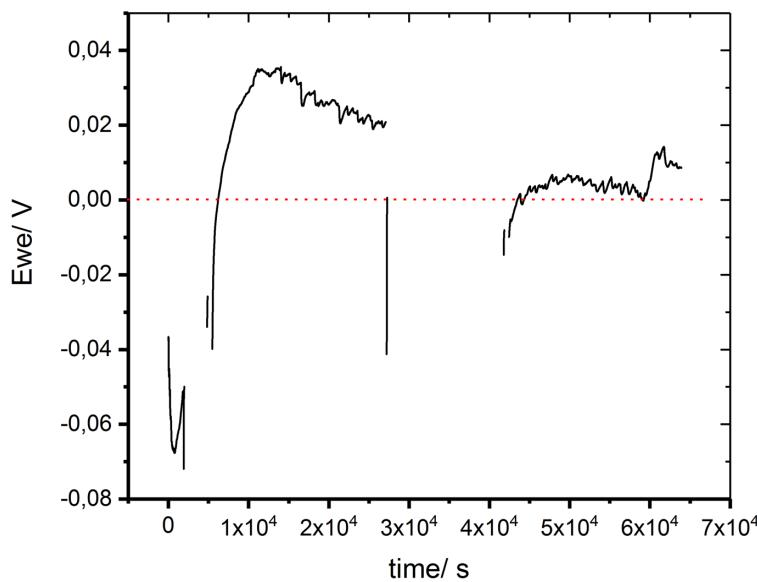
Figure A.16: Example OCV curves of the 0.3 m ES + PVdF-HFP polymer electrolyte at the five different stages of cell conditioning.

Clearly, over the range of experiments, the OCV curve shown in Figure A.16 nearly reaches the theoretical value of 0 V. Furthermore, the chronoamperometry measurement of the 0.3 m ES + PVdF-HFP polymer electrolyte sample is shown in Figure A.17. Based on this curve, an estimation regarding the lithium transference number can be obtained. Based on this finding, the lithium transference number is calculated as $t_+ = 0.124$.
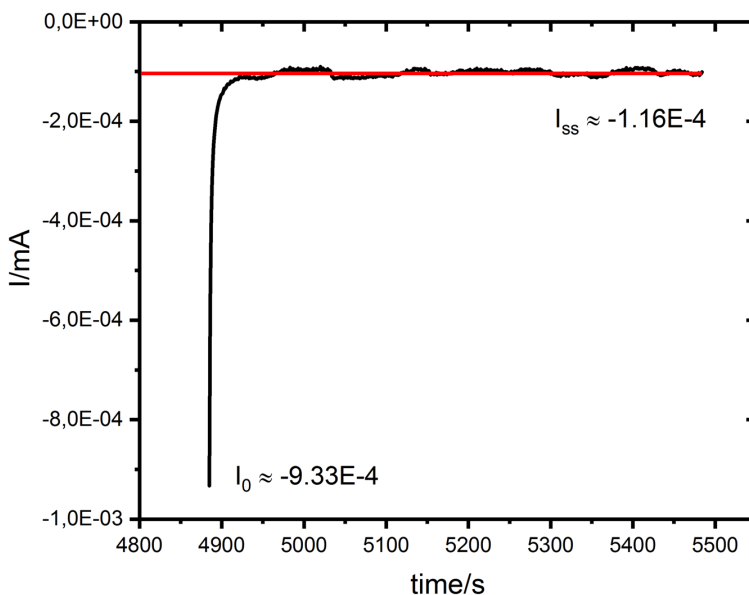
Figure A.17: CA plot of the 0.3 m ES + PVdF-HFP polymer electrolyte showing the evolution of the current over time.
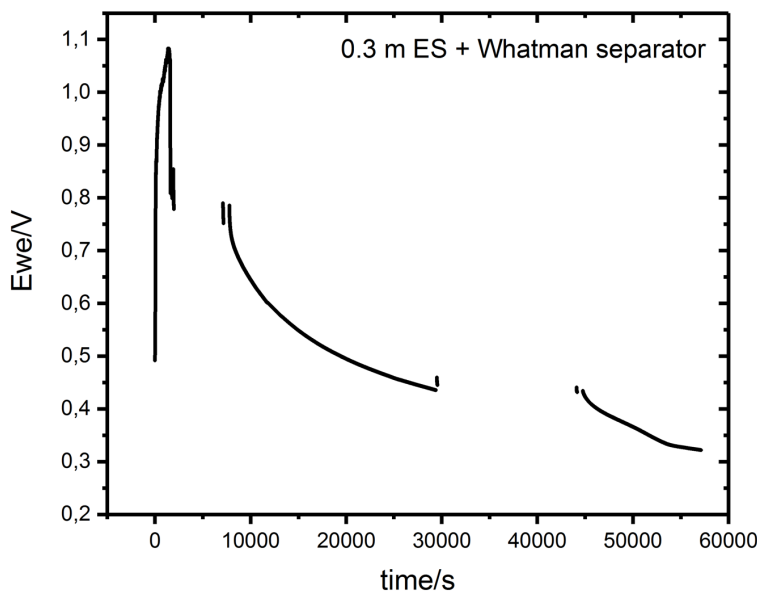
Figure A.18: OCV curves of the 0.3 m ES + Whatman separator at different stages of the cell conditioning.

As seen in Figure A.18, large fluctuations of the cell potential of c. 1.08 V can be found for the 0.3 m ES + Whatman separator, which is not seen for the 0.3 m ES + PVdF-HFP polymer electrolyte. This finding may be explained by a large electrolyte solution concentration gradient present in the 0.3 m ES + Whatman separator. Figure A.19 shows the chronoamperometry measurement of the 0.3 m ES + Whatman separator sample. Based on this finding, the lithium transference number is calculated as $t_+ = 0.186$.
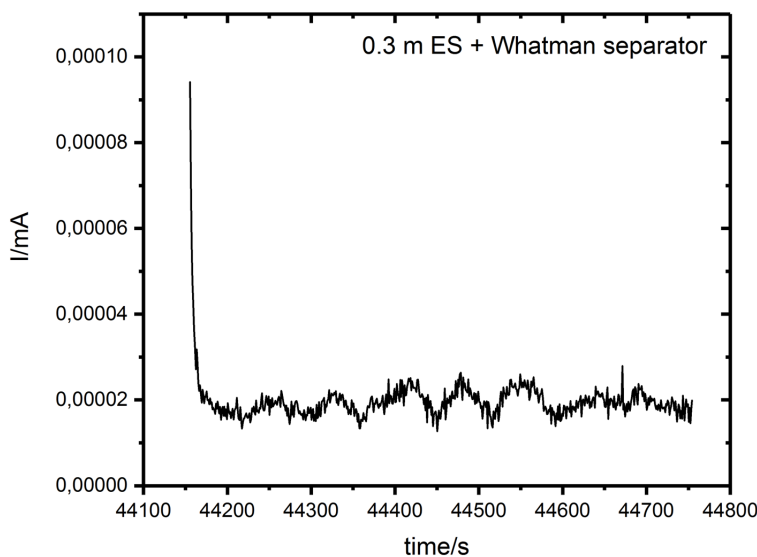

Figure A.19: CA plot of the 0.3 m ES + PVdF-HFP polymer electrolyte showing the evolution of the current over time.

A.6 Supplementary Material for Section 5.5

Additional photographs of the pristine sample and the sample after MAS are shown in Figure A.20. SEM images of the neat PVdF-HFP polymer film and the inner rotor wall are shown in Figures A.21 and A.22.
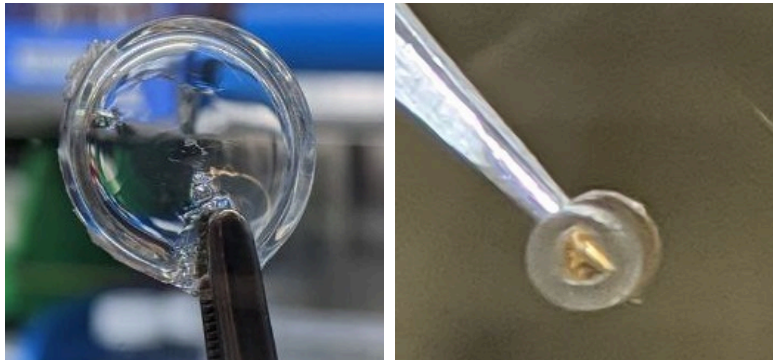

Figure A.20: Photographs of the polymer electrolyte film as prepared (left) and of the polymer electrolyte after exposure to MAS in a 4 mm rotor (right). During MAS the sample assumes the shape of a hollow cylinder and becomes turbid.
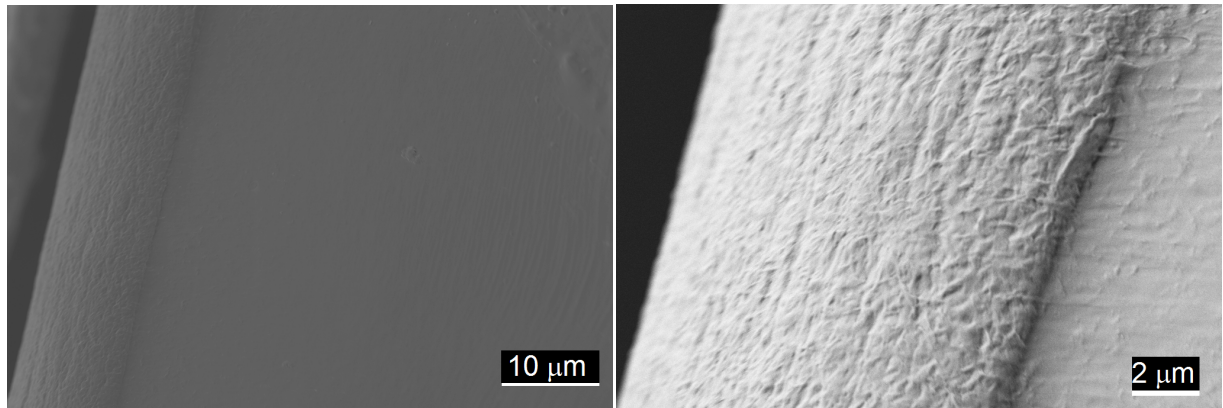

Figure A.21: SEM images of the PVdF-HFP film. Left: Top view of the film (view along the sample axis z_s); Right: Edge view of the film (view axis is close to the sample axis x_s).
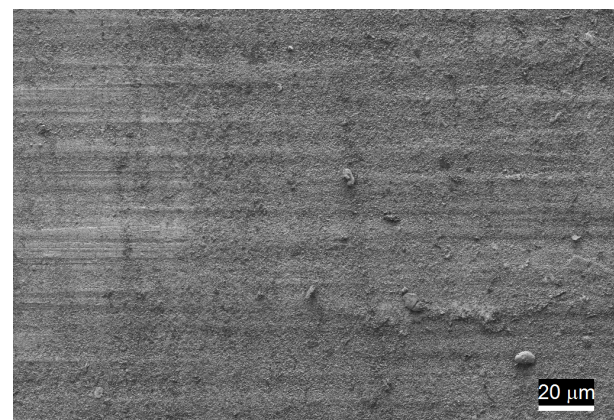

Figure A.22: SEM image of the inner rotor wall of a 4 mm MAS ZrO rotor.

Further, DSC cooling curves are shown in Figure A.23. The region of the barely visible glass transition temperature is indicated by the dotted line. Furthermore, the Nyquist plots are given in Figure A.24. Only for the pristine polymer electrolyte a semi-circle could be observed at −40 °C. The Cole-Cole plots in Figure A.25 were used previously to calculate the activation energies. The precise conductivity values at different temperatures and frequency 10^0 and 10^6 are shown in Table A.4.
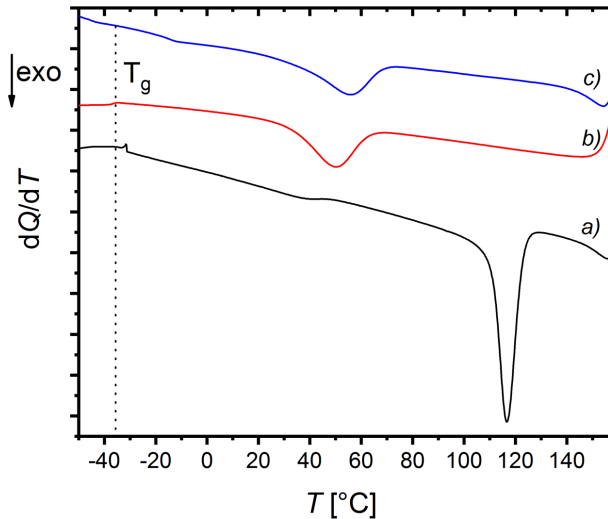

Figure A.23: DSC cooling curves of the first cooling cycle for PVdF-HFP (a), the pristine polymer electrolyte (b) and the polymer electrolyte after MAS (c). The vertical line indicates the glass transition temperature T_g of the pristine polymer electrolyte.
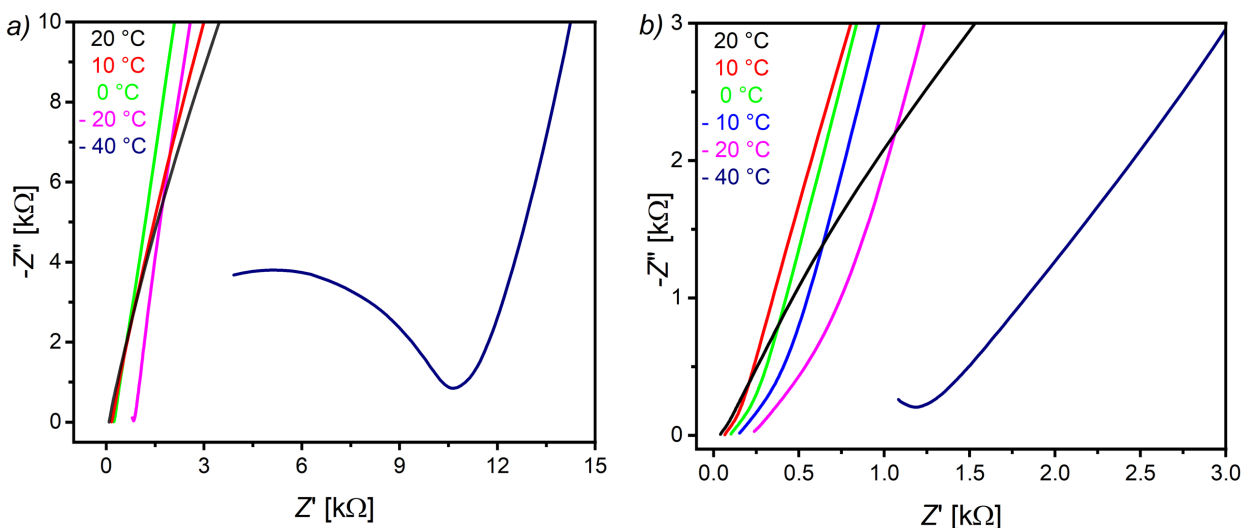

Figure A.24: Nyquist plots at different temperatures for the pristine polymer electrolyte (a) and the polymer electrolyte after MAS (b). The difference in impedance below the glass transition (curve for −40 °C) and above (all other curves) can be recognized.
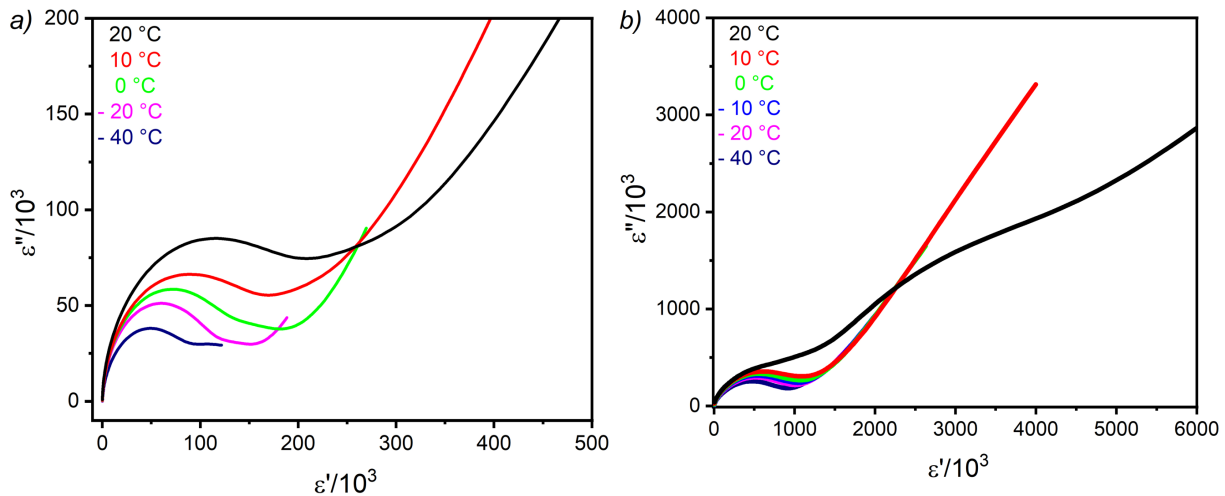
Figure A.25: Cole-Cole plots at different temperatures for the pristine polymer electrolyte (a) and the polymer electrolyte after MAS (b).

Table A.4: Ion conductivities at variable temperatures, obtained from frquency dependent conductivity plots.

f (Hz)	$\sigma^{\parallel}$ of the unspun polymer electrolyte (S·cm^{-1})					
	-40 °C	**-20 °C**	**0 °C**	**10 °C**	**20°C**	
10^0	$1.76 \cdot 10^{-8}$	$2.42 \cdot 10^{-8}$	$5.02 \cdot 10^{-8}$	$1.36 \cdot 10^{-7}$	$2.46 \cdot 10^{-7}$	
10^6	$5.18 \cdot 10^{-6}$	$4.71 \cdot 10^{-5}$	$1.65 \cdot 10^{-4}$	$2.38 \cdot 10^{-4}$	$4.87 \cdot 10^{-4}$	
f (Hz)	$\sigma^{\parallel}$ of the polymer electrolyte after MAS (S·cm^{-1})					
	-40 °C	**-20 °C**	**-10 °C**	**0 °C**	**10 °C**	**20 °C**
10^0	$1.48 \cdot 10^{-7}$	$3.6 \cdot 10^{-7}$	$5.92 \cdot 10^{-7}$	$9.93 \cdot 10^{-7}$	$1.99 \cdot 10^{-6}$	$3.09 \cdot 10^{-6}$
10^6	$8.72 \cdot 10^{-4}$	$4.15 \cdot 10^{-3}$	$6.50 \cdot 10^{-3}$	$9.75 \cdot 10^{-3}$	$1.50 \cdot 10^{-2}$	$2.24 \cdot 10^{-2}$

In Table A.5 the shielding tensor eigenvectors and eigenvalues of the C2–H, C4–H and the C5–H are reported in the principal axis system of the molecular inertia tensor. The molecular coordinates in the same axis system as shown in Figure 5.13.

Table A.5: Nuclear shielding eigenvectors and eigenvalues.

	σ_{xx}	σ_{yy}	σ_{zz}	σ_{iso}
	19.3	25.4	26.8	23.8
	Eigenvectors			
Hydrogen 2	**x**	**y**		**z**
	-0.14	-0.98		-0.17
	0.06	-0.18		0.98
	0.99	-0.13		-0.09
	σ_{xx}	σ_{yy}	σ_{zz}	σ_{iso}
	20.1	25.4	26.4	23.9
	Eigenvectors			
Hydrogen 4	**x**	**y**		**z**
	0.08	-0.99		-0.10
	-0.02	-0.10		-0.99
	-0.99	-0.09		0.01
	σ_{xx}	σ_{yy}	σ_{zz}	σ_{iso}
	20.0	24.9	26.8	23.9
	Eigenvectors			
Hydrogen 5	**x**	**y**		**z**
	-0.07	0.91		0.42
	0.07	0.42		-0.91
	0.99	-0.03		0.07

A.7 Supplementary Material for Section 6.1

The ¹H and ¹³C resonance frequencies were 299.8145 MHz and 75.39 MHz, respectively. A 4 mm MAS probe (Bruker) was used; the spinning frequency was set to 7 kHz. ¹³C MAS time-domain data were obtained by use of direct excitation (DE) or cross polarization (CP) from ¹H with a contact time of 2 ms, using ¹H decoupling. CP excitation curves for contact times between 10 μs and 8 ms are presented below. For ¹³C NMR measurements a spectral width of ± 100 kHz, a pulse duration of 3.5 μs, 8192 time-domain data points, a recycling delay of 3 s for CP and 5 s for DE and typically 4096 scans were used. An exponential apodization corresponding to a line width of 100 Hz was applied to the ¹³C time-domain data to smoothen the spectra.¹³C spectra were externally referenced to the methine carbon signal of adamantane at 29.5 ppm.

As seen in Figure A.26, ¹³C sites which are directly attached to ¹H (aliphatic carbons) reach their intensity maximum at shorter contact times compared to other carbon sites, where H atoms are further distanced. Signal assignment of the ¹³C CP spectra of trehalose- and sucrose-derived hydrochars is carried out in Tables A.6 and A7.
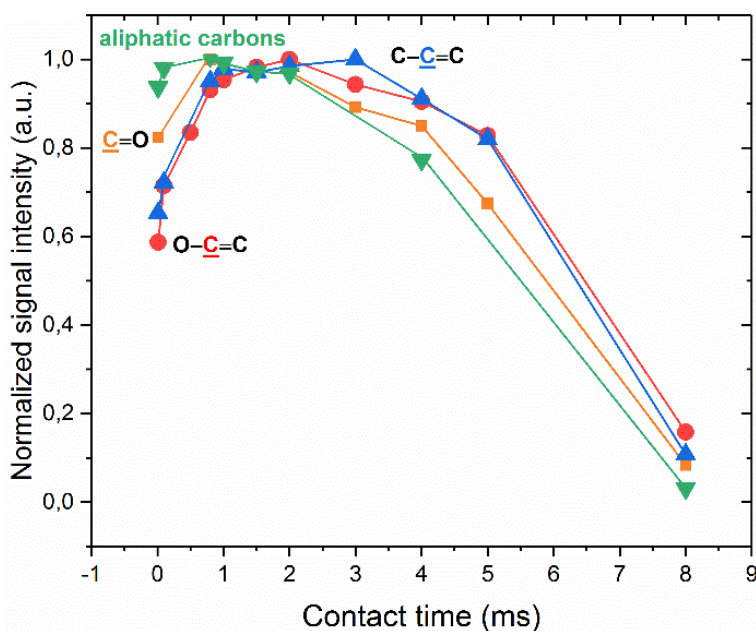

Figure A.26: ¹³C-CP excitation curves shown for different carbon sites. Green triangles: peak maximum in the aliphatic region (peak a in Fig. 3a), blue triangles: furan β-C (peak b), red circles: furan α-C (peak e), orange squares: ketone peak (g).

Table A.6: [13]C chemical shifts of the labeled peaks in Figure 6.2 and corresponding peaks of carbonaceous material, not including embedded levulinic acid, reported by Bacille et al.[1]

This work (Fig. 6.2)		Ref. 1		
Peak	δ /ppm	Peak	δ/ppm	assignment
a (max. of group of unresolved peaks)	29.5	A	13.9	CH_3 (mobile)
		B	23.9	CH_2 (rigid, bridge between furan rings)
		C	28.7, 29.6	CH_2 (rigid), CH_3 (mobile)
		D	38.3	CH_2 (mobile)
		E	50.5	CH
b	114.5	F	110.0	furan β-C, $-C=$ bridge between α-C positions of furan
		G	118.2	furan β-C
c	129.9	H	131.2	quaternary C of graphene
d	141.2	I	140.7	quaternary C of directly connected α-C
e	150.1	J	148–156	α-C
f	177.7	K	175–179	aldehyde C=O
g	208.4	L	202–207	ketone C=O, aldehyde at furan ring
	absent	M	218.4	C=O bridge between furan rings

Table A.7: [13]C chemical shifts of the labeled peaks in Figure 6.5 and corresponding peaks of the carbonaceous material.

This work (Fig. 6.5)		Ref. 1		
Peak	δ /ppm	Peak	δ/ppm	assignment
a (max. of group of unresolved peaks)	29.5	A	13.9	CH_3 (mobile)
		B	23.9	CH_2 (rigid, bridge between furan rings)
		C	28.7, 29.6	CH_2 (rigid), CH_3 (mobile)
		D	38.3	CH_2 (mobile)
		E	50.5	CH
b	116.9	F	110.0	furan β-C, $-C=$ bridge between α-C positions of furan
		G	118.2	furan β-C
c	129.3	H	131.2	quaternary C of graphene
d	144.1	I	140.7	quaternary C of directly connected α-C
e	150.6	J	148–156	α-C
f	175.2	K	175–179	aldehyde C=O
g	208.3	L	202–207	ketone C=O, aldehyde at furan ring
	absent	M	218.4	C=O bridge between furan rings

References

(1) Baccile, N., Laurent, G., Babonneau, F., Fayon, F., Titirici, M. M., & Antonietti, M. (2009). Structural characterization of hydrothermal carbon spheres by advanced solid-state MAS 13C NMR investigations. *The Journal of Physical Chemistry C*, *113*(22), 9644-9654.

A.8 Supplementary Material for Section 6.3

A deconvolution of the ^{13}C DE spectrum of cG@700 (Figure 6.12) is shown in Figure A.27. Two gaussian signals are present at 117.9 ppm and 149.3 ppm. The ^1H NMR spectra in Figure A.28 show that the H_2O signal at -1.5 ppm is persistent against elevated temperatures.
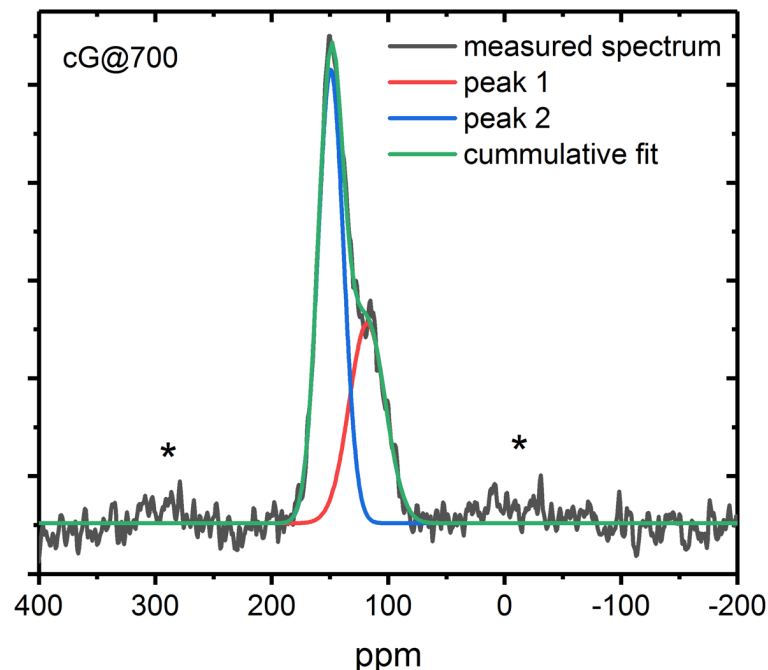

Figure A.27: Gaussian deconvolution of the ^{13}C MAS spectrum of cG@700.
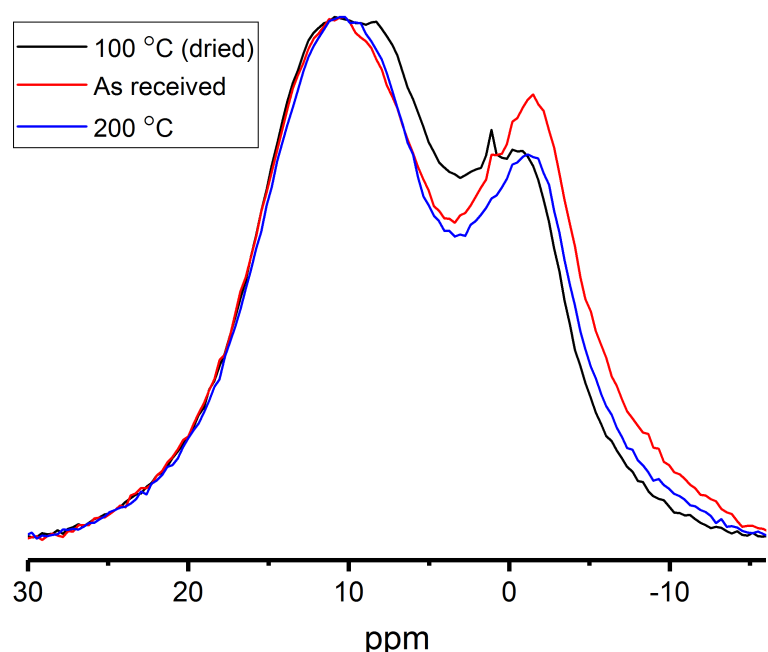

Figure A.28: ^1H 10 kHz MAS spectra of cG@700-SZ10, showing the received material, dried at 100 °C in an oven and dried at 200 °C in an argon glovebox.

Sample degassing is a crucial step in order to distinguish different ^{1}H atoms (structural and from water). As shown in Figures A.28−A.30 the different ^{1}H spectra are highly sensitive to drying times and the use of a vacuum cold trap. In order to remove most of the physiosorbed H_2O from the matrix, sufficiently long vacuum drying times of at least 12 h are required.
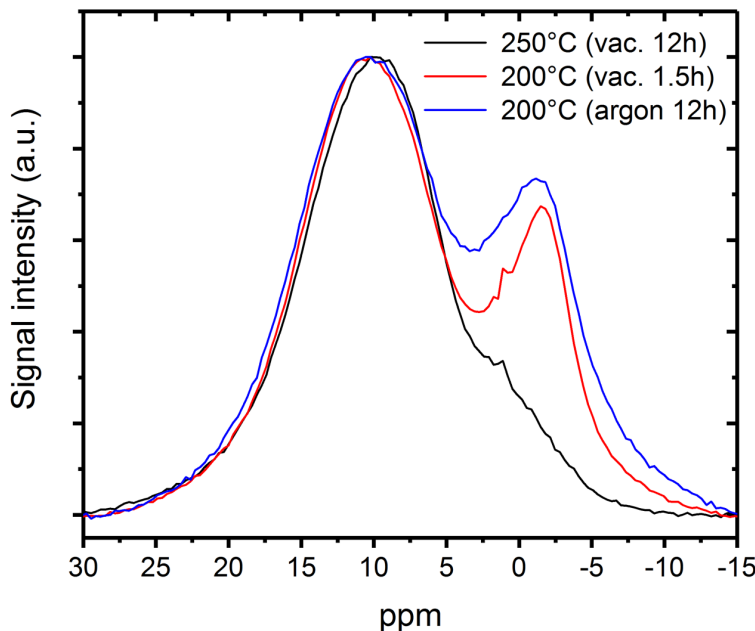

Figure A.29: ^{1}H 10 kHz MAS spectra of cG@700-SZ10, comparing different vacuum drying ($1 \cdot 10^{-3}$ mbar) times with a sample dried in an argon glovebox.
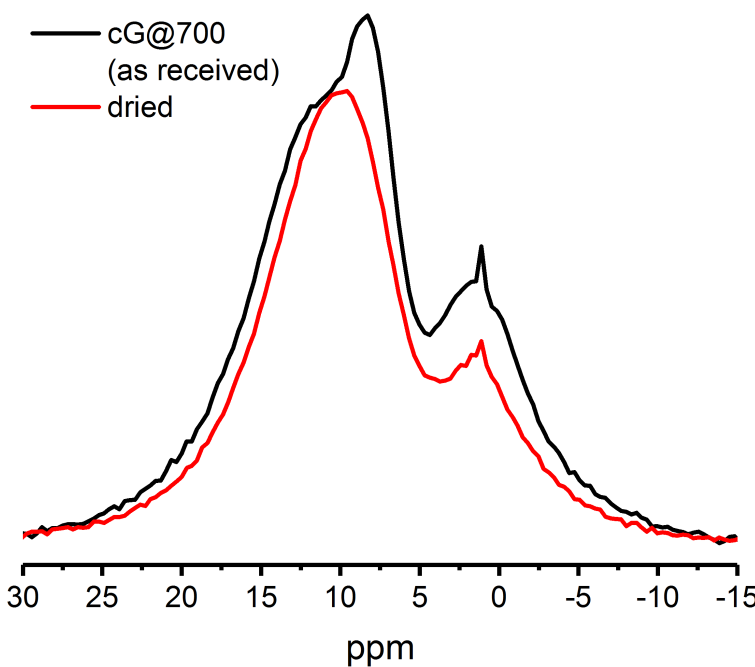

Figure A.30: ^{1}H 10 kHz MAS spectra of cG@700, comparing the received sample with a vacuum dried ($1 \cdot 10^{-3}$ mbar) for 48 h.

Additional support for the interpretation of irreversible H_2O loss (instead of transfer to in-pore H_2O) can be obtained from time-dependent spectra presented in Figure A.31. Clearly, the bulk water signal at 4.7 ppm diminishes in intensity and is not retained as in-pore water. The presented spectra in Figure A.31 additionally demonstrate the water repelling character of the C_1N_1 material, where no additional "in-pore" water can be observed over time.
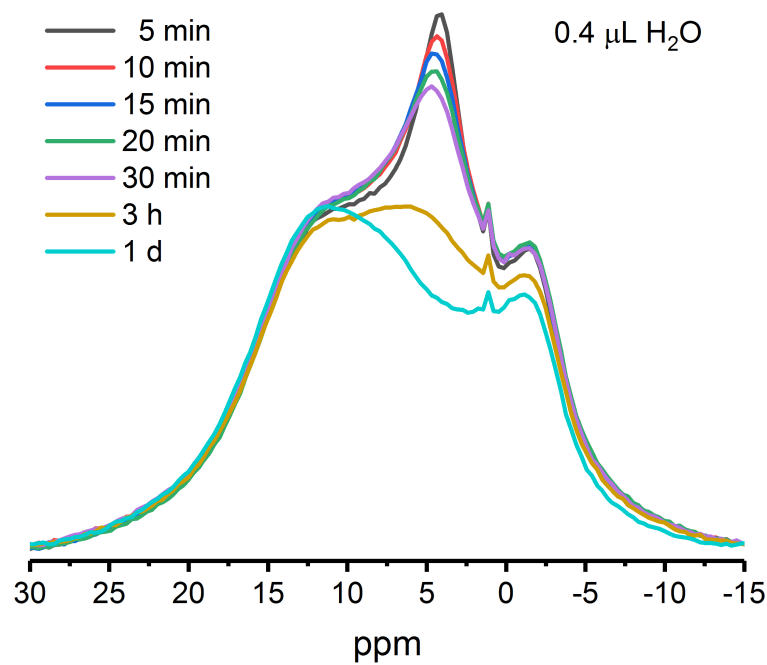

Figure A.31: Time-dependent ^1H 10 kHz MAS spectra of 0.4 μL H_2O added to cG@700-SZ10.